Université du Québec à Chicoutimi

Effect of Scandium on 1xxx and 3xxx Heat Exchanger Alloys

By Alyaa Bakr

Under the supervision of Prof. X.-Grant Chen, co-supervision of

Prof. Paul Rometsch

Thesis Presented to the University of Quebec at Chicoutimi in Partial Fulfillment of the Requirements for the Degree of Philosophy Doctor (Ph.D.) in Engineering

Defended on 20 August 2026

Board of Examiners:

Professor Mousa Javidani, Department of Applied Sciences at UQAC, President of the board of Examiners

Professor Emad Elgallad, Department of Mechanical Engineering, Université de Moncton, External Member of Examiners

Professor X.-Grant Chen, Department of Applied Sciences at UQAC, Internal Member of Examiners

Professor Paul Rometsch, Rio Tinto Aluminum, Saguenay, Quebec, Internal Member of Examiners

Professor Dilip Sarkar, Department of Applied Sciences at UQAC, Internal Member of Examiners

Québec, Canada

Effet du scandium sur les alliages 1xxx et 3xxx pour échangeurs de chaleur

Résumé

Les composants légers en aluminium utilisés dans les échangeurs de chaleur jouent un rôle essentiel dans l'amélioration de l'efficacité énergétique des véhicules et la réduction des émissions de CO_2. Les alliages d'aluminium des séries 1xxx et 3xxx sont largement utilisés dans ces composants en raison de leur excellente formabilité, de leur bonne résistance à la corrosion et de leurs conductivité thermique favorable. Les échangeurs de chaleur sont fabriqués en formant des feuilles et des tubes d'aluminium selon les géométries souhaitées, puis en assemblant les différentes pièces par brasage. Lors du processus de brasage, les composants de l'échangeur de chaleur sont exposés à une courte période de température élevée qui met à l'épreuve leur stabilité granulaire intrinsèque. Cette exposition thermique peut favoriser la recristallisation et la croissance anormale des grains, ce qui dégrade considérablement la résistance mécanique des composants brasés. Les précipités contenant du scandium sont particulièrement efficaces pour contrôler la restauration, la recristallisation et la croissance des grains dans les alliages d'aluminium, améliorant ainsi leur stabilité granulaire lors d'une exposition à haute température. Cette étude vise à explorer l'effet du micro-alliage avec le Sc, ou avec le couple Sc–Zr, sur l'évolution de la microstructure et des propriétés des alliages AA1xxx et AA3xxx utilisés dans les échangeurs de chaleur brasés. Elle est présentée en quatre parties, comme indiqué ci-dessous.

Dans la première partie, une étude portant sur l'impact du micro-alliage au Sc et au Zr sur la stabilité microstructurale d'alliages 1xxx déformés à chaud et soumis à un recuit post-déformation entre 500 et 575 ºC pendant 1 h, afin de simuler des procédés de type brasage, est présentée. Quatre alliages ont été examinés: l'alliage 1xxx de base, Al-0,07Sc, Al-0,07Sc-0,10Zr et Al-0,19Sc-0,15Zr. Le traitement à 500 ºC a conduit à une recristallisation complète de l'alliage de base, tandis que les températures plus élevées ont favorisé une croissance anormale des grains. L'alliage Al-0,07Sc a résisté à la recristallisation à 500 ºC, mais a été entièrement recristallisé à 550 ºC. En revanche, l'alliage Al-0,07Sc-0,10Zr a conservé une bonne stabilité granulaire jusqu'à 550 ºC grâce à la présence de précipités stables $Al_3(Sc,Zr)$; toutefois, une recristallisation partielle a été observée à 575 ºC. L'alliage Al-0,19Sc-0,15Zr a préservé l'essentiel de sa microstructure déformée même après un traitement à 575 ºC. Il a montré la plus grande résistance à la recristallisation parmi les quatre alliages étudiés en raison de la densité numérique plus élevée et de la taille plus fine des précipités $Al_3(Sc,Zr)$, ce qui suggère que cet alliage pourrait être utilisé dans des conditions encore plus sévères, incluant des températures de brasage supérieures à 575 ºC.

Dans la deuxième partie, une étude portant sur des bandes minces extrudées en alliage 1xxx a été menée selon deux voies de traitement thermique avant extrusion : la Route 1 (R1), comprenant une homogénéisation à haute température à 600 °C pendant 4 h, et la Route 2 (R2), comprenant un prévieillissement à 350 °C pendant 24 h. Les effets du microalliage avec le Sc et le Zr sur la structure granulaire, les propriétés mécaniques et la résistance à la corrosion ont ensuite été systématiquement étudiés selon ces deux voies de traitement. Trois alliages ont été étudiés : un alliage 1xxx de base exempt de Sc et de Zr, un alliage Al-Sc-Zr à faible teneur en Sc/Zr (0,10 % mas. Sc, 0,10 % mas. Zr) et un alliage Al-Sc-Zr fortement micro allié (0,19 % mas. Sc, 0,15 % mas. Zr). L'alliage de base a présenté une microstructure entièrement recristallisée avec des grains très grossiers après brasage à 605 ºC pour les deux routes, ce qui s'est traduit par de faibles résistances mécaniques. Avec le micro-alliage Sc et Zr, la structure

granulaire est devenue plus fine et plus stable, et les propriétés mécaniques se sont nettement améliorées. Parmi les trois alliages étudiés, le fort micro-alliage Al-Sc-Zr a été le seul à conserver la majeure partie de sa microstructure déformée après le brasage simulé à 605 ºC. Ces résultats ont été confirmés en extrudant des micro-tubes multi-canaux puis en les soumettant à un brasage simulé. Pour les deux routes, un traitement de vieillissement post-brasage a favorisé la précipitation fine d'$Al_3(Sc,Zr)$ et a considérablement renforcé les alliages contenant du Sc. Globalement, tandis que l'alliage fortement micro allié Al-Sc-Zr a offert la meilleure combinaison de stabilité granulaire, de résistance mécanique, de résistance à la corrosion et d'extrudabilité pour la Route 1 (augmentation de la température d'homogénéisation), l'alliage faiblement micro allié Al-Sc-Zr a tout de même montré des améliorations notables par rapport à l'alliage de base.

Dans la troisième partie, l'étude a débuté par des expériences à l'échelle du laboratoire sur trois alliages de la série 3xxx, avec et sans micro-ajouts de Sc et de Zr. Cette étape visait à établir une compréhension fondamentale du comportement des alliages sous des conditions de déformation à chaud et de brasage représentatives du procédé industriel des échangeurs de chaleur brasés. Après un écrouissage de 2 % suivi du brasage, l'alliage de base a présenté une faible stabilité des grains avec des signes évidents de croissance anormale des grains (AGG), tandis que les alliages contenant du Sc/Zr ont conservé des microstructures stables avec une recristallisation limitée ou inexistante. Par la suite, des essais d'extrusion de bandes plates ont été réalisés afin d'évaluer l'extrudabilité et les performances mécaniques. La pression d'extrusion a augmenté d'environ 13 à 18 % avec les ajouts de Sc/Zr, indiquant une résistance accrue à la déformation et une extrudabilité réduite. La limite d'élasticité a augmenté de 42 MPa pour l'alliage de base à 70-89 MPa après brasage, puis à 109-127 MPa après vieillissement post-brasage, en raison de la précipitation de fines nanoparticules d'$Al_3(Sc,Zr)$, correspondant à des augmentations allant jusqu'à 191 %. Enfin, l'étude a été étendue à la fabrication d'extrusions multi-canaux (MPE), représentatives de la géométrie des tubes plats utilisés dans les échangeurs de chaleur. Les tubes MPE de l'alliage de base ont présenté des grains grossiers et une AGG localisée après le calibrage et le brasage, indiquant une perte de stabilité microstructurale, tandis que les alliages contenant du Sc/Zr ont conservé une microstructure stable lors du brasage.

Dans la quatrième partie, une étude a été menée afin d'explorer le potentiel des ajouts de Sc et de Zr dans un alliage 3xxx typique utilisé pour les tubes MPE des échangeurs de chaleur brasés. Trois alliages ont été étudiés dans ce travail : le premier est un alliage d'aluminium 3xxx typique utilisé dans les échangeurs de chaleur brasés, le second est un alliage (L-ScZr) contenant 0,11 % massique de Sc et 0,10 % massique de Zr, et le troisième est une variante modifiée Sc–Zr (H-ScZr) contenant 0,21 % massique de Sc et 0,15 % massique de Zr. Les trois alliages ont été soumis à un traitement thermique à basse température à 375 °C pendant 24 h, puis extrudés sous forme de tubes multi-canaux (MPE). L'application d'une légère réduction d'épaisseur de seulement 2 %, suivie d'un brasage à 605 ºC pendant 2,5 minutes, a entraîné un grossissement marqué des grains dans l'alliage de base, tandis que les alliages contenant Sc–Zr ont montré une meilleure stabilité des grains, l'alliage H-ScZr présentant la stabilité des grains la plus élevée. L'application d'un traitement de vieillissement post-brasage à 350 ºC pendant 4 heures a entraîné un renforcement significatif des alliages contenant Sc–Zr, avec une augmentation de la limite d'élasticité pouvant atteindre environ 105 % par rapport à l'alliage de base.

Effect of Scandium on 1xxx and 3xxx Heat Exchanger Alloys

Abstract

Lightweight aluminum heat exchanger components play a key role in improving vehicle fuel efficiency and lowering CO2 emissions. 1xxx and 3xxx series aluminum alloys are widely used in heat exchanger components because they offer excellent formability, good corrosion resistance, and favorable thermal conductivity. Heat exchangers are fabricated by forming the aluminum sheets and tubes into the desired geometries and assembling the components together through brazing. During the brazing process, heat exchanger components are exposed to a short period of high temperature that challenges their intrinsic grain stability. This high-temperature thermal exposure can promote recrystallization and abnormal grain growth, which significantly degrade the mechanical performance of brazed components. Sc containing precipitates are highly effective in regulating recovery, recrystallization, and grain growth in Al alloys, thus enhancing their grain stability during high-temperature exposure. This study aims to explore the effect of microalloying with Sc or Sc and Zr on the microstructure and property evolution of AA1xxx and AA3xxx alloys for brazed heat exchangers. It is presented in four parts as outlined below.

In the first part, a study on the impact of Sc and Zr microalloying on the microstructure stability of hot deformed 1xxx alloys subjected to post-deformation annealing from 500 to 575 ºC for 1 h to simulate brazing-type processes is presented. Four alloys were studied: namely 1xxx base, Al-0.07Sc, Al-0.07Sc-0.10Zr and Al-0.19Sc-0.15Zr alloys. Annealing at 500 ºC led to complete recrystallization in the base alloy, while higher annealing temperatures promoted abnormal grain growth. The Al-0.07Sc alloy resisted recrystallization at 500 ºC but was fully recrystallized by 550 ºC. In contrast, the Al-0.07Sc-0.10Zr alloy retained its grain stability up to 550 ºC owing to the presence of stable $Al_3(Sc,Zr)$ precipitates; however, partial recrystallization occurred at 575 ºC. The Al-0.19Sc-0.15Zr alloy preserved most of its deformed microstructure even after annealing at 575 ºC. It showed the highest recrystallization resistance among the four alloys studied owing to its highest number density and finest size of $Al_3(Sc,Zr)$ precipitates, which suggests that this alloy can be applied in even more extreme conditions including brazing temperatures above 575 ºC.

In the second part, a study focused on 1xxx extruded thin strips, using two different pre-extrusion heat-treatment routes: Route 1 (R1), involving high-temperature homogenization at 600 ºC for 4 h, and Route 2 (R2), involving pre-aging at 350 ºC for 24 h. The effects of Sc/Zr microalloying on grain structure, mechanical properties, and corrosion resistance were then systematically investigated under two different processing routes. Three alloys were examined: a 1xxx base alloy free of Sc and Zr, a low Al-Sc-Zr alloy (0.10 wt.% Sc, 0.10wt.% Zr), and a high Al-Sc-Zr alloy (0.19 wt.% Sc, 0.15 wt.% Zr). The base alloy exhibited a very coarse recrystallized grain structure after brazing at 605 ºC under both processing routes, resulting in low mechanical strengths. With Sc and Zr microalloying, the grain structure became finer and more stable, and the mechanical strengths were significantly improved. Among the three alloys studied, the high Al-Sc-Zr alloy was the only one that maintained most of the deformed grain structure after simulated brazing at 605 ºC. Those findings were further validated by extruding micro multi-port tubes and subjecting them to a simulated braze. For both routes, a post-braze aging treatment further promoted fine $Al_3(Sc, Zr)$ precipitation and significantly enhanced the strength of the Sc-containing alloys. Overall, while the high Al-Sc-Zr alloy provided the best combination of grain stability, mechanical strength, corrosion resistance, and extrudability

under Route 1 (high-temperature homogenization), the low Al-Sc-Zr alloy still demonstrated clear improvements over the base alloy.

In the third part, the study began with laboratory-scale experiments on three 3xxx-based alloys, with and without Sc and Zr micro-additions. This stage aimed to establish a fundamental understanding of the alloys' behavior under hot deformation and brazing conditions representative of industrial processing of brazed heat exchangers. Following 2% cold working and brazing, the base alloy exhibited poor grain stability with clear signs of abnormal grain growth (AGG), whereas the Sc/Zr-containing alloys maintained stable microstructures with limited or no recrystallization. Subsequently, flat strip extrusion trials were conducted to evaluate extrudability and mechanical performance. The ram pressure increased by approximately 13-18% with Sc/Zr additions, indicating higher deformation resistance and reduced extrudability. With the addition of Sc and Zr, the yield strength increased from 42 MPa in the base alloy to 70-89 MPa after brazing, and further to 109-127 MPa after post-braze aging due to the precipitation of fine $Al_3(Sc, Zr)$ nanoparticles, corresponding to increases of up to 191%. Finally, the study was scaled up through the fabrication of multi-port extrusions (MPE), representative of flat tube geometries used in heat exchanger applications. The MPE tubes of the base alloy exhibited coarse grains and localized AGG after sizing and brazing, indicating a loss of grain stability, whereas the Sc/Zr-containing alloys preserved a stable microstructure during brazing.

In the fourth part, a study was conducted to explore the potential of Sc and Zr additions in a typical 3xxx alloy used for MPE tubes in brazed heat exchangers. Three alloys were investigated in this study: the first is a typical 3xxx aluminum alloy used in brazed heat exchangers, the second is (L-ScZr) alloy containing 0.11 wt.% Sc and 0.10 wt.% Zr, and the third is a Sc-Zr-modified variant (H-ScZr) containing 0.21 wt.% Sc and 0.15 wt.% Zr. The three alloys were homogenized at 375 ºC for 24 hours and subsequently extruded into multi-port extruded (MPE) tubes. Subjecting the tubes to a small thickness reduction of only 2% followed by brazing at 605 ºC for 2.5 minutes resulted in pronounced grain coarsening in the base alloy, whereas the Sc-Zr showed improved grain stability with the H-ScZr alloy exhibiting the highest grain stability. Post-braze aging at 350 ºC for 4 hours resulted in significant strengthening in the Sc-Zr variants, with the yield strength increasing by up to approximately 105% compared with the base alloy.

Table of Contents

List of Tables

List of Figures

List of Symbols

Al	Aluminum
Sc	Scandium
Zr	Zirconium
Fe	Iron
Si	Silicon
Mn	Manganese
Ti	Titanium
B	Boron
Mg	Magnesium
Cu	Copper
Zn	Zinc
Sn	Tin
T	Temperature
ºC	Temperature unit on Celsius scale
wt.%	Weight percentage
at%	atomic percentage
h	hour
min	minute
s	second
mm	millimeter
μm	micrometer

nm	nanometer
P_z	Zener drag pressure
γ_{GB}	Specific grain boundary energy
f_v	volume fraction of the precipitates
r	average radius of the precipitate

List of abbreviations

OM	Optical Microscopy
SEM	Scanning Electron Microscopy
TEM	Transmission Electron Microscopy
EDS	Energy-Dispersive X-Ray Spectroscopy
SADP	Selected Area Diffraction Pattern
EBSD	Electron Backscatter Diffraction
MPE	Multi Port Extrusion
AGG	Abnormal Grain Growth
YS	Yield Strength
UTS	Ultimate Tensile Strength
DC	Direct chill
SWAAT	Sea Water Acetic Acid Test

Dedication

To my beloved parents, Ali Bakr and Thoraya Salem whose inspiration, unwavering support, and endless encouragement have guided me every step of the way.

To my dear husband, Mostafa, my love and partner, whose patience, understanding, and constant encouragement made this journey possible.

To my lovely son, Ammar, the light of my life and my greatest source of joy and motivation.

To Mohamed, Hassan, Hussein, Hamza and Rowan, for always believing in me and reminding me of my strength.

To Belal, Saadany and Mahmoud for being there along the way.

.

Acknowledgements

I would like to express my deepest gratitude to everyone who has helped, encouraged, and supported me during my Ph.D. journey at the University of Quebec at Chicoutimi (UQAC).

First and foremost, I would like to express my deepest gratitude to my supervisor, Professor X.-Grant Chen, for his continuous encouragement, guidance, and support throughout my Ph.D. journey. I have learned so much from him, both scientifically and personally. His depth of knowledge, passion for research, and commitment to excellence have deeply influenced my development as a researcher. I will always be grateful for the opportunity to be part of his research group and for his patience, understanding, and invaluable advice.

I would also like to express my sincere gratitude to my co-supervisor and industrial partner from Rio Tinto, Professor Paul Rometsch, for his encouragement, valuable advice, and continuous support throughout my research. I am especially thankful for the valuable guidance he provided during the planning of experiments and paper writing. Also, for offering me the chance to observe extrusion trials for the first time. His guidance and encouragement throughout my Ph.D. journey have been truly inspiring.

Special thanks go to Prof. Zhan Zhang and Mr. Zhixing Chen for their invaluable help and support with the SEM and TEM observations, as well as for their training and guidance. I would also like to sincerely thank Mr. Samuel Dessureault for his assistance with alloy casting and Mr. Félix Tremblay for his help in machining all the samples used throughout this PhD project. In addition, I would like to express my deep appreciation to Professor Emad Elgallad for the valuable scientific discussions and insightful advice provided during my Ph.D. studies.

I am deeply thankful to Prof. Mousa Javidan, Prof. Duygu Kocaefe, and Prof. Dilip Sarkar, their warm assistance and whole-hearted support in providing technical guidance and engaging in scientific discussions.

I am deeply thankful to all my colleagues and friends at CURAL for their constant support, kindness, and friendship. The many discussions, laughter, and shared experiences made this journey truly memorable. A heartfelt thank you to my colleagues, Dr. Ahmed Algendy and Dr. Ali El ashery, for their help, encouragement, and support during my Ph.D. experiments and for making the lab a great place to work.

I would like to extend my deepest gratitude to Dr. Khaled Ragab for introducing me to the research group and for his generous support in facilitating my transition and settlement in Chicoutimi.

I gratefully acknowledge the financial support provided by the Natural Sciences and Engineering Research Council of Canada (NSERC) and Rio Tinto Aluminium through the Research Chair in the Metallurgy of Aluminum Transformation at the University of Quebec at Chicoutimi.

Chapter 1
Introduction

1.1 Background

Heat exchangers are widely used in air-conditioning and refrigeration systems, chemical and food-processing plants, aircraft, and automotive applications [1–3]. Heat exchangers are typically fabricated by forming aluminium sheets and tubes into the required geometries and assembling the components [4]. Commercial AA1xxx and AA3xxx aluminum alloys are aluminium alloys are widely used in heat exchangers , owing to their high formability, excellent thermal conductivity, and superior corrosion resistance [5–7]. Driven by stricter energy-efficiency regulations, escalating raw material costs, and growing environmental concerns, there is a rapidly increasing demand for lightweight and high-efficiency heat exchangers [8,9].

Multi-port extruded (MPE) tubes, commonly used in automotive air-conditioning heat exchangers, are flat aluminum extrusions containing multiple parallel channels separated by thin internal webs [9–11]. This geometry increases the surface-area-to-volume ratio, thereby improving heat-transfer efficiency , thereby improving heat-transfer efficiency [12]. MPE tubes are manufactured from homogenized billets through extrusion, followed by mechanical straightening and sizing. During sizing, the tubes undergo a small thickness reduction by cold rolling to achieve the dimensions required for subsequent assembly and brazing [13,14].

During the brazing process, the components are heated to around 600 ºC, allowing them to bond together [15,16]. Residual deformation introduced during sizing, followed by high-temperature brazing, can promote abnormal grain growth (AGG) in MPE tubes, leading to a deterioration of their mechanical strength and pressure-bearing capability [13,14]. AGG is an undesirable microstructural phenomenon, in which a limited number of grains grow disproportionately by consuming the surrounding fine recrystallized grains [17–20]. This results in an extremely non-uniform microstructure, which significantly compromises the performance of MPE tubes [21]. Controlling the post-brazed grain structure is essential to ensure sufficient pressure resistance and prevent refrigerant leakage, because leakage from a single tube can compromise the operation and integrity of the entire heat exchanger [22].

Microalloying aluminium with scandium (Sc) can improve high-temperature performance by restricting recrystallization and preserving grain stability [23–25]. Sc microalloying promotes the formation of a high number density of Al_3Sc nanoprecipitates, which strengthen the alloy, improve thermal stability, and restrict grain-boundary migration during high-temperature exposure [23,24]. The high price of Sc limits its widespread industrial adoption, encouraging the development of more economical alloying approaches [26]. A potentially more economical strategy is to combine Sc with zirconium (Zr), leading to the formation of $Al_3(Sc, Zr)$ precipitates [27]. Owing to the slower diffusivity of Zr compared to Sc in α-Al, $Al_3(Sc, Zr)$ precipitates consist of an Al_3Sc core surrounded by a Zr-enriched shell. These $Al_3(Sc, Zr)$ precipitates are more resistant to coarsening than Al_3Sc precipitates [25,28,29]. Multiple investigations [23,30–34] have shown that the Sc and Zr microadditions enhance alloy strength and retard recrystallization.

1.2 Problem statement

Although numerous studies have demonstrated that trace additions of Sc and Zr enhance the strength of aluminum alloys and delay recrystallization through the formation of fine $Al_3(Sc, Zr)$ nanoprecipitates, their application in brazed heat exchanger components remains insufficiently explored. Several key challenges remain unaddressed:

1) **Influence on recrystallization and grain growth**

   There is limited understanding of how Sc and Zr microadditions affect recrystallization and grain growth in 1xxx and 3xxx alloys used for brazed heat exchangers. Maintaining grain stability during extrusion and brazing is critical to preserving their mechanical integrity and performance.

2) **Process-composition interactions**

   Insufficient knowledge of how homogenization heat treatments, Sc content variations and the combined Sc and Zr additions affect the extrudability and the resulting strength, grain stability, and corrosion behaviour after brazing.

3) **Optimization of alloy chemistry and cost**

   Given the high cost of Sc, it is important to determine an effective Sc level in combination with Zr that provides adequate performance while limiting alloy cost.

4) **Limited data under industrially relevant conditions**

   Comprehensive data are lacking on the mechanical performance and grain stability of Sc–Zr-microalloyed 1xxx and 3xxx alloys processed as MPE tubes.

1.3 Objectives

The general objective of this project is to study the effect of microalloying with Sc or Sc and Zr on the microstructure and property evolution of AA1xxx and AA3xxx alloys for brazed heat exchangers. To achieve this general objective, the research programme was divided into four parts.

Part I: Effect of Sc and Zr microalloying on recrystallization behavior of 1xxx aluminum heat exchanger type alloys during post-deformation annealing.

a) Quantify how varying Sc and Zr microalloying levels influence the formation, size distribution and number density of Al_3Sc and Al_3(Sc, Zr) precipitates during homogenization in 1xxx-series alloys.
b) Determine the grain-structure stability of 1xxx-series alloys microalloyed with Sc or Sc+Zr when subjected to high-temperature post-deformation annealing treatments selected to represent brazing-related thermal exposure.

c) Evaluate how the thermal stability of Al_3Sc and $Al_3(Sc, Zr)$ precipitates under simulated brazing conditions contributes to resistance to recrystallization and abnormal grain growth.

Part II: Study of 1xxx aluminum extrusion alloys for brazed heat exchangers: Influences of Sc/Zr microalloying and thermomechanical processing

a) Investigate the influence of Sc and Zr microadditions on grain stability during extrusion and simulated brazing of 1xxx aluminum alloys processed as flat strips.
b) Assess how different homogenization treatment routes prior to extrusion affect the microstructure and mechanical properties of the extruded strips.
c) Examine the effect of simulated brazing on the room-temperature mechanical performance of the strips, emphasizing the role of Sc and Zr microadditions in strength retention.
d) Evaluate the corrosion resistance of the Sc-containing strips using the SWAAT test, based on weight-loss measurements after 5 and 20 days of exposure and average pit depth measurements after 20 days.
e) Evaluate the applicability of Sc–Zr-microalloyed 1xxx alloys to MPE tubes by examining their extrusion and post-braze grain stability.

Part III: Assessment of the effects of Sc/Zr microalloying on Al-Mn 3xxx brazed heat exchangers: From lab scale to multi-port tube Extrusions.

a) Conduct laboratory-scale experiments on three 3xxx-based alloys, with and without Sc and Zr microadditions, to establish a fundamental understanding of their behavior under hot-deformation and simulated brazing conditions representative of industrial heat-exchanger processing.

b) Scale up the study by extruding industrial billets of 3xxx-based alloys, with and without Sc and Zr microadditions into 30 mm x 1.4 mm flat strips to evaluate their extrudability, post-braze mechanical properties, and strengthening response to post-braze aging.

c) Extrude 3xxx-based billets, with and without Sc and Zr microadditions, into MPE tubes representing the typical geometry used in brazed heat exchangers to validate the observed grain-stability trends in an industrially relevant MPE-tube geometry.

Part IV: The Potential of Sc-Zr Microalloying for Improving grain Stability and Mechanical Strength in 3xxx Multi-Port Extruded (MPE) tubes.

a) Investigate the influence of Sc and Zr microalloying additions on grain stability of 3xxx aluminum alloys during brazing of multi-port extruded (MPE) tubes, with emphasis on mitigating grain coarsening.

b) Evaluate the effect of a small thickness reduction prior to brazing on the microstructural evolution and grain stability of MPE tubes with and without Sc and Zr microadditions.

c) Assess the room-temperature mechanical properties of the brazed MPE tubes, focusing on the role of Sc and Zr microalloying in improving mechanical strength.

d) Examine the effect of post-brazing aging heat treatment on the strengthening response of the Sc–Zr-containing alloys .

1.4 Originality statement

This research presents a comprehensive, multi-scale investigation of the effects of Sc and Zr microalloying on the microstructure and property evolution of 1xxx and 3xxx aluminum alloys developed for brazed heat-exchanger applications. Although Sc/Zr-containing precipitates are known to retard recovery, recrystallization, and grain growth in aluminium alloys, their effects on the microstructural evolution and performance of 1xxx and 3xxx heat-exchanger alloys during brazing have not been sufficiently investigated. To address this knowledge gap, the research was organized into four complementary parts, this research work was organized into four complementary parts covering both 1xxx and 3xxx alloy systems, progressing from fundamental studies to industrial-scale extrusion and brazing processes.

Part I represents the fundamental stage of this research, focusing on the evolution of Sc- and Zr-containing precipitates in 1xxx aluminum alloys and on the alloys' behavior when subjected to hot deformation and simulated brazing cycles. While conventional aluminum brazing is typically performed near 600 ºC, recent developments in filler-metal design have enabled lower brazing temperatures to reduce the risk of abnormal grain growth. Accordingly, the selected short-term thermal exposures between 500 ºC and 575 ºC for 1 hour in this study reflect various potential brazing conditions. The one-hour treatments were selected to provide sufficiently severe and controlled thermal exposures to reveal differences in recrystallization and grain-growth resistance among the investigated alloys. The selected temperature range is also of interest in view of emerging filler alloys that enable brazing at lower temperatures . This part addresses the thermal stability of Al_3Sc and $Al_3(Sc, Zr)$ precipitates and their effect on recrystallization resistance and grain-growth behavior encountered under brazing-relevant thermal conditions.

Part II extends the work to industrially relevant extrusion trials, focusing on the extrusion of 1xxx aluminum flat strips with varying levels of Sc and Zr micro-additions. Two distinct thermomechanical routes were designed to examine their influence on several key aspects, including extrudability, grain stability during extrusion, and resistance to recrystallization under simulated brazing conditions. In this part, the mechanical strength of the alloys was evaluated after brazing, which is a critical property in modern heat exchangers. The corrosion resistance is also investigated through the SWAAT test (ASTM G85), given that corrosion can lead to premature leakage or failure of brazed assemblies. Finally, this part extends the study toward an industrial trial by producing multi-port extruded (MPE) tubes, which represent the typical configuration used in brazed heat-exchanger applications.

Part III focuses on 3xxx aluminum alloys. The conventional 3xxx base alloy is compared with counterparts containing Sc and Zr microadditions to evaluate the effect of these elements on processing behavior and final performance. The study begins with laboratory-scale experiments aimed at understanding the hot-deformation response and the evolution of Mn-based dispersoids and their interaction withe $Al_3(Sc, Zr)$ precipitates. The performance of the alloys is also examined under simulated brazing conditions to assess their thermal stability and resistance to recrystallization. Subsequently, industrial extrusion trials were conducted to produce thin strips, enabling the evaluation of extrudability, post-braze mechanical properties, and the strengthening response to post-braze aging. Finally, the extrusion of MPE tubes demonstrates the industrial relevance of Sc and Zr microadditions, highlighting their role in enhancing grain stability and improving overall performance in brazed heat-exchanger applications.

Part IV of this work focuses on 3xxx aluminum alloys processed as multi-port extruded (MPE) tubes and examines the effect of Sc and Zr microadditions in alloys used for brazed heat exchangers. A comparison was conducted between the base alloy, a low-Sc Zr alloy (L-ScZr), and a high-ScZr alloy (H-ScZr) under industrially relevant processing conditions, including extrusion, thickness reduction, and brazing. The originality of this part lies in evaluating Sc–Zr microalloying directly in 3xxx MPE tubes subjected to extrusion, sizing, brazing, and post-braze aging. Post-brazing aging was performed to evaluate the strengthening response and revealed a significant increase in strength in the Sc-Zr alloys, with the yield strength increasing by up to ~105% relative to the base alloy. These findings contribute to a better understanding of the role of Sc–Zr microalloying in improving grain stability and post-braze age hardening in 3xxx alloys.

1.5 Thesis outline

This is an article-based thesis organized into six chapters, as illustrated below:

Chapter 1 provides the general background on aluminum heat exchangers, outlines the motivation behind Sc and Zr microalloying, and defines the problem statement, objectives, and originality of the thesis.

Chapter 2 presents the first article, "Effect of Sc and Zr microalloying on recrystallization behaviour of 1xxx aluminium heat-exchanger alloys during post-deformation annealing" - published in the *Journal of Materials Science: Materials in Engineering* ,2025.

Chapter 3 is the second article "Study of 1xxx aluminum extrusion alloys for brazed heat exchangers: Influences of Sc/Zr microalloying and thermomechanical processing'' -published in *Journal of Materials Research and Technology*,2026.

Chapter 4 is the third article "Assessment of the effects of Sc/Zr microalloying on Al-Mn 3xxx brazed heat exchangers: From lab scale to multi-port tube extrusions" - published in *Materials Characterization* ,2026.

Chapter 5 is the fourth article "The potential of Sc–Zr microalloying for improving grain stability and mechanical strength in 3xxx multi-port extruded tubes " - under internal review.

Finally, in Chapter 6, the general conclusions and recommendations for future work are presented. Following this chapter, a list of publications, posters and awards is provided.

1.6 Preface

This thesis is presented in an article-based format and consists of four complementary studies addressing the effects of Sc and Zr microalloying on 1xxx and 3xxx aluminum alloys for brazed heat-exchanger applications. Together, the four articles address the overall objectives of the thesis, progressing from fundamental investigations of microstructural stability and recrystallization behavior to industrially relevant extrusion trials involving thin strips and multi-port extruded tubes.

The candidate is the first author of the four articles included in this thesis. The specific contribution of the candidate to each article, together with the roles and affiliations of the coauthors, is provided in the author-contribution statement included with each respective article.

References

[1] Y.-S. Kim, I.-J. Park, B.-S. An, J.G. Park, C.-W. Yang, Y.H. Lee, J.-G. Kim, Improvement of corrosion penetration resistance for aluminum heat exchanger by alloying zirconium, Mater Chem Phys 241 (2020) 122275. https://doi.org/https://doi.org/10.1016/j.matchemphys.2019.122275.

[2] C. Balaji, B. Srinivasan, S. Gedupudi, Chapter 7 - Heat exchangers, in: C. Balaji, B. Srinivasan, S. Gedupudi (Eds.), Heat Transfer Engineering, Academic Press, 2021: pp. 199–231. https://doi.org/https://doi.org/10.1016/B978-0-12-818503-2.00007-1.

[3] Y.S. Kim, I.J. Park, B.S. An, J.G. Park, C.W. Yang, Y.H. Lee, J.G. Kim, Improvement of corrosion penetration resistance for aluminum heat exchanger by alloying zirconium, Mater Chem Phys 241 (2020). https://doi.org/10.1016/j.matchemphys.2019.122275.

[4] M.J. Benoit, H. Jin, B. Shalchi-Amirkhiz, S. Kurukuri, S. Winkler, M.J. Worswick, M.A. Wells, Microstructure evolution of warm deformed multilayered Al alloy sheet during brazing, J Mater Process Technol 281 (2020) 116639. https://doi.org/10.1016/j.jmatprotec.2020.116639.

[5] M. Shakiba, N. Parson, X.G. Chen, Effect of Iron and Silicon Content on the Hot Compressive Deformation Behavior of Dilute Al-Fe-Si Alloys, J Mater Eng Perform 24 (2015) 404–415. https://doi.org/10.1007/s11665-014-1302-3.

[6] W.H. Van Geertruyden, H.M. Browne, W.Z. Misiolek, P.T. Wang, Evolution of surface recrystallization during indirect extrusion of 6xxx aluminum alloys, Metallurgical and Materials Transactions A 36 (2005) 1049–1056. https://doi.org/10.1007/s11661-005-0298-6.

[7] M.M. Lachowicz, M.B. Lachowicz, A. Gertruda, Assessment of the Possibility of Galvanic Corrosion in Aluminum Microchannel Heat Exchangers, Crystals (Basel) 12 (2022). https://doi.org/10.3390/cryst12101439.

[8] G.G.B. Zaffaroni, O. V Mishin, U.M. Ciucani, C. Gundlach, J.H. Nordlien, R. Ambat, Characterization of high frequency welded aluminium microfin tube for heat

exchangers, Mater Charact 173 (2021) 110939. https://doi.org/https://doi.org/10.1016/j.matchar.2021.110939.

[9] W. Fang, D. Tang, H. Wang, D. Li, Y. Peng, Optimization of die design for thin-walled flat multi-port tube with the aid of finite element simulation, J Mater Process Technol 277 (2020) 116418. https://doi.org/10.1016/j.jmatprotec.2019.116418.

[10] D. Tang, W. Fang, X. Fan, D. Li, Y. Peng, Effect of die design in microchannel tube extrusion, Procedia Eng 81 (2014) 628–633. https://doi.org/10.1016/j.proeng.2014.10.051.

[11] X.H. Fan, D. Tang, W.L. Fang, D.Y. Li, Y.H. Peng, Microstructure development and texture evolution of aluminum multi-port extrusion tube during the porthole die extrusion, Mater Charact 118 (2016) 468–480. https://doi.org/10.1016/j.matchar.2016.06.025.

[12] J.C. Guía-Tello, M.I. Pech-Canul, E. Trujillo-Vázquez, M.A. Pech-Canul, Effect of brazing parameters on fillet size and microstructure of cladded fin-microchannel tube joints, Transactions of Nonferrous Metals Society of China (English Edition) 30 (2020) 3240–3253. https://doi.org/10.1016/S1003-6326(20)65457-7.

[13] K. Li, D. Li, T. Zou, D. Shu, D. Tang, Y. Peng, Strength Variation in Processing Multiport Extrusion Tubes of A1100 and A3102 Alloys, J Mater Eng Perform 28 (2019) 3576–3589. https://doi.org/10.1007/s11665-019-04132-w.

[14] G. Vamadevan, F.F. Kraft, Processing effects in aluminum micro-channel tube for brazed R744 heat exchangers, J Mater Process Technol 191 (2007) 30–33. https://doi.org/10.1016/j.jmatprotec.2007.03.040.

[15] A. Kawahara, A. Niikura, T. Doko, Development of aluminum alloy fin stock for heat exchangers using twin-roll continuous casting method, Furukawa Review (2003) 81–87.

[16] L. Long, Q. Pan, M. Li, J. Ye, Y. Sun, W. Wang, Y. Luo, X. Li, Z. Peng, S. Liu, Study on microstructure and mechanical properties of 3003 alloys with scandium and copper addition, Vacuum 173 (2020). https://doi.org/10.1016/j.vacuum.2019.109112.

[17] T.-W. Na, H.-K. Park, C.-S. Park, J.-T. Park, N.-M. Hwang, Misorientation angle analysis near the growth front of abnormally growing grains in 5052 aluminum alloy, Acta Mater 115 (2016) 224–229. https://doi.org/https://doi.org/10.1016/j.actamat.2016.06.007.

[18] F.J. Humphreys, M. Hatherly, Recrystallization and Related Annealing Phenomena, Recrystallization and Related Annealing Phenomena (2012) 1–497. https://doi.org/10.1016/C2009-0-07986-0.

[19] J. Dennis, P.S. Bate, F.J. Humphreys, Abnormal grain growth in Al–3.5Cu, Acta Mater 57 (2009) 4539–4547. https://doi.org/https://doi.org/10.1016/j.actamat.2009.06.018.

[20] R. LIU, K. LI, G. ZHOU, W. TANG, Y. SHEN, D. TANG, D. LI, Simulation of strain induced abnormal grain growth in aluminum alloy by coupling crystal plasticity and phase field methods, Transactions of Nonferrous Metals Society of China 32 (2022) 3873–3886. https://doi.org/https://doi.org/10.1016/S1003-6326(22)66064-3.

[21] E.J. Payton, G. Wang, M.J. Mills, Y. Wang, Effect of initial grain size on grain coarsening in the presence of an unstable population of pinning particles, Acta Mater 61 (2013) 1316–1326. https://doi.org/https://doi.org/10.1016/j.actamat.2012.11.009.

[22] S. Kahl, H.-E. Ekström, J. Mendoza, Tensile, Fatigue, and Creep Properties of Aluminum Heat Exchanger Tube Alloys for Temperatures from 293 K to 573 K (20 °C to 300 °C), Metallurgical and Materials Transactions A 45 (2014) 663–681. https://doi.org/10.1007/s11661-013-2003-5.

[23] J. Røyset, N. Ryum, Scandium in aluminium alloys, International Materials Reviews 50 (2005) 19–44. https://doi.org/https://doi.org/10.1179/174328005X14311.

[24] D.N. Seidman, E.A. Marquis, D.C. Dunand, Precipitation strengthening at ambient and elevated temperatures of heat-treatable Al(Sc) alloys, Acta Mater 50 (2002) 4021–4035. https://doi.org/10.1016/S1359-6454(02)00201-X.

[25] V.G. Davydov, T.D. Rostova, V. V. Zakharov, Y.A. Filatov, V.I. Yelagin, Scientific principles of making an alloying addition of scandium to aluminium alloys, Materials Science and Engineering A 280 (2000) 30–36. https://doi.org/10.1016/S0921-5093(99)00652-8.

[26] Z.H. Jia, J. Royset, J.K. Solberg, Q. Liu, Formation of precipitates and recrystallization resistance in Al-Sc-Zr alloys, Transactions of Nonferrous Metals Society of China (English Edition) 22 (2012) 1866–1871. https://doi.org/10.1016/S1003-6326(11)61399-X.

[27] G. Li, N. Zhao, T. Liu, J. Li, C. He, C. Shi, E. Liu, J. Sha, Effect of Sc/Zr ratio on the microstructure and mechanical properties of new type of Al–Zn–Mg–Sc–Zr alloys, Materials Science and Engineering: A 617 (2014) 219–227. https://doi.org/https://doi.org/10.1016/j.msea.2014.08.041.

[28] N.Q. Vo, D.C. Dunand, D.N. Seidman, Improving aging and creep resistance in a dilute Al–Sc alloy by microalloying with Si, Zr and Er, Acta Mater 63 (2014) 73–85. https://doi.org/https://doi.org/10.1016/j.actamat.2013.10.008.

[29] Y. Wang, B. Xiong, Z. Li, Y. Zhang, H. Teng, Precipitation Behavior of Al3(Sc,Zr) Particles in High-Alloyed Al–Zn–Mg–Cu–Zr–Sc Alloy During Homogenization, Arab J Sci Eng 46 (2021) 6027–6037. https://doi.org/10.1007/s13369-020-05268-x.

[30] J. Liu, P. Yao, N. Zhao, C. Shi, H. Li, X. Li, D. Xi, S. Yang, Effect of minor Sc and Zr on recrystallization behavior and mechanical properties of novel Al–Zn–Mg–Cu alloys, J Alloys Compd 657 (2016) 717–725. https://doi.org/https://doi.org/10.1016/j.jallcom.2015.10.122.

[31] Y. Ding, K. Gao, S. Guo, S. Wen, H. Huang, X. Wu, Z. Nie, D. Zhou, The recrystallization behavior of Al-6Mg-0.4Mn-0.15Zr-xSc (x = 0.04–0.10 wt%) alloys, Mater Charact 147 (2019) 262–270. https://doi.org/10.1016/j.matchar.2018.11.009.

[32] V. Ocenasek, M. Slamova, Resistance to recrystallization due to Sc and Zr addition to Al–Mg alloys, Mater Charact 47 (2001) 157–162. https://doi.org/https://doi.org/10.1016/S1044-5803(01)00165-6.

[33] Y. Wang, Q. Pan, Y. Song, C. Li, Z. Li, Q. Chen, Z. Yin, Recrystallization of Al-5.8Mg-Mn-Sc-Zr alloy, Transactions of Nonferrous Metals Society of China 23 (2013) 3235–3241. https://doi.org/https://doi.org/10.1016/S1003-6326(13)62858-7.

[34] A.Y. Algendy, P. Rometsch, X.G. Chen, Mechanical and corrosion performances of Al–Mg-Mn 5083 rolled alloys microalloyed with Sc and Zr in different thermomechanical processing conditions, J Mater Sci 59 (2024) 14692–14715. https://doi.org/10.1007/s10853-024-10044

[35] T.H. Chuang, L.C. Tsao, T.C. Tsai, M.S. Yeh, C.S. Wu, Development of a low-melting-point filler metal for brazing aluminum alloys, Metallurgical and Materials Transactions A 31 (2000) 2239–2245. https://doi.org/10.1007/s11661-000-0141-z.

Chapter 2

Effect of Sc and Zr microalloying on recrystallization behavior of 1xxx aluminum heat exchanger alloys during post-deformation annealing

(This article is published in *Journal of Material science: Materials in Engineering*. Volume 20, article number 84, 2025)

Résumé

Les alliages d'aluminium de la série 1xxx sont largement utilisés dans les échangeurs de chaleur. Lors du brasage, les composants des échangeurs de chaleur sont exposés pendant une courte durée à des températures élevées, ce qui peut provoquer la recristallisation et la croissance anormale des grains et, par conséquent, compromettre leurs propriétés mécaniques. Cette étude examine l'effet de la microalliage avec le Sc et le Zr sur la stabilité microstructurale d'alliages 1xxx déformés à chaud et soumis à des traitements de recuit post-déformation entre 500 et 575 °C pendant 1 h afin de simuler des procédés de type brasage. Quatre alliages ont été étudiés : un alliage 1xxx de base, Al-0.07Sc, Al-0.07Sc-0.10Zr et Al-0.19Sc-0.15Zr. Un recuit à 500 °C a entraîné une recristallisation complète de l'alliage de base, tandis que des températures de recuit plus élevées ont favorisé la croissance anormale des grains. L'alliage Al-0.07Sc a résisté à la recristallisation à 500 °C, mais était entièrement recristallisé à 550 °C. En revanche, l'alliage Al-0.07Sc-0.10Zr a conservé une bonne stabilité de sa structure granulaire jusqu'à 550 °C grâce à la présence de précipités $Al_3(Sc,Zr)$ stables; toutefois, une recristallisation partielle a été observée à 575 °C. L'alliage Al-0.19Sc-0.15Zr a conservé la majeure partie de sa microstructure déformée même après un recuit à 575 °C. Parmi les quatre alliages étudiés, il a présenté la résistance à la recristallisation la plus élevée, en raison de la densité numérique la plus élevée et de la plus faible taille moyenne des précipités $Al_3(Sc,Zr)$,

ce qui suggère que cet alliage pourrait être utilisé dans des conditions encore plus sévères, notamment à des températures de brasage supérieures à 575 °C.

Abstract

1xxx-series aluminum alloys are widely utilized in heat exchangers. During brazing, heat exchanger components are exposed to a short period of high temperature, which may trigger recrystallization and abnormal grain growth, ultimately compromising their mechanical properties. This study investigates the impact of Sc and Zr microalloying on the microstructure stability of hot deformed 1xxx alloys subjected to post-deformation annealing from 500 to 575 ºC for 1 h to simulate brazing-type processes. Four alloys were studied: namely 1xxx base, Al-0.07Sc, Al-0.07Sc-0.10Zr and Al-0.19Sc-0.15Zr alloys. Annealing at 500 °C led to complete recrystallization in the base alloy, while higher annealing temperatures promoted abnormal grain growth. The Al-0.07Sc alloy resisted recrystallization at 500 °C but was fully recrystallized by 550 °C. In contrast, the Al-0.07Sc-0.10Zr alloy retained its grain stability up to 550 °C owing to the presence of stable $Al_3(Sc,Zr)$ precipitates; however, partial recrystallization occurred at 575 °C. The Al-0.19Sc-0.15Zr alloy preserved most of deformed microstructure even after annealing at 575 °C. It showed the highest recrystallization resistance among the four alloys studied owing to its highest number density and finest size of $Al_3(Sc,Zr)$ precipitates, which suggests that this alloy can be applied in even more extreme conditions including brazing temperatures above 575 °C.

Keywords: 1xxx aluminum alloys, Sc and Zr additions, Hot deformation, High-temperature annealing, Recrystallization.

2.1 Introduction

Aluminum alloys are widely utilized in the automotive industry for heat exchangers, including those used in radiators, air conditioner evaporators, exhaust gas recirculation systems, and water and air charge cooling systems[1,2]. The 1xxx alloys are considered as ideal materials for heat exchanger tubes, owing to their high formability, excellent thermal conductivity, and superior corrosion resistance[3,4]. Heat exchangers are typically fabricated by forming Al sheet and extruded tube stock into the required geometries, followed by brazing to assemble the components together [5]. Brazing sheets are often comprised of a core alloy and a clad layer. The former provides the strength and life cycle requirements, while the latter is usually a low melting point alloy (e.g. an Al-Si 4xxx alloy) that forms the brazed joints between the components of the heat exchanger [6]. Maintaining microstructural stability during brazing is essential, as the elevated temperature can compromise the grain structure, often triggering abnormal grain growth (AGG) [7,8].

AGG is a microstructural phenomenon where certain grains grow extensively by consuming the surrounding finer recrystallized grains [9–12]. This results in an extremely inhomogeneous microstructure, which significantly compromises the properties [13]. Abnormal grains exhibit higher grain boundary migration rates than their surrounding grains [14]. This enhanced boundary mobility can be attributed to several factors such as the crystallographic texture, variation in stored energy between grains, and uneven pinning by precipitates, where boundaries associated with certain grain orientations migrate more easily than others [15]. AGG has been shown to cause significant degradation in the strength of brazed heat exchanger tubes, as reported in several studies. For instance, Kraft [16] observed substantial grain growth during brazing of AA1050 extruded heat exchanger tubes and reported a significantly lower strength in the internal wall of the tube compared to the bulk tube. Tang et al. [17] and Li et al. [18] also reported a significant reduction in the pressure-bearing capacity of post-brazed

AA1100 heat exchanger tubes owing to the AGG in the brazed microstructure. Given the detrimental impact of AGG on the mechanical integrity of brazed heat exchanger tubes, strategies to stabilize the grain structure during high-temperature exposure are crucial. One well established strategy involves the use of fine and stable dispersoids within the Al matrix, which can effectively hinder subgrain boundary movement, suppress recrystallization and restrict grain growth by exerting a pinning force on grain/subgrain boundaries [19–24].

Among the various alloying strategies, microalloying with Sc has proven to be effective in enhancing the strength and the recrystallization resistance in aluminum alloys through the formation of thermally stable Al_3Sc precipitates that inhibit grain boundary motion during high temperature exposures [25–27]. The low lattice mismatch between $L1_2$-Al_3Sc precipitates and the matrix creates a coherent interface, further strengthening the alloy and stabilizing its grain structure [28,29]. These precipitates exert a drag force on grain and sub-grain boundaries, inhibiting the nucleation and growth of recrystallized grains [30,31]. Despite efforts to reduce production costs, Sc remains an expensive alloying element owing to supply limitations and complex extraction processes [32,33]. A more economical alloying strategy involves co-additions with Zr that promotes the formation of Al_3(Sc, Zr) precipitates. These precipitates featuring an Al_3Sc core with a Zr-enriched shell, offers an even more enhanced resistance to thermal coarsening [34–36].

Several studies have demonstrated that Sc/Zr-containing precipitates are highly effective in regulating recovery, recrystallization, and grain growth in Al alloys, thus stabilizing their microstructures during high temperature exposure. For instance, Jia et al. [37] reported that a cold-rolled Al-0.1Sc-0.11Zr (wt.%) alloy showed no recrystallization when isothermally annealed at 250 ºC, and that the recrystallization was initiated only at 550 ºC. Similarly, Ocenasek et al. [38] observed that Al_3(Sc,Zr) precipitates stabilized the deformed microstructure at high annealing temperatures, and the results showed that an Al-Mg alloy with

0.25 wt.% Sc and 0.08 wt.% Zr resisted recrystallization after annealing at 520 ºC for 8 h, with partial recrystallization near 600 ºC. In another study by Babaniaris et al. [39], it was reported that a cold-worked Al-Mg-Si alloy containing 0.25 wt.% Sc and 0.08 wt.% Zr exhibited strong resistance to recrystallization during annealing, remaining non- recrystallized after 8 h at 520 °C. Algendy et al [40] found that after the addition of 0.10 wt.% Sc + 0.08 wt.% Zr in Al-Mg-Mn 5083 rolled alloys, the rolled material retained a deformed fibrous structure during annealing at 400 °C for 30 min, with only 3.4% recrystallized grains. Lai et al [41] reported that the addition of 0.089 wt.% Sc and 0.10 wt.% Zr significantly improved the recrystallization resistance of an Al-5Mg-3Zn rolled alloy, reducing the recrystallized fraction after solution treatment at 465 °C for 30 min from nearly 100% in the unmodified alloy to just 9% in the microalloyed variant. Li et al [42] showed that solution heat treatment at 470 °C for 1 h led to full recrystallization in an Al-Zn-Mg-Mn rolled alloy, while the addition of 0.24 wt.% Sc and 0.12 wt.% Zr suppressed recrystallization. Ye et al. [43] also observed that the recrystallized fraction dropped sharply from 99.8% in the Al-Zn-Mg-Cu rolled alloy free Sc/Zr to just 12.6% in the Sc/Zr-modified alloy after solution treatment at 470 °C for 1 h. Lu et al [44] observed that following a welding thermal cycle, the 7055 alloy with only 0.12 wt.% Zr underwent extensive recovery and recrystallization. In contrast, the 7055 alloy containing 0.22 wt.% Sc and 0.11 wt.% Zr significantly enhanced microstructural stability, preserving 51% of its deformed structure. Xiao et al. [45] observed that $Al_3(Sc,Zr)$ particles in an Al-Zn-Mg-Cu alloy with 0.07 wt.% Sc and 0.07 wt.% Zr remained stable after extrusion and solution heat treatment, promoting an elongated grain structure. Despite the strong recrystallization resistance demonstrated across various Al alloy systems, those studies mainly focused on non-1xxx series alloys. Moreover, they lacked specific emphasis on brazing or simulated brazing conditions. As a result, the behavior of Sc and Zr microalloying in 1xxx alloys under thermal exposures relevant to brazed heat exchangers remains largely underexplored.

This study aims to evaluate the impact of Sc and Zr microalloying on deformed microstructures of 1xxx alloys, particularly in scenarios involving short thermal exposures from 500 to 575 ºC to simulate the brazing process. While conventional aluminum brazing is typically performed at ~600 °C, recent developments in filler metal design have aimed to lower the brazing temperature to mitigate abnormal grain growth. Several studies have proposed low-melting-point filler metals with adequate bonding strength having melting ranges as low as 500-526 °C. These include Al-7Si-20Cu-2Sn-1Mg [46], Zn-15Al [47], and modified Al-12Si alloys containing Cu and Sn [48,49]. The selected thermal exposure temperatures between 500 and 575 °C in this study reflect potential brazing conditions enabled using recently developed low-melting-point filler metals. The hot deformation behavior is assessed through uniaxial hot compression testing, while the microstructural evolution during hot deformation and post-deformation annealing are analyzed using electron backscatter diffraction (EBSD) and transmission electron microscopy (TEM) to assess the effectiveness of the Sc/Zr-containing precipitates in enhancing the thermal stability and recrystallization resistance.

2.2 Experimental procedure

Four experimental 1xxx alloys with and without Sc and Sc+Zr additions were investigated. The alloys were prepared from commercially pure aluminum (99.85%), Al-25%Fe, Al-50%Si, Al-5%Ti- 1%B, Al-2%Sc, and Al-15%Zr master alloys (wt.%). Approximately 5 kg of each material was batched in an electrical resistance furnace, and cast at 720 ºC in a rectangular permanent steel mold with dimensions of 30 × 40 × 80 mm. The chemical compositions of the four alloys, analyzed by optical emission spectroscopy (Thermo ARL 4460), are listed in Table 2-1. All cast ingots were subjected to a low-temperature homogenization treatment at 350 ºC for 24 h with a heating rate of 50 ºC/h, to promote Al_3Sc/$Al_3(Sc,Zr)$ precipitation [50–54].

Table 2-1 Chemical compositions of the experimental alloys (wt.%)

Alloy	Si	Fe	Ti	Sc	Zr	Al
Base alloy	0.12	0.17	0.02	--	--	Bal.
Al-0.07Sc	0.13	0.23	0.02	0.07	--	Bal.
A-0.07Sc-0.1Zr	0.15	0.12	0.02	0.07	0.10	Bal.
Al-0.19Sc-0.15Zr	0.12	0.19	0.02	0.19	0.15	Bal.

Hot compression tests were conducted using a Gleeble 3800 thermomechanical testing unit. Cylindrical samples 10 mm in diameter and 15 mm in height were machined from the homogenized ingots. Hot compression tests were carried out at 450 °C, reflecting typical industrial extrusion conditions for aluminum heat exchanger alloys [7,17,55–57]. A constant strain rate of 1 s^{-1} was applied. Each specimen was heated to 450 °C at a rate of 2 °C/s and held for 2 minutes and then compressed to a true strain of 0.8. At least three repetitions were conducted to ensure reproducibility and reliability. After deformation, the sample was water-quenched to preserve the deformed microstructure. To evaluate the recrystallization behavior of the different alloys, post-annealing treatments were conducted at 500 °C, 550 °C, and 575°C for 1 h. The selected thermal exposure temperatures correspond to niche brazing scenarios made possible using the new developed low-melting-point filler alloys [46–49].

Microstructural characterization of the alloys was performed using an optical microscope (OM, Nikon-Eclipse ME600), a scanning electron microscope (SEM, JEOL 6480LV) and a transmission electron microscope (TEM, JEOL JEM -2100). EBSD analysis was conducted on samples sectioned parallel to the compression axis. EBSD maps, with a step size of 1 μm, were used to reveal sub grain structures and misorientation distributions. TEM analysis, performed at 200 kV, was used to observe the Al_3Sc/$Al_3(Sc,Zr)$ precipitates. TEM samples were prepared using a twinjet electropolishing unit, operated at 15 V and -30 °C, in an electrolyte solution of 30% nitric acid and 70% methanol. Observations of precipitates were made in the dark-field mode near the [001] zone axis.

The size and number density of the spherical Al_3Sc/$Al_3(Sc,Zr)$ precipitates were measured using ImageJ image analysis software on several TEM images. The number density N_d was calculated using the counted number of precipitates *N* in an area of *A* in the TEM images using Eq. 1 [58].

$$N_d = \frac{N}{A*(D+t)} \qquad \text{Equation 1}$$

where *D* is the average diameter of the precipitates, and *t* is the thickness of the TEM sample measured using convergent-beam electron diffraction.

2.3 Results

2.3.1 As-homogenized microstructures

Figure 2-1 displays the SEM micrographs of as-homogenized microstructures of the four investigated alloys. All four alloys exhibited similar microstructures, composed of α-Al matrix and Fe-rich intermetallic particles appearing in both Chinese-script and compact forms distributed along Al dendrite boundaries. The main Fe-rich intermetallic phase was Al_8Fe_2Si identified by SEM-EDS analysis (see Fig. 2-1e-f). A similar Fe-rich intermetallic phase has been reported in aluminum 1xxx alloys with comparable levels of Fe and Si [59,60]. In the SEM images, no primary $Al_3(Sc)$ or $Al_3(Sc,Zr)$ intermetallic particles were found in the as-homogenized microstructures of the three Sc-containing alloys. This observation aligns with literature recommendations maintaining Sc at low levels of <0.30 wt.% to promote the formation of fine $Al_3(Sc,Zr)$ dispersoids while minimizing the risk of primary intermetallic formation [27]. Knipling et al. [35] demonstrated that dilute Al-Sc and Al-Zr alloys exhibited no primary Sc/Zr-containing intermetallic phases in the as-cast state when processed under comparable composition ranges. Similarly, Deng et al. [61] reported the absence of primary $Al_3(Sc_{1-x}Zr_x)$ particles in an Al–Mg–Mn alloy containing 0.10 wt.% Sc and 0.12 wt.% Zr.

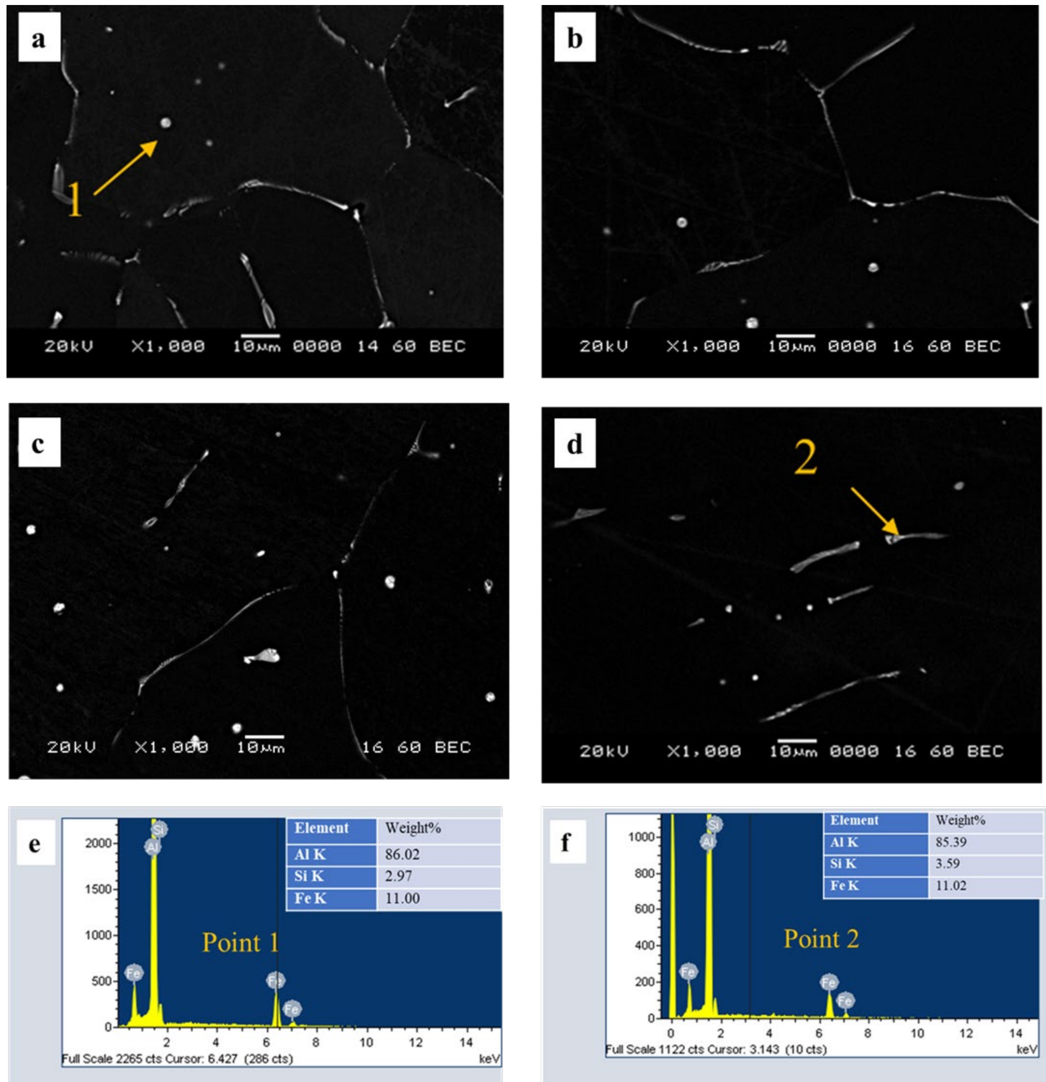

Figure 2-1(a-d) SEM images of as-homogenized microstructures, a) base, b) Al-0.07Sc, c) Al-0.07Sc-0.10Zr and d) Al-0.19Sc-0.15Zr alloys. (e-f) corresponding SEM-EDS point analysis of Fe-rich intermetallic phases observed in (a) and (d).

Figure 2-2 presents the EBSD maps of the as-homogenized grain structures of the four investigated alloys. The base alloy showed an average equivalent grain diameter of 72.5 μm, which increased to 106.8 μm in the Al-0.07Sc alloy. This trend aligns with the previous findings by Huang et al. [62], who reported that trace Sc addition diminished the grain refining effectiveness on Al-Ti-B grain refiners. Deng et al. [63] observed that a low Sc addition of

0.1 wt.% in an Al–Zn–Mg alloy did not refine the grains, whereas the refinement was only achieved at 0.25 wt.% Sc. These results support the understanding that sub-eutectic Sc levels are insufficient to induce nucleation-based grain refinement [64]. The equivalent grain diameters in the Al-0.07Sc-0.1Zr and Al-0.19Sc-0.15Zr alloys were 111.2 and 134.8 μm, respectively. This grain coarsening can be attributed to the poisoning effect of Zr as reported by Bunn et al. [65]. They observed that Zr substitutes for Ti in TiB_2 grain refiners, thereby reducing their effectiveness.

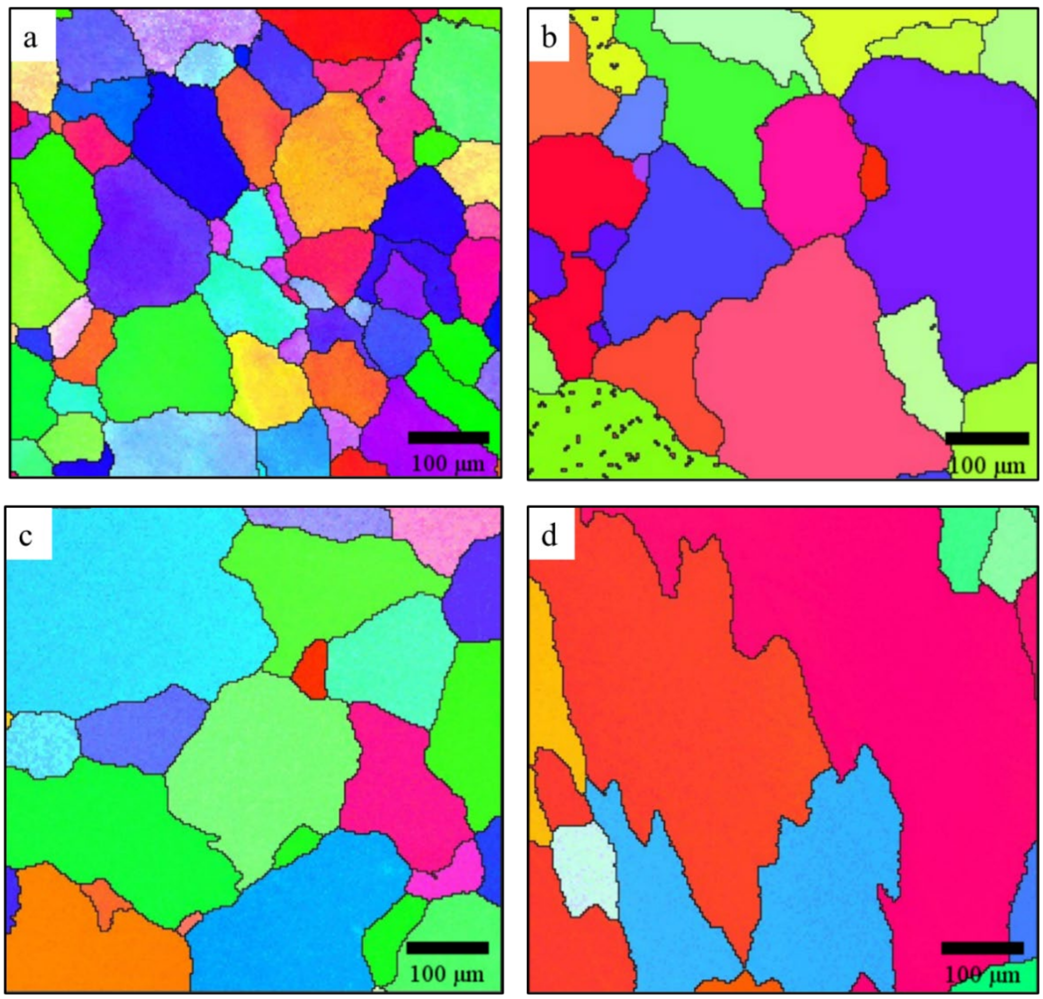

Figure 2-2 EBSD Maps of the as-homogenized grain structures a) base, b) Al-0.07Sc, c) Al-0.07Sc-0.10Zr and d) Al-0.19Sc-0.15Zr alloy.

2.3.2 Precipitation of Al_3Sc and $Al_3(Sc,Zr)$ during homogenization

Figure 2-3(a-c) shows the dark-field TEM images of Al_3Sc and Al_3 (Sc, Zr) nanoprecipitates in the three Sc-containing alloys after low-temperature homogenization. Fig. 3d shows a typical selected area electron diffraction (SAED) pattern obtained along the [001] zone axis, displaying faint spots from the precipitates between the α-Al spots, and confirming that the precipitates have an $L1_2$ structure [66]. Figure 2-4 illustrates the size distribution of the Al_3Sc and $Al_3(Sc,Zr)$ precipitates for the three Sc-containing alloys. Increasing the Sc and Zr content affected the average size and size range of the Al_3Sc and $Al_3(Sc,Zr)$ precipitates. For instance, the Al-0.07 Sc alloy showed a broad size distribution, while the Al-0.07Sc-0.1Zr and Al-0.19Sc-0.15Zr alloys exhibited narrower size distributions. The quantitative results of the precipitate characteristics in the three Sc-containing alloys are displayed in Table 2-2. With increasing contents of Sc and Zr, the average size (D) of the precipitates decreased, and the number density (Nd) increased. The lower diffusivity of Zr in aluminum, compared to that of Sc, leads to its delayed incorporation into precipitates, resulting in a Zr-rich shell that surrounds an Al_3Sc core. This core-shell structure contributes to a slower coarsening rate of $Al_3(Sc,Zr)$ precipitates and results in smaller precipitate sizes and higher number densities [67,68].

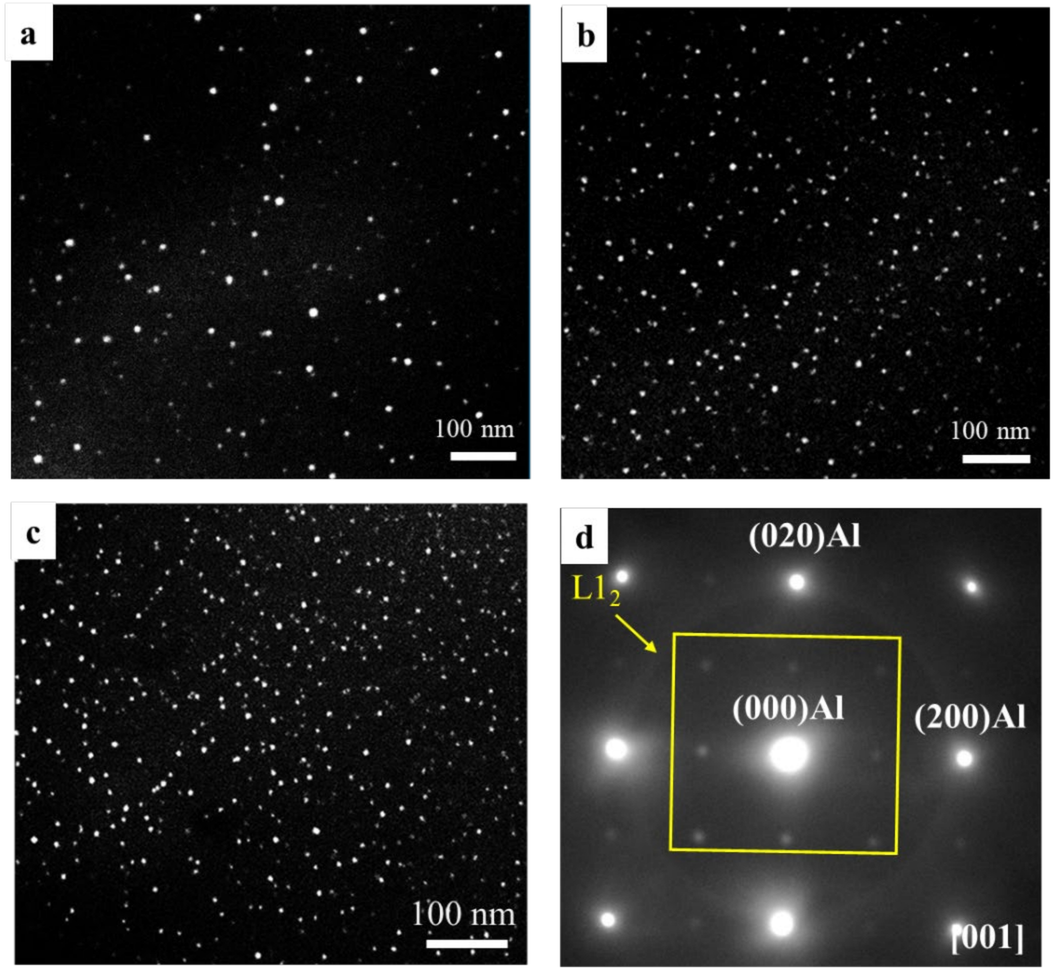

Figure 2-3 Dark-field TEM images of a) Al-0.07Sc, b) Al-0.07Sc-0.10Zr and c) Al-0.19Sc-0.15Zr alloys after homogenization at 350 ºC for 24 h, and d) SAED pattern of the Al-0.19Sc-0.15Zr alloy.

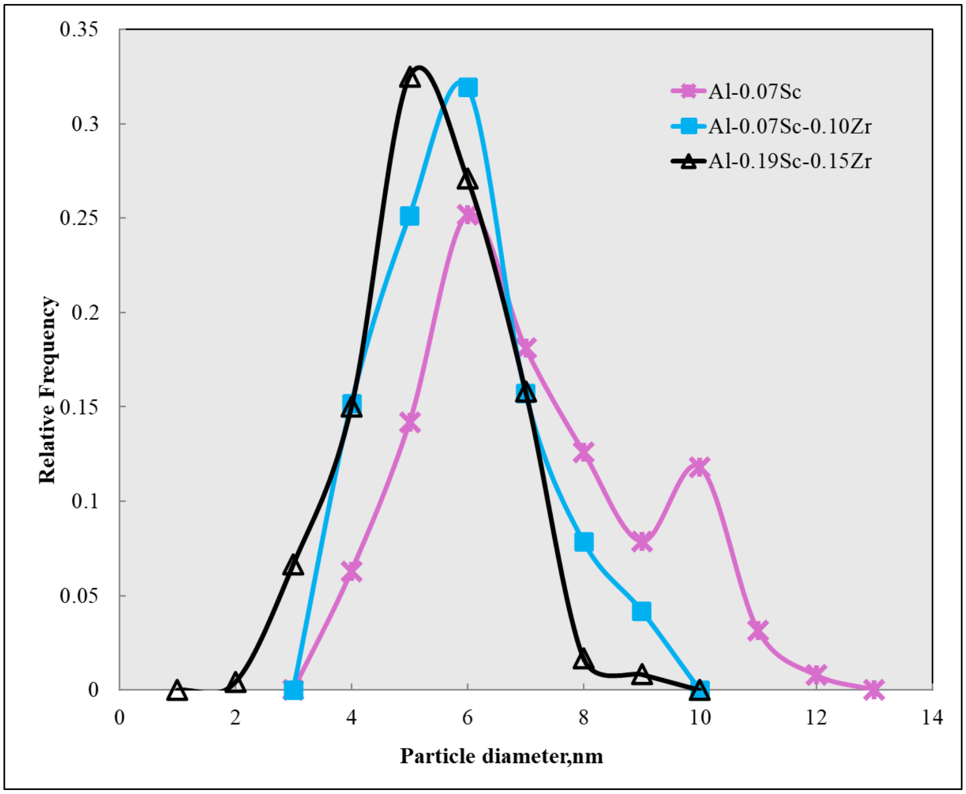

Figure 2-4 Histograms of the precipitate size distributions for the three Sc-containing alloys after homogenization at 350 ºC.

Table 2-2 Quantitative measurements of Al_3Sc/$Al_3(Sc,Zr)$ precipitates after homogenization

Alloy	Average D (nm)	Number density N_d (10^{21} m^{-3})
Al-0.07Sc	6.6±1.9	3.2±0.5
Al-0.07Sc-0.10Zr	5.5±1.3	7.2±0.2
Al-0.19Sc-0.15Zr	4.8±1.2	9.0±0.7

2.3.3 Effect of Sc and Zr on hot deformation

Figure 2-5 shows the true stress-strain curves during hot compression deformation of the four alloys studied. The flow behavior of the alloys exhibited typical characteristics of high-temperature deformation, where dynamic recovery (DRV) was the dominant softening mechanism [69]. Following the initial elastic response, the stress increased rapidly owing to dislocation multiplication and then continued to rise steadily as dynamic recovery progressed [70]. The flow stress of the base alloy exhibited a near plateau after the initial deformation stage (at ~0.2 strain), indicating a balance between the work hardening and dynamic recovery during further deformation. In contrast, all the three Sc-containing alloys showed a continuous increase in flow stress throughout the entire hot compression process. The addition of 0.07 wt.% Sc increased the flow stress from 27 MPa for the base alloy to 36.5 MPa. The combined addition of 0.07 wt.% Sc and 0.10 wt.% Zr further raised the flow stress to 42.3 MPa. The Al-0.19Sc-0.15Zr alloy exhibited the highest flow stress of 53.5 MPa. The higher flow stresses in the Al-Sc and Al-Sc-Zr alloys are attributed to the presence of numerous Al_3Sc and $Al_3(Sc,Zr)$ precipitates in the Al matrix (Fig. 2- 3), which exert a retardation effect on DRV [39].

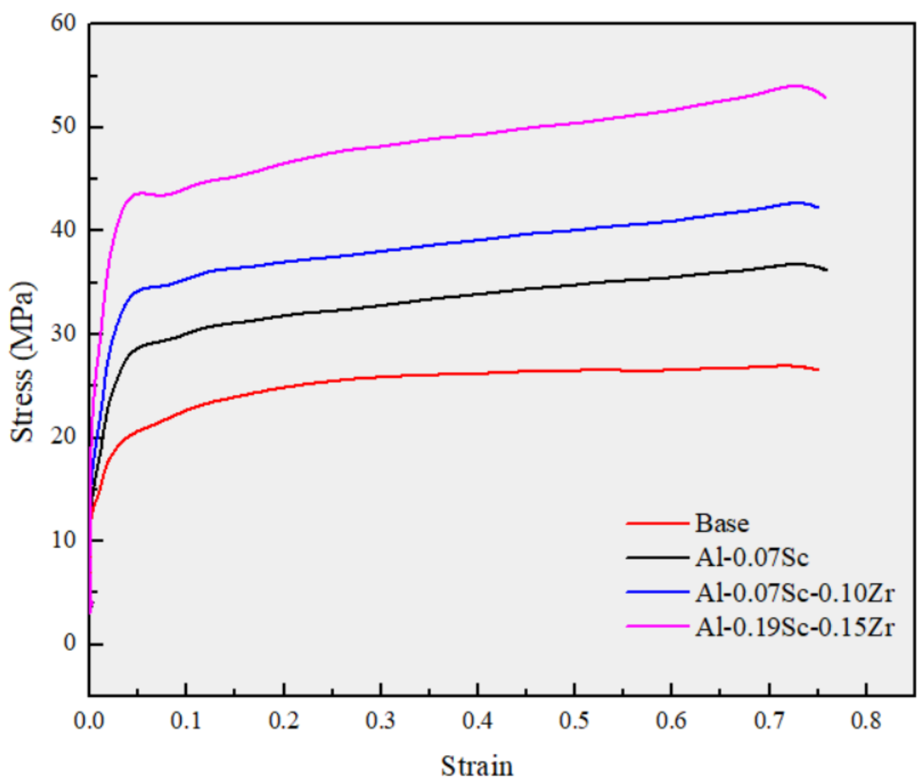

Figure 2-5 True stress–strain curves during hot compression deformation at 450 ºC and 1 s^{-1} for the four experimental alloys.

2.3.4 Microstructures after hot deformation

Figure 2-6 shows the All-Euler EBSD maps of the four investigated alloys, revealing the characteristics of the as-deformed grain structures. The grain structures of all four alloys were primarily composed of low-angle grain boundaries (LAGBs, 2º-5º) and medium-angle boundaries (MAGBs, 5º-15º), indicating that the alloys underwent dynamic recovery during deformation. The original grains were elongated perpendicular to the compression direction, and the as-deformed microstructure displayed a high density of sub grains. Figure 2-7 presents the misorientation angle distributions of grain/sub grain boundaries after hot deformation for the four alloys. Compared to the base alloy, the three Sc-containing alloys showed higher fractions of LAGBs. The percentages of boundaries with misorientations between 15º and 30º were similar across all four alloys, but significant differences were observed in the misorientation ranges of 2º-5º and 5º-15º. The fraction of LAGBs increased from 41.3% in the base alloy to 45.4% in the Al-0.07Sc alloy, and further to 52.3% and 67.9% in the Al-0.07Sc-0.10Zr and Al-0.19Sc-0.15Zr alloys, respectively. Conversely, the fraction of MAGBs decreased progressively, from 47.3% in the base alloy to 42.3% in the Al-0.07Sc alloy, and further to 37.4% in the Al-0.07Sc-0.1Zr alloy, with the lowest value of 27.9% observed in the Al-0.19Sc-0.15Zr alloy. The shift in the misorientation angle distributions for LAGBs and MAGBs indicates that the microalloying with Sc or Sc and Zr imposes greater restrictions on dynamic recovery (DRV) [71].

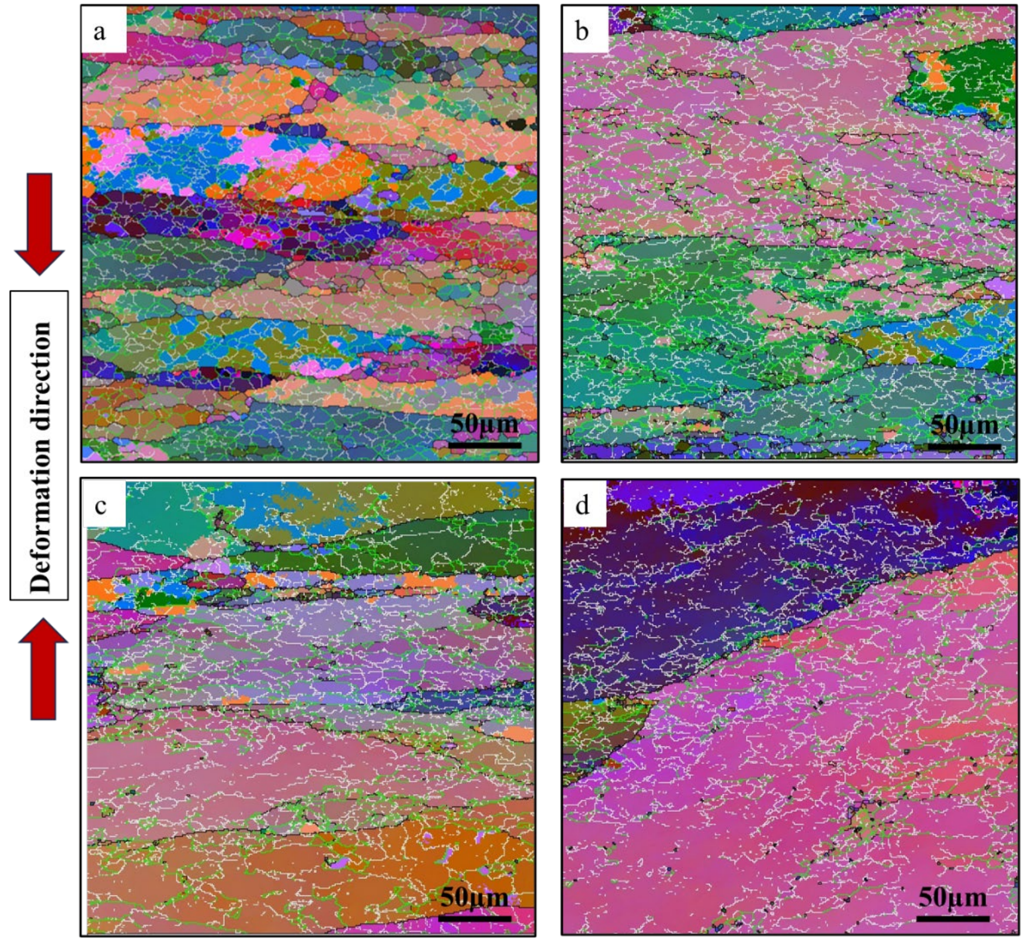

Figure 2-6 All Euler EBSD maps of a) base alloy, b) Al-0.07Sc, c) Al-0.07Sc-0.10Zr and d) Al-0.19Sc-0.15Zr alloys after hot deformation, where the white, green and black lines correspond to misorientation angles of 2–5°, 5–15° and >15°, respectively.

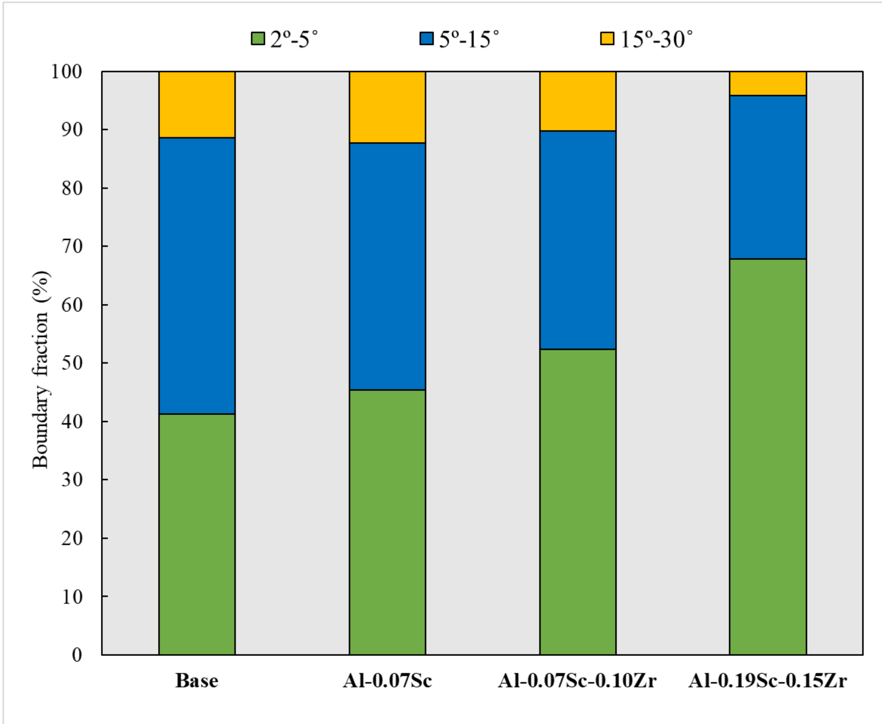

Figure 2-7 Evolution of misorientation angle distribution of boundaries after hot deformation for the four alloys studied.

To further examine the evolution and stability of dispersoids during processing, TEM analysis was performed on the as-deformed Al-0.07Sc-0.10Zr alloy. Figure 2-8a shows a dark-field TEM image of the $Al_3(Sc,Zr)$ precipitates after hot deformation. The precipitates are uniformly distributed in the Al matrix and have an average size of 5.0 ± 1.4 nm ranging from 2.7 nm to 9.9 nm (Figure 2-8b). Histograms of the precipitate size distributions after homogenization and after hot deformation are quite close. This suggests that $Al_3(Sc,Zr)$ precipitates, which formed during homogenization, remained almost unchanged and were thermally stable without coarsening during hot deformation. The fine, coherent nanoprecipitates play a critical role in impeding dislocation motion and delaying the recovery process, contributing to a higher flow stress, and improved microstructural stability during hot deformation [39].

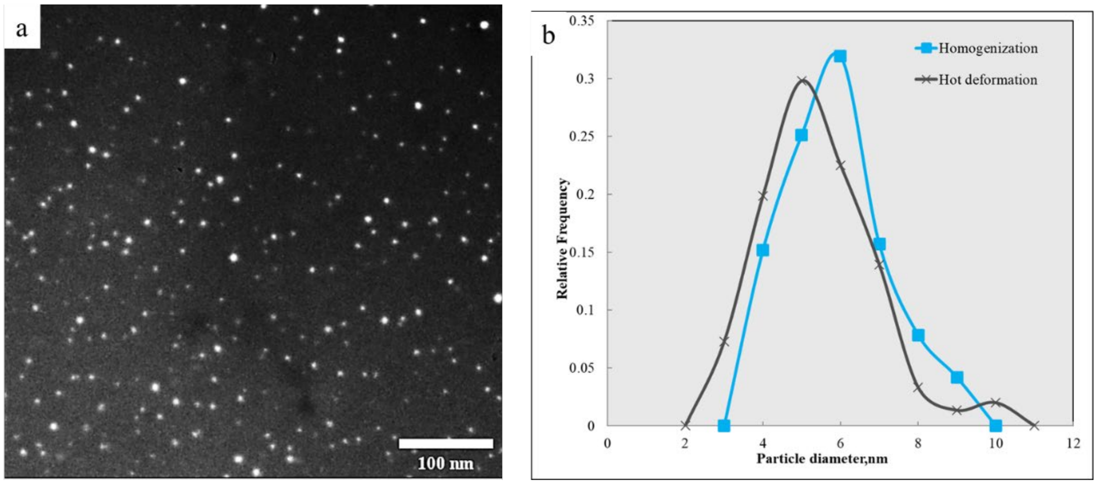

Figure 2-8a) Dark-field TEM image of $Al_3(Sc,Zr)$ precipitates in the Al-0.07Sc-0.10Zr alloy after the hot deformation, b) Histogram of the precipitate size distributions.

2.3.5 Effect of Sc and Zr on recrystallization behavior during post-deformation annealing

Figure 2-9 shows the All-Euler EBSD maps of the four investigated alloys, revealing the grain structures after post-deformation annealing at three different temperatures (500, 550 and 575 °C). Figure 2-10 presents the fractions of grain/sub grain boundaries based on the misorientation angle values after post-annealing. The base alloy, after the annealing at 500 °C, exhibited a coarse grain structure, and all grains showed no substructure inside (Figure 2-9a), indicating that the static recrystallization had been completed during annealing [72]. The grain structure was dominated by 100% of high-angle grain boundaries (HAGBs, >15°) (Fig. 10a). When the annealing temperature increased to 550 °C (Figure 2-9b), some small island grains (indicated by the white arrows) were observed to be trapped between growing larger grains, but a similar coarse grain structure consisting entirely of HAGBs remained (Fig. 10b). As the annealing temperature further increased to 575 °C (Figure 2-9c), the abnormal grain growth (AGG) became pronounced [18] as all grain coarsened dramatically, often reaching several hundred micrometers. The lack of precipitate pinning in the base alloy facilitated the grain growth during high-temperature annealing.

Unlike the base alloy, the Al-0.07Sc alloy exhibited a partially recovered microstructure after the post-annealing at 500 °C (Figure 2-9d), characterized by a high fraction of LAGBs (46.5%) and MAGBs (38.3%) (Figure 2-10a). Only a few newly formed equiaxed grains appeared along the original grain boundaries (indicated by white arrows), suggesting the commencement of static recrystallization [73]. As the annealing temperature increased to 550 and 575 °C, the microstructures transformed to fully recrystallized structures (Figures 2-9e and 2-9f). This was also indicated by the transformation to 100% HAGBs (Figure 2-10b and 2-10c).

For the Al-0.07Sc-0.10Zr alloy, after annealing at 500 °C, the as-deformed grain structure was retained (Figure 2-9g) with 57.8% of the boundaries classified as LAGBs (Figure 2-10a). When the annealing temperature increased to 550 °C, the alloy still showed a recovered structure (Figure 2-9h) but with some small equiaxed grains at the original grain boundaries (see white arrows), suggesting the onset of static recrystallization at this temperature. As the annealing temperature further increased to 575 °C, partial recrystallization was observed, and large recrystallized grain appeared (white arrow in Figure2- 9i). However, despite the occurrence of static recrystallization, the recrystallized fraction at this temperature accounted for only 24.5% of the total area of the microstructure. In comparison, both the base and Al-0.07Sc alloys were completely recrystallized at the same annealing temperature, indicating the Al-0.07Sc-0.10Zr alloy exhibited enhanced resistance to recrystallization and grain growth.

Regardless of the annealing temperature, the Al-0.19Sc-0.15Zr alloy retained a highly stable deformed grain structure characterized by elongated grains subdivided by numerous sub grain boundaries (Figures 2-9j, 2-9k, and 2-9l). The EBSD maps revealed no evidence of new equiaxed recrystallized grains, even at the highest annealing temperature of 575 ºC. Quantitatively, the fraction of LAGBs only slightly decreased with increasing temperature from 56% at 500 ºC to 53% at 550 ºC and further to 48% at 575 ºC (Figures 2-10a to 2-10c).

These results confirm that the Al-0.19Sc-0.15Zr alloy exhibited the highest resistance to recovery and recrystallization among the four alloys investigated.

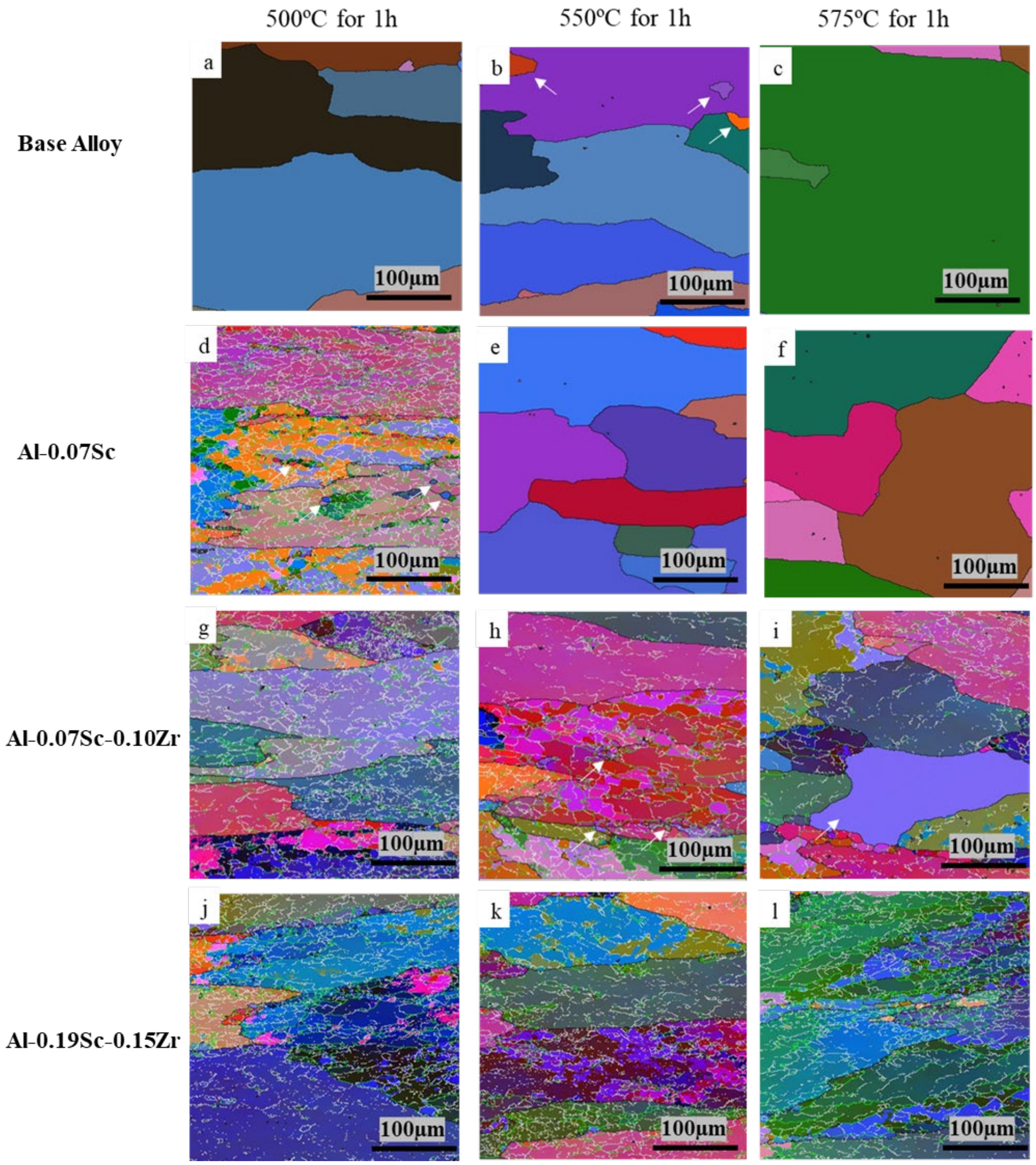

Figure 2-9 All Euler EBSD maps of the four studied alloys after post-deformation annealing.

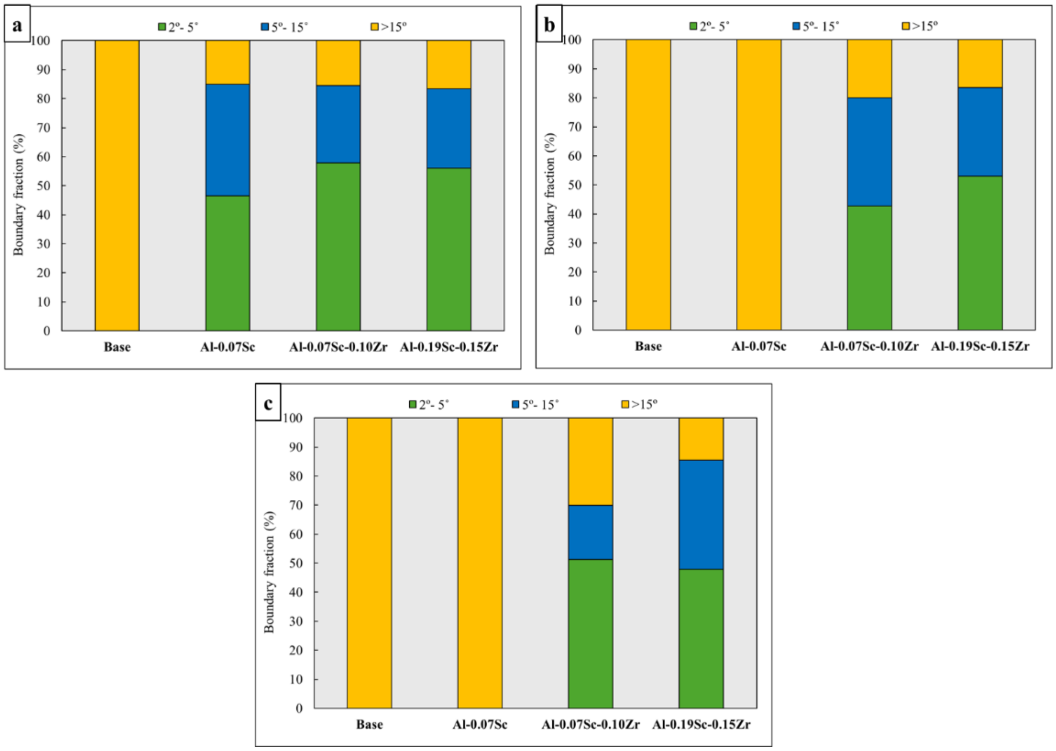

Figure 2-10 Evolution of misorientation angle distribution of boundaries after post-deformation annealing for 1 h at a) 500 ºC, b) 550 ºC and c) 575 ºC.

To further characterize the evolution of the grain structure during the post-annealing, the mean misorientation angles of the grain boundaries were quantitatively analyzed based on the EBSD data and are presented in Figure 2-11. The additions of Sc and Zr decreased the mean misorientation angles at all three annealing temperatures. On the other hand, as the annealing temperature increased, the mean misorientation angles increased in all four alloys. This indicates a higher degree of softening by recovery and recrystallization with rising annealing temperature, aligning with the microstructural observations presented in Figure 2-9. After annealing at 500 ºC, the base alloy exhibited a mean misorientation angle of 32º. This value increased to 37.6º and 50.9º for the fully recrystallized structures following the annealing at 550 and 575 ºC, respectively. On the contrary, after annealing at 500 ºC, all three Sc-containing alloys exhibited mean misorientation angles below 10º due to the remaining deformed grain structure. For the Al-0.07Sc alloy, increasing the annealing temperatures to 550 and 575 ºC resulted in increasing mean misorientation angles to 33.7º and 42.1º, respectively, showing the progression of the recrystallization process. The combined addition of Sc and Zr demonstrated a clear reduction of the mean misorientation angles, showing an increased recrystallization resistance. For instance, after annealing at the highest temperature of 575 ºC, the Al-0.07Sc-0.10Zr alloy exhibited a mean misorientation angle of 15.1º with a partially recrystallized structure while the Al-0.19Sc-0.15Zr alloy showed a lower mean misorientation angle of 10.1º, which further confirms its highest recrystallization resistance among the four alloys studied.

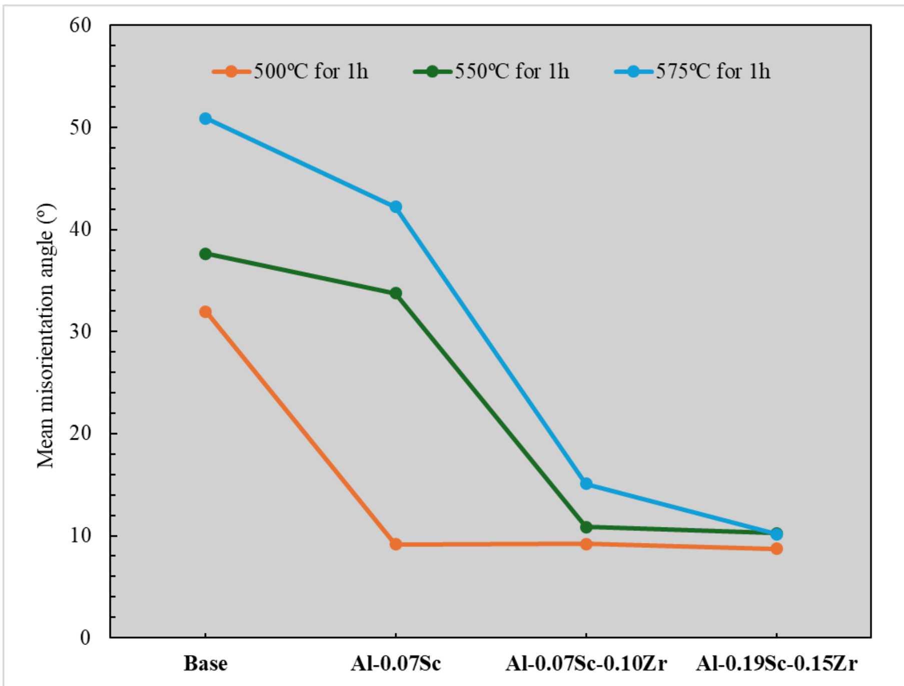

Figure 2-11 Mean misorientation angles after post-deformation annealing at three different temperatures for the four investigated alloys.

Overall, the EBSD analysis including All Euler EBSD maps, misorientation distributions, and mean misorientation angles provided a comprehensive assessment of the microstructural evolution during post-annealing treatments. The results indicate that microalloying with 0.07 wt.% Sc alone was sufficient to maintain grain stability at 500 °C, but recrystallization occurred at higher temperatures. The co-addition of Zr further enhanced the thermal stability, with the

Al-0.19Sc-0.15Zr alloy exhibiting the greatest resistance to recrystallization and grain growth. In contrast, the base alloy exhibited severe microstructural degradation, becoming fully recrystallized and prone to AGG.

2.4 Discussion

2.4.1 Effect of Al_3Sc and $Al_3(Sc,Zr)$ precipitates on recrystallization resistance

The low-temperature homogenization at 350 ºC applied in this study was to promote the formation of $Al_3Sc/Al_3(Sc,Zr)$ precipitates to act as recrystallization inhibitors during both hot deformation and post-annealing. TEM observation (Section 2-3.2) confirmed numerous nanoprecipitates were formed during the low-temperature homogenization in all the three Sc-containing alloys. The fine and coherent Al_3Sc or $Al_3(Sc,Zr)$ precipitates are known to effectively hinder grain boundary migration, and to exert a Zener pinning force, preventing grain growth and recrystallization. The Zener drag pressure (P_z), which is the force per unit area exerted by the particles on the grain boundary, can be expressed by Eq. 2 [10,74,75].

$$\boldsymbol{P}_z = \frac{3 * \boldsymbol{\gamma}_{GB} * f_v}{2\boldsymbol{r}} \qquad \text{Equation 2}$$

where γ_{GB} is the specific grain boundary energy (0.32 J/m^2), r is the average radius of the particle, and f_v is the volume fraction of the precipitates, which can be expressed by Eq. 3 [10].

$$fv = \frac{4}{3}\pi r^3 * N_d \qquad \text{Equation 3}$$

The base alloy possessed relatively few particles (just Fe-rich intermetallic particles) without any precipitates, and therefore, its Zener drag pressure, P_z, is almost negligible. For the three Sc-containing alloys, as shown in Eq. 2, a high value of f_v/r is required to achieve a large

Zener drag pressure on grain boundary migration to retard the recovery and recrystallisation processes [75]. P_z can be greatly increased by maximizing the volume fraction and minimizing the size of particles. As shown in Table 2-2, the Al_3Sc precipitates formed in the Al-0.07Sc alloy exhibited the coarsest precipitate size and the lowest density among the three Sc containing alloys, and therefore, it has the lowest volume fraction (Eq. 3). The co-addition of Zr contributed to reducing the size of the precipitates, and to increase their number density and volume fraction. As shown graphically in Fig. 2-12, the f_v/r ratio increased from 13.6×10^4 m^{-1} in the Al-0.07Sc alloy to 17.2×10^4 m^{-1} in the Al-0.07Sc-0.10Zr alloy, and further to 22.7×10^4 m^{-1} in the Al-0.19Sc-0.15Zr alloy. Correspondingly, among the three Sc-containing alloys, the Al-0.07Sc alloy exhibited the lowest P_z of 0.06 MPa, while the P_z value in the Al-0.07Sc-0.10Zr was 0.08 MPa due to the formation of more stable and finer $Al_3(Sc,Zr)$ precipitates. The Al-0.19Sc-0.15Zr alloy, where the increase of Sc and Zr contents resulted in the highest f_v/r value, exhibited the highest P_z of 0.11 MPa. The higher P_z values account for the improved grain stability observed during the post-annealing in the two Sc/Zr-containing alloys, as compared to the base alloy and the Al-0.07Sc alloy.

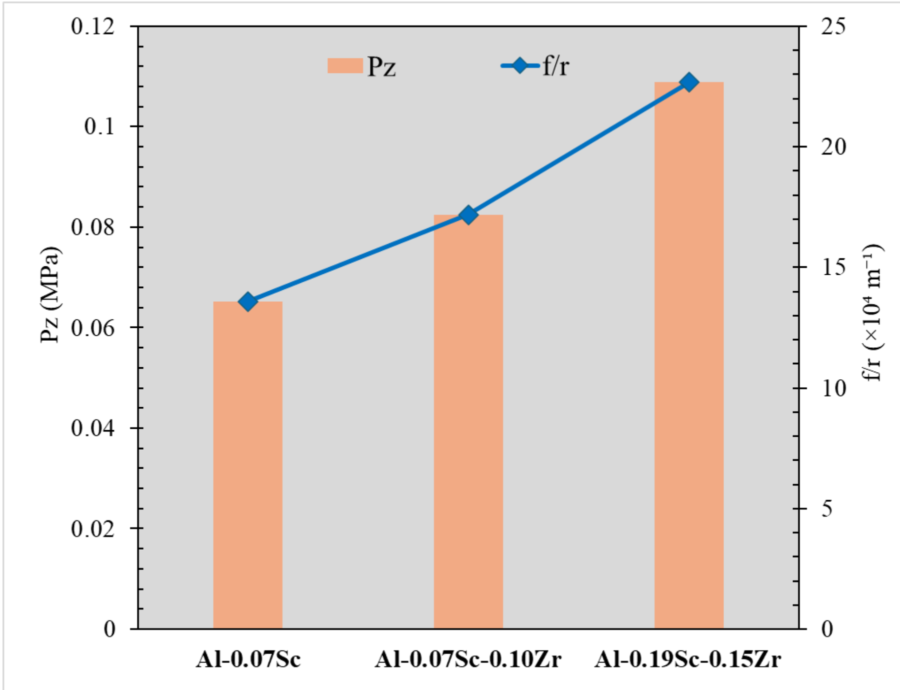

Figure 2-12 P_z and f_v/r values of the four investigated alloys after homogenization.

2.4.2 Evolution of Al_3Sc and $Al_3(Sc,Zr)$ precipitates during post-deformation annealing

The Zener drag pressure analysis in the previous section highlighted the role of dispersoid size and number density in maintaining the grain stability. To further explore the thermal stability of dispersoids, targeted TEM investigations were conducted on selected samples from the three Sc-containing alloys after post-annealing. After annealing at 500 ºC, the Al_3Sc precipitates in the Al-0.07Sc alloy appeared as shown in Figures 2-13a and 2-13b. The precipitates retained their spherical morphology but grew to an average diameter of 42 ± 4.7 nm, which indicates significant coarsening during post-annealing compared to their average diameter of 6.6 ± 1.9 nm after the low-temperature homogenization at 350 ºC (Figures 2-3a, 2-4, and Table 2-2). The presence of Moiré fringes within the precipitates (Figures 2-13a) suggests a slight misalignment with the aluminum matrix, resulting from the change in particle size and a gradual loss of coherency [34,76]. This observation aligns with the findings of

Iwamura et al. al [77], who reported that the critical radius for Al_3Sc to lose coherency with the matrix ranges between 15 and 40 nm. The start of loss in coherency of those particles is also detected by the presence of interfacial dislocations (appearing as parallel lines observed on the precipitates) in the bright field TEM (Figure 2-13b) [78]. The EBSD result of the Al-0.07Sc alloy after annealing at 500 ºC showed a mostly recovered microstructure (Figure 2-9d), indicating that these coarsened Al_3Sc can still successfully resist recrystallization. However, the observed coarsening and partial loss of coherency after the 500 °C treatment indicate a reduced pinning effect of the Al_3Sc precipitates at higher annealing temperatures. Those TEM observations help to explain the EBSD results, which show that the microstructure was fully recrystallized after annealing at 550 °C and 575 °C (Figures 2-9e and 2-9f, respectively), confirming the reduced effectiveness of Al_3Sc precipitates at higher temperatures.

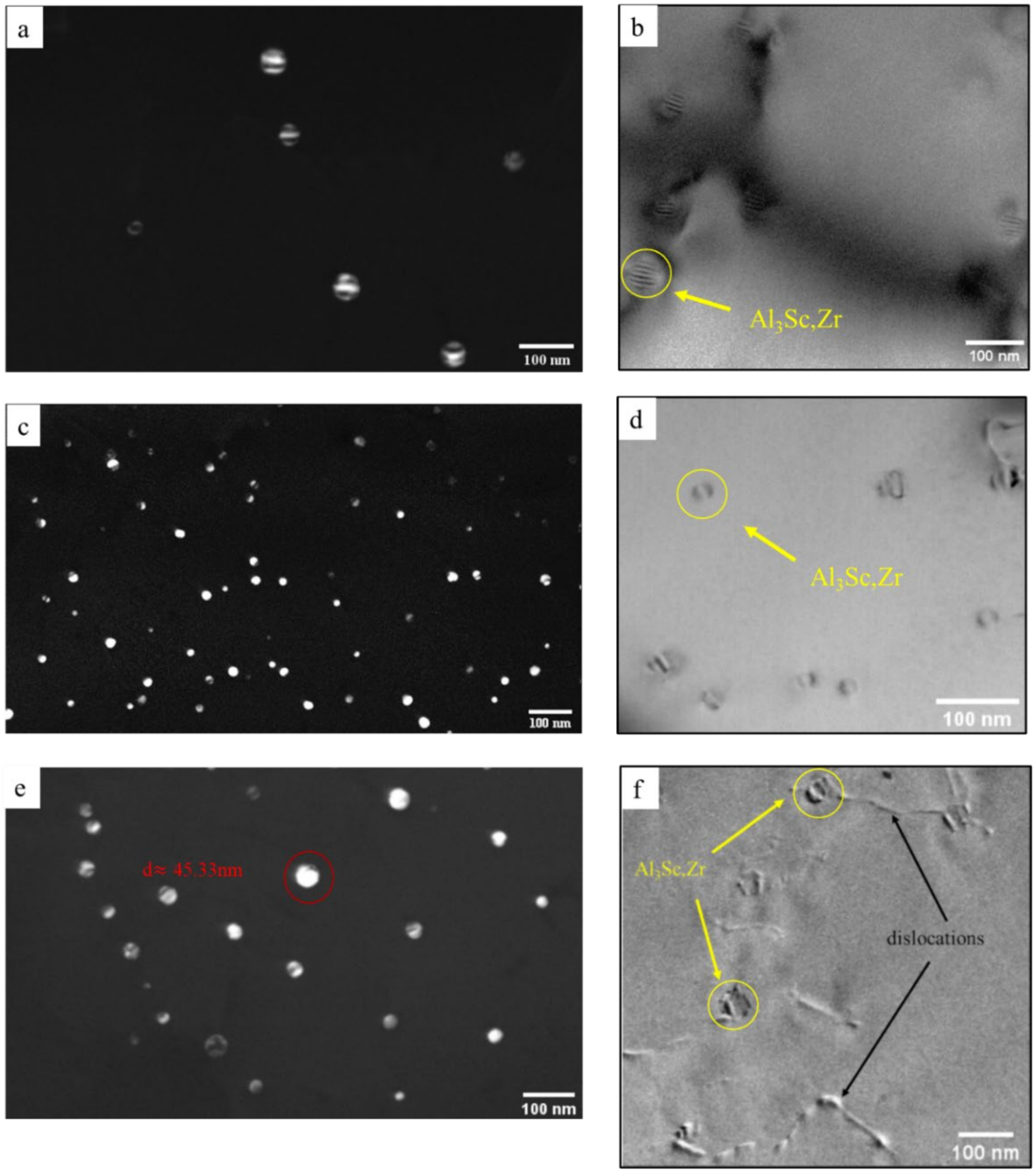

Figure 2-13 TEM micrographs of the Al_3Sc/$Al_3(Sc,Zr)$ precipitates, (a, b) Al-0.07Sc alloy after annealing at 500 ºC for 1 h, (c, d) Al-0.07Sc-0.10Zr alloy after annealing at 550 ºC for 1 h, and (e, f) Al-0.19Sc-0.15Zr alloy after annealing at 575 ºC for 1h.

Unlike the Al-0.07Sc alloy, the Al-0.07Sc-0.10Zr alloy showed excellent resistance to recrystallization with a recovered grain structure after the annealing at 550 ºC. The TEM images in Figs. 2-13c and 2-13d show the $Al_3(Sc,Zr)$ precipitates remained relatively stable with a moderate coarsening to an average diameter of 15.5 ± 3.5nm (Figure 2-13c), compared to 5.5 ± 1.3 nm in the homogenized condition (Table 2-2). The bright-field TEM image in Figure 2-13d reveals $Al_3(Sc,Zr)$ precipitates that exhibited a "bean-like" contrast, a characteristic feature indicating that the coherency between the precipitate and the matrix was maintained [28,77,79]. Even after annealing at 550 ºC for 1 h, those coherent precipitates can still effectively pin grain boundaries and dislocations, thereby hindering grain growth and recrystallization [80].

The enhanced recrystallization resistance observed with Zr co-additions in our results aligns with previous studies that have reported a delayed onset of recrystallization in Al-Sc-Zr alloys compared to Al-Sc alloys. For instance, Zakharov et al. [81] found that a hot-pressed Al-0.2% Sc strip began recrystallizing at 490 ºC and was fully recrystallized at 550 ºC, whereas in the alloy containing Zr, recrystallization started at 570 ºC and ended at 600 ºC. Similar observations were also reported by Jia et al. [37] , who found that the recrystallization onset temperature for a binary extruded Al-Sc alloy was 520ºC, while the addition of Zr increased the onset temperature by 100 ºC.

However, increasing the annealing temperature further to 575ºC resulted in the appearance of large, recrystallized grains in the recovered microstructure of the Al-0.07Sc-0.10Zr alloy (Figure 2-9i), suggesting a localized loss of pinning pressure owing to coarsening of the precipitates at this high temperature. As the precipitates grew, their effectiveness in pinning grain boundaries diminished, allowing some regions to undergo recrystallization [38,82].

The Al-0.19Sc-0.15Zr alloy was the only alloy retaining the mostly deformed microstructure after all the three post-annealing treatments, even at the highest temperature of 575 ºC. The TEM micrographs of the $Al_3(Sc,Zr)$ precipitates after annealing at 575 ºC are displayed in Figures 2-13e and 2-13f. The precipitates exhibit a wide size distribution, with an average diameter of approximately 24.9 ± 8.9 nm and a few large ones reaching the maximum diameter of 45.3 nm (Figure 2-13e). At such a high temperature, the precipitates underwent obvious coarsening compared to their initial size after homogenization. However, most of the precipitates were still found to be coherent. The bright-field TEM image of Figure 2-13f illustrates the bowing of dislocations at their interaction points with the $Al_3(Sc,Zr)$ precipitates, which exerted a pinning effect and acted as obstacles that impede dislocation motion [39,83]. It is apparent that $Al_3(Sc,Zr)$ precipitates in the Al-0.19Sc-0.15Zr alloy exhibited a sufficient thermal stability even during annealing at 575 ºC to effectively inhibit recrystallization and grain growth and maintaining a superior grain stability.

The thermal stability of $Al_3(Sc,Zr)$ precipitates in some aluminum alloys with similar Sc and Zr contents (approximately 0.2 wt.% Sc and 0.15 wt.% Zr) has been documented in the literature. For instance, Deng et al. [84] , observed that in a rolled Al-Zn-Mg alloy containing 0.25 wt.% Sc and 0.1 wt.% Zr, the $Al_3(Sc,Zr)$ particles remained coherent after annealing at 600 °C for 1 h. Lee et al. [85] , reported that an Al–Mg–0.2Sc–0.12Zr alloy, processed by equal-channel angular pressing, exhibited excellent grain stability when subjected to annealing at up to 550 °C. The improved grain stability observed in Sc/Zr-containing alloys at high temperatures highlights their strong potential for high-temperature applications like brazed heat exchangers, where maintaining grain structure and preventing excessive grain growth are crucial.

The influence of thermally stable dispersoids, formed during homogenization, is evident across all subsequent processing stages from hot deformation to post-annealing. Table 2-3 summarizes and compares the overall behavior of the four investigated alloys by presenting the calculated Zener drag pressure P_z (derived from dispersoid characteristics in the as-homogenized condition), the flow stress values (from hot compression tests), and the AGG behavior observed after annealing at 500, 550, and 575 °C. This highlights how the initial dispersoid stability influences the deformation behavior and microstructural evolution across all key processing steps. Alloys containing both Sc and Zr exhibited higher flow stresses and reduced flow softening compared to the Sc-only and base alloys (Figures 2-5), indicating suppressed dynamic recovery [39]. This observation is also supported by the microstructural evolution observed in EBSD analysis of the as-deformed samples (Figures 2-6 and 2-7). The fractions of LAGBs and MAGBs in the two Sc/Zr-containing alloys were greatly increased to retain the deformed structures relative to the Sc-only alloy (Al-0.07Sc) owing to the presence of finer and more numerous $Al_3(Sc,Zr)$ precipitates formed during homogenization. Those precipitates remained stable during the hot deformation (Figure 2-8).

Following the post-annealing heat treatments, the two Sc/Zr-containing alloys exhibited significantly enhanced grain stability. The migration of the grain boundaries was strongly hindered at all three annealing temperatures. This behaviour is attributed to the higher P_z values in the Sc/Zr containing alloys compared with the Al-0.07Sc alloy. Consequently, the two Sc/Zr-containing alloys display a remarkably higher recrystallization resistance.

Table 2-3 Summary of Zener drag pressure (Pz), flow stress at 450 °C, and observed AGG behavior after annealing at 500 °C, 550 °C, and 575 °C for 1 h.

Alloy	Pz (MPa)	Flow Stress (MPa)	AGG at 500 °C/1h	AGG at 550 °C/1h	AGG at 575 °C/1h
Base	0	27	Severe	Severe	Severe
Al-0.07Sc	0.06	36.5	None	Moderate	Severe
Al-0.07Sc-0.10Zr	0.08	42.3	None	None	Moderate
Al-0.19Sc-0.15Zr	0.11	53.5	None	None	None

From an economic perspective, the amount of Sc addition is a key factor, as increasing the Sc content significantly raises the product costs. In this regard, the Al-0.07Sc-0.10Zr alloy remains a viable option in applications where the effective thermal exposure does not exceed about 1 h at 550 °C, thereby balancing cost-effectiveness with performance. Yet in more severe scenarios where the effective thermal exposure is above 1 h at 575 ºC, the Al-0.19Sc-0.15Zr alloy might be a good choice to ensure better grain stability. However, as shown in Figure 5, the flow stress also increases with increasing Sc/Zr content. This will result in a decreased extrudability, which can also increase the overall cost. Possible options to decrease the flow stress and improve the extrudability might be the use of a higher hot deformation temperature or a modified homogenization treatment.

2.5Conclusions

This study investigated the effects of Sc and Zr microalloying on the recrystallization behavior and grain growth of four 1xxx aluminum heat exchanger alloys during three post-deformation annealing treatments at 500, 550 and 575 ºC for 1 h to simulate the high-temperature brazing process. The following conclusions are drawn from the main results:

A low-temperature homogenization at 350 °C for 24 h promoted the formation of numerous $Al_3Sc/Al_3(Sc,Zr)$ nanoprecipitates in the three Sc-containing alloys. With increasing contents of Sc and Zr, the average size of these precipitates decreased, and the number density increased. During hot compression deformation, all the four alloys underwent dynamic recovery. Compared to the base alloy, the three Sc-containing alloys exhibited higher fractions of low-angle grain boundaries, indicating that the microalloying with Sc and Zr imposed large restrictions on the recovery process.

Following the post-deformation annealing at 500 °C, full recrystallization occurred in the base alloy. Increasing the annealing temperature resulted in the occurrence of abnormal grain growth due to the lack of precipitates. In the Al-0.07Sc alloy, the Al_3Sc precipitates effectively retarded recrystallization during annealing at 500 °C, while full recrystallization occurred at the higher annealing temperatures.

The Al-0.07Sc-0.10Zr alloy preserved its mostly deformed and recovered microstructure during annealing up to 550 ºC owing to the stable $Al_3(Sc,Zr)$ precipitates, which exerted a high Zener drag pressure on grain boundary migration that retards the recovery and recrystallisation. Local recrystallization occurred after annealing at the higher temperature of 575 °C.

The Al-0.19Sc-0.15Zr alloy preserved its mostly deformed microstructure even after annealing at 575 °C, showing the highest recrystallization resistance among the four alloys studied owing to its highest number density and finest size of $Al_3(Sc,Zr)$ precipitates.

The Al-0.07Sc-0.10Zr alloy provides a good balance between cost-effectiveness and grain stability, making it suitable when the effective thermal exposure during brazing or other elevated temperature processing does not exceed the equivalent of about 1 h at 550 °C. However, under extreme conditions where the effective thermal exposure is equivalent of 1 h at 575 °C, the Al-0.19Sc-0.15Zr alloy may be more appropriate.

2.6 Authorship contribution

Alyaa Bakr: investigation, formal analysis, methodology, writing—original. Paul Rometsch: conceptualization, methodology, validation, writing—review and editing. X.-Grant Chen: conceptualization, methodology, validation, writing—review and editing, supervision.

References

[1]G.S. Cole, A.M. Sherman, Light weight materials for automotive applications, Mater Charact 35 (1995) 3–9. https://doi.org/https://doi.org/10.1016/1044-5803(95)00063-1.

[2]J.C. Guía-Tello, M.I. Pech-Canul, E. Trujillo-Vázquez, M.A. Pech-Canul, Effect of brazing parameters on fillet size and microstructure of cladded fin-microchannel tube joints, Transactions of Nonferrous Metals Society of China 30 (2020) 3240–3253. https://doi.org/https://doi.org/10.1016/S1003-6326(20)65457-7.

[3]M. Shakiba, N. Parson, X.G. Chen, Effect of Iron and Silicon Content on the Hot Compressive Deformation Behavior of Dilute Al-Fe-Si Alloys, J Mater Eng Perform 24 (2015) 404–415. https://doi.org/10.1007/s11665-014-1302-3.

[4]Y.-S. Kim, I.-J. Park, B.-S. An, J.G. Park, C.-W. Yang, Y.H. Lee, J.-G. Kim, Improvement of corrosion penetration resistance for aluminum heat exchanger by alloying zirconium, Mater Chem Phys 241 (2020) 122275. https://doi.org/https://doi.org/10.1016/j.matchemphys.2019.122275.

[5]M.J. Benoit, H. Jin, B. Shalchi-Amirkhiz, S. Kurukuri, S. Winkler, M.J. Worswick, M.A. Wells, Microstructure evolution of warm deformed multilayered Al alloy sheet during brazing,

J Mater Process Technol 281 (2020) 116639. https://doi.org/10.1016/j.jmatprotec.2020.116639.

[6]W.S. Miller, L. Zhuang, J. Bottema, A.J. Wittebrood, P. De Smet, A. Haszler, A. Vieregge, Recent development in aluminium alloys for the automotive industry, Materials Science and Engineering A 280 (2000) 37–49. https://doi.org/10.1016/S0921-5093(99)00653-X.

[7]K. Li, D. Li, T. Zou, D. Shu, D. Tang, Y. Peng, Strength Variation in Processing Multiport Extrusion Tubes of A1100 and A3102 Alloys, J Mater Eng Perform 28 (2019) 3576–3589. https://doi.org/10.1007/s11665-019-04132-w.

[8]C.N. Niu, X.G. Song, S.P. Hu, G.Z. Lu, Z.B. Chen, G.D. Wang, Effects of brazing temperature and post weld heat treatment on 7075 alloy brazed joints, J Mater Process Technol 266 (2019) 363–372. https://doi.org/https://doi.org/10.1016/j.jmatprotec.2018.11.023.

[9]T.-W. Na, H.-K. Park, C.-S. Park, J.-T. Park, N.-M. Hwang, Misorientation angle analysis near the growth front of abnormally growing grains in 5052 aluminum alloy, Acta Mater 115 (2016) 224–229. https://doi.org/https://doi.org/10.1016/j.actamat.2016.06.007.

[10]F.J. Humphreys, M. Hatherly, Recrystallization and Related Annealing Phenomena, Recrystallization and Related Annealing Phenomena (2012) 1–497. https://doi.org/10.1016/C2009-0-07986-0.

[11]J. Dennis, P.S. Bate, F.J. Humphreys, Abnormal grain growth in Al–3.5Cu, Acta Mater 57 (2009) 4539–4547. https://doi.org/https://doi.org/10.1016/j.actamat.2009.06.018.

[12]R. Liu, K. Li, G. Zhou, W. Tang, Y. Shen, D. Tang, D. Li, Simulation of strain induced abnormal grain growth in aluminum alloy by coupling crystal plasticity and phase field methods, Transactions of Nonferrous Metals Society of China 32 (2022) 3873–3886. https://doi.org/https://doi.org/10.1016/S1003-6326(22)66064-3.

[13]E.J. Payton, G. Wang, M.J. Mills, Y. Wang, Effect of initial grain size on grain coarsening in the presence of an unstable population of pinning particles, Acta Mater 61 (2013) 1316–1326. https://doi.org/https://doi.org/10.1016/j.actamat.2012.11.009.

[14]Z. Wang, Y. Xu, A quasi-in-situ EBSD study on abnormal grain growth in 2219 aluminum alloy friction stir welded joints during post-weld heat treatment, Mater Des 247 (2024) 113386. https://doi.org/https://doi.org/10.1016/j.matdes.2024.113386.

[15]X. Xu, X. Ma, G. Zhao, X. Chen, Y. Wang, Abnormal grain growth of 2196 Al-Cu-Li alloy weld seams during extrusion and heat treatment, J Alloys Compd 867 (2021) 159043. https://doi.org/https://doi.org/10.1016/j.jallcom.2021.159043.

[16]G. Wang, D.S. Xu, E.J. Payton, N. Ma, R. Yang, M.J. Mills, Y. Wang, Mean-field statistical simulation of grain coarsening in the presence of stable and unstable pinning particles, Acta Mater 59 (2011) 4587–4594. https://doi.org/https://doi.org/10.1016/j.actamat.2011.04.004.

[17]I. Andersen, Ø. Grong, N. Ryum, Analytical modelling of grain growth in metals and alloys in the presence of growing and dissolving precipitates—II. Abnormal grain growth, Acta Metallurgica et Materialia 43 (1995) 2689–2700. https://doi.org/https://doi.org/10.1016/0956-7151(94)00489-5.

[18]F.F. Kraft, Method for Predicting and Optimizing the Strength of Extruded Multi-Void Aluminum Heat Exchanger Tube, SAE Transactions 111 (2002) 99–106. http://www.jstor.org/stable/44719187.

[19]D. Tang, X. Fan, W. Fang, D. Li, Y. Peng, H. Wang, Microstructure and mechanical properties development of micro channel tubes in extrusion, rolling and brazing, Mater Charact 142 (2018) 449–457. https://doi.org/10.1016/j.matchar.2018.06.010.

[20]K. Li, T. Zou, D. Li, Y. Peng, D. Shu, On Formation of Abnormally Large Grains in Annealing Prestrained Aluminum Alloy Multiport Extrusion Tubes, Metallurgical and Materials Transactions A 50 (2019) 5734–5749. https://doi.org/10.1007/s11661-019-05453-0.

[21]Z. Guo, G. Zhao, X.-G. Chen, Effects of two-step homogenization on precipitation behavior of Al3Zr dispersoids and recrystallization resistance in 7150 aluminum alloy, Mater Charact 102 (2015) 122–130. https://doi.org/https://doi.org/10.1016/j.matchar.2015.02.016.

[22]X. Wang, G. Zhao, L. Sun, Y. Wang, Z. Lv, S. Xu, X. Ge, Effect of strain and dispersoids on abnormal grain growth, precipitation behavior and mechanical properties at longitudinal weld in Al-Li alloy profile, J Mater Process Technol 322 (2023) 118216. https://doi.org/https://doi.org/10.1016/j.jmatprotec.2023.118216.

[23]H. Li, Z. Gao, H. Yin, H. Jiang, X. Su, J. Bin, Effects of Er and Zr additions on precipitation and recrystallization of pure aluminum, Scr Mater 68 (2013) 59–62. https://doi.org/https://doi.org/10.1016/j.scriptamat.2012.09.026.

[24]Y. Birol, Effect of Cr and Zr on the grain structure of extruded EN AW 6082 alloy, Metals and Materials International 20 (2014) 727–732. https://doi.org/10.1007/s12540-014-4018-x.

[25]J. Lai, C. Shi, X.-G. Chen, Effects of V addition on recrystallization resistance of 7150 aluminum alloy after simulative hot deformation, Mater Charact 96 (2014) 126–134. https://doi.org/https://doi.org/10.1016/j.matchar.2014.07.028.

[26]A. Algendy, K. Liu, X.-G. Chen, Effect of Mn-Bearing Dispersoids on Tensile Properties and Recrystallization Resistance of Al-3Mg-0.8Mn Rolled Alloy, Adv Eng Mater 25 (2023). https://doi.org/10.1002/adem.202300667.

[27]J. Røyset, N. Ryum, Scandium in aluminium alloys, International Materials Reviews 50 (2005) 19–44. https://doi.org/https://doi.org/10.1179/174328005X14311.

[28]D.N. Seidman, E.A. Marquis, D.C. Dunand, Precipitation strengthening at ambient and elevated temperatures of heat-treatable Al(Sc) alloys, Acta Mater 50 (2002) 4021–4035. https://doi.org/10.1016/S1359-6454(02)00201-X.

[29]V.G. Davydov, T.D. Rostova, V. V. Zakharov, Y.A. Filatov, V.I. Yelagin, Scientific principles of making an alloying addition of scandium to aluminium alloys, Materials Science and Engineering A 280 (2000) 30–36. https://doi.org/10.1016/S0921-5093(99)00652-8.

[30]P. Xu, F. Jiang, Z. Tang, N. Yan, J. Jiang, X. Xu, Y. Peng, Coarsening of Al3Sc precipitates in Al-Mg-Sc alloys, J Alloys Compd 781 (2019) 209–215. https://doi.org/https://doi.org/10.1016/j.jallcom.2018.12.133.

[31]A. De Luca, D.C. Dunand, D.N. Seidman, Mechanical properties and optimization of the aging of a dilute Al-Sc-Er-Zr-Si alloy with a high Zr/Sc ratio, Acta Mater 119 (2016) 35–42. https://doi.org/https://doi.org/10.1016/j.actamat.2016.08.018.

[32]B. Forbord, H. Hallem, J. Røyset, K. Marthinsen, Thermal stability of Al3(Scx,Zr1-x)-dispersoids in extruded aluminium alloys, Materials Science and Engineering A 475 (2008) 241–248. https://doi.org/10.1016/j.msea.2007.04.054.

[33]K. Yan, Z. Chen, W.J. Lu, Y. Zhao, W. Le, S. Naseem, Nucleation and growth of Al3Sc precipitates during isothermal aging of Al-0.55 wt% Sc alloy, Mater Charact 179 (2021) 111331. https://doi.org/10.1016/j.matchar.2021.111331.

[34]H.U. Sverdrup, A.E. Sverdrup, On the Supply Dynamics of Scandium, Global Resources, Production, Oxide and Metal Price, a Prospective Modelling Study Using WORLD7, Biophysical Economics and Sustainability 9 (2024) 2. https://doi.org/10.1007/s41247-024-00118-y

[35]S. Phoung, E. Williams, G. Gaustad, A. Gupta, Exploring global supply and demand of scandium oxide in 2030, J Clean Prod 401 (2023) 136673. https://doi.org/https://doi.org/10.1016/j.jclepro.2023.136673.

[36]Yu. Buranova, V. Kulitskiy, M. Peterlechner, A. Mogucheva, R. Kaibyshev, S. V Divinski, G. Wilde, Al3(Sc,Zr)-based precipitates in Al–Mg alloy: Effect of severe deformation, Acta Mater 124 (2017) 210–224. https://doi.org/https://doi.org/10.1016/j.actamat.2016.10.064.

[37]K.E. Knipling, R.A. Karnesky, C.P. Lee, D.C. Dunand, D.N. Seidman, Precipitation evolution in Al-0.1Sc, Al-0.1Zr and Al-0.1Sc-0.1Zr (at.%) alloys during isochronal aging, Acta Mater 58 (2010) 5184–5195. https://doi.org/10.1016/j.actamat.2010.05.054.

[38]K.E. Knipling, D.N. Seidman, D.C. Dunand, Ambient- and high-temperature mechanical properties of isochronally aged Al–0.06Sc, Al–0.06Zr and Al–0.06Sc–0.06Zr (at.%) alloys, Acta Mater 59 (2011) 943–954. https://doi.org/https://doi.org/10.1016/j.actamat.2010.10.017.

[39]Z.H. Jia, J. Royset, J.K. Solberg, Q. Liu, Formation of precipitates and recrystallization resistance in Al-Sc-Zr alloys, Transactions of Nonferrous Metals Society of China (English Edition) 22 (2012) 1866–1871. https://doi.org/10.1016/S1003-6326(11)61399-X.

[40]V. Ocenasek, M. Slamova, Resistance to recrystallization due to Sc and Zr addition to Al–Mg alloys, Mater Charact 47 (2001) 157–162. https://doi.org/https://doi.org/10.1016/S1044-5803(01)00165-6.

[41]S. Babaniaris, M. Ramajayam, L. Jiang, R. Varma, T. Langan, T. Dorin, Effect of Al3(Sc,Zr) dispersoids on the hot deformation behaviour of 6xxx-series alloys: A physically based constitutive model, Materials Science and Engineering: A 793 (2020) 139873. https://doi.org/https://doi.org/10.1016/j.msea.2020.139873.

[42]A.Y. Algendy, P. Rometsch, X.G. Chen, Mechanical and corrosion performances of Al–Mg-Mn 5083 rolled alloys microalloyed with Sc and Zr in different thermomechanical processing conditions, J Mater Sci 59 (2024) 14692–14715. https://doi.org/10.1007/s10853-024-10044-5.

[43]X. Lai, M. Wu, D. Xiao, L. Huang, W. Liu, P. Zhao, Microstructures and mechanical properties of a novel Al-5Mg-3Zn alloy with the combined additions Sc and Zr, Mater Today Commun 41 (2024) 110669. https://doi.org/https://doi.org/10.1016/j.mtcomm.2024.110669.

[44]B. Li, Q. Pan, X. Huang, Z. Yin, Microstructures and properties of Al–Zn–Mg–Mn alloy with trace amounts of Sc and Zr, Materials Science and Engineering: A 616 (2014) 219–228. https://doi.org/https://doi.org/10.1016/j.msea.2014.08.024.

[45]J. Ye, Q. Pan, B. Liu, Q. Hu, L. Qu, W. Wang, X. Wang, Effects of co-addition of minor Sc and Zr on aging precipitates and mechanical properties of Al–Zn–Mg–Cu alloys, Journal of Materials Research and Technology 22 (2023) 2944–2954. https://doi.org/https://doi.org/10.1016/j.jmrt.2022.12.133.

[46]Z. Lu, X. Wu, J. Xu, H. Zhang, L. Yu, L. Zhao, Y. Jiang, Improving mechanical properties of spray formed 7055 aluminium alloy metal-inert gas welds by scandium addition, J Alloys Compd 1013 (2025) 178406. https://doi.org/https://doi.org/10.1016/j.jallcom.2024.178406.

[47]Q. Xiao, J. Huang, Y. Jiang, F. Jiang, Y. Wu, G. Xu, Effects of minor Sc and Zr additions on mechanical properties and microstructure evolution of Al−Zn−Mg−Cu alloys, Transactions of Nonferrous Metals Society of China 30 (2020) 1429–1438. https://doi.org/https://doi.org/10.1016/S1003-6326(20)65308-0.

[48]T.H. Chuang, L.C. Tsao, T.C. Tsai, M.S. Yeh, C.S. Wu, Development of a low-melting-point filler metal for brazing aluminum alloys, Metallurgical and Materials Transactions A 31 (2000) 2239–2245. https://doi.org/10.1007/s11661-000-0141-z.

[49]H. Zhao, S. Elbel, P.S. Hrnjak, Compatibility of Filler and Base Metals in Heat Exchanger Manufacturing Process, (2018).

[50]L.C. Tsao, T.C. Tsai, C.S. Wu, T.H. Chuang, Brazeability of the 6061-T6 aluminum alloy with Al-Si-20Cu-based filler metals, J Mater Eng Perform 10 (2001) 705–709. https://doi.org/10.1361/105994901770344584.

[51]L.C. Tsao, M.J. Chiang, W.H. Lin, M.D. Cheng, T.H. Chuang, Effects of zinc additions on the microstructure and melting temperatures of Al–Si–Cu filler metals, Mater Charact 48 (2002) 341–346. https://doi.org/https://doi.org/10.1016/S1044-5803(02)00276-0.

[52]J. Røyset, N. Ryum, Kinetics and mechanisms of precipitation in an Al-0.2wt.% Sc alloy, Materials Science and Engineering A 396 (2005) 409–422. https://doi.org/10.1016/j.msea.2005.02.015.

[53]X. Na, L. Wenqing, Z. Liu, T. Muthuramalingam, Effect of Scandium in Al–Sc and Al–Sc–Zr Alloys Under Precipitation Strengthening Mechanism at 350 °C Aging, Metals and Materials International 27 (2021) 5145–5153. https://doi.org/10.1007/s12540-020-00844-0.

[54]Y. Su, L. Ding, Y. Zhang, Y. Weng, C. Wang, Z. Jia, L. Zhuang, The dispersoid evolution, recrystallization and mechanical properties of an Al–Mg–Sc alloy under various homogenization and annealing processes, J Mater Sci 60 (2025) 3558–3575. https://doi.org/10.1007/s10853-025-10673-4.

[55]H. Huang, F. Jiang, J. Zhou, L. Wei, J. Qu, L. Liu, Effects of Al3(Sc,Zr) and Shear Band Formation on the Tensile Properties and Fracture Behavior of Al-Mg-Sc-Zr Alloy, J Mater Eng Perform 24 (2015) 4244–4252. https://doi.org/10.1007/s11665-015-1748-y.

[56]H. Huang, F. Jiang, J. Zhou, L. Wei, M. Zhong, X. Liu, Hot deformation behavior and microstructural evolution of as-homogenized Al–6Mg–0.4Mn–0.25Sc–0.1Zr alloy during compression at elevated temperature, J Alloys Compd 644 (2015) 862–872. https://doi.org/https://doi.org/10.1016/j.jallcom.2015.05.048.

[57]D. Tang, W. Fang, X. Fan, D. Li, Y. Peng, Effect of die design in microchannel tube extrusion, Procedia Eng 81 (2014) 628–633. https://doi.org/10.1016/j.proeng.2014.10.051.

[58]J.M. Lee, S.W. Lee, Y.K. Kim, W.H. Jo, C.J. Lee, B.M. Kim, Extrusion of AA 3003 micro condenser tube with multi-hole and thin wall section using porthole die, International Journal of Precision Engineering and Manufacturing - Green Technology 3 (2016) 239–245. https://doi.org/10.1007/s40684-016-0031-5.

[59]W. Fang, D. Tang, H. Wang, D. Li, Y. Peng, Optimization of die design for thin-walled flat multi-port tube with the aid of finite element simulation, J Mater Process Technol 277 (2020) 116418. https://doi.org/10.1016/j.jmatprotec.2019.116418.

[60]F. Qian, S. Jin, G. Sha, Y. Li, Enhanced dispersoid precipitation and dispersion strengthening in an Al alloy by microalloying with Cd, Acta Mater 157 (2018) 114–125. https://doi.org/10.1016/j.actamat.2018.07.001.

[61]Q. Zhao, Z. Qian, X. Cui, Y. Wu, X. Liu, Optimizing microstructures of dilute Al–Fe–Si alloys designed with enhanced electrical conductivity and tensile strength, J Alloys Compd 650 (2015) 768–776. https://doi.org/https://doi.org/10.1016/j.jallcom.2015.08.052.

[62]M. Shakiba, N. Parson, X.G. Chen, Effect of homogenization treatment and silicon content on the microstructure and hot workability of dilute Al-Fe-Si alloys, Materials Science and Engineering A 619 (2014) 180–189. https://doi.org/10.1016/j.msea.2014.09.072.

[63]Y. Deng, G. Zhang, Z. Yang, G. Xu, Microstructure characteristics and mechanical properties of new aerospace Al-Mg-Mn alloys with Al3(Sc1−xZrx) or Al3(Er1−xZrx) nanoparticles, Mater Charact 153 (2019) 79–91. https://doi.org/https://doi.org/10.1016/j.matchar.2019.04.032.

[64]J. Huang, L. Feng, C. Li, C. Huang, J. Li, B. Friedrich, Scripta Materialia Mechanism of Sc poisoning of Al-5Ti-1B grain refiner, 180 (2020) 88–92. https://doi.org/10.1016/j.scriptamat.2020.01.031.

[65]Y. Deng, Z. Yin, K. Zhao, J. Duan, Z. He, Effects of Sc and Zr microalloying additions on the microstructure and mechanical properties of new Al–Zn–Mg alloys, J Alloys Compd 530 (2012) 71–80. https://doi.org/https://doi.org/10.1016/j.jallcom.2012.03.108.

[66]K.B. Hyde, A.F. Norman, P.B. Prangnell, The effect of cooling rate on the morphology of primary Al3Sc intermetallic particles in Al–Sc alloys, Acta Mater 49 (2001) 1327–1337. https://doi.org/https://doi.org/10.1016/S1359-6454(01)00050-7.

[67]A.M. Bunn, P. Schumacher, M.A. Kearns, C.B. Boothroyd, A.L. Greer, Grain refinement by Al–Ti–B alloys in aluminium melts: a study of the mechanisms of poisoning by zirconium, Materials Science and Technology 15 (1999) 1115–1123. https://doi.org/10.1179/026708399101505158.

[68]T. Dorin, M. Ramajayam, A. Vahid, T. Langan, Aluminium Scandium Alloys, in: Fundamentals of Aluminium Metallurgy, 2018: pp. 439–494. https://doi.org/10.1016/B978-0-08-102063-0.00012-6.

[69]A. Tolley, V. Radmilovic, U. Dahmen, Segregation in Al3(Sc,Zr) precipitates in Al-Sc-Zr alloys, Scr Mater 52 (2005) 621–625. https://doi.org/10.1016/j.scriptamat.2004.11.021.

[70]C.B. Fuller, D.N. Seidman, Temporal evolution of the nanostructure of Al(Sc,Zr) alloys: Part II-coarsening of Al3(Sc1−xZrx) precipitates, Acta Mater 53 (2005) 5415–5428. https://doi.org/https://doi.org/10.1016/j.actamat.2005.08.015.

[71]H. Mcqueen, S. Spigarelli, M.E. Kassner, E. Evangelista, Hot Deformation and Processing of Aluminum Alloys, 2016. https://doi.org/10.1201/b11227.

[72]H.J. McQueen, N.D. Ryan, Constitutive analysis in hot working, Materials Science and Engineering: A 322 (2002) 43–63. https://doi.org/10.1016/S0921-5093(01)01117-0.

[73]C. Shi, X.-G. Chen, Effect of Zr addition on hot deformation behavior and microstructural evolution of AA7150 aluminum alloy, Materials Science and Engineering: A 596 (2014) 183–193. https://doi.org/https://doi.org/10.1016/j.msea.2013.12.057.

[74]X. Qian, N. Parson, X.G. Chen, Effects of Mn content on recrystallization resistance of AA6082 aluminum alloys during post-deformation annealing, J Mater Sci Technol 52 (2020) 189–197. https://doi.org/10.1016/j.jmst.2020.04.015.

[75]W. Qian, X. Kai, R. Tao, R. Cao, G. Chen, Y. Zhao, Microstructure evolution and high-temperature performances of AA6111 alloy strengthened by Sc, Zr co-microalloying, Materials Science and Engineering: A 887 (2023) 145788. https://doi.org/https://doi.org/10.1016/j.msea.2023.145788.

[76]A.R. Eivani, S. Valipour, H. Ahmed, J. Zhou, J. Duszczyk, Effect of the Size Distribution of Nanoscale Dispersed Particles on the Zener Drag Pressure, Metallurgical and Materials Transactions A 42 (2011) 1109–1116. https://doi.org/10.1007/s11661-010-0452-7.

[77]B. Forbord, H. Hallem, N. Ryum, K. Marthinsen, Precipitation and recrystallisation in Al-Mn-Zr with and without Sc, Materials Science and Engineering A 387–389 (2004) 936–939. https://doi.org/10.1016/j.msea.2003.10.374.

[78]J. Jiang, F. Jiang, M. Zhang, Z. Tang, M. Tong, Al3(Sc, Zr) precipitation in deformed Al-Mg-Mn-Sc-Zr alloy: Effect of annealing temperature and dislocation density, J Alloys Compd 831 (2020) 154856. https://doi.org/10.1016/j.jallcom.2020.154856.

[79]S. Iwamura, Y. Miura, Loss in coherency and coarsening behavior of Al3Sc precipitates, Acta Mater 52 (2004) 591–600. https://doi.org/10.1016/j.actamat.2003.09.042.

[80]E.A. Marquis, D.N. Seidman, Nanoscale structural evolution of Al3Sc precipitates in Al(Sc) alloys, Acta Mater 49 (2001) 1909–1919. https://doi.org/https://doi.org/10.1016/S1359-6454(01)00116-1.

[81]L. Zou, Q. Pan, Y. He, C. Wang, W. Liang, Effect of minor Sc and Zr addition on microstructures and mechanical properties of Al-Zn-Mg-Cu alloys, Transactions of Nonferrous Metals Society of China 17 (2007) 340–345. https://doi.org/10.1016/S1003-6326(07)60095-8.

[82]H. Xiang, Q.L. Pan, X.H. Yu, X. Huang, X. Sun, X.D. Wang, M.J. Li, Z.M. Yin, Superplasticity behaviors of Al-Zn-Mg-Zr cold-rolled alloy sheet with minor Sc addition, Materials Science and Engineering: A 676 (2016) 128–137. https://doi.org/https://doi.org/10.1016/j.msea.2016.08.109.

[83]V. V. Zakharov, Combined Alloying of Aluminum Alloys with Scandium and Zirconium, Metal Science and Heat Treatment 56 (2014) 281–286. https://doi.org/10.1007/s11041-014-9746-5.

[84]J. Rudnizki, B. Zeislmair, U. Prahl, W. Bleck, Prediction of abnormal grain growth during high temperature treatment, Comput Mater Sci 49 (2010) 209–216. https://doi.org/10.1016/j.commatsci.2010.04.015.

[85]J. Leng, B. Ren, Q. Zhou, J. Zhao, Effect of Sc and Zr on recrystallization behavior of 7075 aluminum alloy, Transactions of Nonferrous Metals Society of China 31 (2021) 2545–2557. https://doi.org/https://doi.org/10.1016/S1003-6326(21)65674-1.

[86]Y. Deng, G. Xu, Z. Yin, X. Lei, J. Huang, Effects of Sc and Zr microalloying additions on the recrystallization texture and mechanism of Al–Zn–Mg alloys, J Alloys Compd 580 (2013) 412–426. https://doi.org/https://doi.org/10.1016/j.jallcom.2013.06.020.

[87]S. Lee, A. Utsunomiya, H. Akamatsu, K. Neishi, M. Furukawa, Z. Horita, T.G. Langdon, Influence of scandium and zirconium on grain stability and superplastic ductilities in ultrafine-grained Al-Mg alloys, Acta Mater 50 (2002) 553–564. https://doi.org/10.1016/S1359-6454(01)00368-8.

Chapter 3

Study of 1xxx aluminum extrusion alloys for brazed heat exchangers: influences of Sc/Zr microalloying and thermomechanical processing

(This article was published in *Journal of Materials Research and Technology*, Volume 42, 2026, pp. 3072–3090)

Résumé

Les alliages d'aluminium commerciaux de la série 1xxx sont largement utilisés dans les échangeurs de chaleur brasés. Toutefois, leur stabilité granulaire limitée lors du brasage à haute température favorise la recristallisation et la croissance anormale des grains, entraînant ainsi une détérioration des propriétés mécaniques. Ce travail porte sur des bandes minces extrudées en alliages 1xxx et vise à étudier systématiquement les effets de la microalliage avec le Sc et le Zr sur la structure granulaire, les propriétés mécaniques et la résistance à la corrosion selon deux voies de traitement. Trois alliages ont été étudiés : un alliage 1xxx de base exempt de Sc et de Zr, un alliage Al-Sc-Zr à faible teneur en éléments d'addition (0,10 % massique de Sc et 0,10 % massique de Zr) et un alliage Al-Sc-Zr à forte teneur en éléments d'addition (0,19 % massique de Sc et 0,15 % massique de Zr). Après brasage à 605 °C, l'alliage de base a présenté, pour les deux voies de traitement, une structure granulaire recristallisée très grossière, associée à de faibles résistances mécaniques. L'ajout de Sc et de Zr a permis d'obtenir une structure granulaire plus fine et plus stable ainsi qu'une amélioration significative des propriétés mécaniques. Parmi les trois alliages étudiés, l'alliage Al-Sc-Zr à forte teneur était le seul à conserver la majeure partie de sa structure granulaire déformée après un brasage simulé à 605 °C. Ces résultats ont ensuite été validés par l'extrusion de microtubes multi-canaux suivie d'un brasage simulé. Pour les deux voies de traitement, un traitement de vieillissement post-brasage a favorisé davantage la précipitation de fines particules $Al_3(Sc,Zr)$ et a considérablement amélioré la résistance mécanique des alliages contenant du Sc. Globalement, bien que l'alliage

Al-Sc-Zr à forte teneur ait offert la meilleure combinaison de stabilité granulaire, de résistance mécanique, de résistance à la corrosion et d'extrudabilité selon la voie 1 (homogénéisation à haute température), l'alliage Al-Sc-Zr à faible teneur a également présenté des améliorations nettes par rapport à l'alliage de base.

Abstract

Commercial 1xxx aluminum alloys are widely used in brazed heat exchangers. However, their limited grain stability during high-temperature brazing promotes recrystallization and abnormal grain growth, leading to a deterioration of mechanical strength. This work focused on 1xxx extruded thin strips, through which the effects of Sc/Zr microalloying on grain structure, mechanical properties and corrosion resistance under two processing routes were systematically investigated. Three alloys were examined: a 1xxx base alloy free of Sc and Zr, a low Al-Sc-Zr alloy (0.10 wt.% Sc, 0.10 wt.% Zr), and a high Al-Sc-Zr alloy (0.19 wt.% Sc, 0.15 wt.% Zr). The base alloy exhibited a very coarse recrystallized grain structure after brazing at 605 °C under both processing routes, resulting in low mechanical strengths. With Sc and Zr microalloying, the grain structure became finer and more stable, and the mechanical strengths were significantly improved. Among the three alloys studied, the high Al-Sc-Zr alloy was the only one that maintained most of the deformed grain structure after simulated brazing at 605 °C. Those findings were further validated by extruding micro multi-port tubes and subjecting them to a simulated braze. For both routes, a post-braze aging treatment further promoted fine Al3(Sc, Zr) precipitation and significantly enhanced the strength of the Sc-containing alloys. Overall, while the high Al-Sc-Zr alloy provided the best combination of grain stability, mechanical strength, corrosion resistance, and extrudability under Route 1 (high-temperature homogenization), the low Al-Sc-Zr alloy still demonstrated clear improvements over the base alloy.

Keywords: 1xxx extrusion alloys, Sc/Zr microalloying, Thermomechanical Processing, Simulated Brazing, Microstructural evolution, Mechanical properties, Corrosion resistance.

3.1 Introduction

Aluminum 1xxx alloys are widely used in heat exchangers due to their excellent thermal conductivity, lightweight nature, and good corrosion resistance [1–3]. Aluminum heat exchangers are utilized in a range of applications, including air conditioners, refrigerators, heat pumps for automobiles and aerospace industries [4]. Heat exchangers are typically manufactured by forming the aluminum sheets and tubes into the desired geometries and assembling the components together [5]. A multi-port extruded (MPE) tube, commonly used in heat exchangers for automotive air conditioning systems, is a flat extruded tube featuring multiple parallel channels separated by thin webs [6–8]. The design of MPE tubes increases the surface area-to-volume ratio, improving heat transfer efficiency [9]. MPE tubes also contribute significantly to weight reduction in heat exchangers, making them suitable for industrial applications focused on energy efficiency and environmental sustainability [4,6].

During the manufacturing process of MPE tubes, the high extrusion ratio and intense deformation cause significant microstructural changes, which directly impact the material's properties [10,11]. Brazing is used to assemble the components of a heat exchanger together [12,13]. During this process, the components are heated to a high temperature (~600 °C), allowing them to bond together [14,15]. Several studies [11,16,17] reported substantially low mechanical properties and pressure-bearing capacity in the as-brazed condition, which was attributed to the recrystallization and abnormal grain growth (AGG) induced by the high-temperature exposure during brazing. An MPE tube should endure internal pressure from the refrigerant, especially in eco-friendly systems that operate at higher pressures [18]. Controlling the post-brazed grain structure is essential to ensure sufficient pressure resistance and to prevent refrigerant leakage, as a leak in one tube in a heat exchanger results in the failure of the entire heat exchanger [19].

Microalloying aluminum alloys with Sc promotes the formation of a high density of Al_3Sc dispersoids that provide high strength and thermal stability and effectively restricts grain boundary movement during high-temperature exposure [20,21]. Al_3Sc dispersoids exert Zener pinning on grain and subgrain boundaries, which delays the recrystallization [22,23]. However, the high cost of Sc limits its widespread commercial use in aluminum alloys, driving research toward more economical alloying strategies [24]. These include incorporating co-additions of Sc with other elements such as Zr [25,26]. When Zr is added alongside Sc, it can form $Al_3(Sc,Zr)$ precipitates, which consist of an Al_3Sc core surrounded by a Zr-enriched shell. $Al_3(Sc,Zr)$ precipitates exhibit a significantly enhanced resistance to coarsening compared to Al_3Sc precipitates, owing to the slower diffusivity of Zr in α-Al [27–29].

Several studies [20,30–34] showed that the incorporation of trace amounts of Sc and Zr into different aluminum alloys significantly contributes to strengthening and delaying recrystallization owing to the formation of numerous fine $Al_3(Sc,Zr)$ dispersoids. However, the effect of micro additions of Sc and Zr on recrystallization and grain growth of 1xxx extruded products, specifically for brazed heat exchangers, remains relatively underexplored. This study aims to investigate the influence of Sc/Zr micro additions on the grain stability, mechanical properties, precipitation microstructure, and corrosion resistance after the extrusion and simulated brazing of 1xxx alloys under two different thermomechanical processing routes. The grain structure characteristics and the precipitation microstructures were analyzed using scanning electron microscopy (SEM), electron backscatter diffraction (EBSD) and transmission electron microscopy (TEM). In addition, the implementation of Sc/Zr micro additions in the potential industrial application of MPE tubes was explored.

3.2 Experimental procedure

Three 1xxx series aluminum alloys, based on an AA1050 composition with and without Sc/Zr micro-additions, were designed and investigated. All three alloys were direct-chill (DC)-cast into extrusion billets with 101 mm diameter at the Arvida Research and Development Centre of Rio Tinto Aluminium in Saguenay, Quebec. Their chemical compositions, analyzed by optical emission spectroscopy, are presented in Table 3-1.

Table 3-1 Chemical compositions of the DC cast alloys (wt.%).

Alloy	**Si**	**Fe**	**Ti**	**Zr**	**Sc**	**Al**
Base alloy	0.10	0.20	0.01	--	--	Bal.
Low Al-Sc-Zr	0.12	0.19	0.02	0.10	0.10	Bal.
High Al-Sc-Zr	0.12	0.19	0.02	0.15	0.19	Bal.

Figure 3-1 shows the details of the two different processing routes including heat treatments, extrusion, simulated brazing, and post aging. R1 used a conventional high-temperature homogenization process, namely, the cast billets were homogenized at 600 ºC for 4 h. In R2, the cast billets were pre-aged at 350 ºC for 24 h prior to extrusion to promote $Al_3(Sc,Zr)$ precipitates in the cast billet microstructure [35–37]. In both processing routes, the billets were then induction-preheated rapidly to 480 °C and extruded into 30 mm x 1.4 mm flat strips with an extrusion ratio of 210 and a ram speed of 6 mm/s, followed by water quenching at the press exit with a quench rate of ~1000 ºC/s.

Test samples were cut from the flat extruded strips and subjected to a simulated brazing cycle by heating up from room temperature to 605 °C in 20 min and holding 2.5 min at this temperature, followed by water quenching. No deliberate cold work was applied to the strips before the simulated braze. In both routes, after the simulated brazing, the samples were subjected to a post-aging treatment at 350 ºC for 4 h to further promote the $Al_3(Sc,Zr)$ precipitation and enhance the alloy's strength.

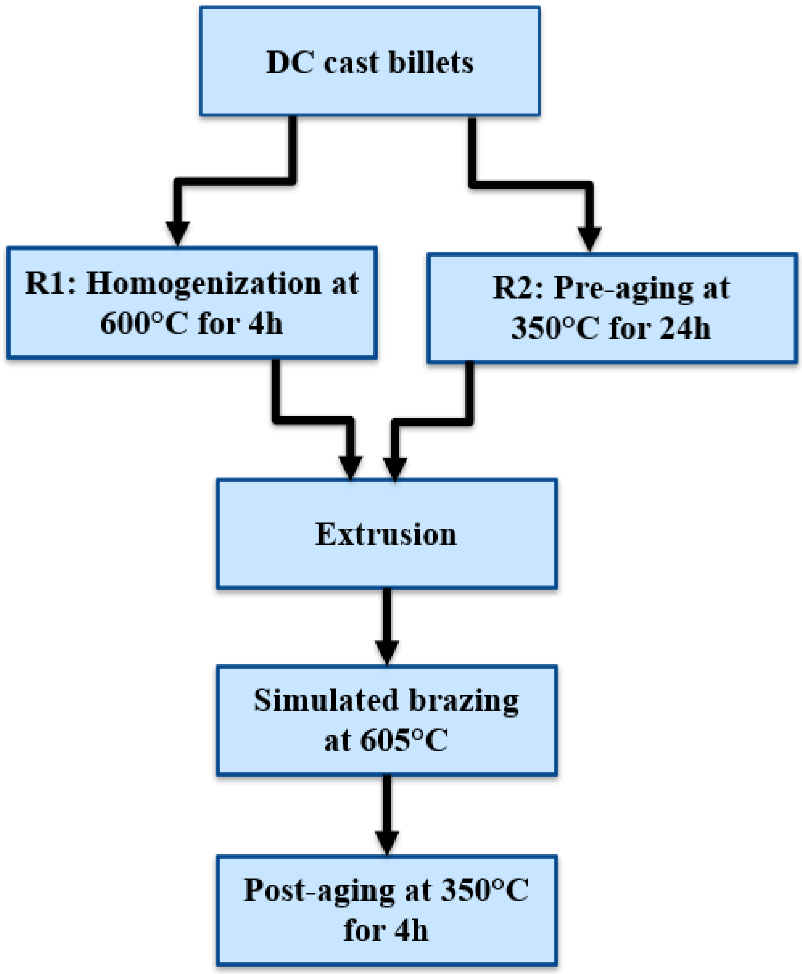

Figure 3-1 Two thermomechanical processing routes to produce the flat extruded strips.

The microstructure of the investigated alloys was characterized by optical microscopy (OM), scanning electron microscopy (SEM) equipped with electron backscatter diffraction (EBSD), and transmission electron microscopy (TEM). The extruded strips were sectioned along the centerline of the strip parallel to the extrusion direction. For OM micrographs, samples from the as-extruded strips were prepared with standard metallographic procedures.

After the final polishing, samples were subjected to Barker's electrolytic etching using 5 ml HBF_4 and 200 ml H_2O for 90 seconds to reveal the grain structure under polarized light. All observations of electro-etched samples and EBSD analyses were conducted on the ND-ED plane (ND: normal direction, ED: extrusion direction).

For the EBSD samples, the scans were performed at step sizes of 1 μm. Misorientation angles of 2-5°, 5-15º and >15º were presented by white, green, and black lines, respectively. The original EBSD datasets were post-processed using HKL Channel 5 software. A TEM operated at 200 kV was used to observe the Sc/Zr-containing nanoprecipitates. The TEM samples were first mechanically ground and then electropolished using a twin-jet electro-polisher operated at 25V and -30 °C with 30 vol.% nitric acid and 70 vol.% methanol. Observations of precipitates were made near the [001] zone axis.

Uniaxial tensile tests were performed at room temperature using an Instron 8801 servo-hydraulic unit for the as-extruded, as-brazed and as-aged conditions. The tensile samples were machined according to ASTM E8 in extrusion direction using full size sheet-type samples with 200 mm length and a 50 mm gauge length. An initial strain rate of 0.015 min^{-1} was applied up to the determination of the yield strength (0.2% offset). After yielding, the strain rate was increased to 0.2 min^{-1} until fracture. For each condition, tensile properties were determined from three independent tests.

To evaluate the corrosion resistance of the strips, samples were subjected to a salt-water acetic acid test (SWAAT) according to ASTM G85 (Annexe A3). The mass loss was measured after exposures of 5 days and 20 days. The SWAAT solution was composed of 5% sodium chloride with the addition of 10 mL of glacial acetic acid per liter of solution, and with the pH adjusted between 2.8 and 3.0. Localized corrosion was evaluated by measuring pit depth after 20 days of exposure. For each alloy, three samples were tested. Pits were first identified on each sample surface, and the six deepest pits per sample were selected, as these represent the most severe localized corrosion events. The average pit depth was then calculated based on these values to provide a quantitative measure of pitting severity.

An industrial application of 1xxx extrusion alloys is to fabricate MPE tubes for brazed heat exchangers. Figure 2 shows a drawing of the MPE profile used in this work. The design of those extruded tubes increases the surface area-to-volume ratio, significantly enhancing heat transfer efficiency. Homogenized billets from the three experimental alloys were preheated to 480 °C using induction heating and subsequently extruded into MPE tubes using a container temperature of 480 ºC and a die temperature of 480 ºC. The extrusion ratio was 415. A standing wave water quench was applied immediately at the press exit, giving a quench rate of >1000 ºC/s. The ram operated at a speed of 3 mm/s. To simulate the manufacturing process, the MPE tubes were fed between two rollers and subjected to cold rolling to achieve a 2% overall thickness reduction. This sizing step ensures that the tubes meet the dimensional tolerances required for assembly during the subsequent brazing process [16,17]. The MPE tubes were then subjected to the same simulated brazing cycle applied on the strips.

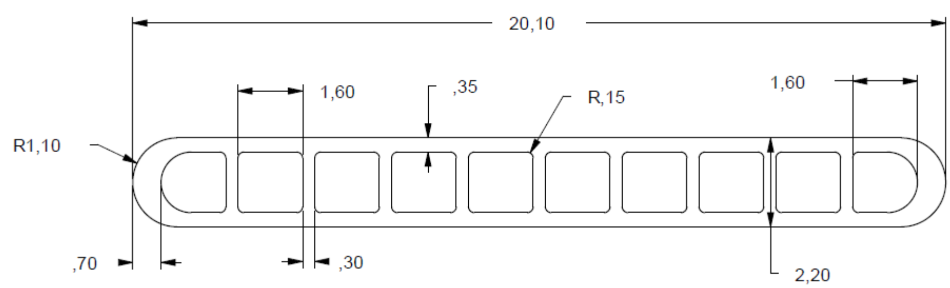

Figure 3-2 Drawing of the extruded MPE tubes in this work (dimensions in mm).

3.3 Results

3.3.1 Initial microstructures

Figure 3 presents SEM micrographs showing the microstructures of the three alloys in the as-cast, pre-aged, and homogenized conditions. Across all conditions, the microstructures primarily consist of α-Al matrix and Fe-rich intermetallic particles. In the as-cast condition (Figs. 3a, 3d, 3g), all three alloys exhibited similar microstructural features: Fe-rich intermetallic particles appearing in Chinese-script compact form distributed along Al dendrite cell/grain boundaries. SEM-EDX confirmed that these Fe-rich intermetallic particles are the Al_8Fe_2Si phase (Fig. 3j). The Sc/Zr microalloying did not affect the type and distribution of Fe-rich intermetallic particles.

After pre-aging in R2 (Figs. 3b, 3e, 3h), the type and quantity of Fe-rich intermetallic particles in the three alloys did not change and remained almost the same as under the as-cast condition, owing to the low treatment temperature of the pre-aging. However, after homogenization in R1 (Figs 3c, 3f, 3i), the Al_8Fe_2Si intermetallics were partially dissolved and their quantity was largely reduced because of the high homogenization temperature at 600 ºC. The remaining intermetallic particles were transformed to a thin plate-like morphology and their EDX compositions suggested the Al_6Fe phase (Fig. 3l) reflecting the transformation from Al-Fe-Si to Al-Fe intermetallic particles commonly reported at high-temperature homogenization treatments [38] . Notably, no primary $Al_3(Sc)$ or $Al_3(Sc,Zr)$ intermetallic phases were observed in the Sc/Zr-containing alloys under any condition. This observation is in good agreement with previous studies on alloys containing comparable Sc and Zr levels, which likewise reported the absence of primary $Al_3(Sc)$ or $Al_3(Sc,Zr)$ phases [29,39,40].

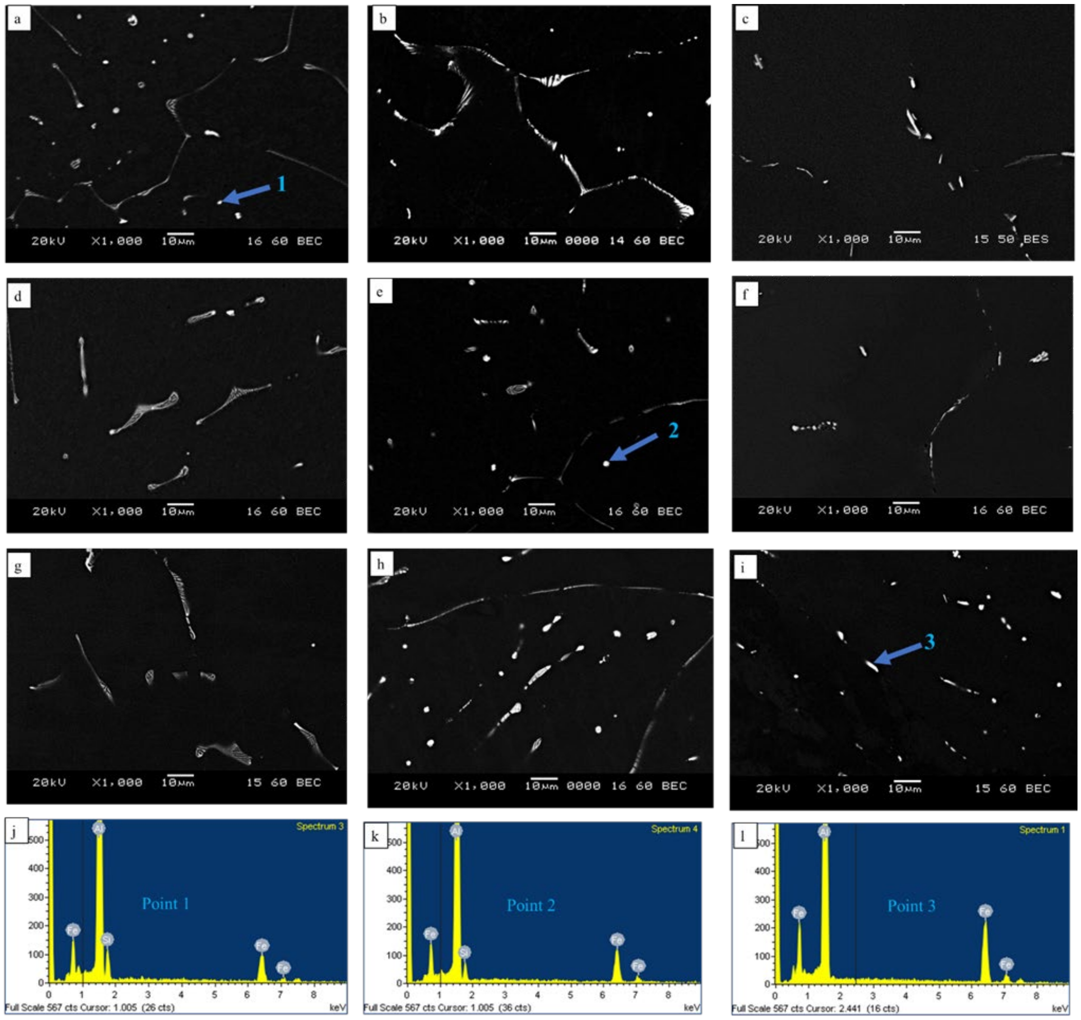

Figure 3-3 Backscattered SEM images showing the microstructures of (a, d, g) as-cast, (b, e, h) pre-aged (R2) and (c, f, i) as-homogenized (R1); (a-c) the base, (d-f) low Al-Sc-Zr, and (g-i) high Al-Sc-Zr alloys; (j-l) SEM-EDS point analysis of Fe-rich intermetallic phases in a, e and i.

3.3.2 Microstructure evolution during R1

Figure 3-4 reveals the OM microstructures of as-extruded samples of the three alloys under polarized light. Coarse recrystallized grains were observed on the strip surface of the base alloy to an average depth of approximately 250 ±29μm (Fig. 4a). The grain structure gradually changed from the surface to the centre region, where small, recrystallized grains appeared. In contrast, both Al-Sc-Zr alloys mainly exhibited fine fibrous grain structures elongated along the extrusion direction (Figs. 4b and 4c). The low Al-Sc-Zr alloy showed a thin recrystallized layer on its surface with a thickness of approximately 64±4 μm (Fig. 4b), while there was no surface recrystallized layer in the high Al-Sc-Zr alloy (Fig. 4c).

The grain structure of the as-extruded strips was further characterized by the EBSD technique. Figure 5 reveals the EBSD inverted pole figure (IPF) maps of the three alloys. For the base alloy (Fig. 5a), many equiaxed grains free of internal substructures were formed. Additionally, subgrains with medium-angle boundaries (5º-15º) were often observed in the microstructure, indicating the occurrence of strong dynamic recrystallization and recovery during extrusion[41]. Both Al-Sc-Zr alloys (Figs. 5b and 5c) exhibited a majority of fibrous grain structures aligned along the extrusion direction, along with many subgrains between the high angle grain boundaries. The three alloys showed a double texture of <001> and <111>, which is a typical characteristic of extruded aluminum microstructures [42]. Sun et al. [43] observed in a 6xxx extrusion alloy that grains of the <100> fiber were subgrains with equiaxed shapes in the interior region while the grains of the <111> fiber tended to retain the deformed grains.

To understand the softening behavior, grain orientation spread (GOS) maps were also generated for the three alloys (Figs. 5d, 5e and 5f). The deformed grains were presented in red color while the substructured and recrystallized grains were presented in yellow and blue respectively. As indicated in Figs 5g, 5h and 5i, the percentage of deformed grains increased from only 0.6% in the base alloy to 33.7% in the low Al-Sc-Zr alloy and further to 44.3% in the high Al-Sc-Zr alloy. The substructured grains accounted for 51.1% in the base alloy and decreased to 30.4% in the high Al-Sc-Zr alloy. The recrystallized grains accounted for 48.3% of the base alloy, whereas it ranged between 22.5 and 25.3% in both Al-Sc-Zr alloys.

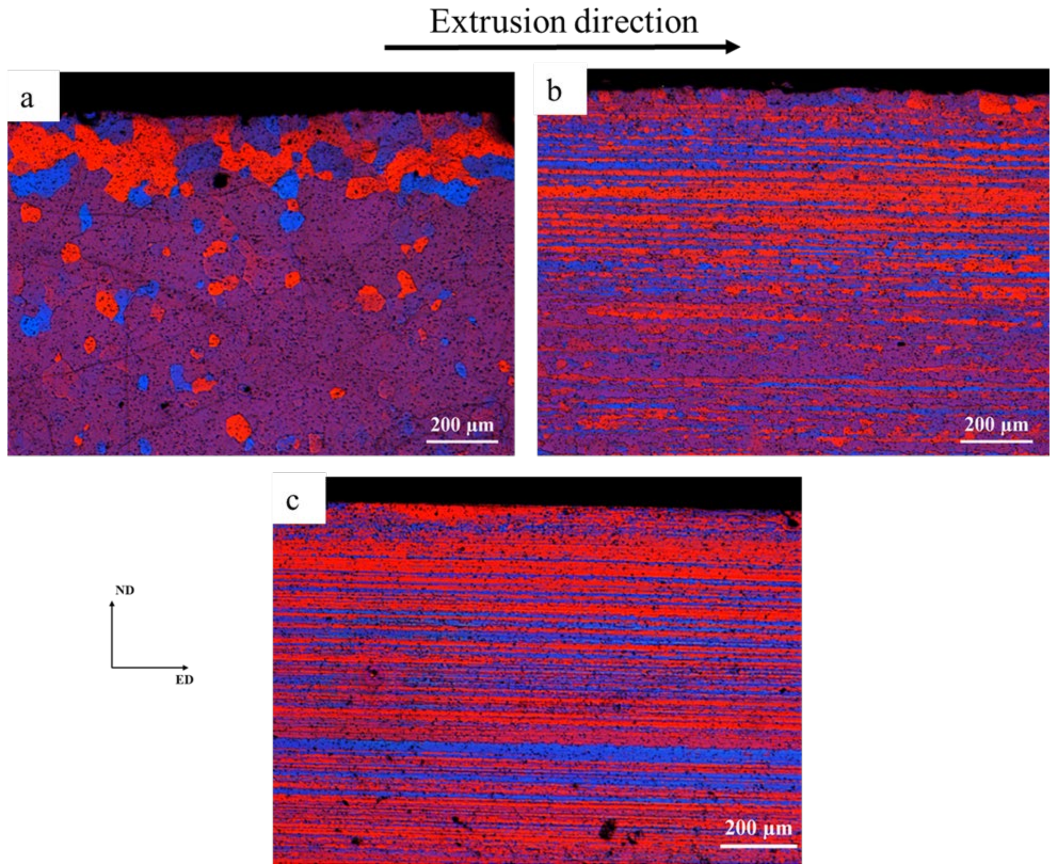

Figure 3-4 Polarized optical micrographs of as-extruded grain structures under R1, (a) base alloy, (b) low Al-Sc-Zr alloy, and (c) high Al-Sc-Zr alloy.

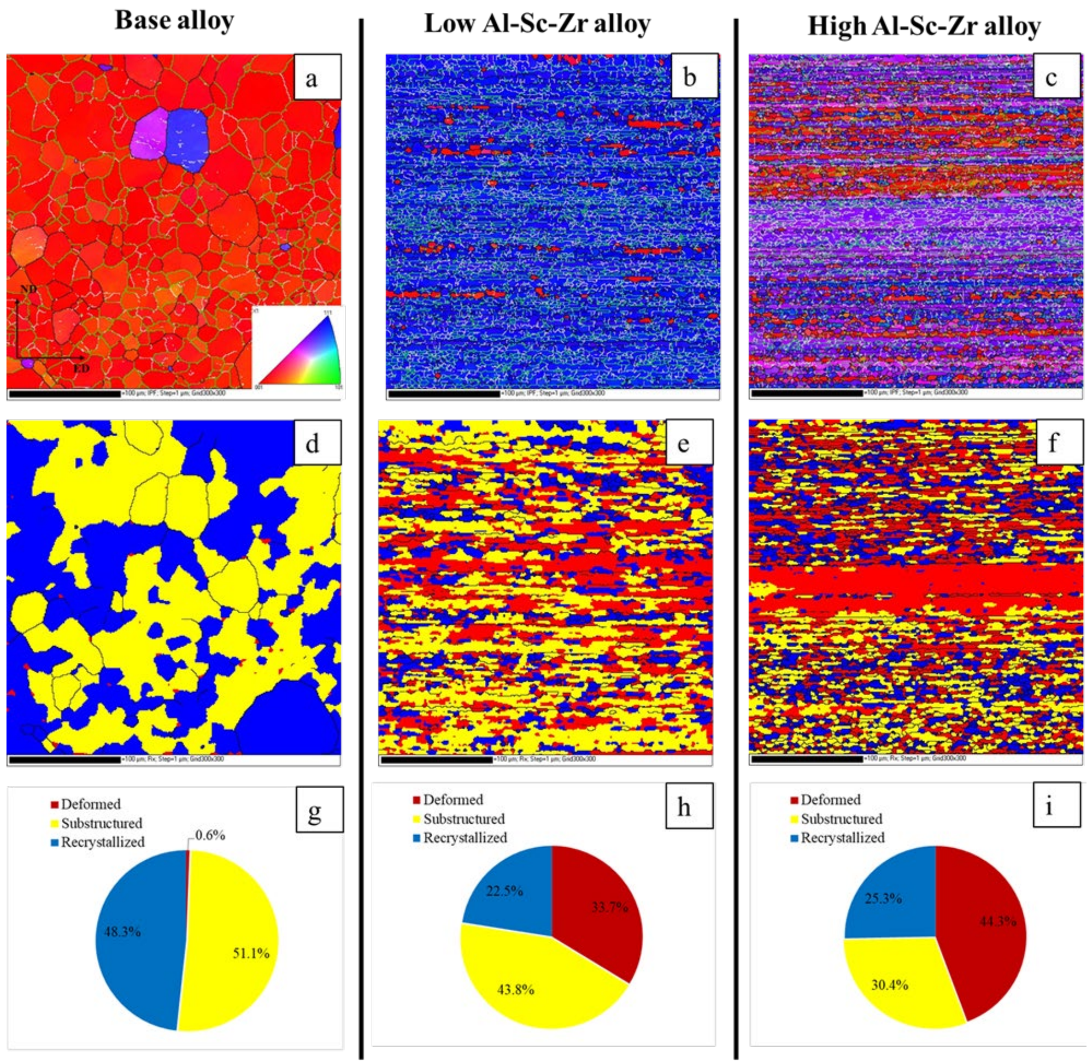

Figure 3-5 EBSD maps of as-extruded grain structure during R1, (a, d) the base, and (b, e) low Al-Sc-Zr and (c, f) high Al-Sc-Zr alloys; (a-c) IPF maps and (d-f) GOS maps; (g-i) the corresponding area fractions of the deformed, substructured and recrystallized grains derived from GOS maps.

Figure 3-6 reveals the OM grain structures after simulated brazing. For the base alloy, the grain size increased dramatically compared to its as-extruded condition, with grains expanding to nearly 1000 μm (Fig. 3-6a). This is a typical sign of abnormal grain growth (AGG). The low Al-Sc-Zr alloy lost its fibrous grain structure during brazing, but the extent of AGG was less severe compared to the base alloy (Fig. 3-6b). In contrast, the as-brazed high Al-Sc-Zr alloy maintained its fibrous deformed grain structure with no signs of grain coarsening (Fig. 3-6c).

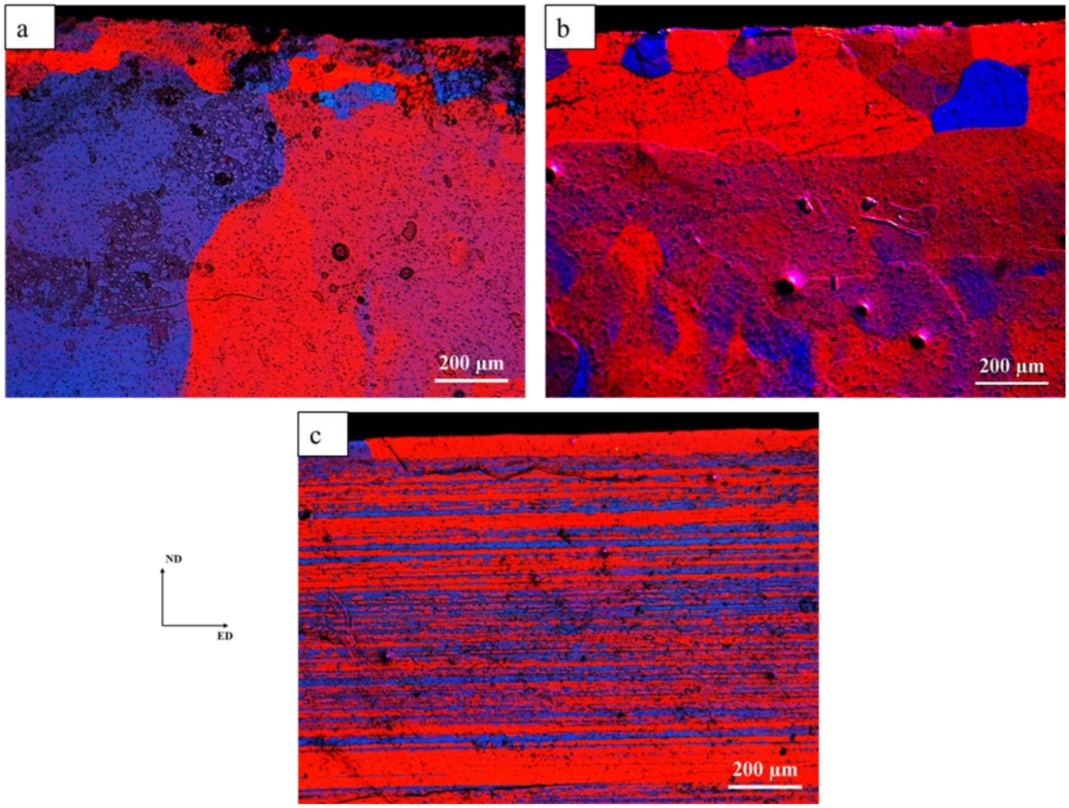

Figure 3-6 Polarized optical micrographs showing as-brazed grain structures under R1, (a) base alloy, (b) low Al-Sc-Zr alloy, and (c) high Al-Sc-Zr alloy.

The as-brazed microstructure of the high Al-Sc-Zr alloy was also characterized by EBSD (Fig. 3-7). The EBSD results revealed that recrystallized grains accounted for 30.3% of the as brazed microstructure, representing an increase compared to the 25.3% observed in the as-extruded condition (Fig. 3-5i). Additionally, the substructures constituted 50% of the microstructure after the brazing cycle, compared to 30.4% in the as-extruded condition. Although recrystallization occurred in the high Al-Sc-Zr alloy during simulated brazing, yet no signs of severe grain growth were observed.

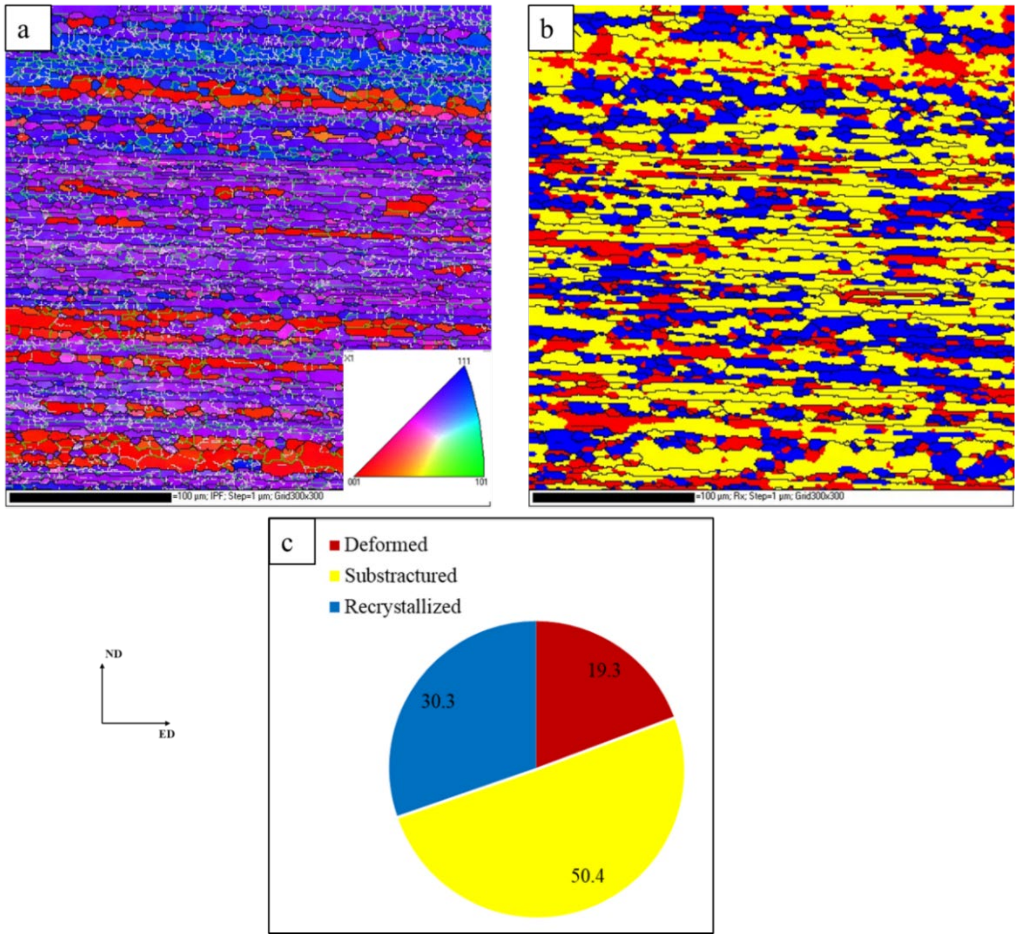

Figure 3-7 EBSD maps of as-brazed grain structure of the high Al-Sc-Zr alloy during R1, (a) IPF map, (b) GOS map, and (c) the corresponding area fractions of the deformed, substructured and recrystallized grains.

3.3.3 Microstructure evolution during R2

Figure 3-8 shows the OM micrographs of the as-extruded three alloys for R2. Like previously observed in the R1 route, coarse grains were observed on the strip surface of the as-extruded base alloy. The as-extruded microstructure of the low Al-Sc-Zr alloy consists of primarily large, elongated grains along the extrusion direction. It must be noted that small traces of very narrow grains could still be observed (white arrow in Fig. 3-8b). In contrast, the high Al-Sc-Zr alloy showed primarily elongated and deformed grains parallel to the extrusion direction with a few smaller more equiaxed grains (white arrow in Fig. 3-8c).

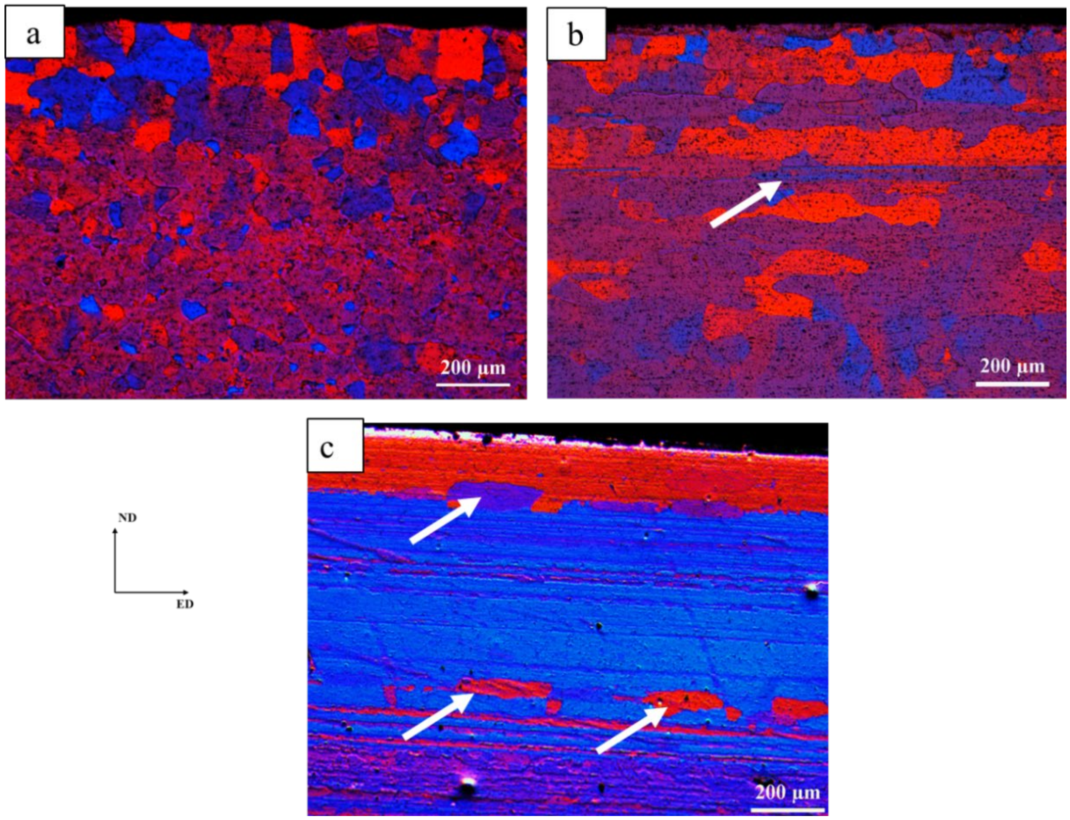

Figure 3-8 Polarized optical micrographs of as-extruded grain structure under R2, (a) base alloy, (b) low Al-Sc-Zr alloy, and (c) high Al-Sc-Zr alloy.

Figure 3-9 reveals the OM grain structure following the brazing cycle for R2. The base alloy showed equiaxed coarse grains. Notably, the as-brazed base alloy following R1 exhibited AGG (Fig. 3-5a), whereas for R2 route it was coarsened grains without severe grain growth (Fig. 3-8a). This difference can be attributed to the variation in the volume fraction of Fe-rich intermetallic particles during pre-aging and homogenization treatments. When analyzing the volume fraction of Fe-rich intermetallic phases from the SEM micrograph of the pre-aged base alloy (Fig. 3-3b), it revealed that the sample pre-aged by R2 contained approximately 2.3% Fe-rich intermetallic particles, whereas the sample homogenized by R1 (Figure 3-3c) exhibited a significantly lower fraction, at only 0.76%. According to Pan et al. [44] , the volume fraction of Fe intermetallic particles plays a crucial role in influencing the recrystallization kinetics of the alloy and in regulating its microstructural evolution throughout subsequent processing stages. Shakiba et al. [45] found that the increase in the volume fraction of Fe intermetallic phases generates a stronger pinning effect on the substructures. Moreover, according to Uttarasak et al. [46], in alloys with a high-volume fraction of secondary phases, the increased pinning pressure effectively restricts grain boundary movement, thereby preventing abnormal grain growth.

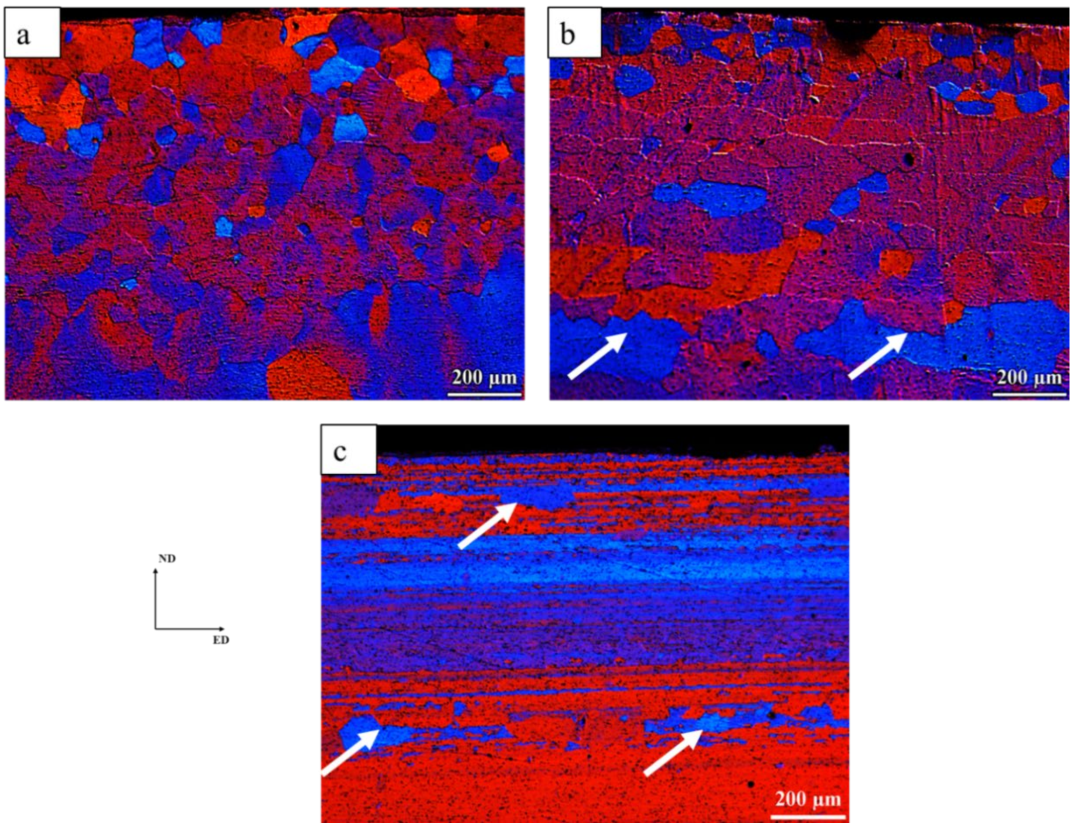

Figure 3-9 Polarized optical micrographs showing as-brazed grain structures under R2, (a) base alloy, (b) low Al-Sc-Zr alloy, and (c) high Al-Sc-Zr alloy.

For the as-brazed low Al-Sc-Zr alloy (Fig. 3-9b), the elongated narrow grains in the as-extruded condition (Fig. 3-8b) no longer existed after the simulated brazing. However, there were still some elongated grains along the extrusion direction as indicated by the white arrows.

In contrast, the as-brazed high Al-Sc-Zr alloy (Figure 3-9c) still preserved its elongated and deformed grain structure along with the appearance of some localized recrystallized grains (see white arrows).

The as-brazed grain structure of the high Al-Sc-Zr alloy was examined by EBSD. Figures 3-10a and 3-10b show that this alloy exhibited partial recrystallization, as indicated by the black arrows in Figure 3-10b, with recrystallized grains accounting for approximately 15.7% of the microstructure and no evidence of severe grain coarsening. Figure 3-10c also showed that substructures constituted 54.6% whereas the deformed grains accounted for 29.5% of the microstructure.

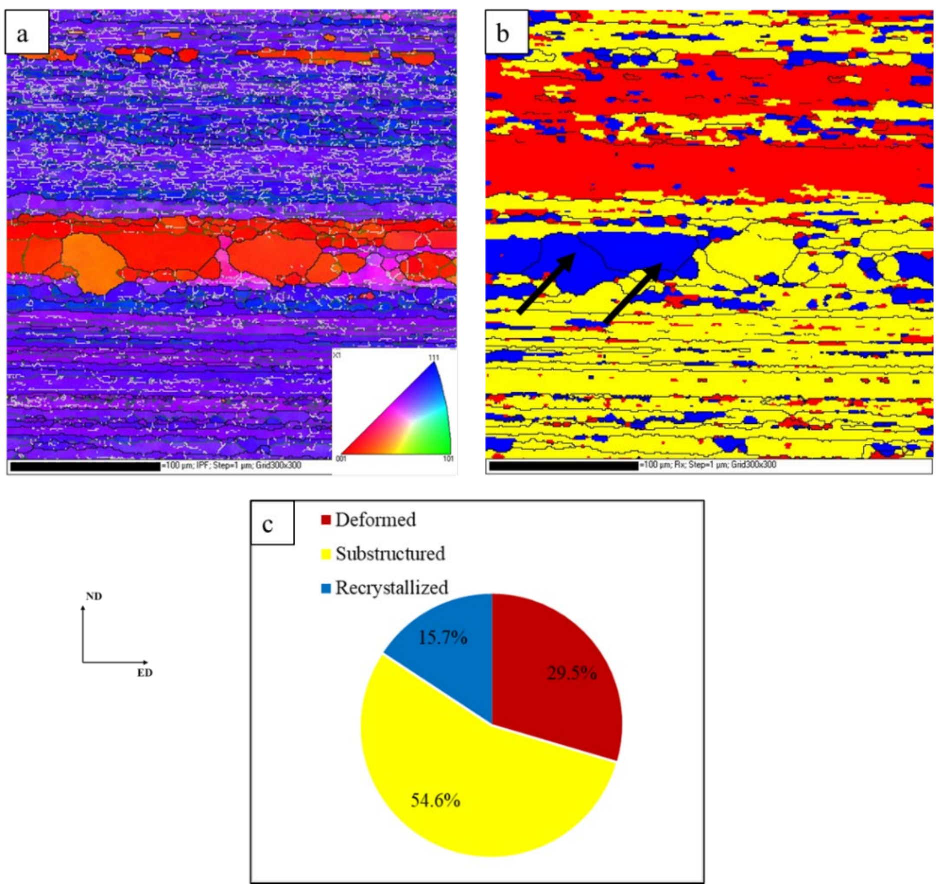

Figure 3-10 EBSD maps of the as-brazed grain structure of the high Al-Sc-Zr alloy for R2, (a) IPF map, (b) GOS map, and (c) the corresponding area fractions of the deformed, substructured and recrystallized grains.

3.3.4 Tensile properties after extrusion, simulated brazing and post-braze aging

Figure 3-11 presents the engineering stress-strain curves of the three investigated alloys after extrusion, simulated brazing and post-braze aging under both processing routes R1 and R2 (Fig. 3-11). All alloys exhibit a sharp increase in stress to yielding, followed by a strain-hardening stage to the UTS and eventual fracture. For both routes, the as-extruded strength values increased with micro-additions of Sc and Zr. After the simulated brazing cycle, all alloys except for high Al-Sc-Zr (R2) showed reduced strength compared with the as-extruded condition. Nevertheless, the Sc-containing alloys still maintained higher strength values than the base alloy, with the high Al-Sc-Zr alloy exhibiting the most significant strength retention. Following post-braze aging, substantial increases in strength were observed in the two Sc-containing alloys, whereas the strength of the base alloy remained nearly unchanged. Table 3-2 displays the corresponding room temperature yield strength (YS) and ultimate tensile strength (UTS) values of the three investigated alloys after extrusion, simulated brazing and post-braze aging.

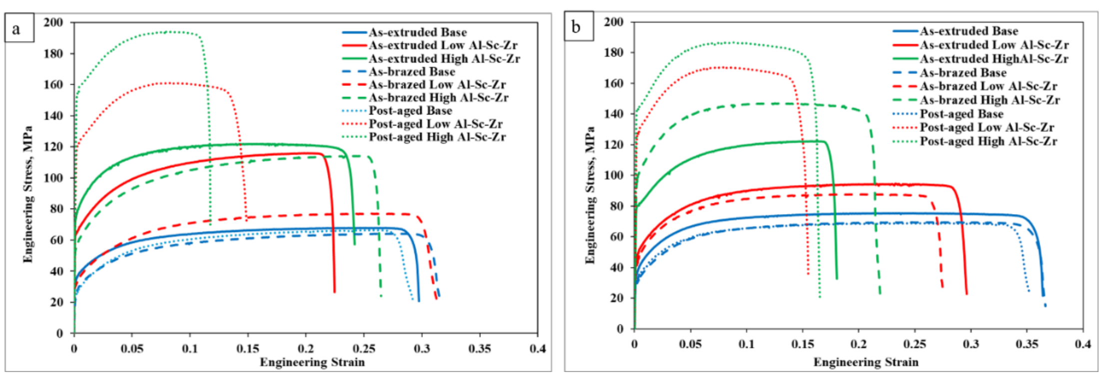

Figure 3-11 Typical engineering stress-strain curves of the three experimental alloys after extrusion, brazing, and post-aging under both processing routes, (a) R1 and (b) R2.

For R1, the as-extruded YS of the base alloy was only 35 MPa while both the low Al-Sc-Zr and high Al-Sc-Zr alloys exhibited significantly higher YS values of 63.8 MPa and 76.9 MPa respectively. The similar trend is true for the UTS. The base alloy showed the lowest value of

69.4 MPa, whereas the low Al-Sc-Zr and high Al-Sc-Zr alloys demonstrated higher UTS values of 113.5 MPa and 120.3 MPa, respectively.

For R1 after the simulated brazing cycle, the three alloys showed a decline in both YS and UTS values compared to the as-extruded condition. Among three alloys, the base alloy exhibited the lowest strength. For instance, the YS of the base alloy dropped to 28.8 MPa. Similarly, the UTS reduced to be only 65 MPa, which is primarily due to substantial grain growth during the brazing process. The low Al-Sc-Zr alloy showed higher YS and UTS values of 35.7 MPa and 81 MPa, respectively. The high Al-Sc-Zr alloy exhibited double the YS value of the base alloy, reaching a value of 58.8 MPa, whereas the UTS reached 113.8 MPa, which represents a 74% increase compared to the base alloy.

Table 3-2 YS and UTS values at ambient temperature of the studied alloys after extrusion, simulated brazing and post-aging for both processing routes R1 and R2.

Alloy	Condition	R1		R2	
		YS± SD (MPa)	UTS ± SD (MPa)	YS± SD (MPa)	UTS ± SD (MPa)
Base alloy	As-extruded	35 ± 1.3	69.4 ± 1.6	36.2 ± 1.7	72.9 ± 2.1
	As-brazed	28.8 ± 0.7	65.2 ± 1.2	30.5 ± 0.6	68.8 ± 0.9
	Post-aged	26.2 ± 0.2	65.4 ± 1.4	30.7 ± 2	69.9 ± 0.8
Low Al-Sc-Zr alloy	As-extruded	63.8 ± 2.3	113.5 ± 3.2	49.3±1.3	92.4 ± 1.1
	As-brazed	35.7 ± 0.9	80.9 ± 2.7	46 ± 1.4	91.2 ± 1.3
	Post-aged	120.9 ± 0.5	160.3 ± 0.5	124.4 ± 1.2	168.0 ± 1.2
High Al-Sc-Zr alloy	As-extruded	76.9 ± 3.5	118.2 ± 3.9	78.8±1.5	121.4 ± 1.5
	As-brazed	58.8 ± 1.7	113.8 ± 1.8	97.7 ± 3.3	143.4 ± 4.3
	Post-aged	156.9 ± 2.3	195.7 ± 2.6	140.9 ± 2.1	182.2 ± 3.5

Following R2, the as-extruded strength values also increased due the micro-addition of Sc and Zr like in the case of R1. For instance, the YS increased from 36.2 MPa of the base alloy to 49.3 MPa of the low Al-Sc-Zr alloy, representing an increase of approximately 36%. It further increased to 78.8 MPa in the high Al-Sc-Zr alloy, which is more than double the strength of the base alloy.

For R2 after the brazing cycle, both the base and low Al-Sc-Zr alloys exhibited a reduction in the YS and UTS values. However, the as-brazed mechanical tensile properties were enhanced after the microalloying with Sc and Zr compared to those of the base alloy. For instance, the as-brazed high Al-Sc-Zr alloy exhibited a YS of 96 MPa, which is almost 3.2 times that of the as-brazed base alloy. Similarly, its UTS was nearly doubled relative to the base alloy. It is also worthwhile noting that the high Al-Sc-Zr alloy displayed even higher strength after brazing compared to its as-extruded condition. This behavior will be discussed in more detail in Section 3-4.2.

Generally, as-brazed strengths in R2 are higher than those recorded in R1. In the base alloy and low Al-Sc-Zr alloys, the increases are just marginal. However, in the high Al-Sc-Zr alloy, the increase in the strengths is significant. For instance, the as-brazed YS value of the high Al-Sc-Zr alloy in R2 was 1.6 times the as-brazed value in R1, whereas the as-brazed UTS in R2 was 1.25 times the as-brazed value recorded for R1. This difference in mechanical properties is closely related to the as-brazed microstructures following two processing routes, as the as-brazed microstructure of the high Al-Sc-Zr alloy in R1 exhibited a higher recrystallized fraction compared that in R2.

For R1 after the post-braze aging, the mechanical properties of the base alloy showed no significant change. In contrast, both the low Al-Sc-Zr and high Al-Sc-Zr alloys experienced substantial increases in strength after the post-braze aging. For instance, in the high Al-Sc-Zr alloy the YS rose to 156.9 MPa (i.e. a 167% increase compared to the as-brazed value) and the UTS increased to 195.7 MPa (i.e. a 72% increase).

Like R1, the post-braze aging in R2 also significantly improved the strength values of the two Sc-containing alloys, whereas the mechanical properties of the base alloy showed almost no significant change. For instance, the YS of the low Al-Sc-Zr alloy increased from 46 MPa after brazing to 124.4 MPa after post-aging, representing an increase of approximately 170%. For the high Al-Sc-Zr alloy, the YS increased from 96.1 MPa after brazing to 140.9 MPa after post-aging (an improvement of approximately 47%). Similarly, the UTS rose from 143.4 MPa to 182.2 MPa, representing a 27% increase.

3.3.5 Extrudability

From an industrial perspective, understanding the effect of Sc and Zr microalloying on extrudability is also necessary. Table 3-3 summarizes the ram pressure values at ram position of 775 mm during extrusion of the strip for all the three alloys under both processing routes. For the base alloy, extrusion pressure values were similar for both R1 and R2. Under R1, both the low and high Al-Sc-Zr alloys exhibited higher extrusion pressures compared with the base alloy (1434 and 1421 psi vs. 1050 psi, respectively), corresponding to increases of approximately 37% and 35% relative to the base alloy. The relatively close pressure values recorded for the two Sc-containing alloys indicate that both compositions developed a similar level of flow resistance during extrusion, consistent with the trend reported by Romstsch et al. [47].

For R2, the ram pressure values showed a noticeable increase with the addition of Sc and Zr. The extrusion pressure increased from 1141 psi for the base alloy to 1529 psi and 1785 psi for the low and high Al-Sc-Zr alloys, corresponding to increases of approximately 34% and 56%, respectively, relative to the base alloy.

When comparing R1 and R2, the high Al-Sc-Zr alloy exhibited a more pronounced increase in ram pressure, rising by approximately 26% at R2, indicating greater resistance to deformation and more difficult material flow during extrusion.

Table 3-3 Extrusion ram pressure values at the ram position of 775 mm of the studied alloys under R1 and R2 processing routes.

Alloy	Ram Pressure (psi)	
	R1	R2
Base alloy	1050	1141
Low Al-Sc-Zr alloy	1434	1529
High Al-Sc-Zr alloy	1421	1785

3.3.6 Corrosion resistance assessed by SWAAT

SWAAT exposures are usually employed to evaluate the corrosion resistance of heat exchanger components [48]. To assess the influence of Sc/Zr microalloying on corrosion performance, SWAATs were conducted on the post-aged strips for 5 and 20 days. Table 3-4 summarizes the corresponding mass loss values for each alloy under both R1 and R2 conditions. Regardless of the processing routes, five days of exposure did not lead to a significant difference in the mass loss between the three investigated alloys, whereas the 20-day exposures resulted in a more pronounced mass loss. It was observed that under R1, the percentage mass loss decreased with increasing addition of Sc and Zr. The high Al-Sc-Zr alloy exhibited a better corrosion resistance than the other two alloys. Its mass loss was 0.67% after 20 days of exposure, representing a reduction of ~18% compared to the base alloy.

Under the R2 condition, the mass loss is generally higher than under R1. This trend is particularly noticeable in the high Al-Sc-Zr alloy, which exhibited signs of localized recrystallization in the post-brazed microstructure. The presence of these localized recrystallized grains may contribute to microstructural inhomogeneity that can increase susceptibility to corrosion [49]. On the other hand, the microalloying with Sc and Zr did not show a clear effect on the mass loss values for R2 compared to the base alloy.

Figure 3-12 presents the average pit depths of the as-brazed strip samples for the three alloys subjected to both processing routes after 20 days exposure. Under R1, the addition of Sc and Zr clearly results in reduced pit penetration compared to the base alloy, with average pit depths decreasing from approximately 116 μm for the base alloy to 71 μm and 63 μm for the low and high Al-Sc-Zr alloys, respectively. This significant reduction in pit depth indicates that the fibrous and stable grain structure induced by Sc and Zr additions effectively suppresses pit propagation. Under R2, the base alloy exhibits a pronounced increase in the pit depth, reaching approximately 178 μm. The deeper pits in the base alloy can be associated with its fully recrystallized grain structure after brazing. In contrast, the low and high Al-Sc-Zr alloys show lower average pit depths of 113 μm and 84 μm relative to the base alloy. These results suggest that, despite the partial recrystallization and increased microstructural heterogeneity induced under R2, the presence of Sc and Zr continues to limit pit growth.

Figure 3-13 reveals an example of the surface attack observed on the base alloy and the high Al-Sc-Zr alloy under R1 after the post-braze aging. It can be noted that the surface attack was more severe and less uniform in the base alloy (Fig. 3-13a).

Table 3-4 Percentage mass loss with standard deviation (± SD) for the three investigated alloys after 5 and 20 days of SWAAT exposure under the post-braze aging condition following R1 and R2 processing routes.

Alloy	Exposure	R1 (%Mass Loss ± SD)	R2 (%Mass Loss ± SD)
Base alloy	5 days	0.28±0.001	0.36±0.03
	20 days	0.82±0.01	0.93±0.1
Low Al-Sc-Zr alloy	5 days	0.27±0.01	0.44±0.05
	20 days	0.76±0.06	0.92±0.02
High Al-Sc-Zr alloy	5 days	0.23±0.01	0.36±0.005
	20 days	0.67±0.09	1.07±0.01

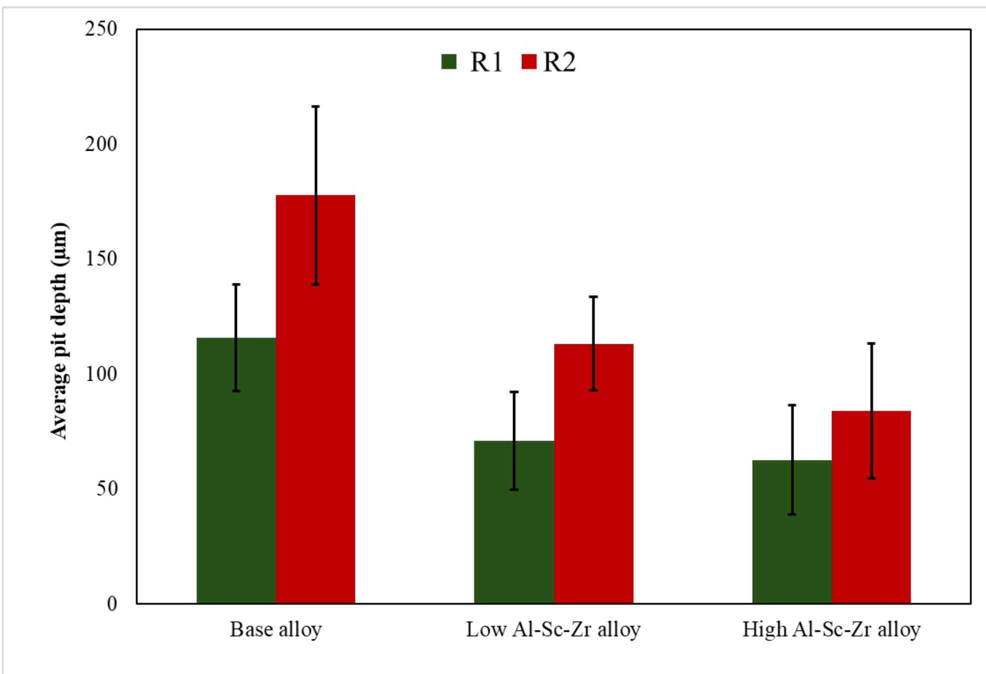

Figure 3-12 Average pit depth measured on as-brazed strip samples after SWAAT exposure for 20 days under processing routes R1 and R2.

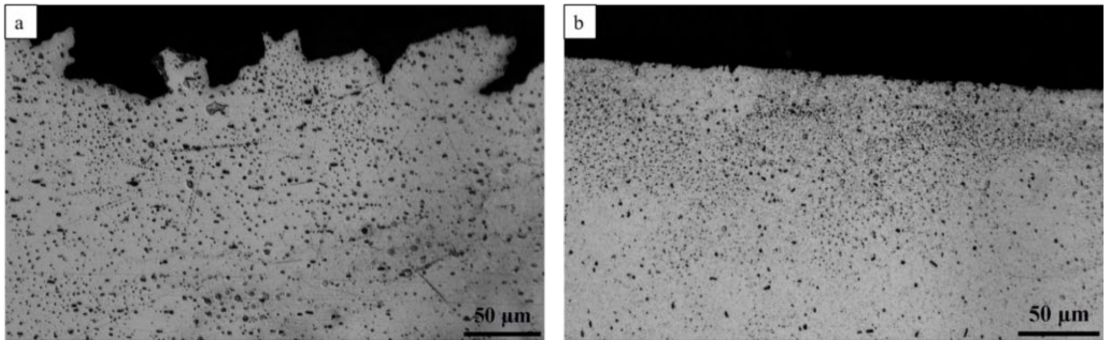

Figure 3-13 OM images showing the corroded surfaces of the post-aged strips after SWAAT exposure for 20 days: a) the base alloy, (b) the high Al-Sc-Zr alloy under R1.

3.3.7 Industrial application of Sc and Zr microalloying for MPE tubes

Figures 3-14 and 3-15 reveal the as-extruded and the as-brazed microstructures of the MPE tubes that followed the R1 and R2 processing routes. As shown in Fig. 14, the as-extruded MPE tube of the base alloy exhibited small equiaxed, recrystallized grains, while the low Al-Sc-Zr alloy also showed small equiaxed grains in addition to some elongated and deformed grains along the walls of the tube. In contrast, the high Al-Sc-Zr alloy showed a different microstructure consisting of fibrous deformed grains. Following a 2% cold rolling thickness reduction (2%cw) and simulated brazing, the base alloy showed abnormal grain growth (AGG) with large, recrystallized grains along the webs and the walls of the tubes, whereas the low Al-Sc-Zr alloy exhibited less severe AGG along the outer walls. However, the high Al-Sc-Zr alloy mostly maintained its elongated and deformed grains and showed no indications of grain growth.

Alloy	As Extruded	2%cw + Simulated Brazed
Base	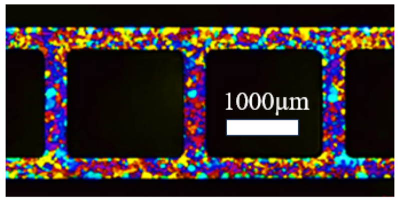	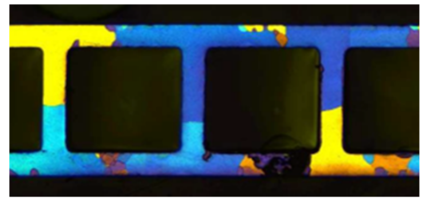
Low Al-Sc-Zr	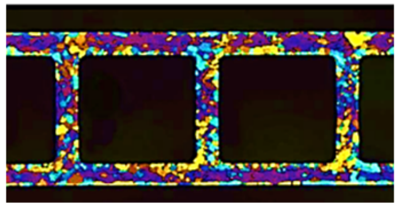	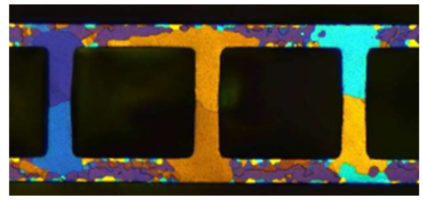
High Al-Sc-Zr	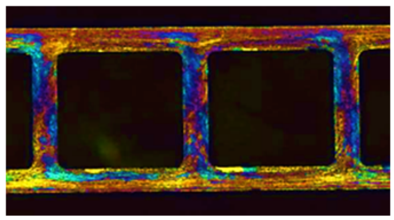	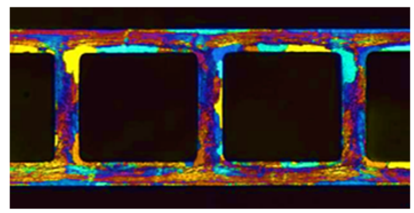

Figure 3-14 Polarized light macrographs showing as-extruded and as-brazed grain structures of the MPE tubes for the R1 route.

For the MPE tubes that followed the R2 (Figure 3-15), the as-extruded base alloy also showed small equiaxed, recrystallized grains uniformly distributed in the entire section, whereas the low Al-Sc-Zr and high Al-Sc-Zr alloys exhibited some elongated and deformed grains mixed with equiaxed and recrystallized grains. After the 2% cold rolling thickness reduction and simulated brazing, the base alloy also showed signs of AGG with large, recrystallized grains appearing in the webs. However, the extent of AGG in the walls and webs was less severe compared to the R1 route. The low Al-Sc-Zr alloy displayed mainly recrystallized grains along with some abnormally grown grains in the webs of the tube. In contrast, the high Al-Sc-Zr alloy maintained its partially deformed and partially recrystallized grains and did not show any signs of AGG following the brazing.

Alloy	As Extruded	2%cw + Simulated Brazed
Base	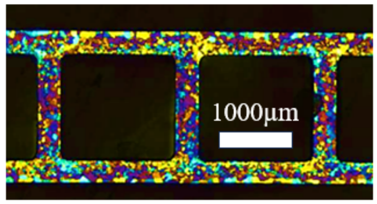	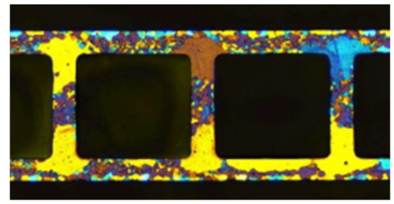
Low Al-Sc-Zr	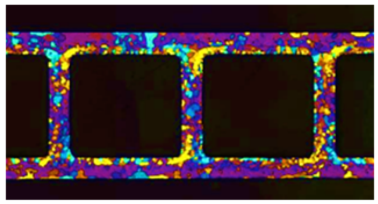	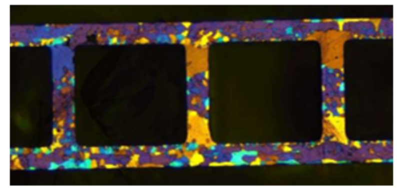
High Al-Sc-Zr	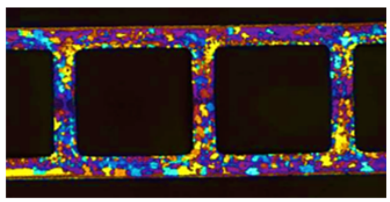	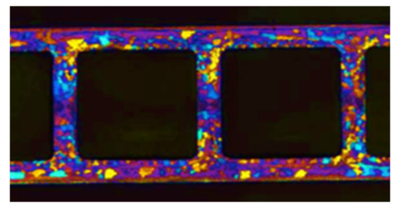

Figure 3-15 Polarized light macrographs showing as-extruded and as-brazed grain structures of the MPE tubes for the R2 route.

3.4 Discussion

3.4.1 Impact of $Al_3(Sc, Zr)$ precipitation during R1

Figure 3-16 shows the key temperatures encountered during the two different processing routes, including homogenization, pre-aging, billet preheat and simulated brazing, as well as the estimated solvus temperatures for Sc in the two Sc-Zr-containing alloys. The solvus temperatures of both alloys were calculated using Thermo-Calc with the TCAL6 database. According to their actual chemical compositions (Table 3-1), the calculated Sc solvus temperatures of the low and high Al-Sc-Zr alloys are 562 °C and 643 °C, respectively.

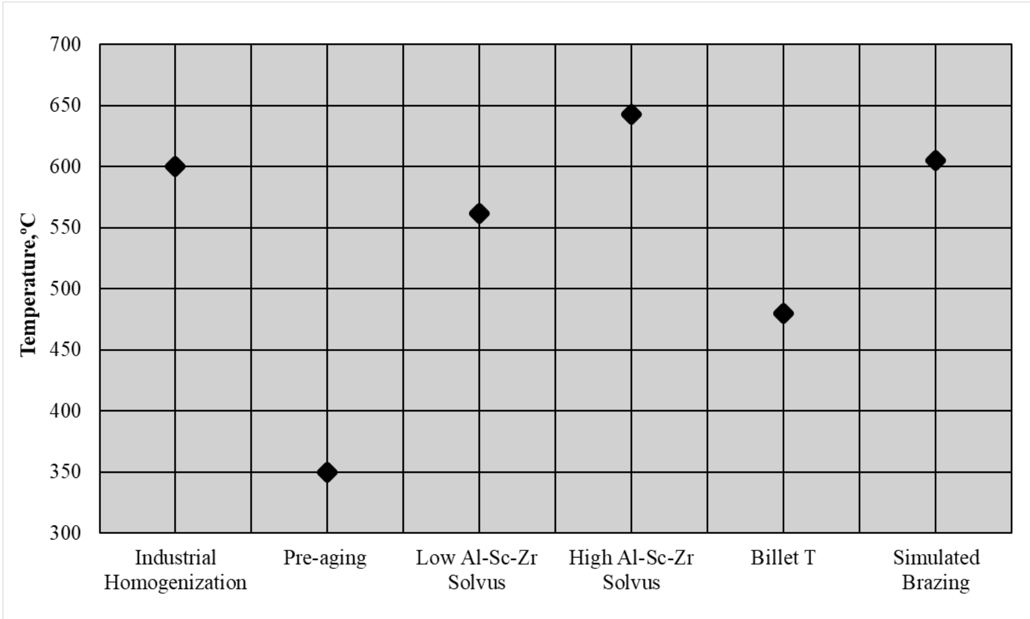

Figure 3-16 Key temperatures encountered during the two processing routes.

During the billet homogenization at 600 ºC under R1 (Fig. 3-1), no precipitates were observed in the low Al-Sc-Zr alloy, indicating all Sc and Zr were dissolved in the Al matrix. This is because the solvus temperature of Sc in this alloy is lower than the homogenization temperature. On the other hand, in the high Al-Sc-Zr alloy, some coarse spherical precipitates with an average diameter of 52.9 nm appeared in the Al matrix (Fig. 3-17a). The selected area electron diffraction pattern (SAED) obtained along the [001] zone axis displays faint spots between the α-Al spots (Fig. 3-17b), confirming that these precipitates are $Al_3(Sc,Zr)$ with an $L1_2$ structure [50]. The solvus temperature of Sc in the high Al-Sc-Zr alloy (643 ºC) is higher than the homogenization temperature, and therefore, the precipitation of $Al_3(Sc,Zr)$ during the homogenization is possible.

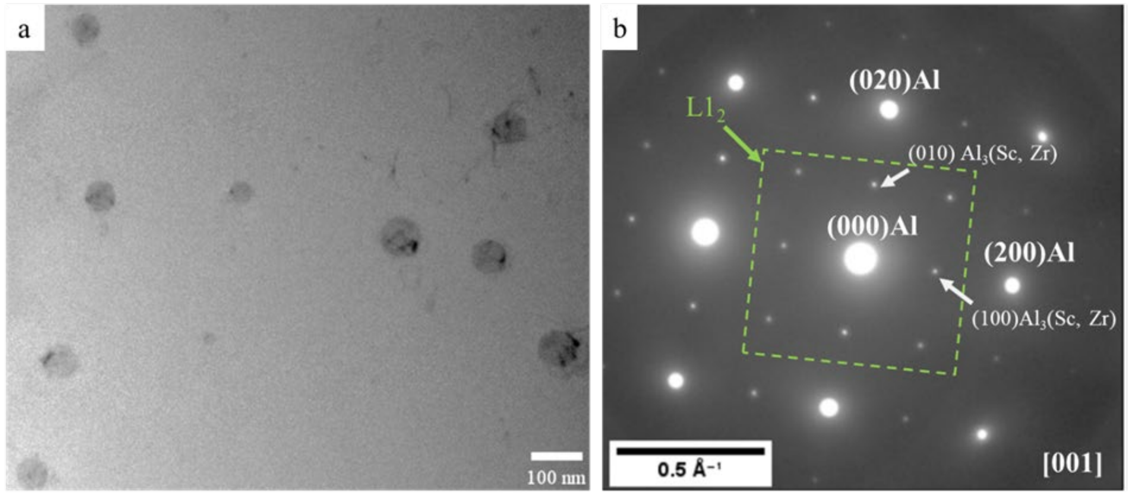

Figure 3-17 (a) Bright-field TEM micrograph of the as-homogenized high Al-Sc-Zr alloy under R1, and (b) corresponding SAED.

In the as-extruded condition under R1, both Al-Sc-Zr alloys exhibited fibrous grain structures along the extrusion direction (Figs. 3-4 and 3-5). Compared to the base alloy, the enhanced resistance to dynamic recovery and recrystallization in these two alloys is attributed to the presence of Sc/Zr- containing precipitates during extrusion. A number of fine precipitates were observed in the TEM micrograph of the as-extruded low Al-Sc-Zr alloy (Figs. 3-18a and 3-18b). Those $Al_3(Sc, Zr)$ precipitates were formed during the heating and hot extrusion, despite the relatively short exposure time [51,52]. According to Fan et al. [53], hot extrusion following homogenization is comparable to an incomplete aging treatment, resulting in the precipitation of Sc solutes to form Al_3Sc particles. In the high Al-Sc-Zr alloy, two distinct types of precipitates were found after extrusion (Figs. 3-18c and 3-18d). The first type is like the one observed in the low Al-Sc-Zr alloy and consists of small and sparsely distributed precipitates (red arrows in Fig. 3-18c) with an average diameter of approximately 10 nm, which formed during the heating and extrusion process. The second type consists of some large precipitates (yellow arrows in Fig 3-18c and 3-18d) with an average diameter of 70.5 nm, which were the pre-existing ones from the homogenization that coarsened during the extrusion. Although the overall number density of precipitates in both alloys was relatively low, their localized positioning allowed them to exert a stronger pinning effect on migrating grain boundaries. This enhanced their effectiveness in inhibiting recrystallization and helped to stabilize the grain structure.

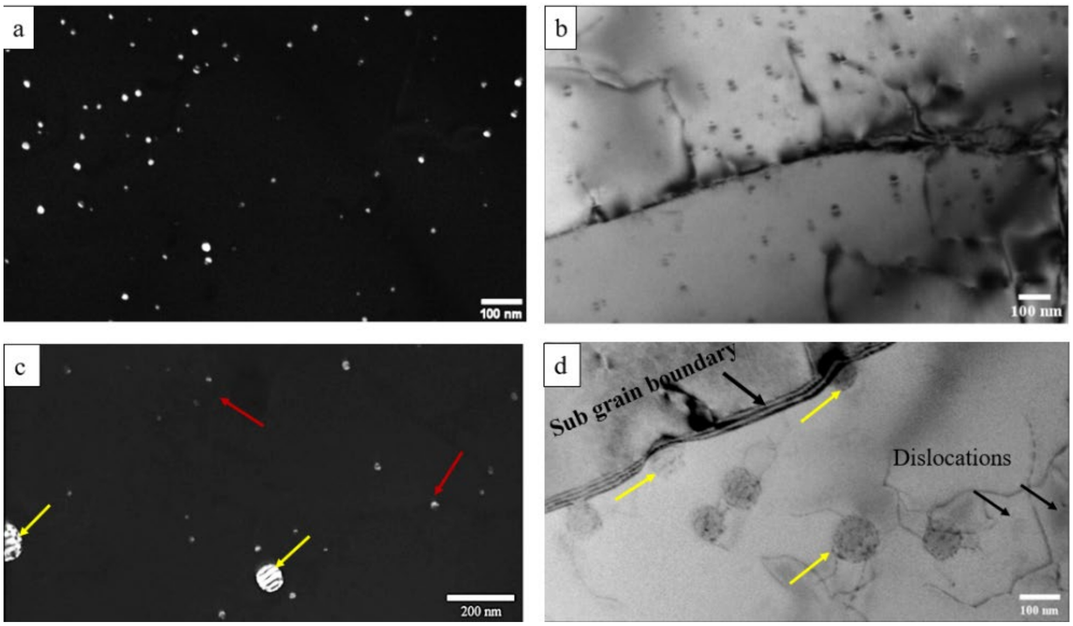

Figure 3-18 TEM micrographs of the as-extruded Sc/Zr containing alloys, (a) dark-field and (b) bright-field TEM of the low Al-Sc-Zr alloy, (c) dark-field and (d) bright-field TEM of the high Al-Sc-Zr alloy.

The $Al_3(Sc,Zr)$ precipitates observed in the as extruded samples of both Sc-containing alloys also contributed to strengthening, leading to a substantial improvement in the as-extruded strength values (Section 3-3.4.). Although both Sc- and Zr-containing alloys exhibited significant strengthening compared with the base alloy, the difference between the two Sc-containing variants remained relatively small. Because of the relatively low number density of $Al_3(Sc,Zr)$ particles precipitated during extrusion and the large size of the pre-existing coarse particles formed during homogenization in the high Al-Sc-Zr alloy, these particles are not expected to make a major contribution to precipitation strengthening. However, they play a crucial role in stabilizing the grain and subgrain structures, as indicated by the EBSD maps

(Fig. 3-5). In addition, these dispersoids increased the hot deformation resistance, which explains the higher extrusion pressures recorded for the two Sc-containing alloys (Table 3-3).

Following the simulated brazing cycle, the base alloy showed significant AGG owing to the high-temperature exposure during brazing (Fig. 3-6a). This rapid grain growth is attributed to the absence of grain boundary stabilizing elements and particles. Notably, no severe grain growth was observed in the as-brazed grain structure of the low Al-Sc-Zr alloy, but it still lost its pre-brazed fibrous grain structure during brazing (Fig. 3-6b). TEM examination of the as-brazed low Al-Sc-Zr alloy did not reveal any Al_3(Sc, Zr) precipitates. However, the drag effect from Sc and Zr solutes dissolved in the Al matrix can still impede grain boundary migration [54,55] . However, the as-brazed high Al-Sc-Zr alloy maintained its fibrous grain structure following the brazing (Fig. 3-6c). TEM study showed that the large Al_3(Sc,Zr) particles still remained in the as-brazed microstructure (Fig. 3-19). The average size of the particles after brazing was measured to be 79 ± 18 nm, indicating a slight coarsening compared to their state before brazing. It is obvious that those particles obstructed grain boundary movement during high-temperature brazing, resulting in a partially deformed and refined grain structure (Fig. 3-7). In addition, the strength after brazing was notably improved in the high Al-Sc-Zr alloy, with the yield strength increasing from 29 MPa in the base alloy to 58 MPa, corresponding to an increase of approximately 2 times. This enhancement can be attributed to the combined effects of the thermally stable Al_3(Sc,Zr) dispersoids and the refined grain structure retained after brazing.

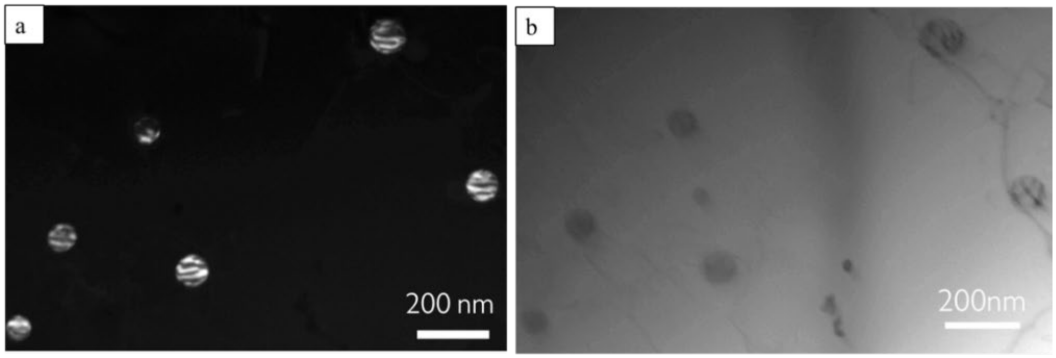

Figure 3-19 TEM micrographs of the as-brazed high Al-Sc-Zr alloy (a) dark-field and (b) bright-field images.

TEM investigation was conducted after the post-braze aging to examine the precipitation of $Al_3(Sc,Zr)$ particles in the two Al-Sc-Zr alloys. Figure 3-20a revealed numerous fine precipitates in the post-aged microstructure of the low Al-Sc-Zr alloy. This indicates that although a dissolution of $Al_3(Sc,Zr)$ precipitates occurred during the brazing cycle, a re-precipitation of $Al_3(Sc,Zr)$ occurred during the post-braze aging. The TEM image of the high Al-Sc-Zr alloy showed two types of particles (Fig. 3-20b). The first one, indicated by the yellow arrows, represents the coarse precipitates that survived the brazing process. The second type consists of fine precipitates that formed during post-braze aging. These fine precipitates are responsible for the significant improvement in the room temperature mechanical properties of the two Al-Sc-Zr alloys relative to the base alloy (Table 3-2). For instance, the YS after post-aging was increased from 26 MPa for the base alloy to 121 MPa for the low Al-Sc-Zr alloy, and further to 157 MPa of the high Al-Sc-Zr alloy. Previous studies [20,56] reported that the aging treatment of Sc-containing aluminum alloys within the temperature range of 250-350 ºC could result in significant precipitation strengthening.

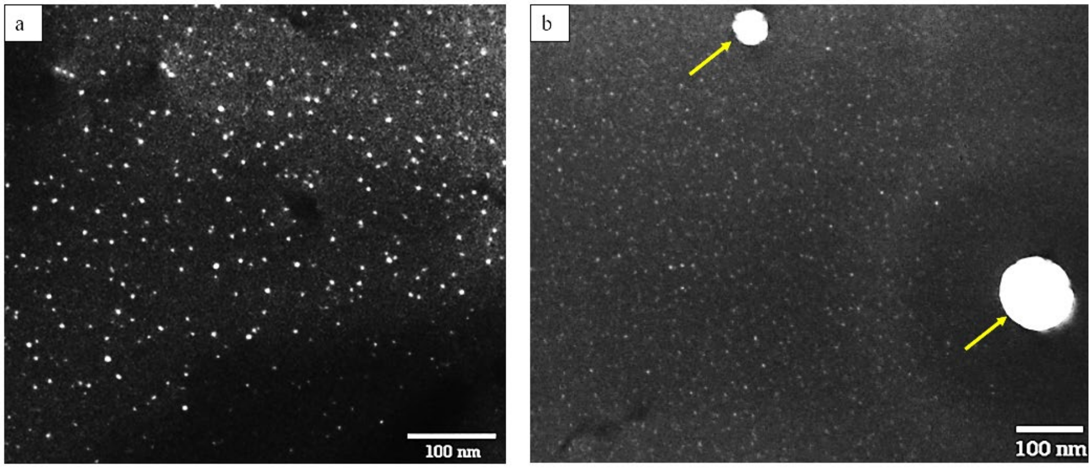

Figure 3-20 Dark-field TEM micrographs of (a) the low Al-Sc-Zr and (b) the high Al-Sc-Zr alloys after the post-brazing aging.

3.4.2 Impact of $Al_3(Sc,Zr)$ precipitation during R2

Unlike R1, the R2 route included a pre-aging treatment where the cast billets were exposed to 350°C/24h prior to extrusion (Fig. 3-1). This promoted $Al_3(Sc,Zr)$ precipitation in both the low and high Sc-Zr alloys, as shown in the dark-field TEM images in Figure 3-21. The embedded SAED patterns obtained along the [001] zone axis displayed faint spots from the precipitates between the α-Al spots, confirming that the precipitates have an $L1_2$ structure [50] . The $Al_3(Sc,Zr)$ precipitates in the low Al-Sc-Zr alloy showed an average diameter of 4.2 ± 0.8 nm with a number density of 7.9×10^{-6} nm^{-3}, while the high Al-Sc-Zr alloy exhibited finer precipitates with an average diameter of 3.8 ± 0.9 nm and a number density of 9.1×10^{-6} nm^{-3}. The remarkable increase in the ram pressure values of both Sc-containing alloys can be attributed to the presence of those fine precipitates formed during pre-aging under R2 Table 3-3[57].

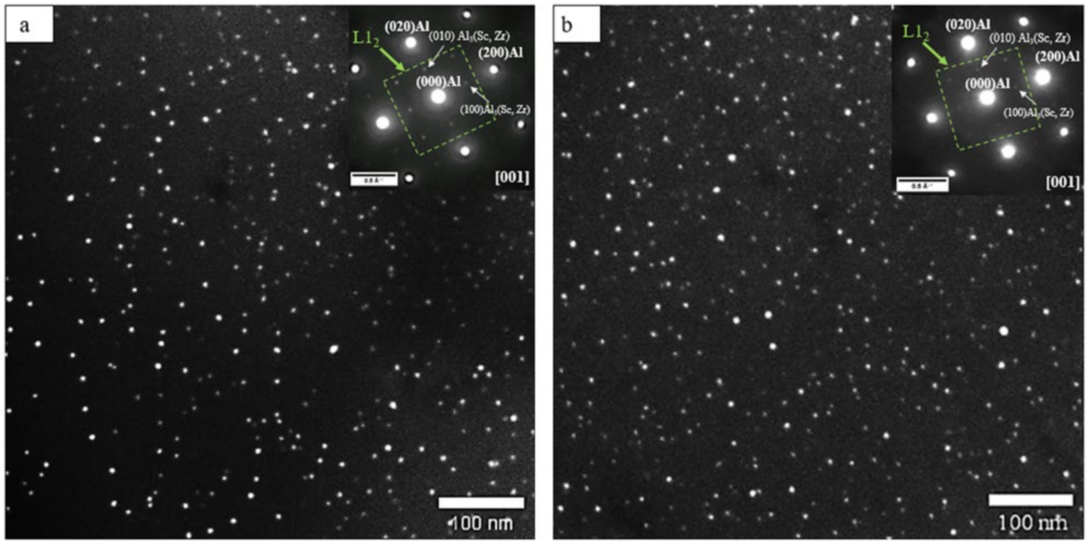

Figure 3-21 Dark-field TEM micrographs showing the $Al_3(Sc,Zr)$ precipitation in the pre-aged billets under R2, (a) the low Al-Sc-Zr and (b) high Al-Sc-Zr alloys.

After extrusion, the low Al-Sc-Zr alloy exhibited only relatively large grains, indicating that recrystallization occurred but without severe grain growth (Fig. 3-8). In contrast, the high Al-Sc-Zr alloy retained mostly elongated and deformed grains. The as-extruded samples of both Sc-containing alloys were thoroughly examined by TEM. As shown in Fig. 3-22a, the fine $Al_3(Sc,Zr)$ precipitates in the low Al-Sc-Zr alloy were barely observed (red arrows), and only a few coarsened $Al_3(Sc,Zr)$ particles were left in the microstructure (yellow arrows). This indicates that a large amount of the fine precipitates previously formed during pre-aging were dissolved and the surviving ones grew up to a large size of ~55 nm. Those fewer large particles were not sufficient to inhibit the recrystallization, resulting in a somewhat coarse recrystallized grain structure after extrusion. However, in the high Al-Sc-Zr alloy, there were still a large number of fine $Al_3(Sc,Zr)$ precipitates remaining after extrusion (Fig. 3-22c). Their average diameter was 4 ± 1.2 nm. This suggests that the majority of fine $Al_3(Sc,Zr)$ precipitates formed during pre-aging were thermally stable that survived the extrusion process without coarsening. The increased Sc and Zr content increased the solvus temperature and contributed to a higher thermal stability of the $Al_3(Sc,Zr)$ precipitates. This resulted in a stronger pinning effect on the dislocations and grain boundaries, enhancing the grain stability in the as-extruded condition as well as increasing the as-extruded strength, as reported in Table 3-2.

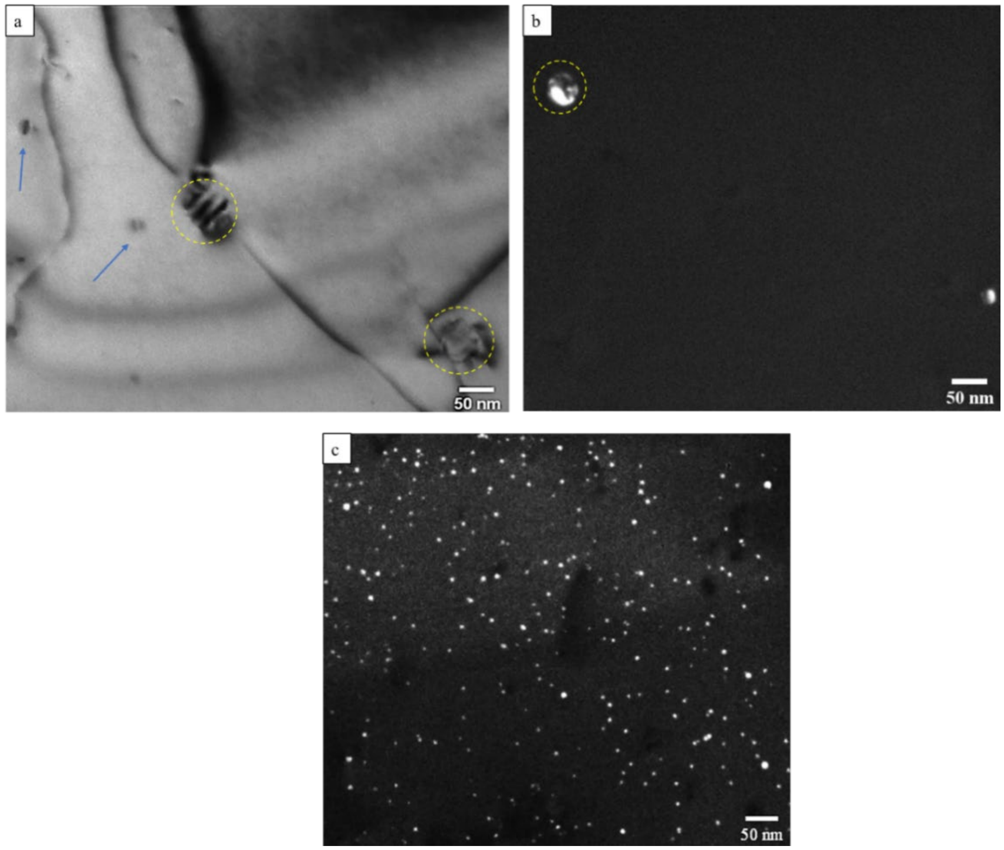

Figure 3-22 $Al_3(Sc,Zr)$ precipitation microstructure in the as-extruded condition, (a, b) bright- and dark-field TEM of the low Al-Sc-Zr alloy and (c) dark-field TEM of the high Al-Sc-Zr alloy.

Following the brazing, the low Al-Sc-Zr alloy showed a coarse recrystallized microstructure, while the high Al-Sc-Zr alloy maintained its mostly fibrous grains (Figure 3-9). TEM examination revealed that no $Al_3(Sc,Zr)$ precipitates were detected in the low Al-Sc-Zr alloy after brazing (TEM micrographs are not shown here), suggesting extensive dissolution. However, a number of $Al_3(Sc,Zr)$ particles remained in the as-brazed microstructure of the high Al-Sc-Zr alloy (Fig. 3-23). Those particles had coarsened significantly when compared to their state after extrusion. The average size of the particles after brazing was measured to be 24.7 ± 9 nm. The TEM micrograph shows that the particles exhibited "bean-like" contrast (red arrows in Figure 3-23), a characteristic feature of maintaining the semi-coherency between the precipitates and the matrix [58]. Although the average size of $Al_3(Sc,Zr)$ precipitates in the high Al-Sc-Zr alloy increased after brazing, the volume fraction of precipitates also increased from 1.7×10^{-4} to 2.6×10^{-3}. This increase of the precipitate population enhances the dislocation pinning effect and thereby reinforces precipitation strengthening [62], resulting in the YS of the high Al-Sc-Zr alloy increasing from 78.8 MPa in the as-extruded condition to 97.7 MPa after brazing (Table 3-2).

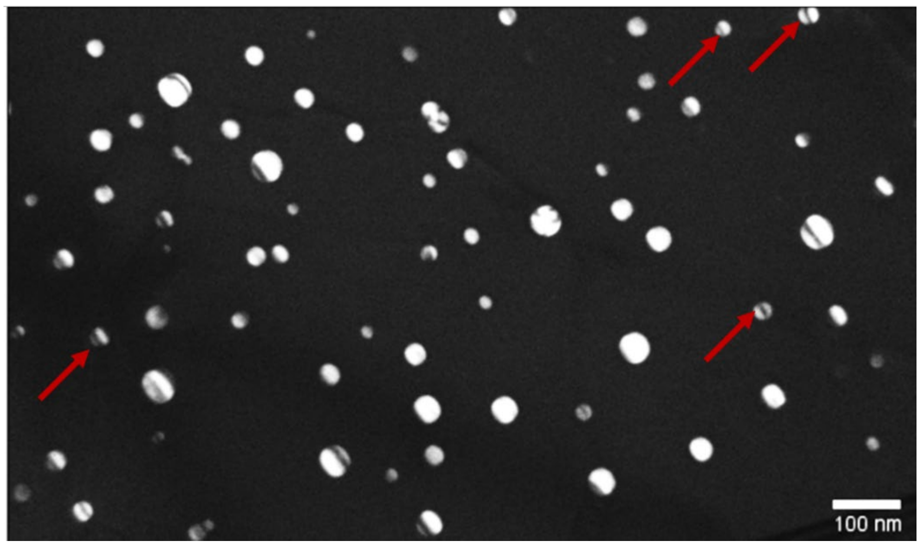

Figure 3-23 Dark-field TEM micrograph of as-brazed microstructure of the high Al-Sc-Zr alloy.

After the post-braze aging, the strengths of the base alloy were almost unchanged, but the strengths of both Al-Sc-Zr alloys significantly improved relative to the as-brazed condition (Table 3-2). TEM study revealed that numerous fine precipitates re-precipitated during the post-aging in both Al-Sc-Zr alloys, similar to the precipitation microstructures under R1 (Fig. 3-20). In the high Al-Sc-Zr alloy, in addition to the pre-existing $Al_3(Sc,Zr)$ particles in the as-brazed condition, many fine $Al_3(Sc,Zr)$ precipitates appeared in the post-aged microstructure (Fig. 3-24). Their average diameter was measured to be 2.5 ± 0.85 nm (highlighted within red rectangles), confirming that they were re-precipitated during the post-braze aging. The presence of numerous re-precipitated $Al_3(Sc,Zr)$ is the main reason for the largely enhanced mechanical strengths after post-aging in both Sc-containing alloys.

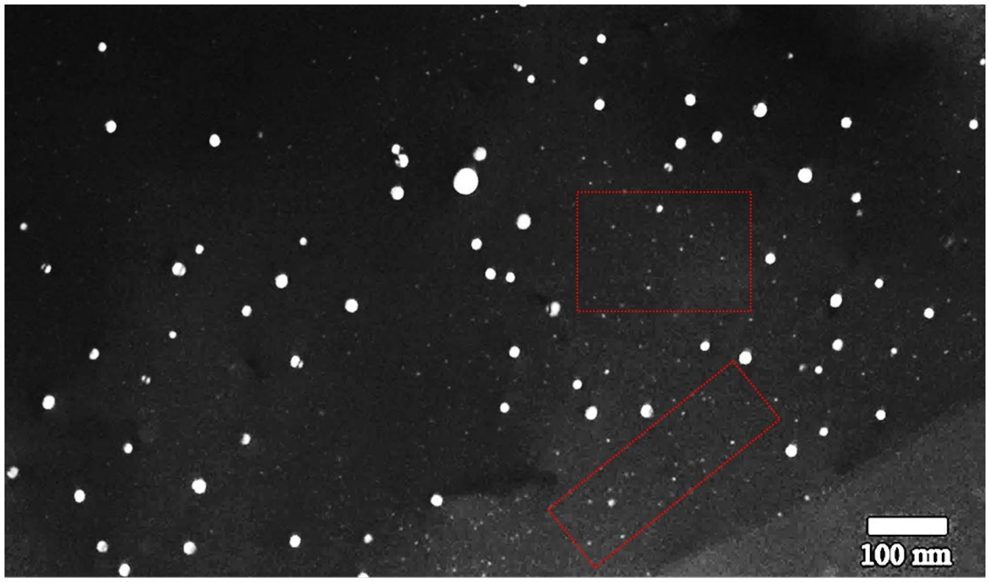

Figure 3-24 Dark-field TEM micrograph of the high Al-Sc-Zr alloy following the post-braze aging.

3.4.3 Performance comparison between the studied alloys and processing routes

The performances of the different alloys and processing routes for the brazed heat exchanger application were compared in terms of the grain structure, mechanical strength, corrosion behavior and extrudability.

The base alloy (a commercially pure 1xxx aluminum alloy) developed a coarse and recrystallized grain structure during high-temperature brazing under both processing routes. However, R1 promoted abnormal grain growth, whereas R2 resulted in more moderate grain coarsening. This can be attributed to differences in the Fe-rich intermetallic particle population during homogenization, as revealed by the microstructural observations in Figure 3-2. Previous studies have shown that the size, morphology, and distribution of Fe-rich intermetallic particles play a critical role in controlling recrystallization kinetics and subsequent microstructural evolution [44,59]. Shakiba et al. [45] reported that an increased volume fraction of Fe intermetallic phases enhanced pinning of substructures. Uttarasak et al. [46] demonstrated that higher pinning pressures associated with secondary phases effectively restricted grain boundary motion and suppressed abnormal grain growth. Accordingly, the reduced pinning efficiency resulting from Fe-rich intermetallic dissolution under R1 promotes abnormal grain growth during brazing, whereas the higher retained fraction of Fe-rich particles under R2 limits grain boundary mobility and restrains excessive grain growth. Nevertheless, in both processing routes the base alloy showed low mechanical strength, with YS values of 26-30 MPa in the as-brazed and post-aged conditions.

With Sc/Zr microalloying, the grain structure became finer and more stable, and the mechanical strength was significantly improved. However, the low Al-Sc-Zr alloy did not retain its fibrous and deformed grain structure. Although fine $Al_3(Sc,Zr)$ precipitates were observed in the as-extruded samples, their presence helps explain the fibrous microstructure in the as-extruded condition. However, those precipitates did not completely survive the high-temperature exposure during brazing. As a result, a recrystallized grain structure in the strips and some AGG in the MPE samples were observed. Given the brazing temperature of 605 ºC being well above the estimated Sc solvus temperature (~562 °C), dissolution of most of these precipitates likely occurred in both routes.

Among the examined alloys, the high Al-Sc-Zr alloy was the only one that maintained most of the fibrous and deformed grain structure in the extruded strips during brazing under both routes, resulting in the highest mechanical strengths. In the as-brazed samples, only partial recrystallization (~30% recrystallized grains) was observed under R1, while R2 showed even less recrystallization (~16%). This is further supported by the microstructure results of the brazed MPE tubes, where this alloy showed no signs of AGG or excessive recrystallization.

For the mechanical properties in the as-brazed condition, the YS of the high Al-Zr-Sc alloy in R2 was approximately 1.67 times higher than that in R1 (98 MPa vs. 59 MPa). Similarly, the UTS increased by a factor of 1.27, rising from 113 MPa under R1 to 143 MPa under R2. However, after the post-aging, the R1 route resulted in slightly higher mechanical strengths compared to the R2 route. The YS and UTS reached 157 MPa and 196 MPa under R1 respectively, whereas the R2 samples recorded 141 and 182 MPa of YS and the UTS, respectively. This slight improvement in the strength under R1 can be attributed to the possible higher availability of residual Sc and Zr in solid solution following the homogenization at 600 ºC, leaving more solutes available for further precipitation during post brazing-aging. Whether processed via route R1 or R2, the mechanical strengths obtained in the present study, particularly in the post-aged condition, are notably higher than those reported in the literature for conventional 1xxx and 3xxx aluminum alloys used in brazed heat exchanger applications. For instance, Li et al. [3] reported that in AA-3102 multi-port extruded (MPE) aluminum tubes, subjected to annealing at 600 ºC for 150 s, the YS and UTS reached ~23 and ~77 MPa, respectively. Vamadevan et al. [16] also reported a pronounced reduction in mechanical properties of AA3102 following simulated brazing. Their YS and UTS decreased to 27.5 MPa and 83 MPa after brazing. In another study by Tang et al [11], AA1100 tubes after brazing at 602 ºC for 3 min exhibited the UTS of ~82MPa. Li et al. [17] also reported that the YS of MPE tubes after annealing at 600 ºC for 3 min reached ~23 MPa for AA1100 and ~21 MPa for AA3102 alloys, respectively.

To further clarify the magnitude of the strength enhancement achieved through Sc/Zr micro-additions, Table 3-5 summarizes the YS and UTS ratios relative to the base alloy under the as-brazed and post-aged conditions for both processing routes. The results demonstrate that, regardless of the processing route, the Sc/Zr-containing alloys exhibit enhanced mechanical performance compared to the base alloy, and the high Al-Sc-Zr alloy shows the most pronounced strengthening response.

Table 3-5 Strength enhancement of Sc/Zr-containing alloys relative to the base alloy

Alloy	Condition	Route	YS ratio (×)	UTS ratio (×)
Low Al-Sc-Zr	As-brazed	R1	1.2	1.2
		R2	1.5	1.3
	Post-aged	R1	4.6	2.5
		R2	4.1	2.4
High Al-Sc-Zr	As-brazed	R1	2.0	1.7
		R2	3.2	2.1
	Post-aged	R1	6.0	3.0
		R2	4.6	2.6

Conventional aluminum heat exchanger tubes are known to be highly susceptible to pitting corrosion, which can lead to leakage and premature failure of the tubes during service [60,61]. In the present work, the micro-additions of Sc and Zr were found to have an impact on the corrosion behavior of the alloys. Under R1 the mass loss decreased with increasing addition of Sc and Zr. The high Al-Sc-Zr alloy exhibited the lowest mass loss and hence a better corrosion resistance. This improvement can be associated with the fibrous grain structure obtained in the as-brazed high Al-Sc-Zr alloy. The authors of the patent [62], claimed that such a fibrous or pancake-like grain structure is beneficial, as it helps prevent premature leakage due to corrosion, thereby extending the service life of the tubes. Fang et al. [49] also confirmed that fibrous non-recrystallized grains showed more corrosion resistance compared to recrystallized grains. Under R2, the mass loss was generally higher than under R1. Particularly, the mass loss of the high Al-Sc-Zr alloy was 1.6 times greater than that recorded under R1 after 20 days exposure. This increase could be related to the non-homogeneous grain structure that developed after brazing, where localized recrystallization occurred in certain regions, as indicated in the as-brazed microstructure of the high Al-Sc-Zr alloy. Despite the partial recrystallization under R2, the overall degradation of Sc/Zr-containing alloys in corrosion resistance was not severe.

While mass loss measurements in SWAAT provide an overall assessment of corrosion severity, they do not fully capture the risk associated with localized pitting, which is the dominant failure mechanism in thin-walled heat exchanger tubes. Figure 12 shows the results of pit depth analysis of the as-brazed strip samples for the three alloys under both processing routes. Under R1, the addition of Sc and Zr clearly results in reduced pit penetration compared to the base alloy. Under R2, the base alloy exhibits a pronounced increase in the pit depth, associated with its fully recrystallized grain structure after brazing. However, both the low and high Al-Sc-Zr alloys show lower pit penetration. Even under the conditions of the partial recrystallization and microstructural heterogeneity induced by R2 (Fig. 9), the Sc/Zr microalloying still reduces the pit growth. It has been reported in previous studies that Sc and Zr additions can improve the corrosion resistance of aluminum alloys. For instance, Algendy et al. [34] reported that the micro-addition of 0.1% Sc and 0.08% Zr to AA5083 alloys limited corrosion penetration by inhibiting recrystallization and maintaining a deformed grain structure. According to Cavanaugh et al. [63], a low level of Sc addition to Al alloys is unlikely to increase pitting corrosion susceptibility. Kim et al. [4] also found that the corrosion resistance of AA1070 aluminum MPE tubes was enhanced after the addition of 0.14% Zr. Ahmad et al.[64], found that the corrosion rate in an Al-Mg alloy was lowered after the additions of 0.15% Sc and 0.14% Zr.

In terms of extrudability, the R2 condition exhibited significantly higher extrusion pressures, particularly for the high Al-Sc-Zr alloy (approximately 1785 MPa in R2 compared to 1421 MPa in R1). The higher pressure in R2 can be attributed to the formation of numerous fine $Al_3(Sc,Zr)$ precipitates during pre-aging, which increased the alloy’s resistance to hot deformation. In contrast, the coarser $Al_3(Sc,Zr)$ particles presented after homogenization in R1 contributed less to the increase of the ram pressure, resulting in only a moderate rise compared with the base alloy. Overall, the R1 condition provided significantly easier processing and better formability.

Based on the overall results, the high Al-Sc-Zr alloy was identified as the best-performing material in the high-temperature brazing condition for heat exchanger applications. Although the differences in the grain structure and mechanical strength after brazing between R1 and R2 were relatively small, R1 provided improved corrosion resistance and better extrudability. In addition, the homogenization treatment at 600 ºC in R1 is more practical from an industrial point of view, offering a good balance between processability and overall performance. Despite ongoing efforts to lower production costs, Sc remains a costly alloying element owing to limited availability and complex extraction routes [65–68]. From an economic standpoint, the amount of Sc addition is a key consideration, as a higher Sc level significantly increases production costs. Increasing the Sc level from 0.10 wt.% in the low Al-Sc-Zr alloy to 0.19 wt.% in the high Al-Sc-Zr alloy is expected to result in a significant increase in material costs. It is noteworthy that the low Al-Sc-Zr alloy still remarkably outperforms the base 1xxx alloy and offers the best cost-effective performance improvement, demonstrating that even a limited Sc addition can clearly improve the strength and grain structure stability. These considerations highlight the importance of optimizing processing routes and microalloying strategies to maximize performance gains while minimizing the Sc content.

3.5Conclusions

This study systematically evaluated the effects of Sc/Zr microalloying on grain structure, mechanical properties, corrosion resistance and extrudability of 1xxx extrusion alloys for brazed heat exchangers under two different thermomechanical processing routes: R1 (homogenized at 600 ºC for 4 h) and R2 (pre-aged at 350 ºC for 24 h). The following conclusions are drawn from the main results:

1) The base alloy exhibited a very coarse recrystallized grain structure after high-temperature brazing under both processing routes, including abnormal grain growth under R1, whereas the low Al-Sc-Zr alloy exhibited a more normal recrystallized grain structure. Among the three alloys studied, the high Al-Sc-Zr alloy was the only one that maintained most of the fibrous and deformed grain structure in the extruded strips during brazing.
2) After brazing, the yield strengths (YS) of the high Al-Sc-Zr alloy were 104% and 220% higher than those of the base alloy under R1 and R2, respectively. Meanwhile, the YS of the high Al-Zr-Sc alloy under R2 was 66 % higher than that under R1 (97.7 MPa vs. 58.8 MPa). However, after post-aging, R1 resulted in slightly higher mechanical strengths compared to the R2. The YS and UTS of the high Al-Sc-Zr alloy reached 156.9 MPa and 195.7 MPa under R1, whereas the R2 samples recorded 140.9 and 182.2 MPa of YS and UTS, respectively.
3) Under R1, the high Al-Sc-Zr alloy exhibited the lowest mass loss and hence the best corrosion resistance (by SWAAT) among the three alloys studied. The mass losses under R2 of all alloys were generally higher than under R1. Under R2, the microalloying with Sc and Zr did not show a notable effect on the corrosion resistance compared to the base alloy.
4) In terms of extrudability, R2 produced noticeably higher extrusion ram pressures than R1, which was attributed to the formation of a high number of fine $Al_3(Sc,Zr)$ precipitates during the 350 ºC pre-age in R2. The lower extrusion pressures in R1 are advantageous for extrudability, making it a better practical choice for industrial applications.

5) For both processing routes, the grain structure trends for the multi-port extruded tubes (MPEs) were consistent with those of the extruded strips after simulated brazing, validating the strip-based approach as being representative for assessing the alloy performance. In each case, the high Al-Sc-Zr alloy mostly maintained its deformed grains and showed no signs of abnormal grain growth.

Overall, the high Al-Sc-Zr alloy under R1 offered the best combination of grain stability, mechanical properties, corrosion resistance and extrudability. From an economic perspective, the Sc content must be optimized as low as possible. The low Al-Sc-Zr alloy still clearly outperformed the base 1xxx alloy in terms of the strengths and grain structure stability.

3.6 Authorship contribution

Alyaa Bakr: Investigation, Formal analysis, Methodology, Writing – original. **Paul Rometsch**: Conceptualization, Methodology, Validation, Writing – review & editing. **X.-Grant Chen**: Conceptualization, Methodology, Validation, Writing – review & editing, Supervision.

References

[1]J. Qin, S.B. Kang, J.H. Cho, Sagging mechanisms in the brazing of aluminum heat exchangers, Scr. Mater. 68 (2013) 941–944. https://doi.org/10.1016/j.scriptamat.2013.02.039.

[2]K. Bordo, V.C. Gudla, L. Peguet, A. Afseth, R. Ambat, Electrochemical profiling of multi-clad aluminium sheets used in automotive heat exchangers, Corros. Sci. 131 (2018) 28–37. https://doi.org/10.1016/j.corsci.2017.11.011.

[3]K. Li, T. Zou, D. Li, Y. Peng, D. Shu, On Formation of Abnormally Large Grains in Annealing Prestrained Aluminum Alloy Multiport Extrusion Tubes, Metallurgical and Materials Transactions A 50 (2019) 5734–5749. https://doi.org/10.1007/s11661-019-05453-0.

[4]Y.-S. Kim, I.-J. Park, B.-S. An, J.G. Park, C.-W. Yang, Y.H. Lee, J.-G. Kim, Improvement of corrosion penetration resistance for aluminum heat exchanger by alloying zirconium, Mater. Chem. Phys. 241 (2020) 122275. https://doi.org/https://doi.org/10.1016/j.matchemphys.2019.122275.

[5]M.J. Benoit, H. Jin, B. Shalchi-Amirkhiz, S. Kurukuri, S. Winkler, M.J. Worswick, M.A. Wells, Microstructure evolution of warm deformed multilayered Al alloy sheet during brazing, J. Mater. Process. Technol. 281 (2020) 116639. https://doi.org/10.1016/j.jmatprotec.2020.116639.

[6]W. Fang, D. Tang, H. Wang, D. Li, Y. Peng, Optimization of die design for thin-walled flat multi-port tube with the aid of finite element simulation, J. Mater. Process. Technol. 277 (2020) 116418. https://doi.org/10.1016/j.jmatprotec.2019.116418.

[7]D. Tang, W. Fang, X. Fan, D. Li, Y. Peng, Effect of die design in microchannel tube extrusion, Procedia Eng. 81 (2014) 628–633. https://doi.org/10.1016/j.proeng.2014.10.051.

[8]X.H. Fan, D. Tang, W.L. Fang, D.Y. Li, Y.H. Peng, Microstructure development and texture evolution of aluminum multi-port extrusion tube during the porthole die extrusion, Mater. Charact. 118 (2016) 468–480. https://doi.org/10.1016/j.matchar.2016.06.025.

[9]J.C. Guía-Tello, M.I. Pech-Canul, E. Trujillo-Vázquez, M.A. Pech-Canul, Effect of brazing parameters on fillet size and microstructure of cladded fin-microchannel tube joints, Transactions of Nonferrous Metals Society of China (English Edition) 30 (2020) 3240–3253. https://doi.org/10.1016/S1003-6326(20)65457-7.

[10]D. Tang, W. Fang, X. Fan, T. Zou, Z. Li, H. Wang, D. Li, Y. Peng, P. Wu, Evolution of the material microstructures and mechanical properties of AA1100 aluminum alloy within a complex porthole die during extrusion, Materials 12 (2018) 1–14. https://doi.org/10.3390/ma12010016.

[11]D. Tang, X. Fan, W. Fang, D. Li, Y. Peng, H. Wang, Microstructure and mechanical properties development of micro channel tubes in extrusion, rolling and brazing, Mater. Charact. 142 (2018) 449–457. https://doi.org/10.1016/j.matchar.2018.06.010.

[12]Z. Yuan, Y. Tu, T. Yuan, Y. Zhang, Y. Huang, Effect of post-brazing heat treatment on the corrosion mechanism of sandwich multi-layered aluminium sheets, Vacuum 183 (2021) 109781. https://doi.org/10.1016/j.vacuum.2020.109781.

[13]J. Lacaze, S. Tierce, M.-C. Lafont, Y. Thebault, N. Pébère, G. Mankowski, C. Blanc, H. Robidou, D. Vaumousse, D. Daloz, Study of the microstructure resulting from brazed aluminium materials used in heat exchangers, Materials Science and Engineering: A 413–414 (2005) 317–321. https://doi.org/https://doi.org/10.1016/j.msea.2005.08.187.

[14]A. Kawahara, A. Niikura, T. Doko, Development of Aluminum Alloy Fin Stock for Heat Exchangers Using Twin-Roll Continuous Casting Method, in: Furukawa Review, 2003. https://api.semanticscholar.org/CorpusID:55706912.

[15]L. Long, Q. Pan, M. Li, J. Ye, Y. Sun, W. Wang, Y. Luo, X. Li, Z. Peng, S. Liu, Study on microstructure and mechanical properties of 3003 alloys with scandium and copper addition, Vacuum 173 (2020) 109112. https://doi.org/https://doi.org/10.1016/j.vacuum.2019.109112.

[16]G. Vamadevan, F.F. Kraft, Processing effects in aluminum micro-channel tube for brazed R744 heat exchangers, J. Mater. Process. Technol. 191 (2007) 30–33. https://doi.org/10.1016/j.jmatprotec.2007.03.040.

[17]K. Li, D. Li, T. Zou, D. Shu, D. Tang, Y. Peng, Strength Variation in Processing Multiport Extrusion Tubes of A1100 and A3102 Alloys, J. Mater. Eng. Perform. 28 (2019) 3576–3589. https://doi.org/10.1007/s11665-019-04132-w.

[18]F.F. Kraft, Method for Predicting and Optimizing the Strength of Extruded Multi-Void Aluminum Heat Exchanger Tube, SAE Transactions 111 (2002) 99–106. http://www.jstor.org/stable/44719187.

[19]S. Kahl, H.-E. Ekström, J. Mendoza, Tensile, Fatigue, and Creep Properties of Aluminum Heat Exchanger Tube Alloys for Temperatures from 293 K to 573 K (20 °C to 300 °C), Metallurgical and Materials Transactions A 45 (2014) 663–681. https://doi.org/10.1007/s11661-013-2003-5.

[20]J. Røyset, N. Ryum, Scandium in aluminium alloys, International Materials Reviews 50 (2005) 19–44. https://doi.org/https://doi.org/10.1179/174328005X14311.

[21]D.N. Seidman, E.A. Marquis, D.C. Dunand, Precipitation strengthening at ambient and elevated temperatures of heat-treatable Al(Sc) alloys, Acta Mater. 50 (2002) 4021–4035. https://doi.org/10.1016/S1359-6454(02)00201-X.

[22]A. Tolley, V. Radmilovic, U. Dahmen, Segregation in Al3(Sc,Zr) precipitates in Al-Sc-Zr alloys, Scr. Mater. 52 (2005) 621–625. https://doi.org/10.1016/j.scriptamat.2004.11.021.

[23]E.A. Marquis, D.N. Seidman, Nanoscale structural evolution of Al3Sc precipitates in Al(Sc) alloys, Acta Mater. 49 (2001) 1909–1919. https://doi.org/https://doi.org/10.1016/S1359-6454(01)00116-1.

[24]Z.H. Jia, J. Royset, J.K. Solberg, Q. Liu, Formation of precipitates and recrystallization resistance in Al-Sc-Zr alloys, Transactions of Nonferrous Metals Society of China (English Edition) 22 (2012) 1866–1871. https://doi.org/10.1016/S1003-6326(11)61399-X.

[25]Y. Sun, Q. Pan, Y. Luo, S. Liu, W. Wang, J. Ye, Y. Shi, Z. Huang, S. Xiang, Y. Liu, The effects of scandium heterogeneous distribution on the precipitation behavior of Al3(Sc, Zr) in aluminum alloys, Mater. Charact. 174 (2021) 110971. https://doi.org/https://doi.org/10.1016/j.matchar.2021.110971.

[26]J.-Y. Zhang, Y.-H. Gao, C. Yang, P. Zhang, J. Kuang, G. Liu, J. Sun, Microalloying Al alloys with Sc: a review, Rare Metals 39 (2020) 636–650. https://doi.org/10.1007/s12598-020-01433-1.

[27]N.Q. Vo, D.C. Dunand, D.N. Seidman, Improving aging and creep resistance in a dilute Al–Sc alloy by microalloying with Si, Zr and Er, Acta Mater. 63 (2014) 73–85. https://doi.org/https://doi.org/10.1016/j.actamat.2013.10.008.

[28]Y. Wang, B. Xiong, Z. Li, Y. Zhang, H. Teng, Precipitation Behavior of Al3(Sc,Zr) Particles in High-Alloyed Al–Zn–Mg–Cu–Zr–Sc Alloy During Homogenization, Arab. J. Sci. Eng. 46 (2021) 6027–6037. https://doi.org/10.1007/s13369-020-05268-x.

[29]V.G. Davydov, T.D. Rostova, V. V. Zakharov, Y.A. Filatov, V.I. Yelagin, Scientific principles of making an alloying addition of scandium to aluminium alloys, Materials Science and Engineering A 280 (2000) 30–36. https://doi.org/10.1016/S0921-5093(99)00652-8.

[30]J. Liu, P. Yao, N. Zhao, C. Shi, H. Li, X. Li, D. Xi, S. Yang, Effect of minor Sc and Zr on recrystallization behavior and mechanical properties of novel Al–Zn–Mg–Cu

alloys, J. Alloys Compd. 657 (2016) 717–725. https://doi.org/https://doi.org/10.1016/j.jallcom.2015.10.122.

[31]Y. Ding, K. Gao, S. Guo, S. Wen, H. Huang, X. Wu, Z. Nie, D. Zhou, The recrystallization behavior of Al-6Mg-0.4Mn-0.15Zr-xSc (x = 0.04–0.10 wt%) alloys, Mater. Charact. 147 (2019) 262–270. https://doi.org/10.1016/j.matchar.2018.11.009.

[32]V. Ocenasek, M. Slamova, Resistance to recrystallization due to Sc and Zr addition to Al–Mg alloys, Mater. Charact. 47 (2001) 157–162. https://doi.org/https://doi.org/10.1016/S1044-5803(01)00165-6.

[33]Y. Wang, Q. Pan, Y. Song, C. Li, Z. Li, Q. Chen, Z. Yin, Recrystallization of Al-5.8Mg-Mn-Sc-Zr alloy, Transactions of Nonferrous Metals Society of China 23 (2013) 3235–3241. https://doi.org/https://doi.org/10.1016/S1003-6326(13)62858-7.

[34]A.Y. Algendy, P. Rometsch, X.G. Chen, Mechanical and corrosion performances of Al–Mg-Mn 5083 rolled alloys microalloyed with Sc and Zr in different thermomechanical processing conditions, J. Mater. Sci. 59 (2024) 14692–14715. https://doi.org/10.1007/s10853-024-10044-5.

[35]J. Røyset, N. Ryum, Kinetics and mechanisms of precipitation in an Al–0.2wt.% Sc alloy, Materials Science and Engineering: A 396 (2005) 409–422. https://doi.org/https://doi.org/10.1016/j.msea.2005.02.015.

[36]X. Na, L. Wenqing, Z. Liu, T. Muthuramalingam, Effect of Scandium in Al–Sc and Al–Sc–Zr Alloys Under Precipitation Strengthening Mechanism at 350 °C Aging, Metals and Materials International 27 (2021) 5145–5153. https://doi.org/10.1007/s12540-020-00844-0.

[37]Y. Su, L. Ding, Y. Zhang, Y. Weng, C. Wang, Z. Jia, L. Zhuang, The dispersoid evolution, recrystallization and mechanical properties of an Al–Mg–Sc alloy under various homogenization and annealing processes, J. Mater. Sci. 60 (2025) 3558–3575. https://doi.org/10.1007/s10853-025-10673-4.

[38]M. Shakiba, N. Parson, X.G. Chen, Effect of homogenization treatment and silicon content on the microstructure and hot workability of dilute Al-Fe-Si alloys, Materials Science and Engineering A 619 (2014) 180–189. https://doi.org/10.1016/j.msea.2014.09.072.

[39]K.E. Knipling, R.A. Karnesky, C.P. Lee, D.C. Dunand, D.N. Seidman, Precipitation evolution in Al-0.1Sc, Al-0.1Zr and Al-0.1Sc-0.1Zr (at.%) alloys during isochronal aging, Acta Mater. 58 (2010) 5184–5195. https://doi.org/10.1016/j.actamat.2010.05.054.

[40]Y. Deng, G. Zhang, Z. Yang, G. Xu, Microstructure characteristics and mechanical properties of new aerospace Al-Mg-Mn alloys with Al3(Sc1−xZrx) or Al3(Er1−xZrx) nanoparticles, Mater. Charact. 153 (2019) 79–91. https://doi.org/https://doi.org/10.1016/j.matchar.2019.04.032.

[41]A. Rollett, G.S. Rohrer, J. Humphreys, Recrystallization and Related Annealing Phenomena, Elsevier, London, United Kingdom, 2017. http://ebookcentral.proquest.com/lib/uqac-ebooks/detail.action?docID=4924517.

[42]M. Yazdani, C. Pot, Q. Boyadjian, Y. Liu, S. Yue, J.F. Béland, P. Bocher, Effect of Unidirectional and Cross-Rolling on the Texture Evolution of a Hot Extruded AA6082 †, Engineering Proceedings 43 (2023). https://doi.org/10.3390/engproc2023043028.

[43]Y. Sun, X. Bai, D. Klenosky, K. Trumble, D. Johnson, A Study on Peripheral Grain Structure Evolution of an AA7050 Aluminum Alloy with a Laboratory-Scale Extrusion Setup, J. Mater. Eng. Perform. 28 (2019) 5156–5164. https://doi.org/10.1007/s11665-019-04208-7.

[44]L. Pan, K. Liu, F. Breton, X. -Grant Chen, Effect of Fe on Microstructure and Properties of 8xxx Aluminum Conductor Alloys, J. Mater. Eng. Perform. 25 (2016) 5201–5208. https://doi.org/10.1007/s11665-016-2373-0.

[45]M. Shakiba, N. Parson, X.G. Chen, Effect of Iron and Silicon Content on the Hot Compressive Deformation Behavior of Dilute Al-Fe-Si Alloys, J. Mater. Eng. Perform. 24 (2015) 404–415. https://doi.org/10.1007/s11665-014-1302-3.

[46]K. Uttarasak, W. Chongchitnan, K. Matsuda, T. Chairuangsri, J. Kajornchaiyakul, C. Banjongprasert, Evolution of Fe-containing intermetallic phases and abnormal grain growth in 6063 aluminum alloy during homogenization, Results Phys. 15 (2019) 102535. https://doi.org/https://doi.org/10.1016/j.rinp.2019.102535.

[47]P. Rometsch, J. Fourmann, Potential for Using Scandium in Extrusion Alloys, in: Thirteenth International Aluminum Extrusion Technology Seminar & Exposition, Wauconda, IL, USA, 2024.

[48]Y.-S. Kim, J.-G. Kim, Investigation of corrosion for aluminium fin-tube heat exchanger according to the corrosion potential and solution conductivity using a boundary element method, in: EUROCORR2018, Krakow, Poland, 2018.

[49]H.C. Fang, K.H. Chen, X. Chen, H. Chao, G.S. Peng, Effect of Cr, Yb and Zr additions on localized corrosion of Al–Zn–Mg–Cu alloy, Corros. Sci. 51 (2009) 2872–2877. https://doi.org/https://doi.org/10.1016/j.corsci.2009.08.001.

[50]T. Dorin, M. Ramajayam, A. Vahid, T. Langan, Chapter 12 - Aluminium Scandium Alloys, in: R.N. Lumley (Ed.), Fundamentals of Aluminium Metallurgy, Woodhead Publishing, 2018: pp. 439–494. https://doi.org/https://doi.org/10.1016/B978-0-08-102063-0.00012-6.

[51]J. Jiang, F. Jiang, M. Zhang, Dynamic recrystallization and precipitation in an Al–Mg–Sc alloy: effect of strain rate, Journal of Materials Research and Technology 19 (2022) 1444–1456. https://doi.org/https://doi.org/10.1016/j.jmrt.2022.05.132.

[52]B. Forbord, L. Auran, W. Lefebvre, H. Hallem, K. Marthinsen, Rapid precipitation of dispersoids during extrusion of an Al-0.91 wt.% Mn-0.13 wt.% Zr-0.17 wt.% Sc-alloy, Materials Science and Engineering A 424 (2006) 174–180. https://doi.org/10.1016/j.msea.2006.03.044.

[53]S. Fan, Z. Li, W. Xiao, P. Yan, J. Feng, Q. Jiang, J. Ma, Y. Gong, Effects of processing paths on the microstructure, mechanical properties and electrical conductivity of dilute Al-Zr-Sc alloy conductive wires, J. Mater. Sci. Technol. 188 (2024) 202–215. https://doi.org/10.1016/j.jmst.2023.11.060.

[54]J. Lai, C. Shi, X.G. Chen, Effects of v addition on recrystallization resistance of 7150 aluminum alloy after simulative hot deformation, Mater. Charact. 96 (2014) 126–134. https://doi.org/10.1016/j.matchar.2014.07.028.

[55]M. Hillert, Solute drag, solute trapping and diffusional dissipation of Gibbs energy, Acta Mater. 47 (1999) 4481–4505. https://doi.org/https://doi.org/10.1016/S1359-6454(99)00336-5.

[56]T. Dorin, M. Ramajayam, T.J. Langan, Impact of Scandium and Zirconium on extrudability, microstructure and hardness of a binary Al-Cu alloy, Mater. Today Proc. 10 (2019) 242–247. https://doi.org/10.1016/j.matpr.2018.10.402.

[57]A. Elasheri, N. Parson, X.-G. Chen, Microstructure, tensile and bending properties of extruded Al–Mg–Si 6xxx alloys with individual and combined additions of Zr and Mn, Materials Science and Engineering: A 894 (2024) 146156. https://doi.org/https://doi.org/10.1016/j.msea.2024.146156.

[58]P. Xu, F. Jiang, Z. Tang, N. Yan, J. Jiang, X. Xu, Y. Peng, Coarsening of Al3Sc precipitates in Al-Mg-Sc alloys, J. Alloys Compd. 781 (2019) 209–215. https://doi.org/https://doi.org/10.1016/j.jallcom.2018.12.133.

[59]M. Karlík, T. Mánik, H. Lauschmann, Influence of Si and Fe on the distribution of intermetallic compounds in twin-roll cast Al–Mn–Zr alloys, J. Alloys Compd. 515 (2012) 108–113. https://doi.org/https://doi.org/10.1016/j.jallcom.2011.11.101.

[60]M.A. Pech-Canul, J.C. Guía-Tello, M.I. Pech-Canul, J.C. Aguilar, J.A. Gorocica-Díaz, R. Arana-Guillén, J. Puch-Bleis, Electrochemical behavior of tube-fin assembly for an aluminum automotive condenser with improved corrosion resistance, Results Phys. 7 (2017) 1760–1777. https://doi.org/https://doi.org/10.1016/j.rinp.2017.05.008.

[61]A. Laferrere, N. Parson, X. Zhou, G. Thompson, Effect of microstructure on the corrosion behaviour of extruded heat exchanger aluminium alloys, Surface and Interface Analysis 45 (2013) 1597–1603. https://doi.org/10.1002/sia.5282.

[62]Vikas Somani, Alfred Wang, Scot Reagen, Corrosion-resistant aluminum alloy for heat exchanger, 2016. https://patents.google.com/patent/US20160369377A1/en.

[63]M.K. Cavanaugh, N. Birbilis, R.G. Buchheit, F. Bovard, Investigating localized corrosion susceptibility arising from Sc containing intermetallic Al3Sc in high strength Al-alloys, Scr. Mater. 56 (2007) 995–998. https://doi.org/10.1016/j.scriptamat.2007.01.036.

[64]Z. Ahmad, B.J. Abdul-Aleem, A. Ul-Hamid, Effect of scandium addition on the mechanical and corrosion behavior of Al-Mg alloys, Trends in Electrochemistry and Corrosion at the Beginning of the 21st Century (2004) 1069–1081.

[65]H.U. Sverdrup, A.E. Sverdrup, On the Supply Dynamics of Scandium, Global Resources, Production, Oxide and Metal Price, a Prospective Modelling Study Using WORLD7, Biophysical Economics and Sustainability 9 (2024) 2. https://doi.org/10.1007/s41247-024-00118-y.

[66]S. Phoung, E. Williams, G. Gaustad, A. Gupta, Exploring global supply and demand of scandium oxide in 2030, J. Clean. Prod. 401 (2023) 136673. https://doi.org/https://doi.org/10.1016/j.jclepro.2023.136673.

[67]C. Kumaş, H. Prasetia, W. Astuti, S. Sumardi, F.R. Mufakhir, M.R.F. Fasya, Red mud as a source of scandium: A review, Journal of Rare Earths (2025). https://doi.org/https://doi.org/10.1016/j.jre.2025.08.008.

[68]S.-L. Liu, X. Liu, H.-R. Fan, A.R. Butcher, Y. Lahaye, R.M. Michallik, E.M. Jolis, S. Lukkari, K.-F. Yang, Q.-W. Wang, Z.-J. Qiu, H.-D. She, Scandium distribution in the Bayan Obo REE-Nb-Fe deposit, China: A multi-scale geochemical perspective, Ore Geol. Rev. 177 (2025) 106466. https://doi.org/https://doi.org/10.1016/j.oregeorev.2025.106466

Chapter 4

Assessment of the effects of Sc/Zr microalloying on Al–Mn 3xxx brazed heat exchangers: From lab scale to multi-port extrusions

(This article was published in *Materials Characterization*, Volume 239, 2026, 116702)

Résumé

Les alliages Al–Mn de la série 3xxx sont largement utilisés dans les échangeurs de chaleur brasés. Toutefois, leur stabilité granulaire limitée lors du brasage à haute température peut favoriser la croissance anormale des grains (AGG), entraînant une dégradation des performances. Cette étude a débuté par des essais à l'échelle du laboratoire sur trois alliages 3xxx, avec et sans microalliage de Sc et de Zr. Cette première étape visait à établir une compréhension fondamentale du comportement de ces alliages dans des conditions de déformation à chaud et de brasage. Après le brasage simulé, l'alliage de base a présenté une faible stabilité granulaire ainsi que des signes d'AGG. En revanche, les deux alliages contenant du Sc et du Zr ont conservé une structure granulaire stable sans grossissement notable. Des essais d'extrusion de bandes plates ont ensuite été réalisés afin d'évaluer l'extrudabilité et les performances mécaniques. Par rapport à l'alliage de base, la pression du vérin a augmenté d'environ 13 % pour l'alliage Al-1Mn-0.10Sc-0.11Zr et d'environ 18 % pour l'alliage Al-1Mn-0.21Sc-0.15Zr. Après le vieillissement post-brasage, la limite d'élasticité a augmenté de 156 % dans l'alliage à plus faible teneur en Sc/Zr et de 191 % dans l'alliage à plus forte teneur en Sc/Zr par rapport à l'alliage de base. Enfin, l'étude a été étendue à la fabrication de tubes extrudés multi-canaux (MPE), représentatifs de la géométrie typique des tubes plats utilisés dans les échangeurs de chaleur. Après brasage, les tubes MPE de l'alliage de base ont présenté de gros grains ainsi qu'une AGG localisée, tandis que le microalliage avec le Sc et le Zr a permis de préserver une stabilité granulaire nettement supérieure au cours du brasage.

Abstract

Al–Mn 3xxx alloys are widely used in brazed heat exchangers. However, their limited grain stability during high-temperature brazing can promote abnormal grain growth (AGG), resulting in a loss of performance. This study began on laboratory scale experiments with three 3xxx alloys with and without Sc/Zr microalloying. The laboratory stage aimed to establish a fundamental understanding of the alloy's behavior under hot deformation and brazing conditions. Following simulated brazing, the base alloy showed poor grain stability and signs of AGG. By contrast, the two Sc/Zr-containing alloys maintained grain stability without coarsening. An extrusion trial of flat strips was then conducted to evaluate the extrudability and mechanical performance. Compared to the base alloy, the ram pressure increased by ~13% in the Al-1Mn-0.10Sc-0.11Zr alloy and by ~18% in the Al-1Mn-0.21Sc-0.15Zr alloy. After post-braze aging, the yield strength increased by 156% in the lower Sc/Zr alloy and by 191% in the higher Sc/Zr alloy relative to the base alloy. Finally, the study was scaled up by fabricating multi-port extruded (MPE) tubes that represent a typical flat tube geometry for heat-exchanger applications. The MPE tubes of the base alloy exhibited large grains and localized AGG after brazing, whereas the Sc/Zr microalloying successfully preserved superior grain stability during brazing.

Keywords: Al-Mn 3xxx alloys, Sc and Zr microalloying, Brazing, Abnormal grain growth, Mechanical properties, multi-port extruded tubes.

4.1 Introduction

Aluminum alloys are widely selected for heat exchanger applications because they combine light weight, excellent thermal conductivity, sufficient mechanical strength, and good resistance to corrosion [1–4]. With stricter energy-efficiency standards, rising raw material costs, and increasing environmental pressures, the demand for lighter and more efficient heat exchangers is growing rapidly [5,6]. To meet these needs, recent innovations have focused on aluminum tubes with enhanced inner surfaces, which improve heat transfer while reducing material usage, system size, and overall cost [7,8]. Multi-port extruded (MPE) tubes have been introduced to reduce the weight and volume of aluminum heat exchangers and enhance heat transfer capabilities [9]. Widely used in automotive air conditioning systems, these tubes feature multiple parallel channels separated by internal webs, allowing refrigerant to flow efficiently through the tube [6].

Starting with direct chill (DC) casting and homogenization of cast billets, the industrial production of MPE tubes proceeds through extrusion, mechanical straightening/sizing, and high-temperature brazing. The sizing step, carried out after extrusion through cold rolling, ensures that the tubes meet precise dimensional specifications for assembly with other heat exchanger components in the subsequent brazing process [10,11]. Brazing sheets typically consist of a core alloy and a clad layer [12]. The core alloy remains solid during the processing and provides the required strength, while the clad layer usually is a lower melting point alloy such as a 4xxx series (melting below 600 °C), facilitating the formation of brazed joints between heat exchanger components [13]. The combination of the strained tubes followed by high-temperature brazing triggers the formation of large grains in the MPE tubes, which in turn reduces their mechanical strength and pressure-bearing capacity [10,11].

Commercial Al-Mn 3xxx alloys are widely used in the fabrication of heat exchanger tubes [14,15]. The 3xxx aluminum alloys are primarily strengthened through work hardening and are therefore considered non-heat treatable. Nevertheless, during thermal processing, Mn-rich dispersoids can precipitate and provide additional strengthening through dispersoid hardening [16]. Therefore, 3xxx alloys have attracted considerable attention owing to their potential suitability for elevated-temperature service [17]. For instance, Liu et al. [17] found that Mn-rich dispersoids maintained excellent thermal stability at 300 °C, enabling the alloy to retain its mechanical properties and creep resistance during prolonged thermal exposures of up to 1000 hours. Liu et al. [18] also reported that the 0.3 wt.% Fe-containing 3004 alloy exhibited superior strength (YS of 86.6 MPa) and excellent creep resistance at 300 °C, demonstrating the strong potential of 3004 alloys for elevated-temperature applications. In another study by Liu et al. [19], it was reported that the addition of 0.3 wt.% Mo enhances the thermal stability of Al-Mn-Mg 3xxx alloys up to 350 °C, with only a slight reduction at 400 °C. However, the Mn-rich dispersoids generated during thermal treatment may lose their stability or partially dissolve under the severe thermal conditions of brazing at 600 °C [20].

Microalloying of Al with Scandium (Sc) is recognized as an effective approach for improving the high-temperature performance of aluminum alloys through effectively suppressing recrystallization and maintaining grain stability [21–23]. The performance improvements resulting from Sc additions are attributed to the precipitation of the $L1_2$-Al_3Sc phase in the Al matrix [24,25]. These precipitates hinder the movement of grain and subgrain boundaries, thereby preventing the nucleation and growth of recrystallized grains [25]. However, the Sc price has remained relatively high in recent years [26–28]. Combining Zr with Sc lowers production costs since Zr can partially replace Sc in the $L1_2$ structure [29]. Microadditions of Zr improve the high-temperature stability of Al_3Sc precipitates by forming a core shell structure with a Sc-rich core and a Zr-rich shell, which increases the resistance to coarsening [30–33]. Numerous investigations have confirmed that Sc/Zr-bearing precipitates are highly effective in suppressing recovery and recrystallization and in retarding grain coarsening, thereby ensuring superior microstructural stability of Al alloys under elevated-temperature conditions [30,34–46]. However, despite these well-established benefits, the specific effects of Sc and Zr additions on the mechanical response and microstructural evolution of brazed 3xxx aluminum alloys remains insufficiently addressed.

In this study, the investigation began on a laboratory scale with three experimental 3xxx alloys, with and without Sc and Zr micro additions. The alloys were first subjected to hot deformation tests, which were conducted to reproduce the conditions of extrusion, followed by cold working at room temperature to simulate sizing operations. These samples were then exposed to a simulated brazing cycle to assess their grain stability. To evaluate the extrudability and mechanical properties after brazing and post-braze aging, DC cast billets were extruded into flat strips of 30 × 1.4 mm and subsequently exposed to the same brazing cycle for comparison. Finally, the study was scaled up by extruding cast billets into MPE tubes that represent the typical geometry used in brazed heat exchangers to examine the grain structure after extrusion and brazing.

4.2 Materials and experimental methods

4.2.1 Lab Scale experiments

Three experimental 3xxx alloys with and without Sc and Zr additions were investigated. The alloys were prepared from commercially pure aluminum (99.85%), Al-25%Fe, Al-50%Si, Al-5%Ti-1%B, Al-2%Sc, and Al-15%Zr master alloys (wt.%). Approximately 5 kg of each material was batched in an electrical resistance furnace and cast at 720 °C in a rectangular permanent steel mold with dimensions of 30 × 40 × 80 mm. These castings were left to cool slowly in air right after they had solidified with the exception of the third alloy (Ex-H-ScZr), which was taken from a slice of the 4-inch cast billet that was fabricated as described in Section 2.2. The chemical compositions of the alloys analyzed by optical emission spectroscopy are presented in Table 4-1. The three alloys were then subjected to a homogenization heat treatment at 600 ºC for 4 h with a heating rate of 100 ºC/h, followed by water quenching.

Table 4-1Chemical compositions of experimental alloys

Alloy	*Elements in wt.%*						
	Si	Fe	Ti	Mn	Zr	Sc	Al
Base	0.13	0.43	0.02	1.17	0	0	Bal.
L-ScZr	0.19	0.35	0.03	1.13	0.09	0.08	Bal.
Ex-H-ScZr	0.10	0.40	0.02	1.01	0.15	0.21	Bal.

The investigation began with hot compression tests, which were conducted using a Gleeble 3800 thermomechanical testing unit. Cylindrical samples 10 mm in diameter and 15 mm in height were machined from the homogenized ingots. The tests were performed at 500 °C with a fixed strain rate of 1 s^{-1}. Each sample was heated to 500 °C at a rate of 2 °C/s and held at this temperature for 2 min before hot deformation to a true strain of 0.8. At least three repetitions were conducted to ensure reproducibility of the results. After hot deformation, the samples were water-quenched to preserve the deformed microstructure.

Following the hot compression tests, the Gleeble 3800 unit was also used to provide a 2% cold reduction in thickness on the deformed samples at room temperature for simulating the sizing of the MPE tubes. Then the samples were subjected to a simulated brazing cycle by heating up from room temperature to 605 °C in 20 minutes followed by holding at 605 °C for 2.5 minutes and finally water-quenching. A post-braze aging treatment was subsequently performed at 350 °C for 4 h. Previous studies [24,47,48] demonstrate that most Sc- and Sc/Zr-containing alloys were artificially aged at 300-350 °C to promote the precipitation of Al_3Sc or $Al_3(Sc,Zr)$ nanoprecipitates. For example, Algendy et al. [49] applied an aging treatment at 350 °C for the investigated Sc/Zr-containing alloys, achieving the peak-aged condition after 4 h of aging, which provides the basis of the aging treatment employed in the present study.

4.2.2 Extrusion Trials

4.2.2.1 Extrusion of flat strips

Following the laboratory-scale experiments, the study was scaled up to extrusion trials to evaluate extrudability as well as the brazed mechanical properties. Three 3xxx DC cast alloys, with and without Sc/Zr micro-additions, were prepared. The alloys were DC-cast into extrusion billets with a 101 mm (4 inches) diameter at the Arvida Research and Development Centre of Rio Tinto Aluminum in Saguenay, Quebec. The cooling rate during solidification is expected to be ≥5 ºC/s [50]. The chemical compositions, analyzed by optical emission spectroscopy, are presented in Table 4-2. These are similar chemical compositions to the three alloys used in lab scale experiments. The cast billets were homogenized at 600 ºC for 4 h with a heating rate of 130-140 ºC/h followed by rapid cooling at a rate exceeding 900 ºC/h.

Table 4-2 Chemical compositions of DC cast billets.

Alloy	*Elements in wt.%*						
	Si	Fe	Ti	Mn	Zr	Sc	Al
Ex-Base	0.09	0.40	0.01	1.00	0	0	Bal.
Ex-L-ScZr	0.10	0.40	0.02	0.98	0.11	0.10	Bal.
Ex-H-ScZr	0.10	0.40	0.02	1.01	0.15	0.21	Bal.

The homogenized billets were induction-heated to 480 ºC and extruded into 30 × 1.4 mm flat strips followed by the water quench at the press exit. The extrusion ratio was 210, and the exit speed was 75 m/min. Test samples were cut from the flat extruded strips and subjected to the same simulated brazing cycle used in the lab scale experiments, except that the 2% thickness reduction was applied by cold rolling in this case. Brazed strips from each alloy were subjected to a post-braze aging treatment at 350 ºC for 4 h. Uniaxial tensile tests were then performed on both the brazed and post-braze aged samples using an Instron 8801 servo-hydraulic unit. Tensile specimens were prepared according to ASTM E8 in the extrusion direction, using full-size sheet samples with a 200 mm length and 50 mm gauge length.

4.2.2.2 Fabrication of multi-port extruded tubes

After the extrusion of flat strips, the study was further scaled up by extruding multi-port profiles, which represent typical components used in brazed heat exchangers. This step allowed the validation of the effects of Sc and Zr microalloying under industrially relevant conditions, where extrusion parameters and the brazing response closely reflect actual service requirements. Figure 4-1a presents a section of a typical automotive air conditioning condenser showing fins brazed to MPE tubes, while Figure 1b shows a schematic of the MPE tube profile extruded in the current work, which incorporates ten parallel micro-channels.

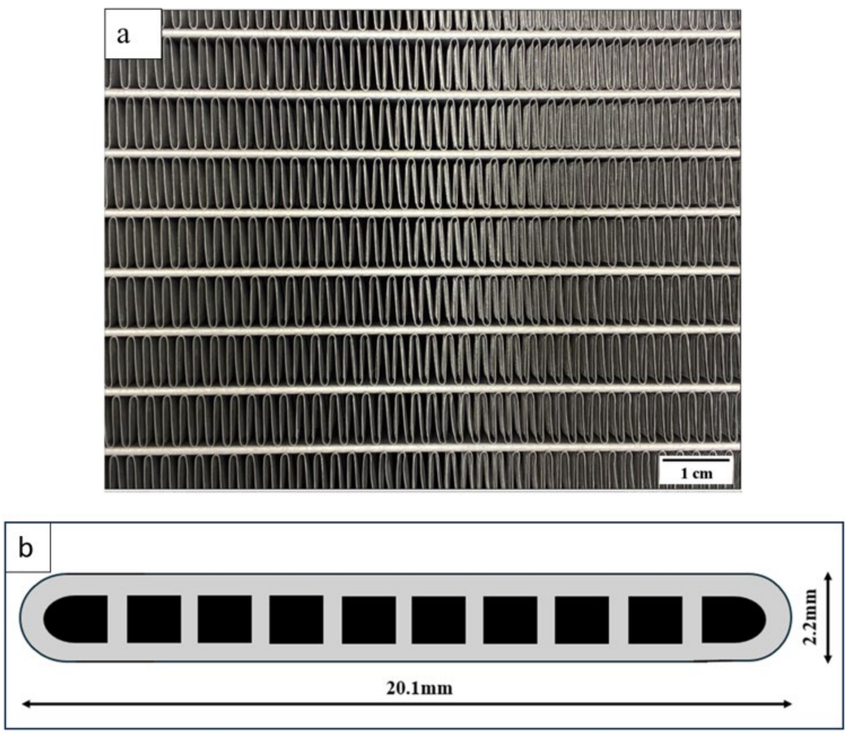

Figure 4-1 a) Section of a typical brazed heat exchanger, and b) schematic of the MPE tube profile extruded in this work

The MPE tubes were fabricated from the same DC cast alloys used on the extrusion of the strips, and the cast billets were homogenized with the same conditions as those applied for the strip extrusion. The billets were then induction-heated to 480 ºC and extruded with an extrusion ratio of 415 at an exit speed of 75 m/min, followed by standing wave water quenching immediately at the press exit. Following extrusion, the tubes were subjected to a 2% height reduction by rolling at room temperature to replicate dimensional adjustments typically performed before brazing. The tubes were then subjected to the same simulated brazing cycle as described previously.

4.2.3 Microstructural characterization

Microstructural characterization of all the alloys was performed using an optical microscope (OM, Nikon-Eclipse ME600) and scanning electron microscope (SEM, JEOL 6480LV). Samples of both alloys were prepared with standard metallographic procedures. To reveal the grain structure, samples were subjected to electrolytic etching using 5 ml HBF4 and 200 ml H_2O for 60 seconds.

Electron backscatter diffraction (EBSD) analysis was carried out to reveal grain/subgrain structures and misorientation distributions. The EBSD analysis was conducted in the central region of hot-deformed samples sectioned parallel to the compression axis. The low angle (2-5º), medium angle (5-15º), and high angle (>15º) grain boundaries were represented by grey, green, and black lines in the EBSD maps, respectively.

Transmission electron microscopy (TEM, JEOL JEM -2100) was used to observe the Mn-rich dispersoids and $Al_3(Sc,Zr)$ precipitates. TEM samples were prepared using a twinjet electropolishing unit, operated at 15 V and -30 °C, in an electrolyte solution of 30% nitric acid and 70% methanol. Observations of $Al_3(Sc,Zr)$ precipitates were made in the dark-field mode near the [001] zone axis.

4.3 Results and Discussion

4.3.1 Lab scale results

4.3.1.1 As-homogenized microstructures

Figure 4-2 displays as-homogenized microstructures of the three investigated alloys. The three alloys exhibited a similar microstructure, composed of α-Al matrix, and intermetallic particles near the dendrite boundaries [43]. The phases observed were identified as Al-Fe-Mn-Si-type intermetallics as indicated by the SEM-EDS results. However, the two Sc-containing alloys showed refinement of the dendrites. It was reported by Lathabai et al. [44] that a refinement of the dendritic substructure within the grains was observed following the addition of Sc to an Al-Mg alloy. Xu et. al [45] also observed a significant dendrite refinement in an Al-Si-Mg alloy upon the addition of 0.2 wt.% Sc. SEM observations of the as-homogenized Sc/Zr alloys revealed no appearance of primary $Al_3(Sc,Zr)$ particles, indicating most Sc and Zr were dissolved in the Al matrix. This observation agrees with what was reported by Davydov et al. [46], who recommended that in alloys with joint Sc and Zr additions, the Sc content should be maintained within 0.07-0.30 wt.% and the Zr content within 0.07-0.15 wt.% since exceeding these ranges may promote the formation of coarse primary $Al_3(Sc,Zr)$ particles.

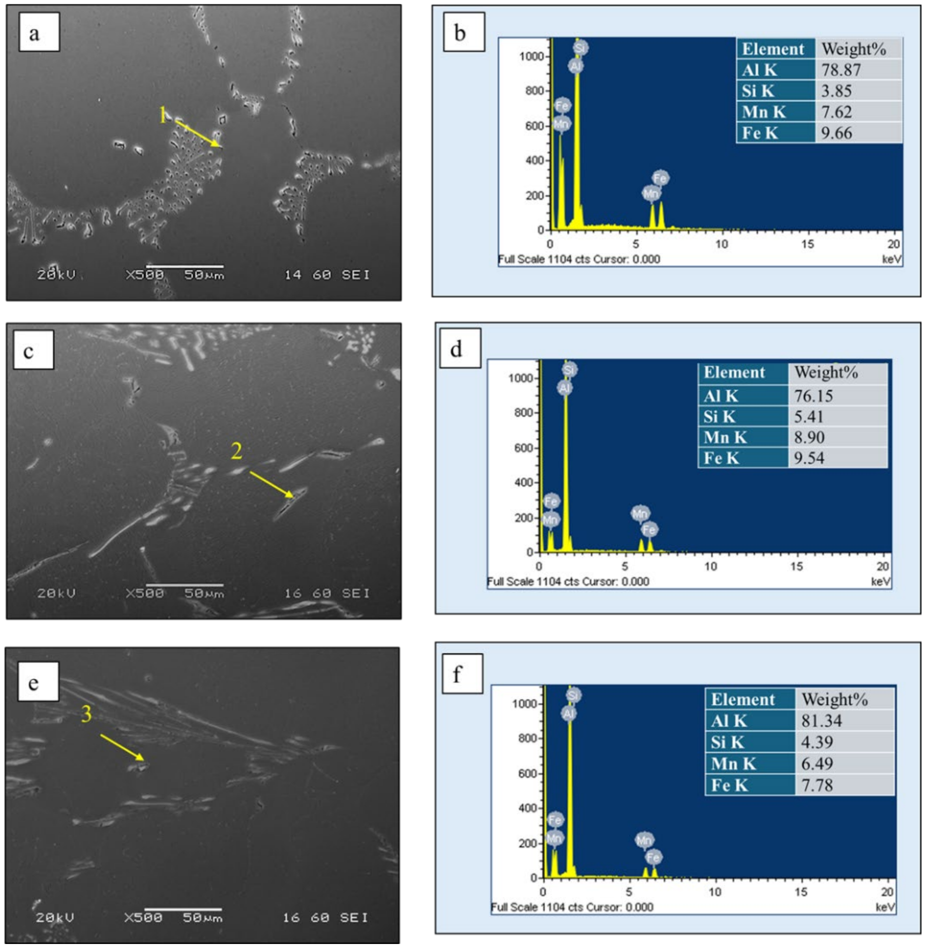

Figure 4-2 SEM micrographs of as-homogenized microstructures: (a) the base alloy, (c) L-ScZr, and (e) Ex-H-ScZr alloys. (b, d, and f) corresponding SEM-EDS point analysis of Fe-rich intermetallic phases observed in a, c and e, respectively.

4.3.1.2 Evolution of dispersoids during homogenization

TEM investigations were conducted on the three experimental alloys after homogenization at 600 ºC for 4 h (Figure 4-3). The base alloy contains coarse Mn-rich dispersoids (Figure 4-3a). When the alloy is heated to 600 ºC, the enhanced diffusion rate of Mn facilitates long-distance atomic movement, promoting the formation of Mn-rich dispersoids and further coarsening during homogenization [55,56].

In the two Sc/Zr-modified alloys (Figure 4-3b , 4-3c and 4-3e), both Mn-dispersoids and Sc/Zr-containing precipitates coexist. Fig. 4-3d reveals a typical selected area electron diffraction (SAED) pattern obtained along the [001] zone axis, displaying faint spots between the α-Al spots, confirming that the $Al_3(Sc,Zr)$ precipitates have an $L1_2$ structure [29]. The Ex-H-ScZr alloy (Figure 4-3e and 4-3f) showed slightly more $Al_3(Sc,Zr)$ precipitates when compared to the L-ScZr alloy. It was also observed that the Mn-rich dispersoids in the Sc/Zr-containing alloys appeared significantly coarser than those in the base alloy. A similar observation of coarsened Mn-rich dispersoids following the addition of Sc and Zr has been reported in previous studies [57,58]. A possible explanation is that the presence of Sc or Sc and Zr reduces the solubility of Mn in the aluminum matrix [25,59]. As a result, more Mn is consumed in the Fe/Mn-containing intermetallic phases, reducing the amount of Mn that remains dissolved in the aluminum matrix. This leaves less Mn solutes available to form Mn-rich dispersoids during subsequent heat treatments [57].

The TEM micrographs of the L-ScZr alloy (Fig. 4-3b and 4-3c) also reveal that some of the $Al_3(Sc,Zr)$ precipitates are attached to the surface of Mn-rich dispersoids, indicating that the $Al_3(Sc,Zr)$ phase may have formed via heterogeneous nucleation [60]. This suggests that the $Al_3(Sc,Zr)$ precipitates can nucleate on Mn-rich dispersoids and thereby contribute to a higher quench sensitivity compared to the binary Al-Sc C-curves shown by Røyset et al. [25]. Furthermore, based on the Sc solvus temperature of 560 ºC calculated with Thermo-Calc using the actual chemical composition of the L-ScZr alloy (Table 4-1), it was expected that all Sc-containing precipitates should have dissolved during homogenization at 600 ºC. However, considering that the permanent mold casting was cooled slowly after casting, it was possible that some coarse $Al_3(Sc,Zr)$ were formed during cooling and/or subsequent re-heating. However, considering that the permanent mold castings were cooled slowly after casting, it is possible that some $Al_3(Sc,Zr)$ particles were formed during cooling and that further precipitation may have occurred upon reheating to the homogenization temperature. In general, slow cooling after permanent mold casting can promote precipitation of $Al_3(Sc,Zr)$ during cooling, whereas rapid cooling tends to retain Sc solutes in a supersaturated solid solution [61].

In addition, $Al_3(Sc,Zr)$ possesses good thermal stability due to a Zr-rich outer shell in the Ll_2-$Al_3(Sc,Zr)$ structure, which could not be fully redissolved during homogenization at 600 °C for a relatively short period.

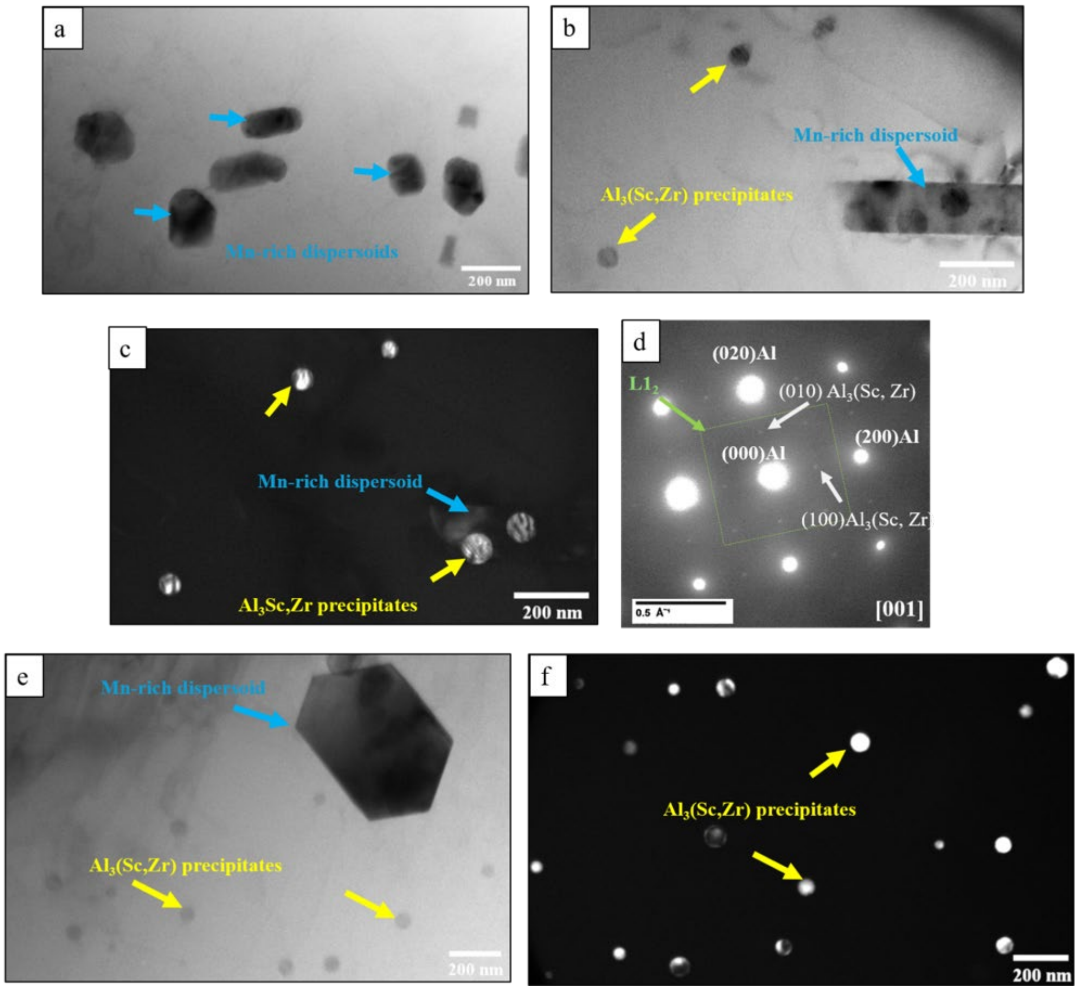

Figure 4-3 TEM micrographs of as-homogenized microstructures: (a) base alloy, and (b, c) L-ScZr alloy, and (e,f) Ex-H-ScZr alloy; (a, b, and c) bright-field images, (e and f) dark-field images; (d) SAED pattern obtained from the $Al_3(Sc,Zr)$ precipitates in b and c along the [001] zone axis. Yellow arrows indicate $Al_3(Sc,Zr)$ precipitates while the blue arrows show Mn-rich dispersoids.

4.3.1.3 Hot compression

Figure 4-4 reveals the true stress-strain curves during hot compression deformation of the three alloys investigated. The alloys displayed a flow behavior primarily governed by dynamic recovery (DRV) [62] . At the early stage of hot deformation, the three alloys exhibited a rapid rise in flow stress, owing to dislocation multiplication and a high rate of strain hardening, which gradually decreased as deformation progressed, followed by dynamic softening [62]. The Ex-H-ScZr alloy exhibited the steepest rise in flow stress, indicating the highest initial work-hardening rate. Then the alloy shows a gradual and slow increase in flow stress. The flow stress, determined at a true strain of 0.7, increased from 31.7 MPa in the base alloy to 37.6 MPa in the L-ScZr alloy and further to 38.8MPa in the Ex-H-ScZr alloy. The elevated flow stresses observed in the two Sc/Zr-containing alloys are mainly owing to the $Al_3(Sc,Zr)$ precipitation in the aluminum matrix (Figure 3b-f), which hinders DRV by impeding dislocation movement [40].

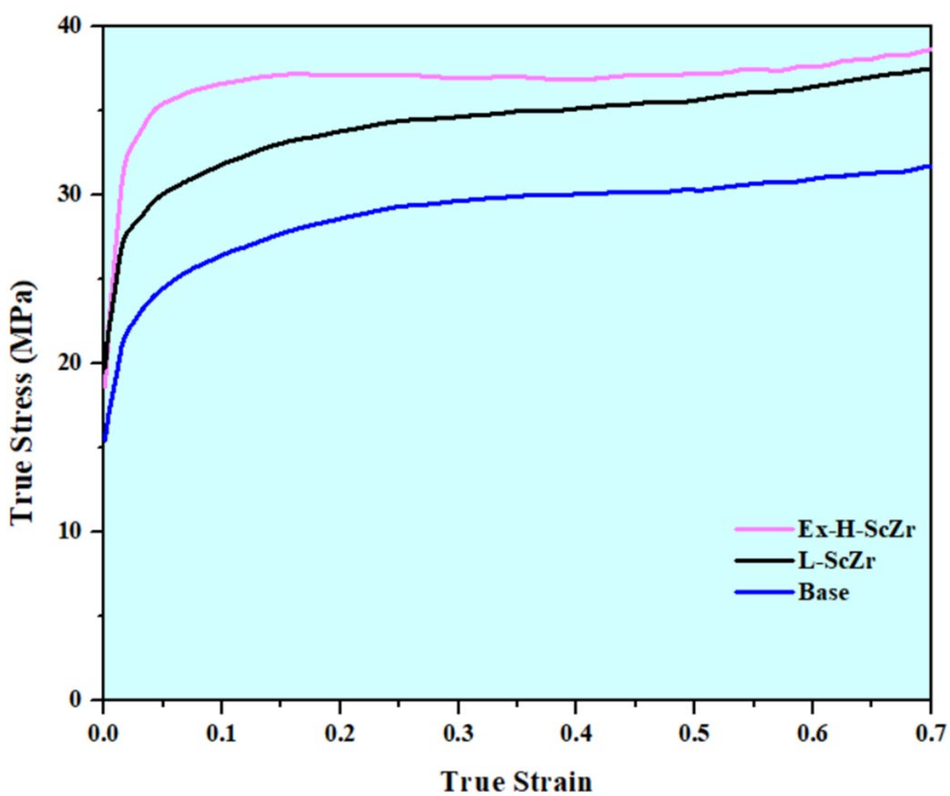

Figure 4-4 True stress-strain curves during hot compression deformation at 500 ºC and $1s^{-1}$.

4.3.1.4 Microstructure evolution before and after simulated brazing

Figure 4-5 reveals the EBSD maps of the three investigated alloys after hot deformation and after 2% cold working (CW) and simulated brazing at 605 ºC for 2.5 min. As illustrated in Figures 4-5a, 4-5c and 4-5e, the three deformed alloys showed elongated grains perpendicular to the compression direction after hot deformation, which is characteristic of dynamic recovery [63]. All deformed grains contained a high density of subgrains. In the base alloy, a small amount of newly formed small grains free of internal substructures were observed along the grain boundaries (yellow arrows in Figure 4-5a), indicating the occurrence of recrystallization during hot deformation [64,65]. For the two Sc/Zr-containing alloys, the microstructure remained predominantly a deformed grain structure. Figures 5c and 5e reveal that within elongated grains, the subgrain boundaries were primarily composed of low-angle grain boundaries (2°-5° misorientation, thin grey lines) and partially of medium-angle grain boundaries (5°-15° misorientation, thin green lines), indicating that these two alloys underwent only dynamic recovery during hot deformation.

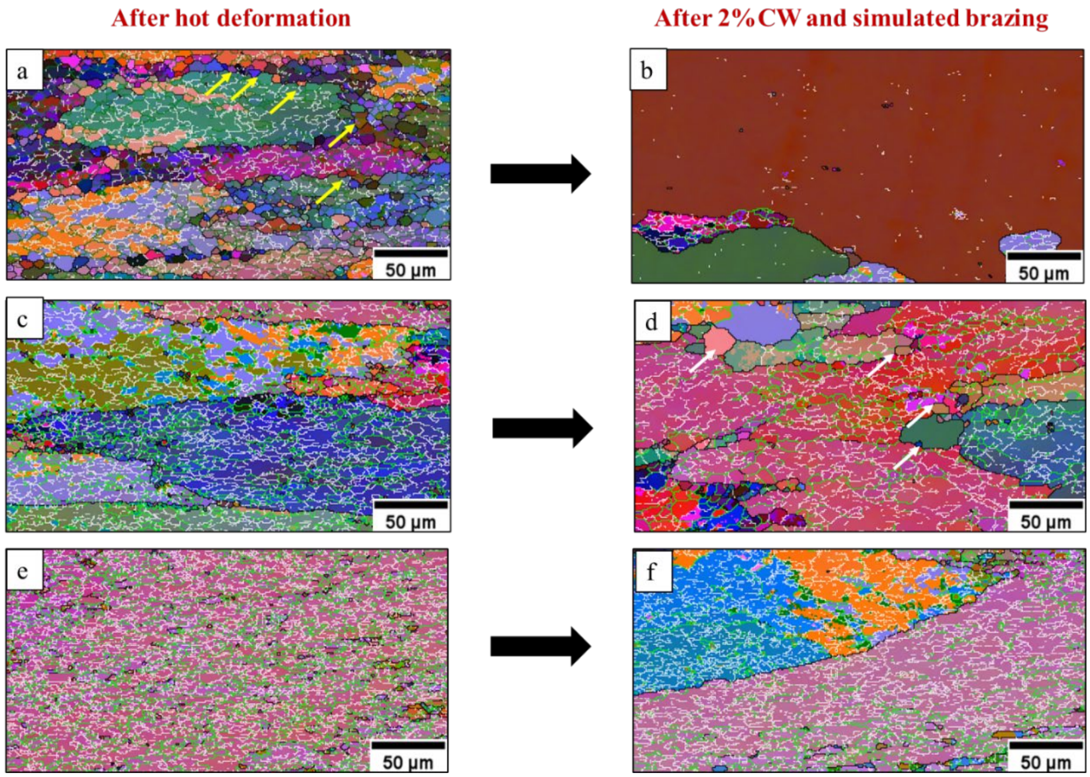

Figure 4-5 All Euler EBSD maps of (a, b) base alloy, (c, d) L-ScZr and (e, f) Ex-H-ScZr alloys; (a, c and e) as-deformed, (b, d and f) as-brazed grain structures.

After brazing, the base alloy (Figure 4-5b) almost lost its elongated and substructed grains and exhibited a very coarse, recrystallized grain structure, indicating AGG. This highlights the poor grain stability of the base alloy during high-temperature brazing. By contrast, the L-ScZr alloy (Figure 4-5d) showed only a few small, recrystallized grains (white arrows) and retained most of the elongated and deformed grain structure. This alloy did not show grain coarsening following the brazing, confirming the strong pinning effect of $Al_3(Sc,Zr)$ precipitates and their ability to suppress the recrystallization and grain coarsening. For the Ex-H-ScZr alloy (Figure 5f), it still maintained its deformed microstructure dominated by subgrains and did not show any recrystallized grains, indicating a superior grain stability even after the severe high-temperature exposure during brazing.

To investigate the evolution of dispersoids during hot deformation, TEM analysis was conducted on the as-deformed samples. The base alloy exhibited only coarse Mn-rich dispersoids indicated by blue arrows (Figure 4-6a). However, the two Sc/Zr-modified alloys (Figure 4-6b and 4-6c) contain three distinct types of particles: 1) Mn-rich dispersoids like those observed in the base alloy, 2) coarse $Al_3(Sc,Zr)$ precipitates formed during homogenization (white arrows), and 3) the fine $Al_3(Sc,Zr)$ precipitates (in yellow rectangles), which are coherent with the matrix [66] and formed during hot deformation. The resistance to recrystallization and grain growth in the two Sc/Zr-containing alloys during hot deformation is attributed to the presence of both the coarse and fine $Al_3(Sc,Zr)$ particles, which effectively pin grain boundaries.

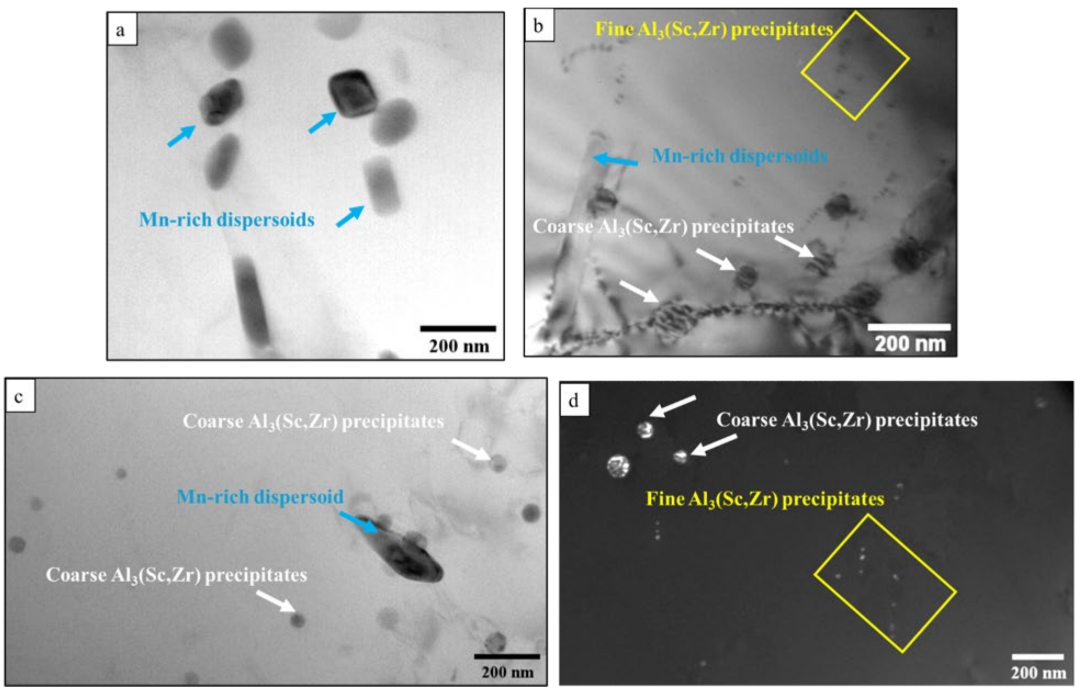

Figure 4-6 TEM micrographs of the as-deformed samples, (a) base, (b) L-ScZr and (c, d) Ex-H-ScZr alloys; (a-c) bright-field and (d) dark-field images.

Figure 4-7 shows TEM microstructures of the three brazed samples. In the base alloy (Figure 4-7a), only coarse Mn-rich dispersoids were detected after brazing. In contrast, the two Sc/Zr alloys (Figure 4-7b-d) exhibited several stable $Al_3(Sc,Zr)$ particles (yellow arrows), which have a coffee bean structure and are semi-coherent with the Al matrix, in addition to Mn-rich dispersoids. The fine $Al_3(Sc,Zr)$ precipitates formed during hot deformation were transformed to coarse and stable $Al_3(Sc,Zr)$ particles during high-temperature brazing. The enhanced grain stability of the two Sc/Zr-containing alloys during brazing (Figure 4-5d and 4-5f) can be attributed to the presence of stable $Al_3(Sc,Zr)$ particles, which remained almost intact during high-temperature brazing and effectively hindered recrystallization by pinning grain/subgrain boundaries.

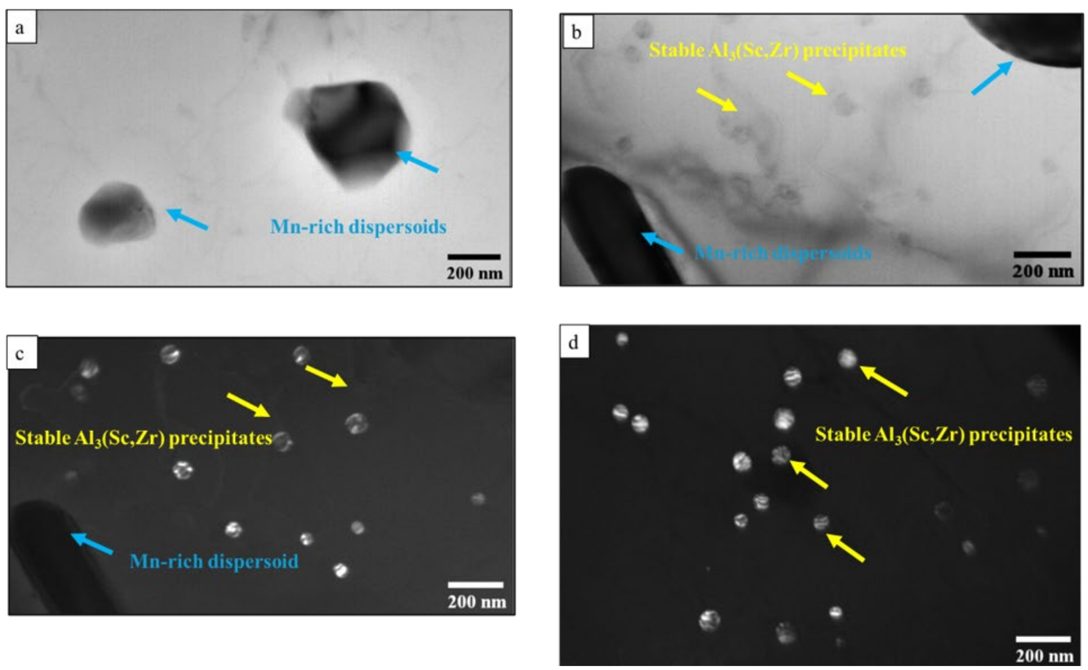

Figure 4-7 TEM micrographs of the as-brazed samples, (a) base, (b and c) L-ScZr and (d) Ex-H-ScZr alloys; (a, b) bright-field and (c, d) dark-field images.

4.3.1.5 Response to the post-brazing aging

Figure 4-8 displays the microhardness results after hot deformation, brazing (including 2% cold working prior braze) and post-braze aging. After hot deformation, the base alloy exhibited a hardness of 47.4 HV, while the L-ScZr alloy showed a higher value of 51.2 HV corresponding to an increase of approximately 8%. A more pronounced increase was observed for the Ex-H-ScZr alloy, which reached a hardness of 56.6 HV, representing an improvement of approximately 19% relative to the base alloy.

Following the brazing, the base alloy showed a low hardness of 40.4 HV, representing a 15% reduction compared to its as-deformed condition. Vamadevan et al. [11] reported that AA3102 micro-channel tubes after brazing showed a 17% reduction in strength compared to tubes that did not undergo the brazing thermal cycle. The reduction in microhardness is attributed to the abnormal grain growth observed in the as-brazed base alloy (Figure 4-5a), which can significantly deteriorate the mechanical properties [67,68]. In contrast, both the L-ScZr and Ex-H-ScZr alloys showed higher hardness values of 50.6 and 54.2 HV respectively. The enhanced hardness of the two Sc/Zr containing alloys further supports the microstructural observations of enhanced grain stability for both as-brazed samples (Figure 4-5d and 4-f).

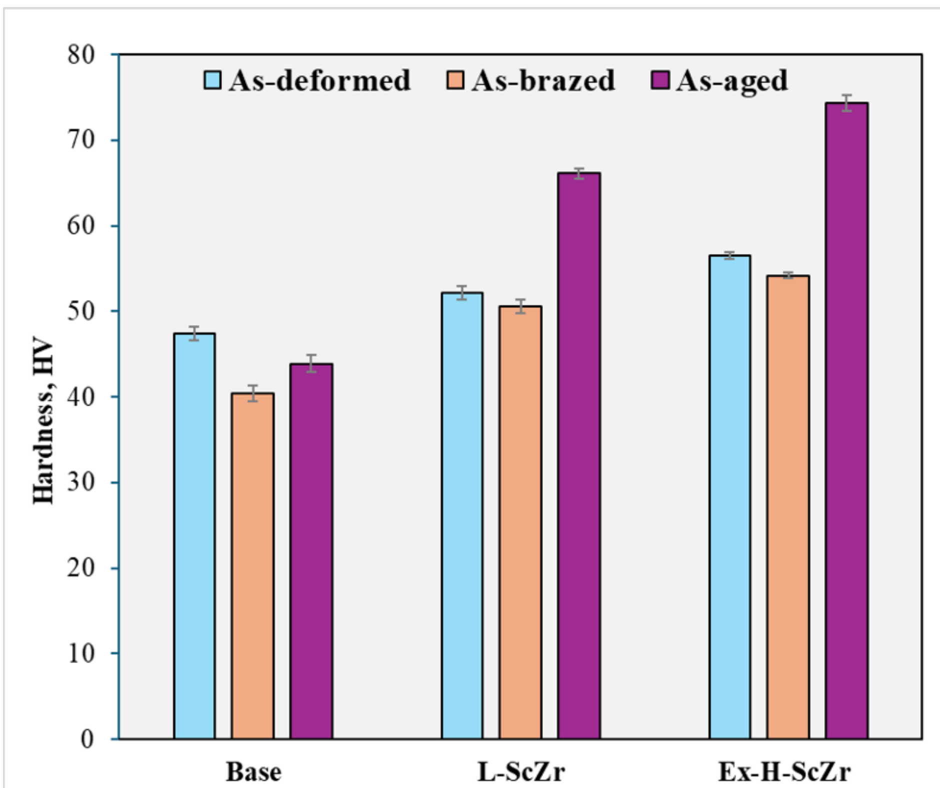

Figure 4-8 Microhardness measurement after hot deformation, simulated brazing and post-braze aging for the three experimental alloys.

After the post-braze aging, the microhardness of the base alloy was barely changed. However, the L-ScZr alloy exhibited a significantly higher hardness value of 66 HV, corresponding to a 51% increase compared to that of the as-aged base alloy. The Ex-H-ScZr alloy showed an even higher hardness value of 74.3 HV, corresponding to a 69% increase compared to that of the base alloy. These significant increases in both the L-ScZr and Ex-H-ScZr alloys can be attributed to the precipitation of fine $Al_3(Sc,Zr)$ precipitates during post-braze aging. According to previous studies [69,70], an aging treatment of Sc-containing aluminum alloys in the temperature range of 250-350 ºC led to a significant precipitation hardening. Figure 4-9 shows TEM micrographs of the post-braze aged L-ScZr alloy. Figure 4-9a shows the presence of a large number of nanoparticles in the Al matrix (fine black points) in addition to submicron Mn-rich dispersoids (blue arrows). Dark-field TEM (Figure 4-9b) confirmed that those fine particles are $Al_3(Sc,Zr)$ nanoprecipitates formed during post-braze aging (red arrows), in addition to some pre-existing coarse $Al_3(Sc,Zr)$ particles formed in earlier processing steps (yellow arrows).

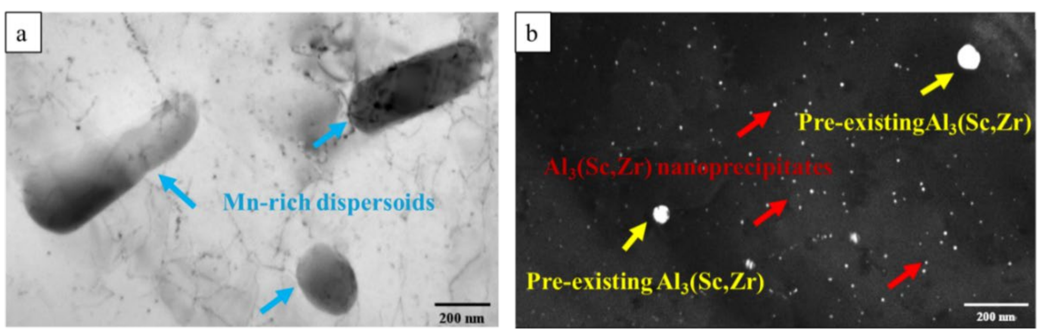

Figure 4-9 a) Bright-field TEM image showing Mn-rich dispersoids and fine nanoprecipitates, b) dark-field TEM image confirming the formation of $Al_3(Sc,Zr)$ nanoprecipitates during post-braze aging in the L-ScZr alloy.

4.3.2 Extrusion of thin strips

4.3.2.1 Extrusion pressures

The laboratory-scale experiments provided an initial understanding of the alloy's response to hot deformation and simulated brazing. Extrusion of flat strips was subsequently conducted to evaluate their behavior under more industrial conditions. The main extrusion process parameters for each alloy are summarized in Table 3. The ram pressure at a fixed ram position of 800 mm for the base alloy was 1342 psi, and it increased by approximately 13.3% for the Ex-L-ScZr alloy (1521 psi) and 17.8% for the Ex-H-ScZr alloy (1581 psi), respectively, indicating a progressively higher deformation resistance with additions of Sc and Zr. This increase is consistent with the higher flow stress observed for the Sc/Zr-containing alloys at the laboratory scale. It is also worth mentioning that, although the billet temperatures of the three alloys prior to extrusion were comparable, the exit temperature of the base alloy was approximately 498 ºC, whereas a higher exit temperature of approximately 513 ºC was recorded for the Ex-L-ScZr alloy. This increase can be directly associated with the higher extrusion pressures required for the Sc/Zr-containing alloys, a trend that has also been reported in a previous study [71].

Table 4-3Extrusion parameters for the thin strips

Billet	**Billet Temperature (°C)**	**Ram Pressure (psi)**	**Ram Speed (mm/s)**
Ex-Base	483	1342	6
Ex-L-ScZr	487	1521	6
Ex-H-ScZr	489	1581	6

To provide microstructural insight into the higher extrusion pressures measured in the Sc/Zr-containing alloys, TEM investigations were conducted on samples extracted from the extruded profiles. The TEM micrograph of the base alloy (Figure 4-10a) showed only coarse

Mn-rich dispersoids in the Al matrix (blue arrows). The Ex-L-ScZr alloy (Figure 4-10b) exhibited a limited number of coarse $Al_3(Sc,Zr)$ precipitates, which were formed during homogenization and/or extrusion. In the Ex-L-ScZr alloy the Sc solvus temperature predicted by Thermo-Calc was 589 ºC, and the cooling rates after casting, homogenization and extrusion were ≥ 5 ºC/s, ≥ 0.25 ºC/s and > 1000 ºC/s, respectively. The sizes of all observed particles were between 31 and 60 nm, except for one isolated coarse particle of approximately 113 nm, indicated by the green arrow. In addition to the $Al_3(Sc,Zr)$ precipitates, Mn-rich dispersoids were also observed. By contrast, the Ex-H-ScZr alloy contained numerous fine $Al_3(Sc,Zr)$ precipitates with an average diameter of 11.3±1.2 nm (red arrows), as shown in Figure 4-10c and 10d. The increased population of fine $Al_3(Sc,Zr)$ precipitates in the extruded strips compared to the samples after hot deformation can be attributed to the higher dislocation density induced by extrusion, which likely provided favorable and abundant nucleation sites for fine $Al_3(Sc,Zr)$ precipitation [72]. In addition, a few relatively coarse $Al_3(Sc,Zr)$ precipitates were also observed (Figure 4-10e), like those reported in Figure 4-6c and 4-6d following hot deformation. In addition to these precipitates, coarse Mn-rich dispersoids were also detected as shown in Figure 4-10d. It is worth mentioning that Thermo-Calc predictions indicate a remarkably high Sc solvus temperature in the Ex-H-ScZr alloy (~655 ºC), suggesting that continuous precipitation during extrusion was possible owing to the remaining high amounts of Sc and Zr in solution.

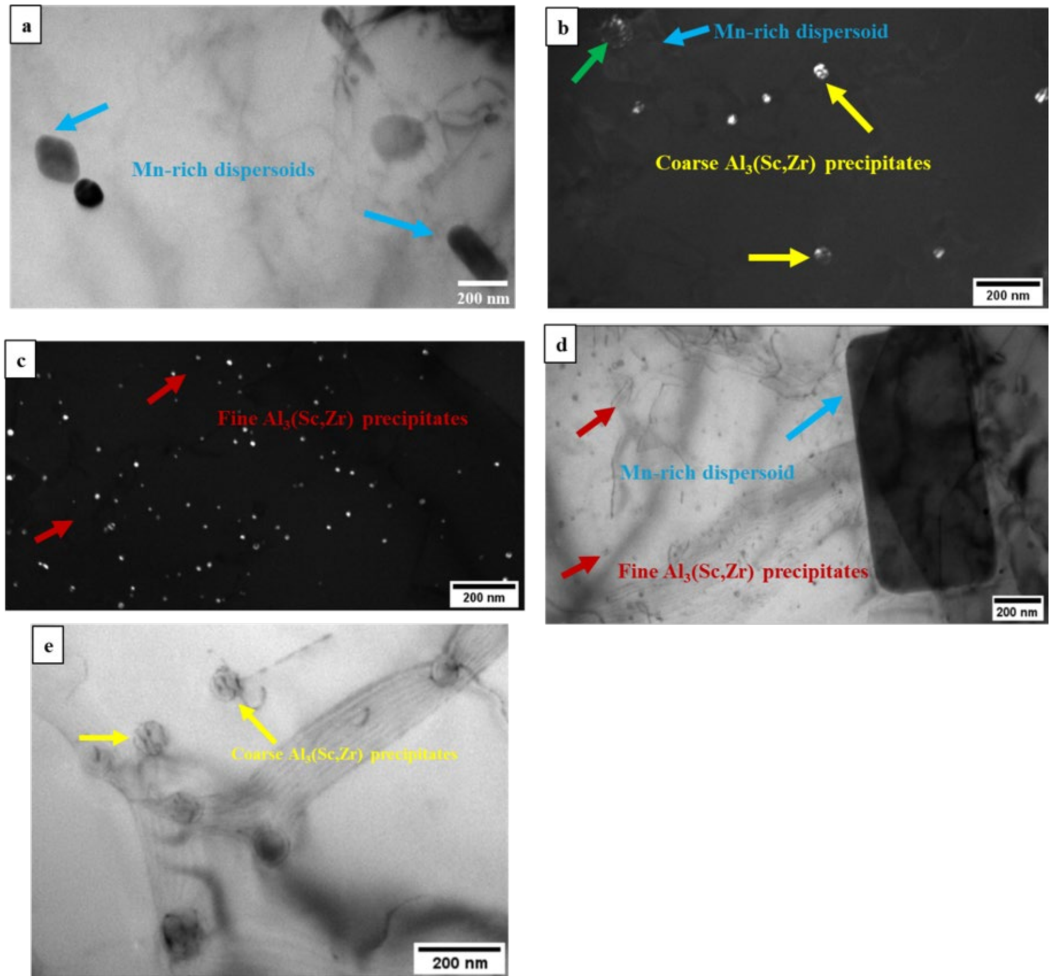

Figure 4-10 TEM micrographs of the extruded samples: (a) Base alloy, (b) Ex-L-ScZr and (c, d, and e) Ex-H-ScZr alloys; (a, d, e) bright-field and (b, c) dark-field images.

4.3.2.2 Mechanical properties of thin strips after brazing and post-braze aging

Samples from the extruded flat strips were cut and subjected to the same simulated brazing cycle used in the lab scale experiments. Following sizing and brazing, the samples were subjected to post-braze aging. Tensile tests were performed in the as-brazed condition as well as after post-braze aging. The results are displayed in Figure 4-11, which reveals the mechanical response of the three alloys studied under both conditions. Overall, post-braze aging led to a pronounced increase in strength for the Sc/Zr-containing alloys, accompanied by a reduction in ductility.

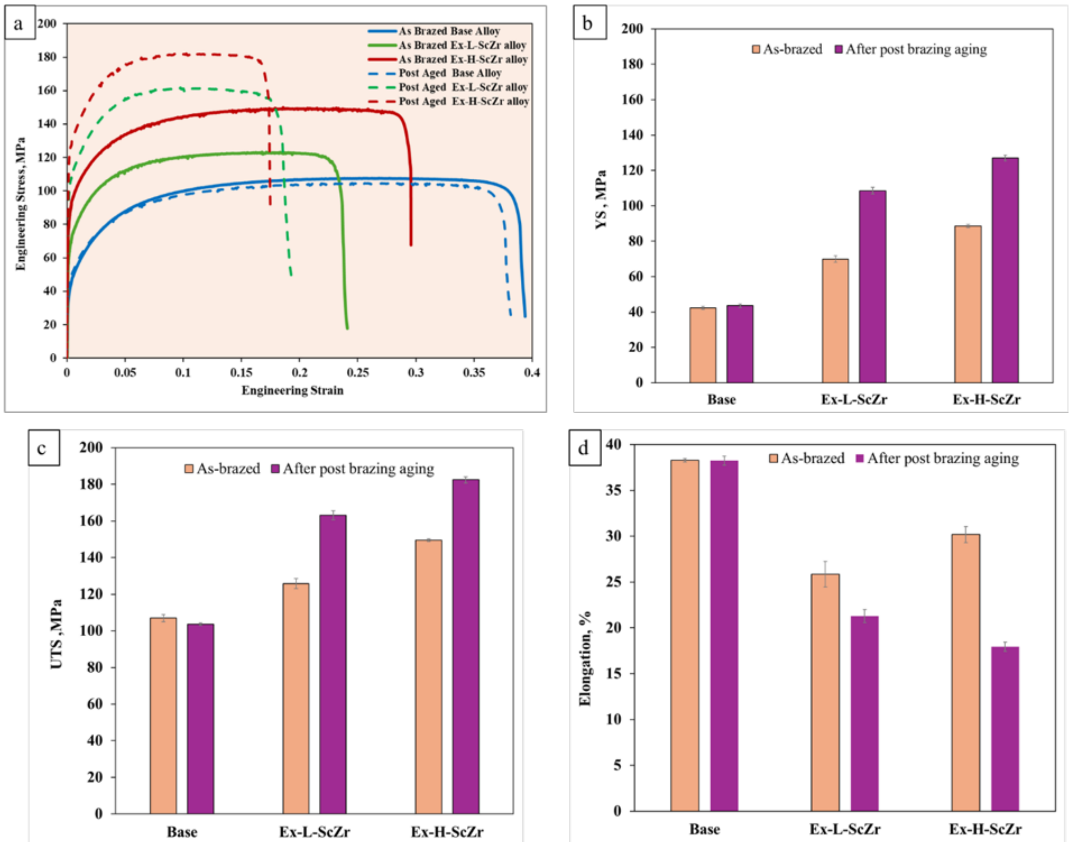

Figure 4-11 Tensile properties for the three alloys, (a) engineering stress-strain curves, (b) yield strength, (c) ultimate tensile strength, and (d) elongation to fracture.

Figure 4-11a shows the typical engineering stress-strain curves. After simulated brazing, the base alloy exhibited the lowest stress value among the investigated alloys, while the stress level increased with the addition of Sc and Zr, confirming the contribution of Sc towards improving the tensile strengths. Following post-braze aging, the base alloy exhibited non-noticeable changes in mechanical strength, indicating the absence of any age-hardening response. In contrast, the two Sc/Zr-containing alloys showed a remarkable improvement in strength compared to their respective as-brazed conditions or the base alloy. Figure 4-11(b, c, d) presents the tensile properties (YS, UTS and elongation, respectively).

After simulated brazing, the base alloy exhibited low strengths, with a YS of 42.3 MPa and a UTS of 106.9 MPa. These values are comparable to those reported by Cao et al. [73], who observed a post-brazed YS of 40.3 MPa and a UTS of 114 MPa for a conventional 3003 alloy. The Ex-L-ScZr alloy (Figure 4-11b-c) showed a substantial increase in strength, with a YS of 69.9 MPa and a UTS of 125.8 MPa, representing increases of 65% and 18%, respectively, compared to the base alloy. A more pronounced enhancement was observed for the Ex-H-ScZr alloy, which exhibited a YS of 88.6 MPa and a UTS of 149.6 MPa, corresponding to approximately 110% and 40% increases relative to the base alloy, respectively. Long et al. [74] reported a comparable improvement in the post-brazed YS of 3003-0.25Sc-0.5Cu rolled plates of approximately 72.6 % compared to the Sc-free variant. Following the post-braze aging, the Ex-L-ScZr alloy exhibited a YS of 108.6 MPa, corresponding to an improvement of 60 % relative to the as-brazed condition and 156% compared to the as-aged base alloy, whereas the UTS reached 163.1 MPa, representing increases of 40 % compared to the as-brazed condition and 60 % compared to the as-aged base alloy. The Ex-H-ScZr alloy showed an even more pronounced strengthening effect after the post-braze aging, reaching a YS of 127 MPa and a UTS of 182.4 MPa. When compared with the as-aged base alloy, these values correspond to increases of 191% in YS and 76% in UTS, respectively. Figure 4-11d shows the elongation values of the three alloys after simulated brazing and post-braze aging. After simulated brazing, the base alloy exhibited an elongation of 38.3%, which remained nearly unchanged after aging. In contrast, the Sc/Zr-containing alloys showed lower ductility in the as-brazed condition, with elongations of 25.8% and 30.2% for the Ex-L-ScZr and Ex-H-ScZr alloys, respectively. Following post-braze aging, the elongation further decreased to 21.3% and 17.9% for the Ex-L-ScZr and Ex-H-ScZr alloys, corresponding to reductions of approximately 17% and 41%, respectively, relative to their as-brazed values.

A TEM study was first conducted on the as-brazed samples (Figure 4-12). Figure 4-12a reveals that the base alloy predominantly contained few and coarse Mn-rich dispersoids, which is consistent with the TEM observation in the lab scale sample after brazing. These Mn-rich dispersoids provide limited precipitation strengthening, which is consistent with the relatively low YS and UTS values observed for the base alloy in the as-brazed condition. For the Ex-L-ScZr alloy, a limited number of $Al_3(Sc,Zr)$ precipitates appeared in the Al matrix. The TEM micrograph reveals two relatively coarse precipitates (~85-95 nm), as indicated by the yellow arrows in Figure 4-12b, while the remaining particles are significantly finer, with sizes ranging from 11 to 40 nm (red arrows in Figure 4-12b). In addition, a few Mn-rich dispersoids were observed (not shown in the image). Similarly, in the Ex-H-ScZr alloy, a number of coarse $Al_3(Sc,Zr)$ precipitates were detected in the Al matrix, which exerted a pinning effect on grain/subgrain boundaries (Figure 4-12c). In addition, there were a small number of relatively finer Sc-containing precipitates with an average diameter of ~10 nm observed in the matrix, as highlighted in the red rectangle, which seem to have coarsened less during brazing. The presence of these $Al_3(Sc,Zr)$ precipitates in the Sc/Zr-containing alloys contributed to their enhanced strength after brazing compared to the base alloy. Overall, fluctuations in temperature and strain during extrusion and subsequent brazing strongly influence the stability and coarsening behavior of both pre-existing and newly formed $Al_3(Sc,Zr)$ precipitates.

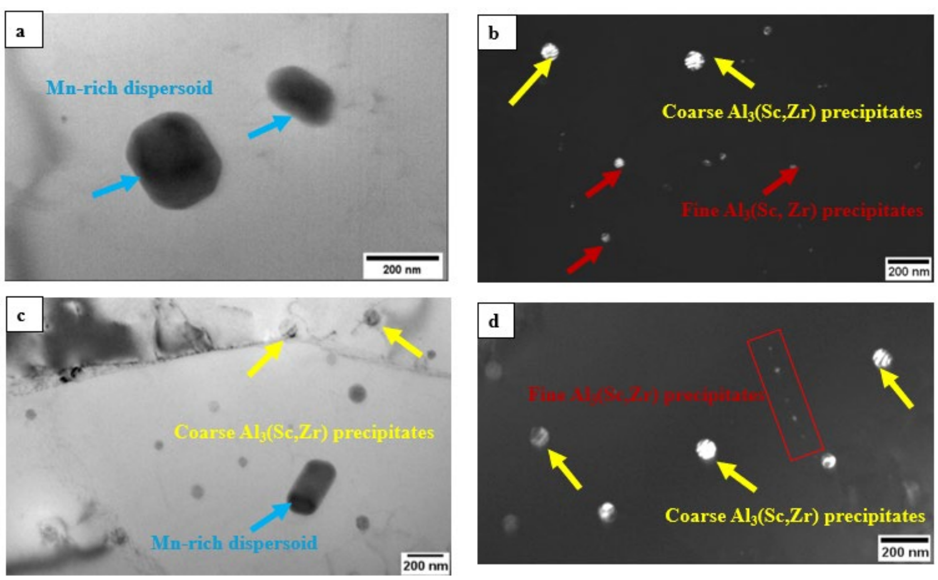

Figure 4-12 TEM micrographs of as-brazed samples, (a) Base alloy, (b) Ex-L-ScZr alloy, (c, d) Ex-H-ScZr alloy; (a, c) bright-field and (b, d) dark-field images.

The substantial strengthening accompanied by a reduction in elongation for the two Sc containing alloys is attributed to the precipitation strengthening effect of the fine $Al_3(Sc,Zr)$ nanoprecipitates formed during post-braze aging. For example, Figure 4-13 shows a TEM micrograph of as-aged Ex-H-ScZr sample. The micrograph reveals the precipitation of a high number density of fine $Al_3(Sc,Zr)$ precipitates (red arrows) with an average diameter of 5.6 ± 1.1 nm, which significantly contributed to the strengthening response. Some coarse precipitates (yellow arrows) with an average diameter of 72.5 nm were also observed. Unlike the brazed samples (Fig. 12), where the fine precipitates were more or less localized, the post-braze aged samples exhibited a uniform distribution of fine precipitates throughout the microstructure, which significantly contributed to the precipitation strengthening of the two Sc/Zr-containing alloys.

The precipitation behavior of $Al_3(Sc,Zr)$ and the evolution of such precipitates during homogenization, extrusion, brazing, and post-braze aging are complex, resulting in different precipitate sizes and morphology, and therefore different contributions for precipitation strengthening and grain stability. Røyset et al. [24] reported that relatively coarse $Al_3(Sc,Zr)$ precipitates formed during high-temperature processing, typically in the size range of 20-100 nm, contribute primarily to grain and subgrain stability, whereas fine $Al_3(Sc,Zr)$ precipitates formed during aging treatments, typically ranging from 2-6 nm, are mainly responsible for precipitation strengthening. The above results in the present work are consistent with their conclusion. The coarse $Al_3(Sc,Zr)$ precipitates formed prior to high-temperature brazing (during homogenization and extrusion) were mainly responsible for the enhanced resistance to recrystallization and grain growth during high-temperature brazing, whereas the fine $Al_3(Sc,Zr)$ precipitates formed during post-braze aging mostly contributed to the precipitation strengthening. Nevertheless, both populations of $Al_3(Sc,Zr)$ precipitates contributed together to the significant increase in tensile strength (Fig. 11).

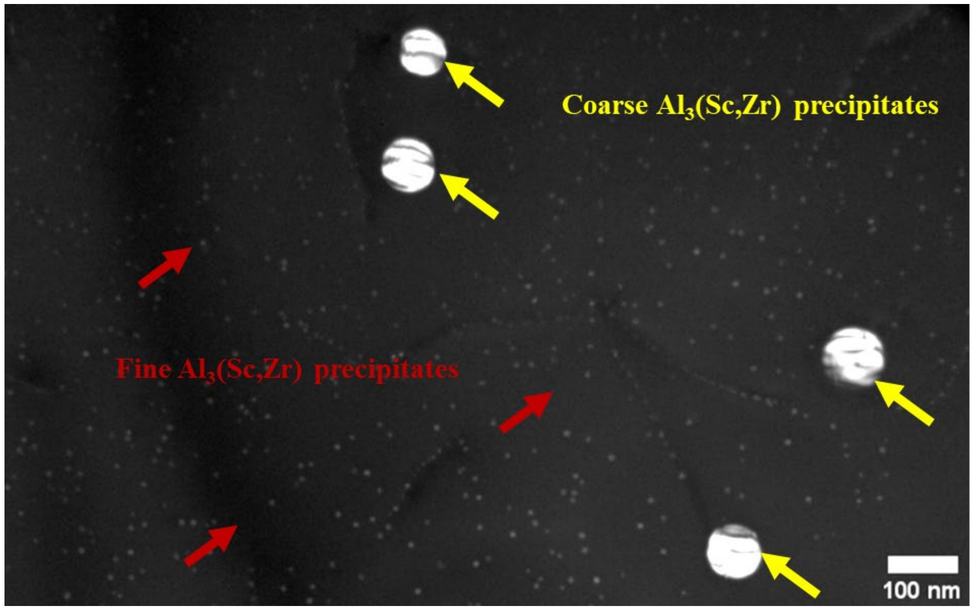

Figure 4-13 Dark field TEM micrograph of the Ex-H-ScZr sample after post-braze aging.

For comparison with the mechanical properties of other aluminum alloys for brazed heat exchanger applications, data from the literature were collected and analyzed, as summarized in Figure 4-14. The comparison shows that the two post-braze aged Sc/Zr-containing alloys achieved significantly higher YS than the other alloy systems while retaining reasonable elongation. For instance, Cao et al. [20] studied a brazed Al-Mn-Fe-Si (3xxx) alloy modified with 0.5 wt.% Cu and treated at 600 °C for 5 minutes. They found that the Cu-containing alloy achieved a YS of 60 MPa and a UTS of 156 MPa, representing 13 % and 25 % improvements over the Cu-free alloy (53.3 MPa and 124.6 MPa), respectively. In another study [75] on brazed automotive heat exchangers specifically examining Al-Mn fin stock materials with Zr added to enhance thermal stability, it was found that after a simulated braze at 600 °C for 3 min, the Zr-modified alloy achieved a YS of 51 MPa and a UTS of 128 MPa after brazing. Zhang et al. [76] studied a rolled Al-Mn-Si-Zn alloy with a microaddition of Zr. After a heat treatment of 5 min at 600 °C to simulate brazing, the results showed that the Zr-containing alloy exhibited a YS of 51.9 MPa and a UTS of 142.1 MPa. By contrast, the low Sc-containing alloy (0.1 wt.% Sc, Ex-L-ScZr) in this study achieved a significantly higher YS of 108 MPa with a UTS of 163 MPa. These comparisons clearly demonstrate that microalloying with Sc and Zr provides a much higher post-braze strengthening potential than conventionally alloying with Cu or Zr.

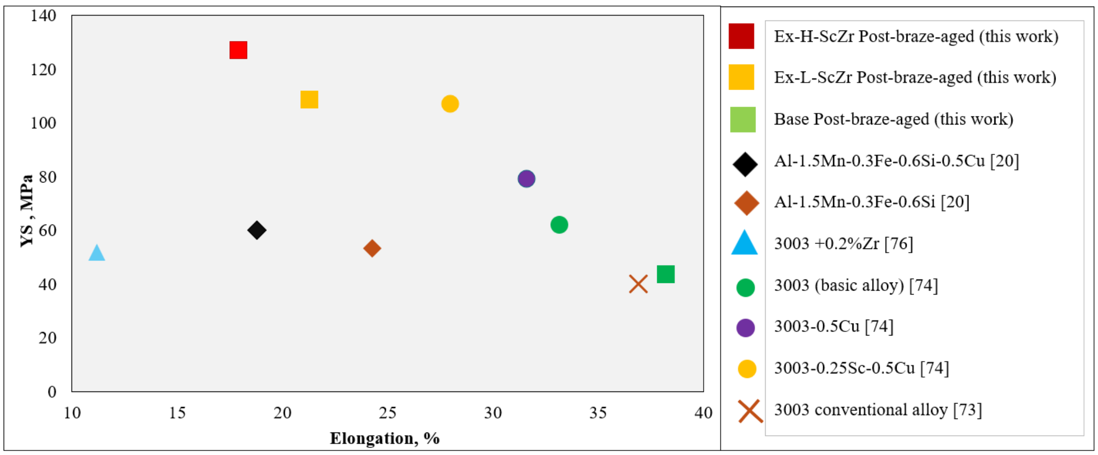

Figure 4-14 Comparison of the yield strength and elongation values of the investigated alloys in the post-braze aged condition with literature data for other brazed aluminum alloys used in heat exchanger applications.

4.3.3 Fabrication of multi-port extruded tubes

After completing the laboratory studies and strip extrusions, the investigation was scaled up for extruding MPE tubes to evaluate industrial relevance. Figure 4-15 presents the electro-etched OM microstructures in the cross-sections of the micro-port tubes for three alloys in both as-extruded and brazed conditions.

In the as-extruded condition, the base alloy exhibited a fine, equiaxed, recrystallized grain structure (Figure 4-15a), while the Ex-L-ScZr alloy displayed similar recrystallized grains (Figure 4-15c), which were slightly coarser than those of the base alloy. This behavior can be explained by differences in the Mn-rich dispersoid population between the two alloys, as discussed in Section 3.1.2. As a result, grain boundary migration is less effectively restricted, leading to a slightly coarser equiaxed grain structure compared to the base alloy. In contrast, the Ex-H-ScZr alloy exhibited partially deformed/elongated grains (Figure 4-15e). This behavior is associated with a restriction of dynamic recrystallization during extrusion owing to the presence of a larger number of fine $Al_3(Sc,Zr)$ precipitates (Figure 4-10c). The nature of the grain morphology and structure in the longitudinal sections of the MPE tubes were also examined as shown in Figure 4-16. After extrusion, both the base and Ex-L-ScZr alloys (Figures 4-16a and 4-16c) exhibited an equiaxed, recrystallized grain structure, whereas the Ex-H-ScZr alloy showed partially deformed/elongated grains (Figure 4-16e).

It is worth mentioning that the extrusion condition has a significant effect on the extruded grain structures. For instance, Rometsch & Fourmann [71] reported that for the extrusion of 41.7 mm x 3 mm flat strip from billets with similar chemical compositions as of the base, Ex-L-ScZr and Ex-H-ScZr alloys, the base alloy showed a recrystallized grain structure, while the Ex-L-ScZr and the Ex-H-ScZr alloys exhibited a fibrous and non-recrystallized grain structure. Under their processing conditions, the extrusion ratio was 70 and exit speed was 51 m/min, which are significantly lower than those used in the present work for extruding the micro-port profiles. The higher extrusion ratio in the present work resulted in significantly higher extrusion pressures, which increased the driving force for recrystallization.

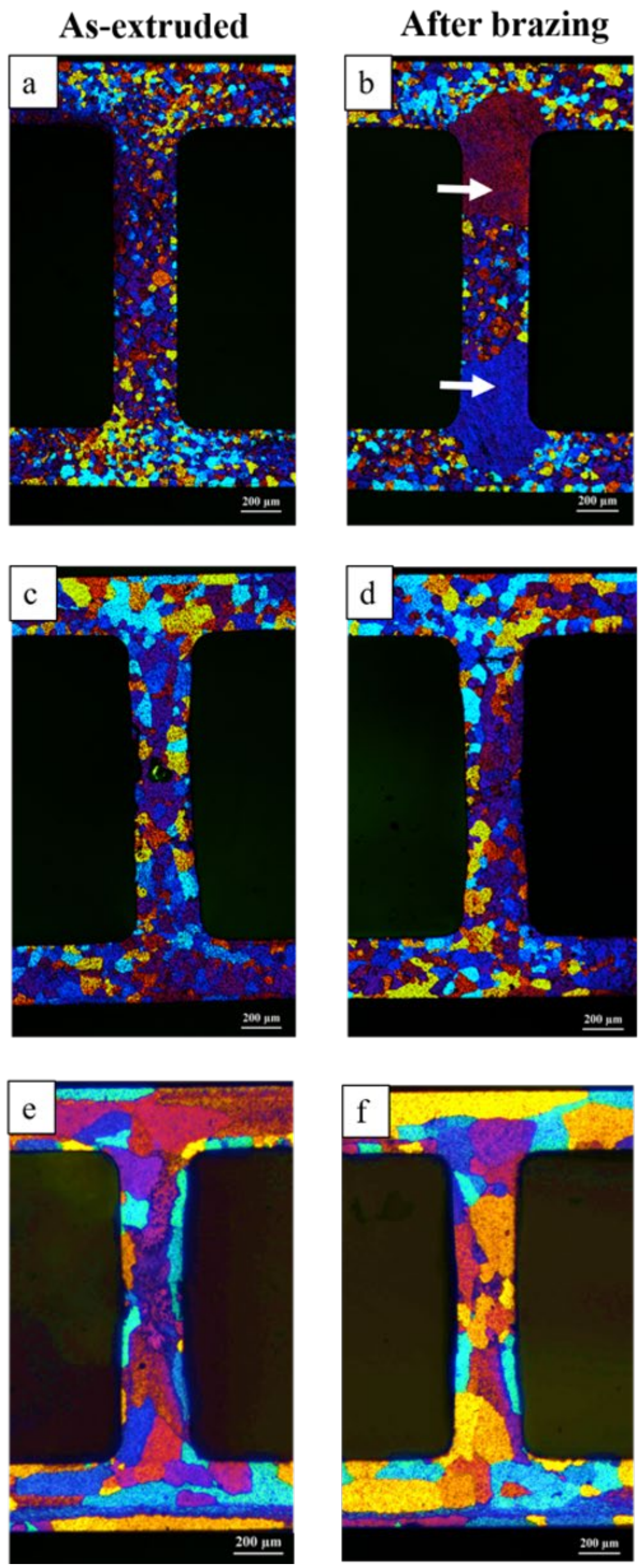

Figure 4-14 Electro-etched OM microstructures, (a, b) Base alloy (c, d) Ex-L-ScZr alloy and (e, f) Ex-H-ScZr alloy; (a, c, e) as-extruded and (b, d, f) as-brazed conditions.

After brazing, large abnormal grains (white arrows) were observed in the base alloy (Figure 4-15b), reflecting pronounced grain growth and a loss of microstructural stability. Abnormal grain growth (AGG) is stimulated by the residual strain generated during the roll leveling and sizing thickness reduction [11,77]. It was also observed that the AGG is localized at the intersections of the internal web and outer wall, as the highest residual strain is concentrated in those regions [77]. In contrast, the Ex-L-ScZr alloy maintained its equiaxed, recrystallized grain structure without grain coarsening and any signs of AGG (Figure 4-15d). The Ex-H-ScZr alloy mostly retained its as-extruded grain structure (Figure 4-15f), indicating a high degree of grain stability during brazing. The large number of fine $Al_3(Sc,Zr)$ precipitates in the Ex-H-ScZr alloy pinned the grain boundaries in the transverse direction of the grains, making it difficult for recrystallization to progress normal to the extrusion direction and thereby preserving the elongated grain morphology [78].

The longitudinal sections of the MPE tubes following the brazing are shown in Figure 4-16. The base alloy showed a huge abnormal grain near the intersection of the web and wall (white arrow in Figure 4-16b). In contrast, the Ex-L-ScZr alloy (Figure 4-16d) exhibited a recrystallized grain structure without severe grain growth. The Ex-H-ScZr alloy (Figure 4-16f), on the other hand, mostly retained its partially deformed/elongated grains. These results confirm the grain structure changes induced by the Sc/Zr micro-additions as shown in the cross-sections of the tube (Figure 4-15).

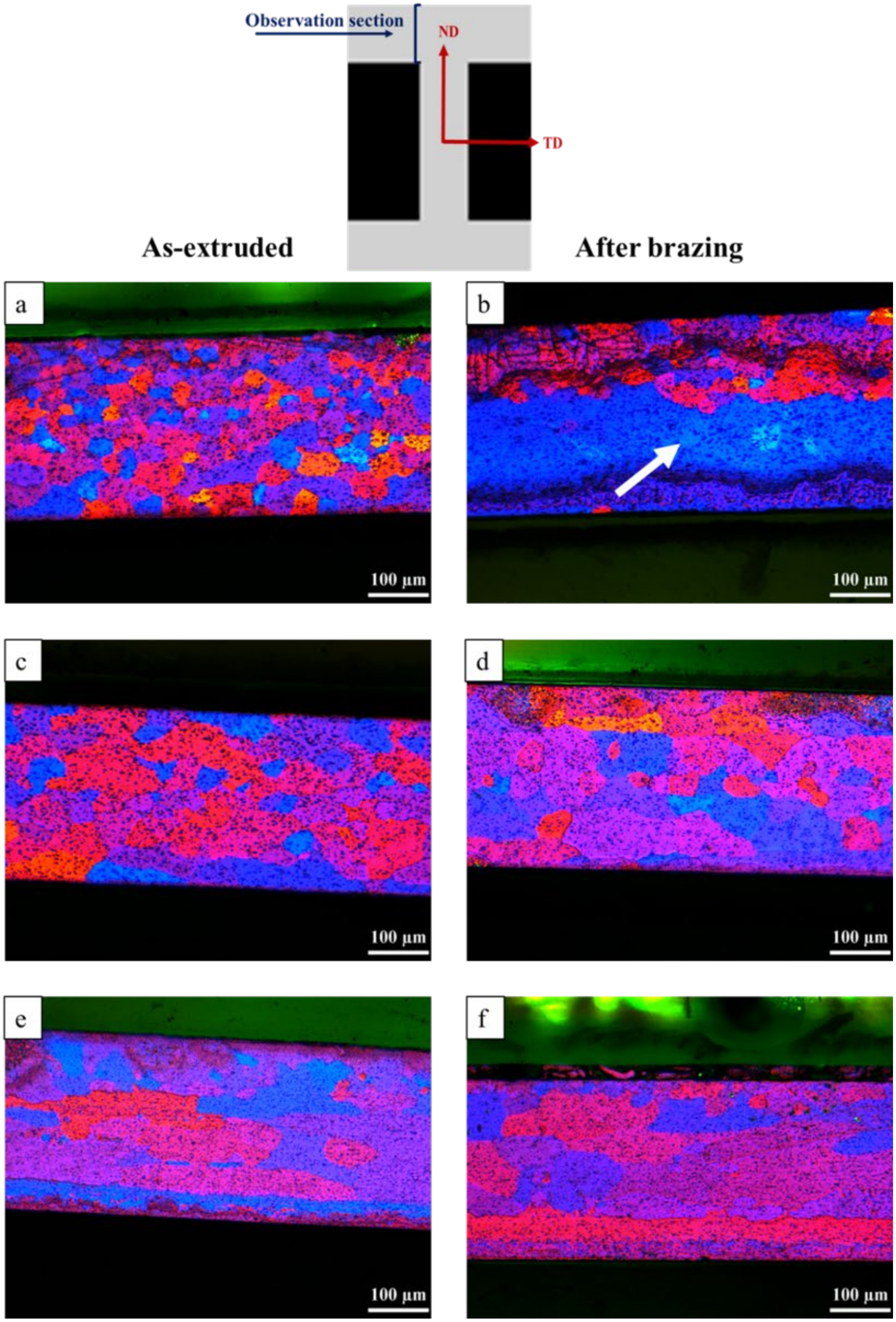

Figure 4-15 Electro-etched OM microstructures of the longitudinal section of MPE tubes taken near the intersection between the outer wall and the internal web, (a, b) Base alloy (c, d) Ex-L-ScZr alloy and Ex-H-ScZr alloy (e, f) ; (a, c, e) as-extruded and (b, d, f) as-brazed conditions.

These findings are consistent with the earlier observations from the lab-scale experiments, where the base alloy was shown to be more susceptible to the AGG, while the Sc/Zr-containing alloys exhibited higher grain stability and better resistance to such microstructural degradation during high-temperature brazing. Given the strong cost sensitivity associated with the high Sc price, the low Sc-containing alloy (0.1 wt.% Sc in Ex-L-ScZr) offers a cost-effective balance between mechanical performance and processability. If the heat exchanger tubes require higher strength, a higher Sc-containing alloy (e.g. 0.2 wt.% Sc in Ex-H-ScZr) can be a favorable option. However, while a 15-20% higher YS is achievable with an increased Sc content of 0.2%, this comes with a significant increase in material and production costs.

4.4 Conclusions

This study systematically evaluated the effects of Sc/Zr microalloying on the microstructure, hot deformation, grain stability and mechanical properties of Al-Mn 3xxx alloys intended for brazed heat exchangers. The investigation began with laboratory-scale experiments to understand the material behavior and went further to the extrusion of flat strips to evaluate the extrudability and mechanical performance. Finally, the study was scaled up by fabricating multi-port extruded tubes used in heat exchanger applications. From the main results it was concluded that:

1) In the lab-scale work, Sc/Zr microalloying increased the deformation resistance of the investigated alloys, and the flow stress increased from 31.7 MPa in the base alloy to 37.6 MPa in the L-ScZr alloy (0.08Sc+0.09Zr) and further to 38.8 MPa in the Ex-H-ScZr (0.21Sc+0.15Zr) alloy. The presence of $Al_3(Sc,Zr)$ precipitates effectively suppressed recrystallization during hot deformation.
2) Following 2% cold working and simulated brazing in the lab-scale work, the base alloy showed abnormal grain growth (AGG). By contrast, the L-ScZr alloy

retained a mostly deformed grain structure with a small number of recrystallized grains, whereas the Ex-H-ScZr alloy still maintained its fully deformed microstructure without signs of recrystallization.

3) For the flat strip extrusion, the ram pressure increased by approximately 13.3% for the Ex-L-ScZr (0.10Sc+0.11Zr) alloy and by 17.8% for the Ex-H-ScZr alloy (0.21Sc+0.15Zr) compared to the base alloy, indicating a moderate reduction of extrudability with the additions of Sc and Zr.
4) Sc/Zr microalloying significantly improved the final mechanical performance of the extruded flat strips. Following post-braze aging, the yield strength increased by 156% in the Ex-L-ScZr alloy and by 191% in the Ex-H-ScZr alloy relative to the base alloy.
5) For the multi-port extruded (MPE) tubes, after high-temperature brazing, the base alloy exhibited grain coarsening and localized abnormal grain growth (AGG). In contrast, the Ex-L-ScZr alloy showed a recrystallized grain structure without the grain coarsening, while the Ex-H-ScZr alloy retained its partially deformed/elongated grains, indicating superior grain stability during brazing.

Overall, these findings provide guidance for balancing performance, processability, and cost in the design of alloys for brazed heat exchanger applications.

4.5 Authorship contribution

Alyaa Bakr: Writing – original draft, Methodology, Investigation, Formal analysis. **Paul Rometsch:** Writing – review & editing, Validation, Methodology, Conceptualization. **X.-Grant Chen:** Writing – review & editing, Validation, Supervision, Project administration, Methodology, Conceptualization.

References

[1]J. Lacaze, S. Tierce, M.C. Lafont, Y. Thebault, N. Pébère, G. Mankowski, C. Blanc, H. Robidou, D. Vaumousse, D. Daloz, Study of the microstructure resulting from brazed aluminium materials used in heat exchangers, Materials Science and Engineering A 413–414 (2005) 317–321. https://doi.org/10.1016/j.msea.2005.08.187.

[2]J.M. Lee, S.W. Lee, Y.K. Kim, W.H. Jo, C.J. Lee, B.M. Kim, Extrusion of AA 3003 micro condenser tube with multi-hole and thin wall section using porthole die, International Journal of Precision Engineering and Manufacturing - Green Technology 3 (2016) 239–245. https://doi.org/10.1007/s40684-016-0031-5.

[3]Y. Ji, Y. Guo, Y. Xia, D.-H. Xia, Z. Qin, D. Zhou, Z. Gao, W. Hu, Effect of bending deformation on the corrosion behavior of non-brazed and brazed Al composite, Electrochim. Acta 481 (2024) 143928. https://doi.org/https://doi.org/10.1016/j.electacta.2024.143928.

[4]S. Tierce, N. Pébère, C. Blanc, C. Casenave, G. Mankowski, H. Robidou, Corrosion behaviour of brazed multilayer material AA4343/AA3003/AA4343: Influence of coolant parameters, Corros. Sci. 49 (2007) 4581–4593. https://doi.org/https://doi.org/10.1016/j.corsci.2007.04.013.

[5]G.G.B. Zaffaroni, O. V Mishin, U.M. Ciucani, C. Gundlach, J.H. Nordlien, R. Ambat, Characterization of high frequency welded aluminium microfin tube for heat exchangers, Mater. Charact. 173 (2021) 110939. https://doi.org/https://doi.org/10.1016/j.matchar.2021.110939.

[6]W. Fang, D. Tang, H. Wang, D. Li, Y. Peng, Optimization of die design for thin-walled flat multi-port tube with the aid of finite element simulation, J. Mater. Process. Technol. 277 (2020) 116418. https://doi.org/10.1016/j.jmatprotec.2019.116418.

[7]L. Zhao, Z. Qian, X. Wang, Q. Wang, C. Li, Z. Zhang, Analysis of the thermal improvement of plate fin-tube heat exchanger with straight and curved rectangular winglet vortex generators, Case Studies in Thermal Engineering 51 (2023) 103612. https://doi.org/https://doi.org/10.1016/j.csite.2023.103612.

[8]H. Kalantari, S.A. Ghoreishi-Madiseh, J.C. Kurnia, A.P. Sasmito, An analytical correlation for conjugate heat transfer in fin and tube heat exchangers, International Journal of Thermal Sciences 164 (2021) 106915. https://doi.org/https://doi.org/10.1016/j.ijthermalsci.2021.106915.

[9]D. Tang, Q. Zhang, D. Li, Y. Peng, A physical simulation of longitudinal seam welding in micro channel tube extrusion, J. Mater. Process. Technol. 214 (2014) 2777–2783. https://doi.org/https://doi.org/10.1016/j.jmatprotec.2014.06.004.

[10]K. Li, D. Li, T. Zou, D. Shu, D. Tang, Y. Peng, Strength Variation in Processing Multiport Extrusion Tubes of A1100 and A3102 Alloys, J. Mater. Eng. Perform. 28 (2019) 3576–3589. https://doi.org/10.1007/s11665-019-04132-w.

[11]G. Vamadevan, F.F. Kraft, Processing effects in aluminum micro-channel tube for brazed R744 heat exchangers, J. Mater. Process. Technol. 191 (2007) 30–33. https://doi.org/10.1016/j.jmatprotec.2007.03.040.

[12]W.S. Miller, L. Zhuang, J. Bottema, A.J. Wittebrood, P. De Smet, A. Haszler, A. Vieregge, Recent development in aluminium alloys for the automotive industry, Materials Science and Engineering A 280 (2000) 37–49. https://doi.org/10.1016/S0921-5093(99)00653-X.

[13]J.C. Guía-Tello, M.I. Pech-Canul, E. Trujillo-Vázquez, M.A. Pech-Canul, Effect of brazing parameters on fillet size and microstructure of cladded fin-microchannel tube joints, Transactions of Nonferrous Metals Society of China (English Edition) 30 (2020) 3240–3253. https://doi.org/10.1016/S1003-6326(20)65457-7.

[14]J.S. Moema, C.W. Siyasiya, V.K. Morudu, T. Buthelezi, The Effect of Soaking Time on Mechanical Properties of Roll-Bonded AA3003 and AA4045 Used for Heat Exchangers, Metals (Basel). 13 (2023). https://doi.org/10.3390/met13101636.

[15]K. Li, T. Zou, D. Li, Y. Peng, D. Shu, On Formation of Abnormally Large Grains in Annealing Prestrained Aluminum Alloy Multiport Extrusion Tubes, Metallurgical and Materials Transactions A 50 (2019) 5734–5749. https://doi.org/10.1007/s11661-019-05453-0.

[16]P. Thirathipviwat, T. Kotake, T. Suzuki, M. Hasegawa, K. Matsumoto, S. Sato, Effect of fine dispersoids on dislocation density and dislocation rearrangement of Al-Mn alloy during tensile deformation, Materials Science and Engineering: A 927 (2025) 147997. https://doi.org/https://doi.org/10.1016/j.msea.2025.147997.

[17]K. Liu, X.-G. Chen, Development of Al–Mn–Mg 3004 alloy for applications at elevated temperature via dispersoid strengthening, Mater. Des. 84 (2015) 340–350. https://doi.org/https://doi.org/10.1016/j.matdes.2015.06.140.

[18]K. Liu, X.-G. Chen, Evolution of Intermetallics, Dispersoids, and Elevated Temperature Properties at Various Fe Contents in Al-Mn-Mg 3004 Alloys, Metallurgical and Materials Transactions B 47 (2016) 3291–3300. https://doi.org/10.1007/s11663-015-0564-y.

[19]K. Liu, H. Ma, X.-G. Chen, Enhanced elevated-temperature properties via Mo addition in Al-Mn-Mg 3004 alloy, J. Alloys Compd. 694 (2017) 354–365. https://doi.org/https://doi.org/10.1016/j.jallcom.2016.10.005.

[20]C. Cao, D. Chen, X. Fang, J. Ren, J. Shen, L. Meng, J. Liu, L. Qiu, Y. Fang, Effects of Cu addition on the microstructure and properties of the Al–Mn–Fe–Si alloy, J. Alloys Compd. 834 (2020) 155175. https://doi.org/https://doi.org/10.1016/j.jallcom.2020.155175.

[21]Y. Wang, Y. Li, T. Zhang, H. Wang, H. Zou, B. Gao, H. Tang, Effects of scandium on the microstructure and mechanical properties of 2524 aluminum alloy, J. Alloys Compd. 1014 (2025) 178733. https://doi.org/https://doi.org/10.1016/j.jallcom.2025.178733.

[22]Y. Deng, Z. Yin, K. Zhao, J. Duan, Z. He, Effects of Sc and Zr microalloying additions on the microstructure and mechanical properties of new Al–Zn–Mg alloys, J. Alloys Compd. 530 (2012) 71–80. https://doi.org/https://doi.org/10.1016/j.jallcom.2012.03.108.

[23]A.Y. Algendy, K. Liu, P. Rometsch, N. Parson, X.G. Chen, Evolution of discontinuous/continuous Al3(Sc,Zr) precipitation in Al-Mg-Mn 5083 alloy during thermomechanical process and its impact on tensile properties, Mater. Charact. 192 (2022). https://doi.org/10.1016/j.matchar.2022.112241.

[24]J. Røyset, N. Ryum, Kinetics and mechanisms of precipitation in an Al–0.2wt.% Sc alloy, Materials Science and Engineering: A 396 (2005) 409–422. https://doi.org/https://doi.org/10.1016/j.msea.2005.02.015.

[25]J. Røyset, N. Ryum, Scandium in aluminium alloys, International Materials Reviews 50 (2005) 19–44. https://doi.org/https://doi.org/10.1179/174328005X14311.

[26]Yu. Buranova, V. Kulitskiy, M. Peterlechner, A. Mogucheva, R. Kaibyshev, S. V Divinski, G. Wilde, Al3(Sc,Zr)-based precipitates in Al–Mg alloy: Effect of severe deformation, Acta Mater. 124 (2017) 210–224. https://doi.org/https://doi.org/10.1016/j.actamat.2016.10.064.

[27]K.E. Knipling, R.A. Karnesky, C.P. Lee, D.C. Dunand, D.N. Seidman, Precipitation evolution in Al-0.1Sc, Al-0.1Zr and Al-0.1Sc-0.1Zr (at.%) alloys during isochronal aging, Acta Mater. 58 (2010) 5184–5195. https://doi.org/10.1016/j.actamat.2010.05.054.

[28]K.E. Knipling, D.N. Seidman, D.C. Dunand, Ambient- and high-temperature mechanical properties of isochronally aged Al–0.06Sc, Al–0.06Zr and Al–0.06Sc–0.06Zr (at.%) alloys, Acta Mater. 59 (2011) 943–954. https://doi.org/https://doi.org/10.1016/j.actamat.2010.10.017.

[29]T. Dorin, M. Ramajayam, A. Vahid, T. Langan, Aluminium Scandium Alloys, in: Fundamentals of Aluminium Metallurgy, 2018: pp. 439–494. https://doi.org/10.1016/B978-0-08-102063-0.00012-6.

[30]Z.H. Jia, J. Royset, J.K. Solberg, Q. Liu, Formation of precipitates and recrystallization resistance in Al-Sc-Zr alloys, Transactions of Nonferrous Metals Society of China (English Edition) 22 (2012) 1866–1871. https://doi.org/10.1016/S1003-6326(11)61399-X.

[31]A. De Luca, D.C. Dunand, D.N. Seidman, Microstructure and mechanical properties of a precipitation-strengthened Al-Zr-Sc-Er-Si alloy with a very small Sc content, Acta Mater. 144 (2018) 80–91. https://doi.org/https://doi.org/10.1016/j.actamat.2017.10.040.

[32]Y. Harada, D.C. Dunand, Microstructure of Al3Sc with ternary transition-metal additions, Materials Science and Engineering: A 329–331 (2002) 686–695. https://doi.org/https://doi.org/10.1016/S0921-5093(01)01608-2.

[33]C. Zhang, Y. Jiang, F. Cao, T. Hu, Y. Wang, D. Yin, Formation of coherent, core-shelled nano-particles in dilute Al-Sc-Zr alloys from the first-principles, J. Mater. Sci. Technol. 35 (2019) 930–938. https://doi.org/https://doi.org/10.1016/j.jmst.2018.11.004.

[34]Y. Huang, L. Xia, H. Yang, C. Wang, Y. Wu, X. Liu, Effect of Trace Sc Addition on Microstructure and Mechanical Properties of Al-Zn-Mg-Cu-Zr Alloy, Materials 18 (2025). https://doi.org/10.3390/ma18030648.

[35]Q. Sun, H. Wang, S. Yu, H. Ma, J. Zheng, Z. Hu, Effect of Sc on the recrystallization behavior and mechanical properties of Al-Zn-Mg-Cu-Zr alloys under isothermal multidirectional compression, Mater. Today Commun. 39 (2024) 108986. https://doi.org/https://doi.org/10.1016/j.mtcomm.2024.108986.

[36]Y. Zhang, L. Ding, Z. Zhang, J. Zhi, Y. Ning, Y. Weng, Z. Jia, L. Zhuang, Synergistic effects of annealing and deformation temperatures on mechanical properties of Al-Mg-Sc-Zr alloy, Materials Science and Engineering: A 971 (2026) 150472. https://doi.org/https://doi.org/10.1016/j.msea.2026.150472.

[37]Y. Cui, T. Gong, Z. Du, W. Guo, W. Wang, Effects of Trace Sc and Zr Additions on Recrystallization Behavior and Mechanical Properties of Cold-Rolled 1235 Aluminum Alloy, J. Mater. Eng. Perform. (2026). https://doi.org/10.1007/s11665-026-14003-w.

[38]X. Sun, S. Zhang, H. Wang, D. Yin, M.-C. Zhao, Microstructure and precipitation evolution of a (Sc, Zr, Er, Ti) multi-microalloyed Al–Li–Mg alloy from solution treatment to peak aging, Journal of Materials Research and Technology 40 (2026) 415–426. https://doi.org/https://doi.org/10.1016/j.jmrt.2025.12.136.

[39]V. Ocenasek, M. Slamova, Resistance to recrystallization due to Sc and Zr addition to Al–Mg alloys, Mater. Charact. 47 (2001) 157–162. https://doi.org/https://doi.org/10.1016/S1044-5803(01)00165-6.

[40]S. Babaniaris, M. Ramajayam, L. Jiang, R. Varma, T. Langan, T. Dorin, Effect of Al3(Sc,Zr) dispersoids on the hot deformation behaviour of 6xxx-series alloys: A physically

based constitutive model, Materials Science and Engineering: A 793 (2020) 139873. https://doi.org/https://doi.org/10.1016/j.msea.2020.139873.

[41]A.Y. Algendy, P. Rometsch, X.G. Chen, Mechanical and corrosion performances of Al–Mg-Mn 5083 rolled alloys microalloyed with Sc and Zr in different thermomechanical processing conditions, J. Mater. Sci. 59 (2024) 14692–14715. https://doi.org/10.1007/s10853-024-10044-5.

[42]X. Lai, M. Wu, D. Xiao, L. Huang, W. Liu, P. Zhao, Microstructures and mechanical properties of a novel Al-5Mg-3Zn alloy with the combined additions Sc and Zr, Mater. Today Commun. 41 (2024) 110669. https://doi.org/https://doi.org/10.1016/j.mtcomm.2024.110669.

[43]B. Li, Q. Pan, X. Huang, Z. Yin, Microstructures and properties of Al–Zn–Mg–Mn alloy with trace amounts of Sc and Zr, Materials Science and Engineering: A 616 (2014) 219–228. https://doi.org/https://doi.org/10.1016/j.msea.2014.08.024.

[44]J. Ye, Q. Pan, B. Liu, Q. Hu, L. Qu, W. Wang, X. Wang, Effects of co-addition of minor Sc and Zr on aging precipitates and mechanical properties of Al–Zn–Mg–Cu alloys, Journal of Materials Research and Technology 22 (2023) 2944–2954. https://doi.org/https://doi.org/10.1016/j.jmrt.2022.12.133.

[45]Z. Lu, X. Wu, J. Xu, H. Zhang, L. Yu, L. Zhao, Y. Jiang, Improving mechanical properties of spray formed 7055 aluminium alloy metal-inert gas welds by scandium addition, J. Alloys Compd. 1013 (2025) 178406. https://doi.org/https://doi.org/10.1016/j.jallcom.2024.178406.

[46]Q. XIAO, J. HUANG, Y. JIANG, F. JIANG, Y. WU, G. XU, Effects of minor Sc and Zr additions on mechanical properties and microstructure evolution of Al−Zn−Mg−Cu alloys, Transactions of Nonferrous Metals Society of China 30 (2020) 1429–1438. https://doi.org/https://doi.org/10.1016/S1003-6326(20)65308-0.

[47]X. Na, L. Wenqing, Z. Liu, T. Muthuramalingam, Effect of Scandium in Al–Sc and Al–Sc–Zr Alloys Under Precipitation Strengthening Mechanism at 350 °C Aging, Metals and Materials International 27 (2021) 5145–5153. https://doi.org/10.1007/s12540-020-00844-0.

[48]Y. Su, L. Ding, Y. Zhang, Y. Weng, C. Wang, Z. Jia, L. Zhuang, The dispersoid evolution, recrystallization and mechanical properties of an Al–Mg–Sc alloy under various homogenization and annealing processes, J. Mater. Sci. 60 (2025) 3558–3575. https://doi.org/10.1007/s10853-025-10673-4.

[49]A.Y. Algendy, P. Rometsch, X.-G. Chen, Tailoring microstructure and mechanical properties of an AA5454 extruded aluminum alloy with Sc/Zr microalloying and processing conditions, Materials Science and Engineering: A 948 (2025) 149318. https://doi.org/https://doi.org/10.1016/j.msea.2025.149318.

[50]The Aluminum Association, Standard Test Procedure for Aluminum Alloy Grain Refiners, 2012.

[51]O. Engler, T. Brüggemann, J. Hasenclever, Evolution of micro-chemistry during solidification and homogenisation of AA 3xxx aluminium–manganese alloys, Materials Science and Technology (United Kingdom) 37 (2021) 893–908. https://doi.org/10.1080/02670836.2021.1963540.

[52]S. Lathabai, P.G. Lloyd, The effect of scandium on the microstructure, mechanical properties and weldability of a cast Al–Mg alloy, Acta Mater. 50 (2002) 4275–4292. https://doi.org/https://doi.org/10.1016/S1359-6454(02)00259-8.

[53]C. Xu, W. Xiao, S. Hanada, H. Yamagata, C. Ma, The effect of scandium addition on microstructure and mechanical properties of Al–Si–Mg alloy: A multi-refinement modifier, Mater. Charact. 110 (2015) 160–169. https://doi.org/https://doi.org/10.1016/j.matchar.2015.10.030.

[54]V.G. Davydov, T.D. Rostova, V. V. Zakharov, Y.A. Filatov, V.I. Yelagin, Scientific principles of making an alloying addition of scandium to aluminium alloys, Materials Science and Engineering A 280 (2000) 30–36. https://doi.org/10.1016/S0921-5093(99)00652-8.

[55]Z. Yuan, Y. Tu, T. Yuan, Y. Huang, Y. Zhang, Effect of the interaction between Fe and Si on the precipitation behavior of dispersoids in Al–Mn alloys during homogenization, Vacuum 184 (2021) 109915. https://doi.org/https://doi.org/10.1016/j.vacuum.2020.109915.

[56]Y.J. Li, L. Arnberg, Quantitative study on the precipitation behavior of dispersoids in DC-cast AA3003 alloy during heating and homogenization, Acta Mater. 51 (2003) 3415–3428. https://doi.org/https://doi.org/10.1016/S1359-6454(03)00160-5.

[57]A.Y. Algendy, K. Liu, P. Rometsch, N. Parson, X.-G. Chen, Effects of AlMn dispersoids and Al3(Sc,Zr) precipitates on the microstructure and ambient/elevated-temperature mechanical properties of hot-rolled AA5083 alloys, Materials Science and Engineering: A 855 (2022) 143950. https://doi.org/https://doi.org/10.1016/j.msea.2022.143950.

[58]Z. Li, Z. Zhang, X.-G. Chen, Improvement in the mechanical properties and creep resistance of Al-Mn-Mg 3004 alloy with Sc and Zr addition, Materials Science and Engineering: A 729 (2018) 196–207. https://doi.org/https://doi.org/10.1016/j.msea.2018.05.055.

[59]L.L. Rokhlin, N.R. Bochvar, I.E. Tarytina, N.P. Leonova, Phase composition and recrystallization of Al-based Al-Sc-Mn-Zr alloys, Russian Metallurgy (Metally) 2010 (2010) 241–247. https://doi.org/10.1134/S0036029510030158.

[60]S. Pan, F. Qian, C. Li, Z. Wang, Y. Li, Synergistic strengthening by nano-sized α-Al(Mn,Fe)Si and Al3Zr dispersoids in a heat-resistant Al–Mn–Fe–Si–Zr alloy, Materials Science and Engineering A 819 (2021). https://doi.org/10.1016/j.msea.2021.141460.

[61]Q. Dong, A. Howells, D.J. Lloyd, M. Gallerneault, V. Fallah, Effect of solidification cooling rate on kinetics of continuous/discontinuous Al3(Sc,Zr) precipitation and the subsequent age-hardening response in cold-rolled AlMgSc(Zr) sheets, Materials Science and Engineering: A 772 (2020) 138693. https://doi.org/https://doi.org/10.1016/j.msea.2019.138693.

[62]H.J. McQueen, S. Spigarelli, M.E. Kassner, E. Evangelista, Hot deformation and processing of aluminum alloys, CRC press, 2016. https://doi.org/https://doi.org/10.1201/b11227.

[63]W. Liu, H. Zhao, D. Li, Z. Zhang, G. Huang, Q. Liu, Hot deformation behavior of AA7085 aluminum alloy during isothermal compression at elevated temperature, Materials Science and Engineering: A 596 (2014) 176–182. https://doi.org/https://doi.org/10.1016/j.msea.2013.12.012.

[64]C. Shi, J. Lai, X.-G. Chen, Microstructural Evolution and Dynamic Softening Mechanisms of Al-Zn-Mg-Cu Alloy during Hot Compressive Deformation, Materials 7 (2014) 244–264. https://doi.org/10.3390/ma7010244.

[65]W. Qian, X. Kai, R. Tao, R. Cao, G. Chen, Y. Zhao, Microstructure evolution and high-temperature performances of AA6111 alloy strengthened by Sc, Zr co-microalloying, Materials

Science and Engineering: A 887 (2023) 145788. https://doi.org/https://doi.org/10.1016/j.msea.2023.145788.

[66]Z. Yin, Q. Pan, Y. Zhang, F. Jiang, Effect of minor Sc and Zr on the microstructure and mechanical properties of Al-Mg based alloys, Materials Science and Engineering A 280 (2000) 151–155. https://doi.org/10.1016/S0921-5093(99)00682-6.

[67]F.F. Kraft, Method for Predicting and Optimizing the Strength of Extruded Multi-Void Aluminum Heat Exchanger Tube, SAE Transactions 111 (2002) 99–106. http://www.jstor.org/stable/44719187.

[68]C.N. Niu, X.G. Song, S.P. Hu, G.Z. Lu, Z.B. Chen, G.D. Wang, Effects of brazing temperature and post weld heat treatment on 7075 alloy brazed joints, J. Mater. Process. Technol. 266 (2019) 363–372. https://doi.org/https://doi.org/10.1016/j.jmatprotec.2018.11.023.

[69]T. Dorin, M. Ramajayam, T.J. Langan, Impact of Scandium and Zirconium on extrudability, microstructure and hardness of a binary Al-Cu alloy, Mater. Today Proc. 10 (2019) 242–247. https://doi.org/10.1016/j.matpr.2018.10.402.

[70]J. Royset, Scandium in Aluminium alloys overview: Physical Metallurgy, Properties and applications, Metallurgical Science AndTechnology 25 (2007) 11–21.

[71]P. Rometsch, J. Fourmann, Potential for Using Scandium in Extrusion Alloys, in: Thirteenth International Aluminum Extrusion Technology Seminar & Exposition, Wauconda, IL, USA, 2024.

[72]G.M. Novotny, A.J. Ardell, Precipitation of Al3Sc in binary Al–Sc alloys, Materials Science and Engineering: A 318 (2001) 144–154. https://doi.org/https://doi.org/10.1016/S0921-5093(01)01326-0.

[73]Q. Cao, N. Zhao, C. Xia, Z. Zhang, L. Cheng, D. Zhou, Effect of brazing and artificial aging on the microstructure and mechanical properties of a high-strength four-layer laminar aluminum alloy, Vacuum 239 (2025) 114388. https://doi.org/https://doi.org/10.1016/j.vacuum.2025.114388.

[74]L. Long, Q. Pan, M. Li, J. Ye, Y. Sun, W. Wang, Y. Luo, X. Li, Z. Peng, S. Liu, Study on microstructure and mechanical properties of 3003 alloys with scandium and copper addition, Vacuum 173 (2020) 109112. https://doi.org/https://doi.org/10.1016/j.vacuum.2019.109112.

[75]D. Shimosaka, M. Ueno, Effects of Si and Zr addition on strength and recrystallization behavior of Al-Mn alloy fin stocks for automotive heat exchanger, MATEC Web of Conferences 326 (2020) 5006. https://doi.org/10.1051/matecconf/202032605006.

[76]J. Zhang, D. Ding, W. Zhang, S. Kang, X. Xu, Y. Gao, G. Chen, W. Chen, X. You, Effect of Zr addition on microstructure and properties of Al–Mn–Si–Zn-based alloy, Transactions of Nonferrous Metals Society of China 24 (2014) 3872–3878. https://doi.org/https://doi.org/10.1016/S1003-6326(14)63545-7.

[77]D. Tang, X. Fan, W. Fang, D. Li, Y. Peng, H. Wang, Microstructure and mechanical properties development of micro channel tubes in extrusion, rolling and brazing, Mater. Charact. 142 (2018) 449–457. https://doi.org/https://doi.org/10.1016/j.matchar.2018.06.010.

[78]F.J. Humphreys, M. Hatherly, Recrystallization and Related Annealing Phenomena, Recrystallization and Related Annealing Phenomena (2012) 1–497. https://doi.org/10.1016/C2009-0-07986-0.

Chapter 5

The potential of Sc-Zr microalloying to improve grain stability and mechanical strength in 3xxx multi-port extruded (MPE) tubes

(This manuscript is currently under internal review)

Résumé

Les alliages Al–Mn de la série 3xxx sont largement utilisés pour la fabrication de tubes extrudés multicanaux (MPE) en raison de leur bonne formabilité, de leur résistance à la corrosion et de leurs propriétés favorables au transfert thermique. Toutefois, le brasage à haute température peut provoquer une recristallisation importante et une croissance anormale des grains (AGG), susceptibles de réduire considérablement la résistance mécanique et la tenue en pression des tubes MPE. Cette étude évalue l'effet de la microalliage avec le Sc et le Zr sur un alliage 3xxx typiquement utilisé dans les échangeurs de chaleur brasés. Trois alliages ont été étudiés : un alliage 3xxx de base, un alliage à faible teneur en Sc/Zr (L-ScZr) contenant 0,11 % massique de Sc et 0,10 % massique de Zr, et un alliage à forte teneur en Sc/Zr (H-ScZr) contenant 0,21 % massique de Sc et 0,15 % massique de Zr. Tous les alliages ont été soumis à un traitement thermique à basse température à 375 °C pendant 24 h, puis extrudés sous forme de tubes MPE. Après une réduction d'épaisseur de 2 % et un brasage à 605 °C pendant 2,5 min, l'alliage de base a présenté un grossissement prononcé des grains, tandis que les deux alliages contenant du Sc et du Zr ont démontré une meilleure stabilité granulaire, l'alliage H-ScZr présentant la plus forte résistance à la recristallisation et au grossissement des grains. Un traitement de vieillissement post-brasage à 350 °C pendant 4 h a entraîné un renforcement significatif des alliages Sc-Zr, la limite d'élasticité augmentant jusqu'à environ 105 % par rapport à celle de l'alliage de base après vieillissement post-brasage. Ces résultats démontrent que la microalliage avec le Sc et le Zr améliore efficacement la stabilité granulaire et les performances mécaniques des alliages 3xxx destinés aux échangeurs de chaleur brasés.

Abstract

Al-Mn 3xxx alloys are widely used for multi-port extruded (MPE) tubes due to their good formability, corrosion resistance, and favorable heat-transfer characteristics. However, the high-temperature brazing triggers extensive recrystallization and abnormal grain growth (AGG), which can significantly reduce the strength and pressure-bearing capacity of MPE tubes. This study evaluates the effect of Sc and Zr microalloying on a typical 3xxx alloy used for brazed heat exchangers. Three alloys were investigated: a base 3xxx alloy, a low-Sc/Zr alloy (L-ScZr) containing 0.11 wt.% Sc and 0.1 wt.% Zr, and a high-Sc/Zr alloy (H-ScZr) containing 0.21 wt.% Sc and 0.15 wt.% Zr. All alloys were subjected to a low-temperature heat treatment at 375 °C for 24 h and were subsequently extruded into MPE tubes . Following a thickness reduction of 2% and brazing at 605 ºC for 2.5 min, the base alloy exhibited pronounced grain coarsening, whereas both Sc/Zr-containing alloys demonstrated improved grain stability, with the H-ScZr alloy showing the greatest resistance to recrystallization and grain coarsening. Post-brazing aging at 350 ºC for 4 h resulted in a significant strengthening response in the Sc-Zr alloys, with the yield strength increasing by up to ~105% relative to the post-aged base alloy . These results demonstrate that Sc-Zr microalloying effectively enhances grain stability and mechanical performance of 3xxx alloys for brazed heat exchanger applications.

Keywords: Al-Mn 3xxx alloys, Sc and Zr microalloying, Multi port extruded tubes, Simulated Brazing, Grain stability.

5.1 Introduction

Reducing vehicle mass is an important strategy for improving fuel efficiency and lowering CO_2 emissions and has therefore become a major focus in recent automotive development [1,2].

Aluminum alloys are extensively used in the automotive sector for various heat exchangers, including radiators, air-conditioning evaporators, exhaust-gas-recirculation coolers, and water- and air-charge coolers [3,4]. Compared with conventional heat-exchanger tubes that have large channel diameters, multi-port extruded (MPE) tubes provide notable advantages in heat-transfer efficiency and reduced weight [5]. MPE tubes are often produced from Al–Mn 3xxx alloys because they combine adequate strength and formability with low density, good thermal conductivity, and corrosion resistance. [6].

Brazing is commonly used to join the components of aluminium heat exchangers [7,8]. During brazing, the assembly is heated to approximately 600 °C, allowing the lower-melting filler or clad alloy to form joints between the components [9,10]. Brazing temperatures can trigger extensive recrystallization and abnormal grain growth (AGG), which severely alter the microstructure [11,12]. The move toward environmentally friendly CO_2 (R744) refrigerants requires heat-exchanger systems that can operate at much higher pressures and temperatures than traditional R134a units. Consequently, aluminum micro-channel tubes used in gas coolers must withstand significantly greater mechanical demands [13]. Multiple studies [11,13,14] have reported low mechanical strength and limited pressure-bearing capacity in the as-brazed condition.

Scandium is widely regarded as one of the most effective microalloying elements for improving the mechanical performance of aluminium alloys [15–17]. The benefits of Sc additions arise from Al_3Sc precipitation. These particles exhibit high thermal stability and help preserve grain and subgrain structures. [17,18]. The high cost of Sc restricts its widespread use, prompting interest in combined additions of Sc and zirconium [19–22]. When added with Sc, Zr can partially substitute for Sc in Al_3Sc, forming $Al_3(Sc,Zr)$ precipitates with greater resistance to thermal coarsening [23,24].

Numerous studies have shown that Sc/Zr-containing dispersoids retard recovery, recrystallization, and grain coarsening, ensuring enhanced microstructural stability in Al alloys at elevated temperatures. For instance, Algendy et al. [25] reported that the as-extruded AA5454 alloy showed a fully recrystallized grain structure, whereas the variant containing 0.1 wt.% Sc and 0.1 wt.% Zr retained a non-recrystallized, fibrous microstructure with elongated grains. In another study, Wang et al. [26] found that a cold-rolled Al-Mg-Mn alloy without Sc and Zr fully recrystallized during post-rolling annealing for 1h at 350 ºC and showed strong grain coarsening at 500 ºC. By contrast, adding 0.25 wt.% Sc and 0.10 wt.% Zr greatly improved grain stability, as the alloy retained a fibrous deformed structure even after post-rolling annealing at 550 ºC. Ye et al. [27] demonstrated that for an Al-Zn-Mg-Cu alloy, a solid solution treatment at 470 ºC for 1 hour led to almost complete recrystallization in the base alloy, whereas adding 0.12 wt.% Sc and 0.11 wt.% Zr reduced the recrystallized fraction to only 12.6%. Qiu et al.[28] reported that, for the annealing of as-rolled 5182 sheets at 400 °C for 2 h, the base alloy exhibited a recrystallized fraction of 99.0%, whereas the alloy containing 0.1 wt.% Sc and 0.1 wt.% Zr remained largely un-recrystallized, with a low recrystallized fraction of 10.4%. Dorin et al. [29] observed that after a 1 h solution treatment at 500 ºC, an Al-Cu alloy was fully recrystallized, whereas the alloy containing 0.1 wt.% Sc and 0.14 wt.% Zr remained completely un-recrystallized.

Although previous studies demonstrated that Sc and Zr additions can effectively suppress recrystallization in aluminum alloys, their combined effect in the 3xxx alloys used in heat-exchanger applications under brazing-type thermal conditions remains insufficiently explored. Motivated by findings from our previous work [30], this research further investigates the potential of Sc–Zr microalloying as a strategy for improving the thermal stability and mechanical performance of 3xxx aluminium alloys for brazed heat exchangers

5.2 Materials and methods

Three Al–Mn 3xxx alloys were investigated: one base alloy and two alloys containing different Sc and Zr levels . The alloys were direct-chill (DC)-cast into extrusion billets with a diameter of 101 mm at the Arvida Research and Development Centre of Rio Tinto Aluminium in Saguenay, Quebec. Their chemical compositions, analyzed by optical emission spectroscopy, are presented in Table 5-1. The cast billets were subjected to a low-temperature heat treatment at 375 °C for 24 h to promote dispersoid and $Al_3(Sc,Zr)$ precipitation [33].

Table 5-1Chemical compositions of the DC cast alloys (wt.%).

Alloy	Si	Fe	Mn	Ti	Sc	Zr	Al
Base	0.09	0.40	1	0.01	-	-	Bal.
L-ScZr	0.10	0.40	0.98	0.02	0.11	0.10	Bal.
H-ScZr	0.10	0.40	1.01	0.02	0.21	0.15	Bal.

The treated billets were preheated to 480 °C using induction heating and extruded into MPE tubes. The extrusion ratio was 415. A standing wave water quench was applied immediately at the press exit. The ram operated at a speed of 3 mm/s. Test samples were cut from the MPE tubes and fed into a cold-rolling machine, where they were subjected to a 2% thickness reduction. The samples were then subjected to a simulated brazing cycle by heating from room temperature to 605 °C over 20 min, holding at 605 °C for 2.5 min, and then water-quenching. After the simulated brazing cycle, the samples were aged at 350 ºC for 4 hours to promote additional $Al_3(Sc, Zr)$ precipitation and improve the alloy's strength.

Microstructural characterization of the alloys was performed using an optical microscope (OM, Nikon-Eclipse ME600), a scanning electron microscope (SEM, JEOL 6480LV) and a transmission electron microscope (TEM, JEOL JEM -2100). For OM micrographs, samples were prepared with standard metallographic procedures. To examine the grain structure of the

MPE tubes, the polished samples were etched using Barker's electrolytic reagent (5 mL HBF_4 in 200 mL H_2O), allowing the grain structure to be revealed under polarized light. A TEM operated at 200 kV was used to observe the Mn-dispersoids and Sc/Zr-containing precipitates. The TEM samples were first mechanically ground and then electropolished using a twin-jet electro-polisher operated at 25V and -30 °C with 30 vol.% nitric acid and 70 vol.% methanol.

To evaluate the effect of Sc–Zr microalloying on tube strength, tensile tests were conducted on specimens after 2% thickness reduction and simulated brazing . Post-braze-aged specimens were also tested to assess the additional strengthening response. Tensile tests were performed directly on the MPE tube specimens with an overall length of 200 mm and a gauge length of 50 mm. The tests were conducted using an initial crosshead speed of 1.27 mm/min; after yielding, the speed was increased to 50.8 mm/min . The initial cross-sectional area of the MPE tube sample was determined using a mass-based approach according to $A = W/\rho L$, where A is the cross-sectional area (mm^2), W is the specimen weight (g), ρ is the density of aluminum (2.66×10^{-3} g/mm^3), and L is the specimen length (mm).

5.3 Results and discussion

5.3.1 Initial microstructure

Figure 5-1 presents representative optical and SEM micrographs of the as-cast base and H-ScZr alloys . All the three alloys exhibited similar microstructures, composed of an α-Al matrix and Fe/Mn-rich intermetallic particles with Chinese-script morphologies distributed along dendrite boundaries.

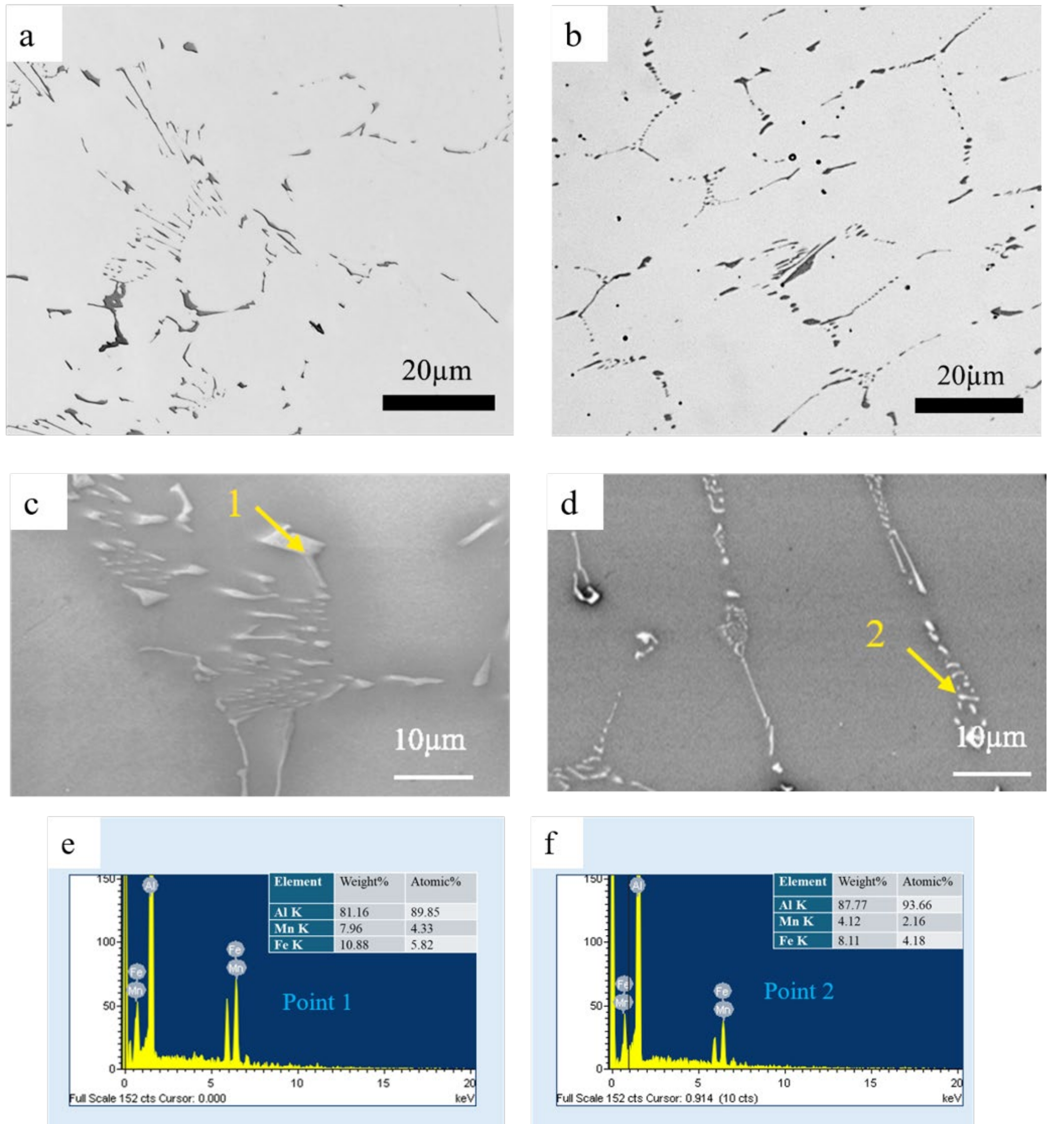

Figure 5-1(a, b) Optical micrographs (c,d) SEM images of as cast microstructures, a) the base and b) H-ScZr alloys. (e, f) Corresponding SEM-EDS spectra of the Fe/Mn-rich intermetallic particles shown in (c) and (d).

SEM-EDS indicated that the intermetallic particles were likely $Al_6(Fe,Mn)$. (see Fig. 5-1e,f). A similar Fe/Mn-rich intermetallic phase has also been reported in 3xxx aluminum alloys with comparable levels of Fe and Mn [31,32,33] . In both L-ScZr and H-ScZr alloys, only Fe/Mn-rich intermetallic particles were observed, no coarse primary Al_3Sc or $Al_3(Sc,Zr)$

particles were detected by SEM, suggesting that most Sc and Zr remained in solid solution or in particles below the SEM detection limit . This is consistent with what was reported by Li et al. [33] for alloys with comparable Sc and Zr contents.

5.3.2 Evolution of dispersoids and precipitates after low-temperature homogenization at 375ºC/24h.

Figure 5-2(a-c) shows the TEM images of Mn-containing dispersoids and the $Al_3(Sc, Zr)$ nanoprecipitates after the low-temperature homogenization at 375ºC/24h. The 375 °C treatment promoted the precipitation of Mn-containing dispersoids and $Al_3(Sc,Zr)$ particles, consistent with the findings of Li et al. [33]. A small amount of Mn-containing dispersoids were observed in the as-homogenized base alloy.

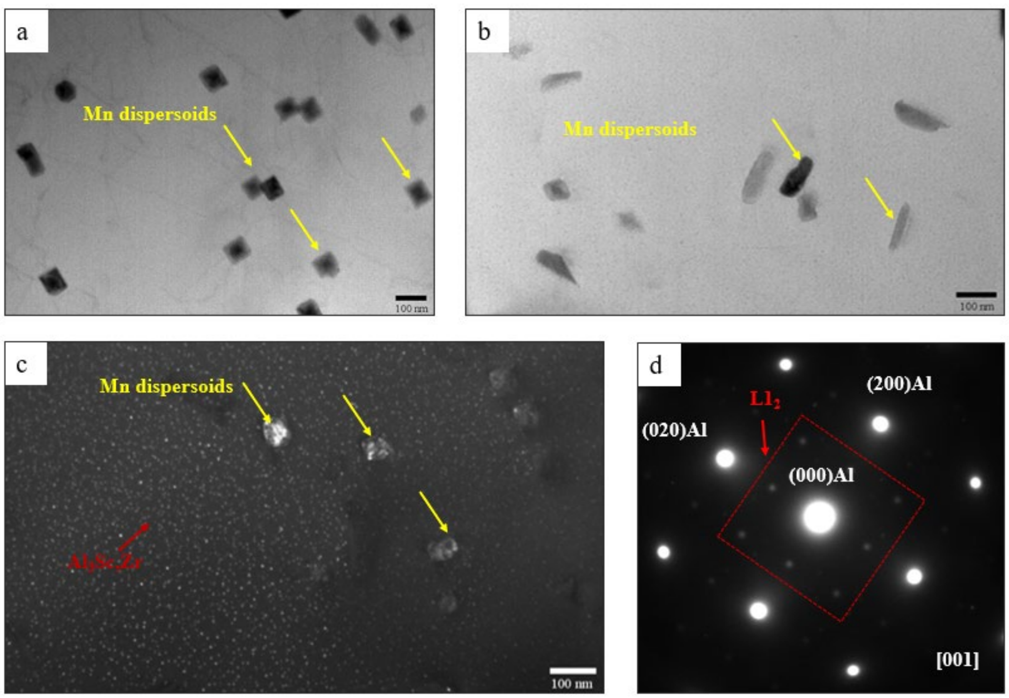

Figure 5-2 TEM micrographs of the as-homogenized precipitation microstructure (a) the base alloy, (b and d) H- Sc Zr alloy; (a, b) Bright-field images, (c) Dark-field image, and d) SAED pattern of the H- Sc Zr alloy.

According to Li et al. [34], the presence of Mg promoted the early precipitation of fine Mg_2Si nanoparticles, which could act as effective nucleation sites for the subsequent formation of Mn-containing dispersoids during homogenization. In the absence of Mg, Mn-rich dispersoid precipitation is less favourable, resulting in lower number density and volume fraction than in Mg-containing alloys. For brazed MPE-tube applications, Mg additions must be limited because excessive Mg can impair brazability and corrosion resistance [35,36].

In both L-ScZr and H-ScZr alloys, in addition to the Mn-containing dispersoids, a large number of $Al_3(Sc,Zr)$ nanoprecipitates were observed. The selected-area electron diffraction (SAED) pattern taken along the [001] zone axis (Figure 5-2d) shows weak superlattice reflections between the α-Al diffraction spots, confirming an $L1_2$ structure [37]. It can also be observed that fewer Mn-containing dispersoids were formed in the Sc-Zr alloys compared to the base alloy. This trend is consistent with reports [33,38] suggesting that Sc and Zr reduce Mn solubility in α-Al and promote Mn incorporation into coarse intermetallic phases. Consequently, less Mn solutes remained available in the solid solution to precipitate Mn-containing dispersoids during heat treatment.

5.3.3 Extrusion and braze of multi-port tubes

From an industrial standpoint, it is also important to evaluate how Sc and Zr microalloying influences the extrudability of the alloy. Figure 5-3 shows the breakthrough extrusion pressures of the three alloys defined as the maximum ram pressure required to initiate metal flow through the die [37]. The base alloy exhibited a breakthrough pressure of 2514 psi, whereas the L-ScZr alloy reached 2845 psi and the H-ScZr alloy reached 2988 psi, corresponding to the increases of 13.2% and 18.8%, respectively. Rometsch et al. [39] investigated the extrusion behavior of flat strips with the same chemical composition and homogenization treatment as the present study. They reported an increase in the mid-stroke ram pressure following Sc and Zr microalloying. In the present study, the mid-stroke ram pressure increased by approximately

11% for the L-ScZr alloy and 22% for the H-ScZr alloy compared with the 3xxx base alloy. Dorin et al. [40] reported that the breakthrough pressure of a binary Al-Cu alloy with the addition of 0.1 wt.% Sc and 0.15 wt.% Zr increased the extrusion breakthrough pressure by 9.1% relative to the base alloy.

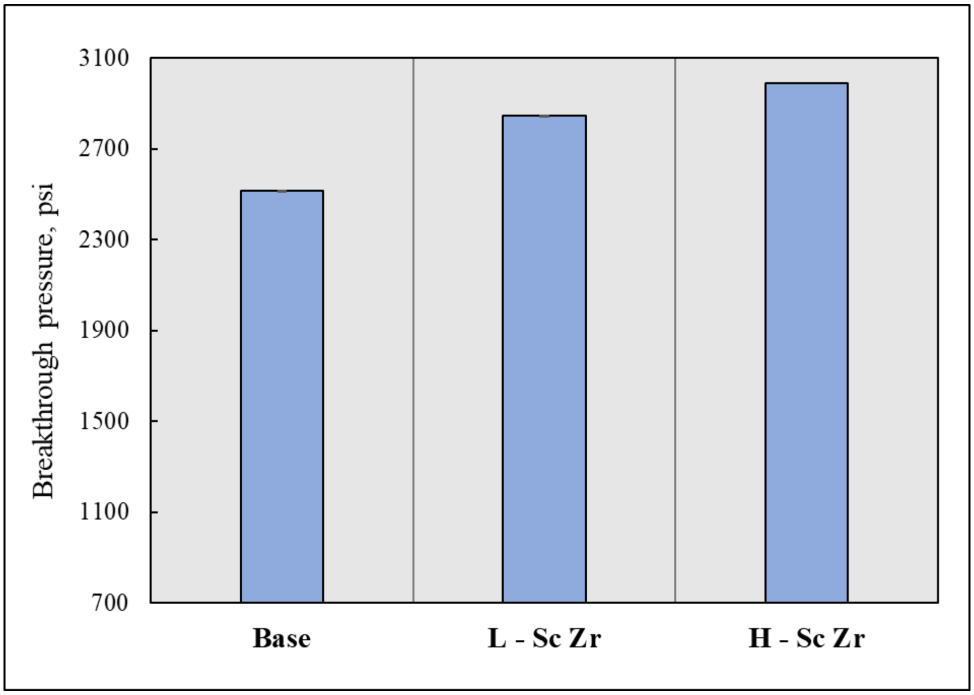

Figure 5-3 Breakthrough extrusion pressure of the three experimental alloys.

Figure 5-4 reveals the as-extruded grain structure of the cross-sections of the MPE tubes for the three investigated alloys. The base alloy (Figure 5-4a,b) exhibits a coarse, recrystallized grain structure. With the addition of Sc and Zr, the L-ScZr alloy (Figure 5-4c,d) shows a partially recrystallized but refined grain structure with a greater fraction of elongated, deformed grains . The H-ScZr alloy exhibited an even finer microstructure dominated by elongated, deformed grains (Figure 5-4e,f).

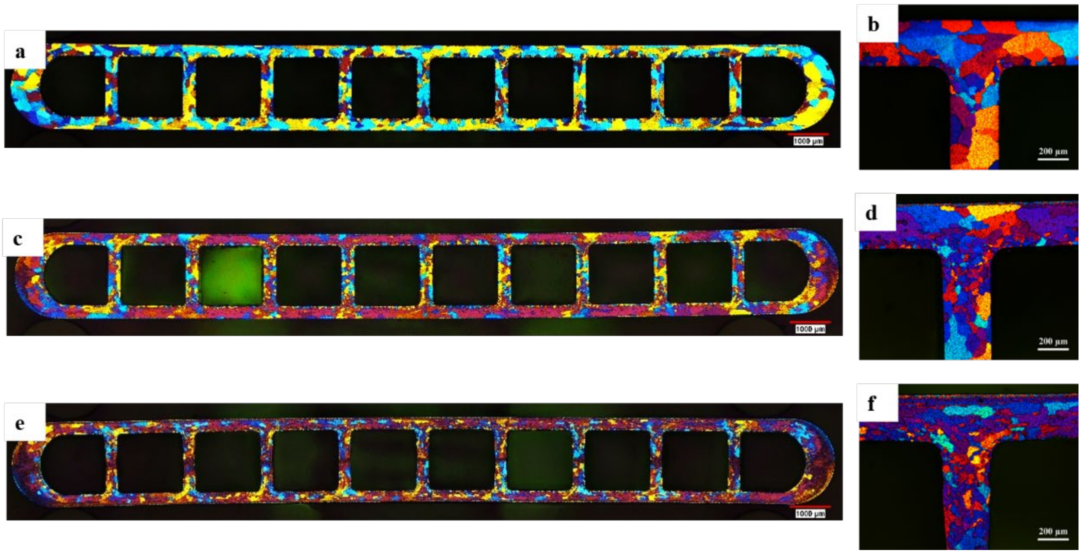

Figure 5-4 As-extruded grain structure of the base alloy (a, b), L-ScZr alloy (c, d), and H-ScZr alloy (e, f). Panels (a), (c), and (e) show the whole multi-port cross-sections, while panels (b), (d), and (f) show corresponding enlarged views.

Applying a 2% thickness reduction followed by brazing at 605ºC for 2.5 minutes produced extensive recrystallization and grain coarsening, with some local features of large grains , as indicated by the white arrow in Figure 5-5b. The grain coarsening is stimulated by the residual strain generated during the cold roll leveling for the thickness reduction [13,41]. Previous studies [6,13,14,42] consistently demonstrate that residual strain promotes extensive grain coarsening during brazing, resulting in substantial mechanical property degradation in multi-port extruded tubes. The L-ScZr alloy (Figure 5-5c,5-5d) exhibited slightly coarser grains in the outer wall of the tube compared to the as-extruded condition; however, the degree of grain coarsening remained less severe than that observed in the base alloy. In the intersection of the internal web and outer wall, the grains near the web–wall intersection remained similar in size to those in the as-extruded condition.

In contrast, the H-ScZr alloy (Figure 5-5e,5f) showed the greatest grain stability, with little visible change from the as-extruded condition. Such strong grain stability and resistance to recrystallization have also been previously reported in 3xxx microalloyed with Sc and Zr. For instance, Forbord et al. [43] reported that for an Al-Mn alloy containing 0.17 wt.% Sc and 0.13 wt.% Zr, cold-rolled samples were annealed from room temperature up to 550 ºC. Remarkably, the alloy retained a fibrous, un-recrystallized microstructure even at 550 ºC. In another study by Vlach et al. [44], a cold-rolled Al-Mn alloy containing 0.21 wt.% Sc and 0.17 wt.% Zr exhibited a complete suppression of recrystallization even after 32 hours of annealing at 550 ºC. In another study by Dong et al. [45], the recrystallization response of heavily cold-rolled Al-Mn-Sc-Zr-(Mg) sheets was evaluated at 590 ºC - a typical brazing temperature for Al-Mn alloys, showing that the grain growth was predominantly restricted by $Al_3(Sc, Zr)$ precipitates.

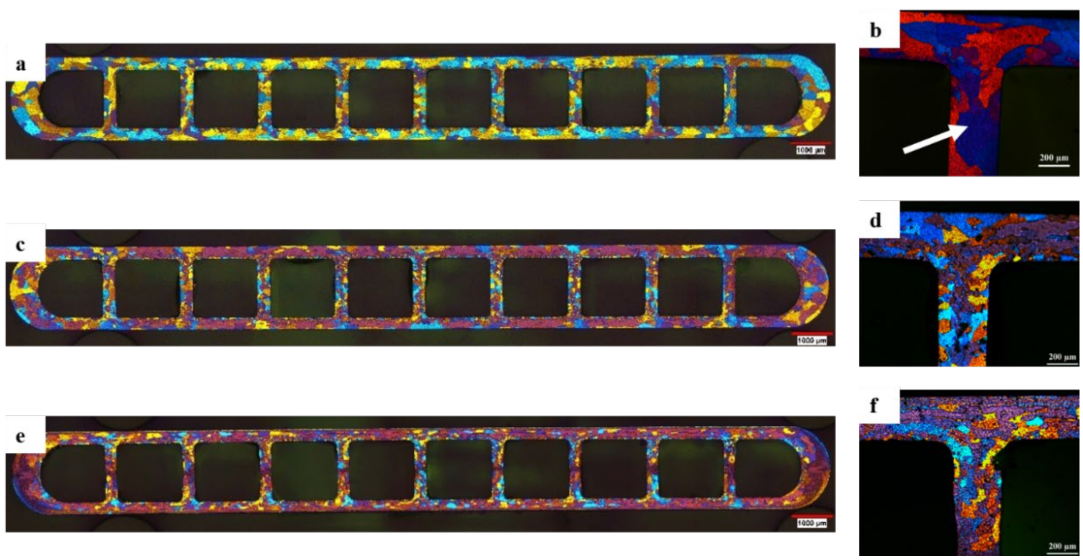

Figure 5-5 As-brazed grain structure of the base alloy (a, b), L-ScZr alloy (c, d), and H-ScZr alloy (e, f). Panels (a), (c), and (e) show the whole multi-port cross-sections, while panels (b), (d), and (f) show corresponding enlarged views.

5.3.4 Mechanical properties of the tubes after brazing and post-braze aging

Samples from the extruded MPE tubes were cut and subjected to 2% thickness reduction and brazing. Following brazing, the samples were subjected to post-braze aging. Tensile tests were performed in the as-brazed condition as well as after post-braze aging. The results are displayed in Figure 5-6, which reveals the mechanical response of the three alloys studied under both conditions.

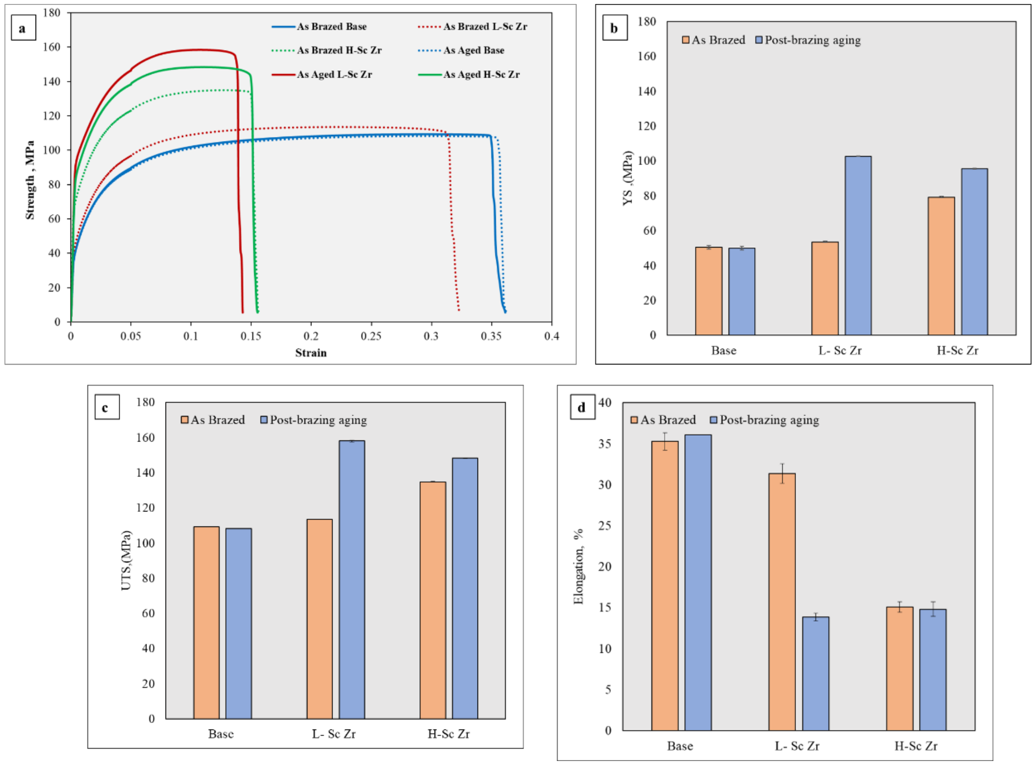

Figure 5-6 Tensile properties for the three alloys, (a) engineering stress-strain curves, (b) yield strength, (c) ultimate tensile strength, and (d) elongation to fracture.

Figure 5-6a shows the typical engineering stress-strain curves at both as-brazed and post-braze aged conditions. After brazing, the base alloy exhibited the lowest YS value of 50.5 MPa (Figure 5-6a). The low strength can be attributed to the limited grain stability. The Mn-rich dispersoids in the base alloy (Fig. 5-2a) were insufficient to suppress recrystallization and grain coarsening during extrusion and subsequent brazing. In comparison, the L-ScZr alloy showed a higher YS of 53.6 MPa, corresponding to a modest improvement of 6.1% over the base alloy. A more pronounced enhancement was observed in the H-ScZr alloy, which exhibited a YS of 79.3 MPa, representing an increase of 57.2%. The UTS followed a similar trend, increasing from 109.3 MPa in the base alloy to 134.75 MPa in the H-ScZr alloy, corresponding to an improvement of 23.2%. The strength improvements in the Sc/Zr-modified alloys are attributed to the presence of $Al_3(Sc,Zr)$ nanoprecipitates in addition to Mn-rich dispersoids ((Fig. 5-2b-c), which impeded dislocation motion and contributed to strengthening .

The YS and UTS values after post-braze aging are presented in Figure 5-6b-c. The base alloy exhibited almost no change compared with the as-brazed condition, maintaining a YS of ~50 MPa. In contrast, both Sc/Zr-containing alloys showed a remarkable increase in strengths after aging. The post-aged L-ScZr alloy reached a YS of 102.7 MPa, approximately 105% higher than the post-aged base alloy, whereas the H-ScZr alloy exhibited a YS of 95.5 MPa, representing an improvement of 91%. As demonstrated in prior investigations [16,47], aging within the 250-350 ºC temperature window promotes significant precipitation strengthening in alloys containing Sc/Zr due to the formation of fine $Al_3(Sc,Zr)$ precipitates.

Interestingly, the L-ScZr alloy exhibited a slightly higher post-aging strength than the H-ScZr alloy. This behavior can be attributed to the partial dissolution of $Al_3(Sc, Zr)$ precipitates during brazing at 605 ºC in the L-ScZr alloy, as its calculated Sc solvus temperature (~592 ºC) is below the brazing temperature. Consequently, more Sc may have remained in or returned to solid solution during brazing, leaving a greater solute reservoir for precipitation during post-braze aging . In contrast, the H-ScZr alloy, with a higher Sc solvus temperature (~655 ºC), retains a larger fraction of the $Al_3(Sc,Zr)$ precipitates formed during the 375 °C heat treatment, resulting in comparatively less solutes available for re-precipitation of fine $Al_3(Sc,Zr)$ particles during aging. Compared to the as-brazed condition, the post-brazing aging treatment resulted in an increase of approximately 49 MPa in YS for the L-ScZr alloy and about 16 MPa for the H-ScZr alloy.

The post-aged UTS values of the L-ScZr and H-ScZr alloys were 158 and 148.2 MPa, representing increases of approximately 46% and 37%, respectively, relative to the base alloy. The post-aged strengths obtained in the present study were higher than the as-brazed strengths reported in several studies; however, the different thermal treatments should be considered when interpreting this comparison. The values reported by Zhang et al. [48] are noticeably lower in YS but comparable in UTS. Their hot- and cold-rolled Al-Mn-Si-Zn alloy foil containing 0.2% Zr exhibited YS of 51.87 MPa and UTS of 142.10 MPa after a simulated brazing treatment at 600 ºC for 5 min. Shimosaka et al. [49] also reported that adding 0.1 wt.% Zr to an Al-Mn fin stock resulted in lower YS of only 43 MPa and UTS of 105 MPa after brazing at 600 ºC for 3 minutes. In another study by Cao et al. [46], it is reported that a 0.5 wt.% Cu-modified Al-Mn-Fe-Si alloy brazed at 600 ºC for 5 minutes attained a YS of 60 MPa and a UTS of 156 MPa. Under the conditions tested, the Sc/Zr-modified alloys exhibited higher YS and comparable or higher UTS than the cited Zr- or Cu-modified Al–Mn alloys.

From an economic standpoint, the amount of Sc addition is a key consideration in any Sc/Zr-modified aluminum alloys, because Sc is an expensive alloying element and a higher Sc level significantly increases material and production costs. Based on the overall results, it is evident that the low-Sc alloy provides a favourable balance between post-aging strength and Sc content. . For the H-ScZr alloy, the Sc content is 0.21 wt.%, which is almost double that of the L-ScZr alloy, and is therefore expected to significantly increase material cost. Not only does the L-ScZr alloy clearly outperform the base 3xxx alloy in terms of mechanical properties, but it also demonstrates higher strength than the H-ScZr alloy after aging.

5.4 Conclusions

This study evaluated the effects of Sc/Zr microalloying on extrusion pressure, grain stability, and mechanical properties of Al–Mn 3xxx MPE tubes subjected to sizing, brazing, and post-braze aging. Homogenized billets of three alloys were extruded into multi-port tubes and subjected to thickness reduction and high-temperature brazing. It was concluded that:

1) The 375 °C heat treatment promoted the precipitation of Mn-containing dispersoids in the base alloy and both Mn-rich dispersoids and $Al_3(Sc,Zr)$ particles in the Sc/Zr-containing alloys. The addition of Sc and Zr increased the extrusion pressure by

approximately 13% and 19% for the L-ScZr and H-ScZr alloys, respectively, relative to the base alloy.

2) Introducing a thickness reduction of 2% followed by brazing at 605ºC leads to pronounced grain coarsening in the base alloy. In contrast, both Sc/Zr-containing alloys showed improved grain stability.

3) After brazing, the base alloy exhibited a low YS of 50.5 MPa. In comparison, the L-ScZr alloy showed a higher YS of 53.6 MPa, representing 6% improvement relative to the base alloy, while the H-ScZr alloy exhibited a significantly higher YS of 79.3 MPa, corresponding to an increase of 57%.

4) After post-brazing aging at 350 ºC for 4 h, the base alloy showed almost no change compared to the as-brazed condition. In contrast, both Sc/Zr-containing alloys exhibited a pronounced strengthening response. The L-ScZr alloy reached a YS of 102.7 MPa (105% increase relative to the base alloy), while the H-ScZr alloy achieved a YS of 95.5 MPa, corresponding to an improvement of 91%. The L-ScZr alloy, containing approximately 0.1 wt.% Sc, provided the highest post-aging YS and may offer the most favourable performance-to-Sc-content balance among the alloys examined.

References

[1] C. Xia, S. Deng, C. Ni, Y. Ji, W. Zheng, J. Luo, W. Xu, W. Li, Y. Pang, Study on laminar structure and process on high strength brazed aluminum alloy for heat exchangers, Vacuum 215 (2023) 112303. https://doi.org/https://doi.org/10.1016/j.vacuum.2023.112303.

[2] Q. Cao, N. Zhao, C. Xia, Z. Zhang, L. Cheng, D. Zhou, Effect of brazing and artificial aging on the microstructure and mechanical properties of a high-strength four-layer laminar aluminum alloy, Vacuum 239 (2025) 114388. https://doi.org/https://doi.org/10.1016/j.vacuum.2025.114388.

[3] G.S. Cole, A.M. Sherman, Light weight materials for automotive applications, Mater Charact 35 (1995) 3–9. https://doi.org/https://doi.org/10.1016/1044-5803(95)00063-1.

[4] J.C. Guía-Tello, M.I. Pech-Canul, E. Trujillo-Vázquez, M.A. Pech-Canul, Effect of brazing parameters on fillet size and microstructure of cladded fin-microchannel tube joints, Transactions of Nonferrous Metals Society of China 30 (2020) 3240–3253. https://doi.org/https://doi.org/10.1016/S1003-6326(20)65457-7.

[5] Y.-S. Kim, I.-J. Park, B.-S. An, J.G. Park, C.-W. Yang, Y.H. Lee, J.-G. Kim, Improvement of corrosion penetration resistance for aluminum heat exchanger by alloying zirconium, Mater Chem Phys 241 (2020) 122275. https://doi.org/https://doi.org/10.1016/j.matchemphys.2019.122275.

[6] K.A.I. Li, T. Zou, D. Li, Y. Peng, D.A. Shu, On Formation of Abnormally Large Grains in Annealing Prestrained Aluminum Alloy Multiport Extrusion Tubes.

[7] Z. Yuan, Y. Tu, T. Yuan, Y. Zhang, Y. Huang, Effect of post-brazing heat treatment on the corrosion mechanism of sandwich multi-layered aluminium sheets, Vacuum 183 (2021) 109781. https://doi.org/10.1016/j.vacuum.2020.109781.

[8] J. Lacaze, S. Tierce, M.-C. Lafont, Y. Thebault, N. Pébère, G. Mankowski, C. Blanc, H. Robidou, D. Vaumousse, D. Daloz, Study of the microstructure resulting from brazed aluminium materials used in heat exchangers, Materials Science and Engineering: A 413–414 (2005) 317–321. https://doi.org/https://doi.org/10.1016/j.msea.2005.08.187.

[9] A. Kawahara, A. Niikura, T. Doko, Development of aluminum alloy fin stock for heat exchangers using twin-roll continuous casting method, Furukawa Review (2003) 81–87.

[10] L. Long, Q. Pan, M. Li, J. Ye, Y. Sun, W. Wang, Y. Luo, X. Li, Z. Peng, S. Liu, Study on microstructure and mechanical properties of 3003 alloys with scandium and copper addition, Vacuum 173 (2020) 109112. https://doi.org/https://doi.org/10.1016/j.vacuum.2019.109112 .

[11] K. Li, D. Li, T. Zou, D. Shu, D. Tang, Y. Peng, Strength Variation in Processing Multiport Extrusion Tubes of A1100 and A3102 Alloys, J Mater Eng Perform 28 (2019) 3576–3589. https://doi.org/10.1007/s11665-019-04132-w.

[12] C.N. Niu, X.G. Song, S.P. Hu, G.Z. Lu, Z.B. Chen, G.D. Wang, Effects of brazing temperature and post weld heat treatment on 7075 alloy brazed joints, J Mater Process Technol 266 (2019) 363–372. https://doi.org/https://doi.org/10.1016/j.jmatprotec.2018.11.023.

[13] G. Vamadevan, F.F. Kraft, Processing effects in aluminum micro-channel tube for brazed R744 heat exchangers, J Mater Process Technol 191 (2007) 30–33. https://doi.org/10.1016/j.jmatprotec.2007.03.040.

[14] D. Tang, X. Fan, W. Fang, D. Li, Y. Peng, H. Wang, Microstructure and mechanical properties development of micro channel tubes in extrusion, rolling and brazing, Mater Charact 142 (2018) 449–457. https://doi.org/10.1016/j.matchar.2018.06.010.

[15] F.F. Kraft, Method for Predicting and Optimizing the Strength of Extruded Multi-Void Aluminum Heat Exchanger Tube, SAE Transactions 111 (2002) 99–106.

[16] J. Royset, Scandium in Aluminium alloys overview: Physical Metallurgy, Properties and applications, Metallurgical Science AndTechnology 25 (2007) 11–21.

[17] J. Røyset, N. Ryum, Kinetics and mechanisms of precipitation in an Al-0.2wt.% Sc alloy, Materials Science and Engineering A 396 (2005) 409–422. https://doi.org/10.1016/j.msea.2005.02.015.

[18] J. Røyset, N. Ryum, Scandium in aluminium alloys, International Materials Reviews 50 (2005) 19–44. https://doi.org/10.1179/174328005X14311.

[19] Y. Wang, B. Xiong, Z. Li, Y. Zhang, H. Teng, Precipitation Behavior of Al3(Sc,Zr) Particles in High-Alloyed Al–Zn–Mg–Cu–Zr–Sc Alloy During Homogenization, Arab J Sci Eng 46 (2021) 6027–6037. https://doi.org/10.1007/s13369-020-05268-x.

[20] Z.H. Jia, J. Royset, J.K. Solberg, Q. Liu, Formation of precipitates and recrystallization resistance in Al-Sc-Zr alloys, Transactions of Nonferrous Metals Society of China (English Edition) 22 (2012) 1866–1871. https://doi.org/10.1016/S1003-6326(11)61399-X.

[21] Y. Sun, Q. Pan, Y. Luo, S. Liu, W. Wang, J. Ye, Y. Shi, Z. Huang, S. Xiang, Y. Liu, The effects of scandium heterogeneous distribution on the precipitation behavior of Al3(Sc, Zr) in aluminum alloys, Mater Charact 174 (2021) 110971. https://doi.org/https://doi.org/10.1016/j.matchar.2021.110971.

[22] J.-Y. Zhang, Y.-H. Gao, C. Yang, P. Zhang, J. Kuang, G. Liu, J. Sun, Microalloying Al alloys with Sc: a review, Rare Metals 39 (2020) 636–650. https://doi.org/10.1007/s12598-020-01433-1.

[23] B. Forbord, W. Lefebvre, F. Danoix, H. Hallem, K. Marthinsen, Three dimensional atom probe investigation on the formation of Al3(Sc,Zr)-dispersoids in aluminium alloys, Scr Mater 51 (2004) 333–337. https://doi.org/https://doi.org/10.1016/j.scriptamat.2004.03.033.

[24] C.B. Fuller, D.N. Seidman, D.C. Dunand, Mechanical properties of Al(Sc,Zr) alloys at ambient and elevated temperatures, Acta Mater 51 (2003) 4803–4814. https://doi.org/https://doi.org/10.1016/S1359-6454(03)00320-3.

[25] A.Y. Algendy, P. Rometsch, X.-G. Chen, Tailoring microstructure and mechanical properties of an AA5454 extruded aluminum alloy with Sc/Zr microalloying and processing conditions, Materials Science and Engineering: A 948 (2025) 149318. https://doi.org/https://doi.org/10.1016/j.msea.2025.149318.

[26] Y. Wang, Q. Pan, Y. Song, C. Li, Z. Li, Q. Chen, Z. Yin, Recrystallization of Al-5.8Mg-Mn-Sc-Zr alloy, Transactions of Nonferrous Metals Society of China 23 (2013) 3235–3241. https://doi.org/https://doi.org/10.1016/S1003-6326(13)62858-7.

[27] J. Ye, Q. Pan, B. Liu, Q. Hu, L. Qu, W. Wang, X. Wang, Effects of co-addition of minor Sc and Zr on aging precipitates and mechanical properties of Al–Zn–Mg–Cu alloys, Journal of Materials Research and Technology 22 (2023) 2944–2954. https://doi.org/https://doi.org/10.1016/j.jmrt.2022.12.133.

[28] Y. Qiu, X. Yang, J. Li, S. Xiang, J. Shi, J. Xu, R.E. Sanders, The influence of Sc and Zr additions on microstructure and corrosion behavior of AA5182 alloy sheet, Corros Sci 199 (2022) 110181. https://doi.org/10.1016/j.corsci.2022.110181.

[29] T. Dorin, M. Ramajayam, J. Lamb, T. Langan, Effect of Sc and Zr additions on the microstructure/strength of Al-Cu binary alloys, Materials Science and Engineering: A 707 (2017) 58–64. https://doi.org/10.1016/j.msea.2017.09.032.

[30] A. Bakr, P. Rometsch, X.-G. Chen, Effect of Sc and Zr microalloying on recrystallization behavior of 1xxx aluminum heat exchanger alloys during post-deformation annealing, Journal of Materials Science: Materials in Engineering 20 (2025) 84. https://doi.org/10.1186/s40712-025-00307-7.

[31] M. and K.S. and B.T. and K.S. and M.J. Vončina Maja and Petrič, Evaluation of EN AW 3003 Aluminium Alloy Homogenization with Specific Electrical Resistivity Measurement, in: S. Broek (Ed.), Light Metals 2023, Springer Nature Switzerland, Cham, 2023: pp. 294–301.

[32] Z. Yuan, Y. Tu, T. Yuan, Y. Huang, Y. Zhang, Effect of the interaction between Fe and Si on the precipitation behavior of dispersoids in Al–Mn alloys during homogenization, Vacuum 184 (2021) 109915. https://doi.org/https://doi.org/10.1016/j.vacuum.2020.109915.

[33] Z. Li, Z. Zhang, X.-G. Chen, Improvement in the mechanical properties and creep resistance of Al-Mn-Mg 3004 alloy with Sc and Zr addition, Materials Science and Engineering: A 729 (2018) 196–207. https://doi.org/https://doi.org/10.1016/j.msea.2018.05.055.

[34] Z. LI, Z. ZHANG, X.-G. CHEN, Effect of magnesium on dispersoid strengthening of Al—Mn—Mg—Si (3xxx) alloys, Transactions of Nonferrous Metals Society of China 26 (2016) 2793–2799. https://doi.org/https://doi.org/10.1016/S1003-6326(16)64407-2.

[35] H. Jin, M.S. Kozdras, B.S. Amirkhiz, S.L. Winkler, Liquid–Solid Interaction in Al-Si/Al-Mn-Cu-Mg Brazing Sheets and Its Effects on Mechanical Properties, Metallurgical and Materials Transactions A 49 (2018) 3091–3107. https://doi.org/10.1007/s11661-018-4670-8.

[36] H. Jin, Development of an Aluminum Brazing Sheet Product with Barrier Layer for High-Performance Automotive Heat Exchangers, Metallurgical and Materials Transactions A 52 (2021) 1409–1426. https://doi.org/10.1007/s11661-021-06172-1.

[37] T. Dorin, M. Ramajayam, A. Vahid, T. Langan, Aluminium Scandium Alloys, in: Fundamentals of Aluminium Metallurgy, 2018: pp. 439–494. https://doi.org/10.1016/B978-0-08-102063-0.00012-6.

[38] A.Y. Algendy, K. Liu, P. Rometsch, N. Parson, X.-G. Chen, Effects of AlMn dispersoids and Al3(Sc,Zr) precipitates on the microstructure and ambient/elevated-temperature mechanical properties of hot-rolled AA5083 alloys, Materials Science and Engineering: A 855 (2022) 143950. https://doi.org/https://doi.org/10.1016/j.msea.2022.143950.

[39] P. Rometsch, J. Fourmann, Potential for Using Scandium in Extrusion Alloys, in: Thirteenth International Aluminum Extrusion Technology Seminar & Exposition, Wauconda, IL, USA, 2024.

[40] T. Dorin, M. Ramajayam, T.J. Langan, Impact of Scandium and Zirconium on extrudability, microstructure and hardness of a binary Al-Cu alloy, Mater Today Proc 10 (2019) 242–247. https://doi.org/https://doi.org/10.1016/j.matpr.2018.10.402.

[41] D. Tang, X. Fan, W. Fang, D. Li, Y. Peng, H. Wang, Microstructure and mechanical properties development of micro channel tubes in extrusion, rolling and brazing, Mater Charact 142 (2018) 449–457. https://doi.org/https://doi.org/10.1016/j.matchar.2018.06.010.

[42] K. Li, D. Li, T. Zou, D. Shu, D. Tang, Y. Peng, Strength Variation in Processing Multiport Extrusion Tubes of A1100 and A3102 Alloys, J Mater Eng Perform 28 (2019) 3576–3589. https://doi.org/10.1007/s11665-019-04132-w.

[43] B. Forbord, H. Hallem, N. Ryum, K. Marthinsen, Precipitation and recrystallisation in Al–Mn–Zr with and without Sc, Materials Science and Engineering: A 387–389 (2004) 936–939. https://doi.org/https://doi.org/10.1016/j.msea.2003.10.374.

[44] M. Vlach, I. Stulikova, B. Smola, T. Kekule, H. Kudrnova, S. Danis, R. Gemma, V. Ocenasek, J. Malek, D. Tanprayoon, V. Neubert, Precipitation in cold-rolled Al–Sc–Zr and Al–Mn–Sc–Zr alloys prepared by powder metallurgy, Mater Charact 86 (2013) 59–68. https://doi.org/https://doi.org/10.1016/j.matchar.2013.09.010.

[45] Q. Dong, A. Howells, M.F. Gallerneault, V. Fallah, Precipitation-induced mitigation of recrystallization in ultra-thin, cold-rolled AlScZrMn(Mg) sheets at brazing temperatures: The critical effect of alloy composition and thermal processing route, Acta Mater 186 (2020) 308–323. https://doi.org/10.1016/j.actamat.2020.01.003.

[46] C. Cao, D. Chen, X. Fang, J. Ren, J. Shen, L. Meng, J. Liu, L. Qiu, Y. Fang, Effects of Cu addition on the microstructure and properties of the Al–Mn–Fe–Si alloy, J Alloys Compd 834 (2020) 155175. https://doi.org/https://doi.org/10.1016/j.jallcom.2020.155175.

[47] T. Dorin, M. Ramajayam, T.J. Langan, Impact of Scandium and Zirconium on extrudability, microstructure and hardness of a binary Al-Cu alloy, Mater Today Proc 10 (2019) 242–247. https://doi.org/10.1016/j.matpr.2018.10.402.

[48] J. Zhang, D. Ding, W. Zhang, S. Kang, X. Xu, Y. Gao, G. Chen, W. Chen, X. You, Effect of Zr addition on microstructure and properties of Al–Mn–Si–Zn-based alloy, Transactions of Nonferrous Metals Society of China 24 (2014) 3872–3878. https://doi.org/https://doi.org/10.1016/S1003-6326(14)63545-7.

[49] D. Shimosaka, M. Ueno, Effects of Si and Zr addition on strength and recrystallization behavior of Al-Mn alloy fin stocks for automotive heat exchanger, MATEC Web of Conferences 326 (2020) 5006. https://doi.org/10.1051/matecconf/202032605006.

Chapter 6
Conclusions, recommendations and publications

6.1 General conclusions

This thesis systematically established the effects of Sc and Zr microalloying on processability, grain stability, and mechanical performance in 1xxx and 3xxx aluminium alloys for brazed heat-exchanger applications. The principal conclusions of this thesis are as follows:

In the 1xxx alloys:

1) The low-temperature homogenization at 350 ºC/24 h promoted the formation of fine, thermally stable Al_3Sc and $Al_3(Sc,Zr)$ nanoprecipitates . Increasing the Sc and Zr contents increased precipitate number density while reducing the mean precipitate size, thereby improving grain stability during post-deformation annealing. The 0.07 wt.% Sc alloy retained a largely recovered, un-recrystallized structure only up to 500 ºC; the co-alloyed variant containing 0.07 wt.% Sc + 0.10 wt.% Zr maintained stability up to 550 ºC; and the high-Sc/Zr alloy containing 0.19 wt.% Sc + 0.15 wt.% Zr preserved its deformed structure even at 575 °C.
2) In extruded 1xxx strips and MPE tubes, Sc and Zr microalloying improved the alloy response during brazing. The base alloy showed recrystallization and abnormal grain growth whereas the 0.19 wt.% Sc ,0.15 wt.% Zr alloy, maintained fibrous or recovered microstructures. These stability improvements produced substantial strengthening: After brazing , the alloy with 0.19 wt.% Sc and 0.15 wt.% Zr alloy showed yield-strength increases of 104% under R1 (600 ºC homogenization) and 220% under R2 (350 ºC pre-age) relative to the base alloy. The alloy containing approximately 0.10 wt.% Sc and 0.10 wt.% Zr also showed greater grain stability and higher strength than the base alloy.

3) After post-braze aging, the high-Sc/Zr alloy reached 156.9 MPa (YS) and 195.7 MPa (UTS) under R1(600 ºC homogenization), compared with 140.9 MPa and 182.2 MPa under R2 (350 ºC pre-age). Alongside higher strength, this alloy exhibited improved corrosion resistance under R1 and maintained greater microstructural stability under both processing routes.
4) Among the two routes, R1 provided lower extrusion pressure together with strong post-braze mechanical performance and improved corrosion resistance, whereas R2 increased extrusion pressure because of the high number density of fine $Al_3(Sc,Zr)$ precipitates formed during pre-aging.
5) SWAAT testing was used to evaluate corrosion performance, particularly the risk of localized pitting and leakage in heat-exchanger tubes . Sc/Zr additions generally reduced pit penetration, particularly under R1. Their effect on total mass loss depended on the processing route and was less consistent under R2.

In the 3xxx alloys:

1) Sc-Zr microalloying produced consistent benefits across hot deformation, brazing, strip extrusion, and MPE-tube processing. After a 2% cold reduction and brazing at 605 ºC for 2.5 min, the base alloy exhibited abnormal grain growth and low hardness (40.4 HV), whereas the Sc-Zr alloys retained stable elongated or recovered grains and achieved higher hardness (up to 54.2 HV). Post-brazing aging at 350 °C for 4 h promoted $Al_3(Sc, Zr)$ precipitation, increasing the hardness by ~69% relative to the post-aged base alloy.
2) In the extruded 3xxx flat strips, the ram pressure increased by approximately 13.3% for the Ex-L-ScZr (0.11Sc+0.1Zr) alloy and by 17.8% for the Ex-H-ScZr alloy (0.21Sc+0.15Zr) compared to the base alloy. Mechanical testing revealed that the base alloy exhibited a low yield strength (YS) of 42 MPa after brazing. In

comparison, the Ex-L-ScZr alloy showed an improved YS of 70 MPa, while the Ex-H-ScZr alloy reached 89 MPa.

3) Following post-braze aging, a significant enhancement in strength was observed for the two 3xxx Sc/Zr-containing alloys due to the precipitation of fine $Al_3(Sc,Zr)$ nanoparticles. Relative to the post-aged base alloy, the YS increased by 156% in the Ex-L-ScZr alloy and by 191% in the Ex-H-ScZr alloy.

4) In brazed MPE tubes, homogenized at 600ºC, 4hrs, the 3xxx base alloy developed localized abnormal grain growth, whereas the Ex-L-ScZr tube showed a recrystallized equiaxed structure without evidence of AGG. In contrast, the Ex-H-ScZr alloy retained predominantly elongated grains, indicating greater resistance to recrystallization during brazing.

5) In the MPE-tube study, The low-temperature heat treatment at 375 °C promoted Mn-rich dispersoid precipitation in the base alloy and $Al_3(Sc,Zr)$ nanoprecipitation in the Sc/Zr-containing alloys.

6) Following a 2% thickness reduction and brazing at 605 ºC for 2.5 min, the base alloy MPE tube underwent severe grain coarsening, while the Sc–Zr-containing alloys showed substantially less grain coarsening than the base alloy.

7) Tensile testing of the extruded MPE tubes revealed that, after brazing, the base alloy exhibited the lowest strength (YS ≈ 50.5 MPa), whereas the L-ScZr alloy showed a slight improvement and the H-ScZr alloy demonstrated a significant increase in yield strength (≈79.3 MPa). Post-brazing aging at 350 ºC for 4 h resulted in almost no strengthening in the base alloy, while both Sc-Zr containing alloys exhibited a pronounced aging response, with yield strength increasing by up to ~105%.

6.2 Recommendations

Based on the findings of this thesis, the following directions are recommended for future work:

1) Determine the minimum Sc content needed to maintain grain stability during brazing while meeting service-strength requirements . Although Sc provides major improvements in recrystallization resistance and mechanical performance, it remains an expensive alloying addition. It is therefore important to identify the lowest effective Sc level that can still deliver the necessary grain stability during brazing and the required strength for service.
2) Optimize homogenization heat treatments to maximize the benefits of Sc and Zr. Since homogenization strongly influences the formation, size, and distribution of Al_3Sc and $Al_3(Sc, Zr)$ dispersoids, further work should determine the heat-treatment temperature and holding time that provide the best balance of precipitate stability, mechanical properties, and extrusion pressure.
3) Identify the processing conditions that allow the alloys to fully benefit from Sc-Zr microalloying. In particular, future work should examine how pre-aging conditions and extrusion parameters affect dispersoid evolution, grain stability, and mechanical properties.
4) For MPE-tube applications, include pressure-bearing capacity tests in future evaluations. While tensile properties of strips and tubes were thoroughly examined in this thesis, it is still recommended to perform pressure-bearing tests, including burst-pressure and pressure-cycling tests t to assess whether the tubes meet the pressure and leakage requirements for service.

5) Because corrosion resistance is critical to the durability of heat-exchanger tubes, future work should evaluate corrosion behaviour using SWAAT and compare the experimental alloys with conventional 3xxx heat-exchanger alloys..

6.3 List of publications

1) Bakr, A., Rometsch, P., Chen, XG. (2024). Hot Deformation Behavior and Post-brazing Grain Structure of Dilute Al–(Sc–Zr) Alloys for Brazed Heat Exchangers. In: Wagstaff, S. (eds) Light Metals 2024. TMS 2024. The Minerals, Metals & Materials Series. Springer, Cham. https://doi.org/10.1007/978-3-031-50308-5_143
2) Bakr, A., Rometsch, P., Chen, XG. (2024). Effect of Sc and Zr Microalloying on Grain Structure After Hot Deformation and Brazing in Al–Mn 3xxx Alloys. In: Wagstaff, S. (eds) Light Metals 2024. TMS 2024. The Minerals, Metals & Materials Series. Springer, Cham. https://doi.org/10.1007/978-3-031-50308-5_142
3) Bakr, A., Rometsch, P. & Chen, XG. Effect of Sc and Zr microalloying on recrystallization behavior of 1xxx aluminum heat exchanger alloys during post-deformation annealing. J Mater. Sci: Mater Eng. 20, 84 (2025). https://doi.org/10.1186/s40712-025-00307-7
4) Bakr, A., Rometsch, P., Chen, XG. Study of 1xxx aluminum extrusion alloys for brazed heat exchangers: Influences of Sc/Zr microalloying and thermomechanical processing, Journal of Materials Research and Technology, Volume 42,2026, Pages 3072-3090, ISSN 2238-7854 https://doi.org/10.1016/j.jmrt.2026.04.006 .
5) Bakr, A., Rometsch, P., Chen, XG., Assessment of the effects of Sc/Zr microalloying on Al –Mn 3xxx brazed heat exchangers: From lab scale to multi-

port tube extrusions, Materials Characterization, Volume 239,2026,116702, ISSN 1044-5803 https://doi.org/10.1016/j.matchar.2026.116702. .

6) Bakr, A., Rometsch, P., and Chen, X.-G. "The potential of Sc–Zr microalloying for improving grain stability and strength in 3xxx aluminium alloys used in brazed heat exchangers." Manuscript under internal review.

6.4 Scientific Posters

1) Effect of Sc on the extrusion process of 1xxx heat exchanger aluminium alloys. "Alyaa Bakr, Paul Rometsch, and X.-Grant Chen." REGAL Students Day, Canada, October. 2022.

2) Dilute Al–Sc–Zr alloy for the retardation of grain coarsening in 1xxx alloys designed for brazed heat exchangers "Alyaa Bakr, Paul Rometsch, and X.-Grant Chen." REGAL Students' Day, Canada, October. 2023. **(Awarded first prize).**

3) Effects of Sc and Zr Micro-additions on 1xxx Extrusions for Brazed Heat Exchangers "Alyaa Bakr, Paul Rometsch, and X.-Grant Chen." REGAL Students' Day, Canada, October. 2024